„Impedance-based battery monitoring"

Von der Fakultät für Elektrotechnik und Informationstechnik
der Rheinisch-Westfälischen Technischen Hochschule Aachen
zur Erlangung des akademischen Grades eines
Doktors der Ingenieurwissenschaften
genehmigte Dissertation

Diplom-Ingenieur (FH)

Oliver Sven Bohlen

aus

Zweibrücken

Berichter:

Professor Dr. rer. nat. Dirk Uwe Sauer
Universitätsprofessor Dr. ir. Rik W. De Doncker
Universitätsprofessor Dr.-Ing. Dr. med. Steffen Leonhardt

Tag der mündlichen Prüfung: 28.01.2008

This document has also been published by the
Shaker Verlag Aachen as:

Aachener Beiträge des ISEA

Herausgeber:

Univ.-Prof. Dr. ir. Rik W. De Doncker
Leiter des Instituts für Stromrichtertechnik und
Elektrische Antriebe der RWTH Aachen (ISEA)
52056 Aachen

D 82 (Diss. RWTH Aachen)

ISBN 978-2-8322-7606-5
ISSN 1437-675X

Shaker Verlag GmbH – Postfach 101818 – 52018 Aachen
Telefon: 02407 / 95 96 0 – Telefax: 02407 / 95 96 9
Internet: www.shaker.de – E-Mail: info@shaker.de

”Flat battery?” said Arthur.
”No,” said Ford, ”there is a moving disturbance in the fabric of space-time, an eddy, a pool of instability, and it’s somewhere in our vicinity.”
Douglas Adams: Life, the Universe, and Everything [1]

Vorwort

Nicht nur das Verhalten von Batterien ist manchmal schwer vorauszusagen. Ich hätte nicht gedacht, dass ich mich mit diesem Thema einmal etliche Jahre lang befassen würde, und noch weniger, dass es mich dazu nach Aachen – ins Rheinland ohne Rhein – verschlagen würde.

Trotzdem kam ich im Frühjahr 2001 an das Institut für Stromrichtertechnik und Elektrische Antriebe (ISEA) der RWTH Aachen. Dort entstand die vorliegende Arbeit während meiner Tätigkeit als wissenschaftlicher Mitarbeiter.

Prof. Dirk Uwe Sauer verdanke ich das Thema Energiespeicher, das zwar mich einige Nerven – und einigen Batterien das “Leben” – gekostet hat, sich aber nicht zuletzt dank seiner ausgezeichneten fachlichen Betreuung als Glücksfall für mich herausstellte. Prof. De Doncker gab mir als Institutsleiter die Möglichkeit, am ISEA zu arbeiten und zu lernen; dafür und für die Übernahme des Korreferats bin ich ihm zu Dank verpflichtet. Prof. Leonhardt gilt mein Dank für das gründliche und kritische Lesen meiner Arbeit als Korreferent.

Bedanken möchte ich mich auch bei meinen Kollegen Julia Kowal, Thomas Plum, Marc Thele und Tilman Sanders für das Korrekturlesen der Arbeit und die wertvollen Anregungen. Besonderer Dank gilt allen Hiwis, Studien- und Diplomarbeitern, die ich während meiner Zeit am ISEA betreuen durfte und von denen ich einiges lernen konnte. Insbesondere Holger Blanke, Holger Weber, Knut Kasper, Jens Oesterdiekhoff, Christian Linnemann und Christian Scharwächter haben dabei wesentlich zum Gelingen dieser Arbeit beigetragen. Holger Blanke war über seine Diplomarbeit hinaus jahrelang eine unentbehrliche Unterstützung im Labor.

Die Jahre am ISEA waren eine bereichernde und gute Zeit, sei es in fachlicher Diskussion mit und ohne Kaffee, im Labor oder am Kicker, im Hörsaal oder beim Wasserski. Ich durfte lernen wie man Batterien und Messtechnik testet, was Fastelovend und Puffel sind, wie man den Lousberglauf und die PESC04 übersteht, Schaltnetzteile und PPT-Präsenstationen baut und vieles mehr. Dafür möchte ich allen Kollegen danken, die für dieses spezielle Miteinander gesorgt haben. Ganz besonders gilt dies für die Batteriegruppe, die natürlich beste ”Randgruppe” des ISEA.

Meinen Eltern möchte ich an dieser Stelle danken, dass Sie mich stets unterstützt haben, das zu tun, an dem ich Freude habe.

Schließlich möchte ich ganz besonders meiner Frau Anja danken, die nicht nur die unzähligen Formelzeichen kontrolliert hat, sondern auch die wechselnden Launen eines Promovierenden ertragen durfte und mich oft genug mit Motivation und Keksen versorgte.

München, den 29. Juli 2008

Contents

Chapter 1

Introduction

Electrical storage devices and batteries in particular are essential in many applications. Most often, the function of the system depends crucially on the proper operation of the battery. In conventional vehicles, the electric load on the starter battery is continuously increasing due to the growing electrification in modern automotives. In electric and hybrid electric vehicles, the battery is an essential part of the electric drive train. A save operation of the energy storage system is only possible, if its state is monitored continuously.

Nevertheless, in many cases the state of the battery is assessed rather roughly or even not monitored at all. The main obstacle is the difficulty of such a task. A battery is a complex non-linear electrochemical system that is influenced by many parameters and that changes its properties due to ageing processes. For the analysis, however, only the cell voltage, the current and the external temperature are accessible to most measurement systems, since sensors for internal chemical or physical properties of the battery are not available at reasonable cost.

This thesis is a contribution to battery monitoring, i.e. the determination of the current state of the storage device during its operation. Impedance measurement – a well-established analysis method in battery research – is employed as a special technique to gather information about the internal state of the device.

Chapter 2 provides a brief overview of impedance spectroscopy, an analysis method widely used in electrochemistry and in many other fields of science. An introduction to the technology, the design and the electrical behaviour of the storage devices discussed in this thesis, namely the electrochemical double-layer capacitor (EDLC) and the lead-acid battery, is given in chapter 3.

Chapter 4 treats the aspect of impedance based battery diagnosis, beginning with a short definition of the key figures of merit - state of charge, state of health and pulse power performance - and a literature survey on impedance measurements for battery monitoring. Chapters 2 to 4 describe the state of the art.

In chapter 5 impedance spectroscopy is applied to the modelling and the diagnosis of the two storage technologies. For the EDLC, an ageing model was developed that predicts the change of the parameters of an impedance model over the complete life time of the devices. The results of extensive ageing test and the ageing model are described in section 5.1.

For the lead-acid battery, an impedance model is presented in section 5.2 that allows

the description of the battery behaviour during a pulse power discharge. In both sections the focus is on the determination of impedance model parameters from sparse impedance measurements, which is a prerequisite for efficient monitoring techniques.

Impedance spectroscopy normally requires expensive laboratory equipment. In order to employ this technique in mass market applications, special methods are necessary that yield reliable results even with cost-effective measurement instrumentation and under harsh environmental conditions. These measurement methods and algorithms are discussed in chapter 6. Section 6.1 provides a brief overview of the typical measurement instrumentation of a state-of-the-art battery monitoring system. In section 6.2 a novel method is proposed and presented in detail that meets the special requirements of robustness and computational efficiency in automotive battery management systems. In contrast to standard impedance measurement methods, this procedure operates passive, i.e. without a distinct excitation signal but with random noise or signals with a fluctuating frequency. Impedance measurements provide momentary information about the battery at its current state. Characteristic maps can be used to describe a battery characteristic over the complete operating range. The battery behaviour however changes due to ageing; efficient algorithms for tracking these changes and adapting the characteristic maps accordingly have therefore been developed, these are described in section 6.3.

In chapter 7, the results of the lab-based impedance analysis from chapter 5 are combined with the measurement techniques described in chapter 6. A monitoring system for double-layer capacitors in hybrid electric vehicles is described in section 7.1, impedance-based cranking capability-prognosis for starter batteries in conventional vehicles is given as an application example in section 7.2. For both applications, the measurement equipment and the algorithms are described in detail and exemplary measurement results are presented and discussed.

This thesis is concluded in chapter 8 with a summary and a critical discussion of the role of impedance measurements for battery monitoring. The target applications for the methods presented in this thesis are automotive systems. The novel passive impedance measurement technique and cranking capability prognosis are currently implemented in battery monitoring systems for series-production vehicles. Many of the concepts presented here are, however, generic and may be transferred to storage systems in other applications.

Chapter 2

Impedance spectroscopy

Impedance spectroscopy is a common analysis method in electrochemistry, but it is also applied in many other fields of science, such as medicine, biology, geology and many more. Some arbitrary examples are the analysis of corrosion processes [59], surface treatment of electrodes [164], non-invasive monitoring of human lung ventilation [101] and the determination of frost hardiness of trees [124]. The fundamental principles of impedance spectroscopy will be outlined in this chapter, yet always with focus on the analysis of electrochemical storage systems.

2.1 Fundamental concept

Impedance spectroscopy is a measurement method that allows determining the transfer function of a system in the frequency domain. The complex transfer function $\underline{H}(\omega)$ of a system connects the input or excitation signal $\underline{X}(\omega)$ with the output or system response $\underline{Y}(\omega)$, as illustrated in figure 2.1. It is often convenient to describe the system behaviour in the frequency domain, since differential equations that describe the system in the time domain pass into simple linear equations in the frequency domain. Moreover, analysis in the frequency domain provides an alternative view of the system that might reveal some properties better than in the time domain. The Fourier transform links the two domains and allows calculating the time response of a system from its frequency response and vice versa [10].

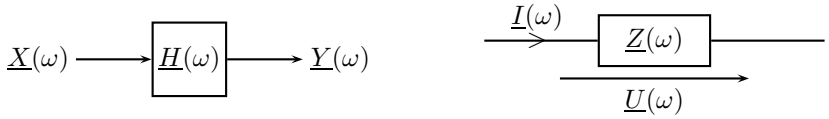

Figure 2.1: Transfer function (left) and impedance element (right).

For electrical and electrochemical systems, the impedance $\underline{Z}(\omega)$ is equivalent to the transfer function with the current $\underline{I}(\omega)$ as the input and the voltage $\underline{U}(\omega)$ as the output signal (cf. figure 2.1). Likewise, voltage can be interpreted as the input signal, current as the output and the reciprocal of the impedance, the complex conductance, as the

transfer function[1].

By imposing a sinusoidal current or voltage signal on the system and measuring the amplitude and phase shift of the output signal, the complex impedance for this frequency can be determined. This procedure is repeated for sufficiently many frequencies in the range of interest in order to derive a continuous spectrum.

One benefit of impedance spectroscopy is the fact that spectra measured on electrochemical systems can often be interpreted as the impedance spectra of lumped element models composed of the standard devices resistor, inductor and capacitor. These models can be used to distinguish real electrochemical effects in the system from each other, such as the ohmic resistance caused by grids and electrolyte in a battery from the charge transfer reaction that appears as a resistor in parallel to the double layer capacitance. Moreover, the models can be used to implement fast and highly dynamic simulation models [29, 78, 89].

Strictly spoken, this approach is only applicable to linear, time-invariant (LTI) systems. However, the method can be extended to non-stationary and non-linear systems such as batteries by restricting the measurement range to quasi-stationary operation and piece-wise linearisation. Section 2.5 describes the typical measurement procedure of impedance spectroscopy on batteries and similar storage systems and explains how a non-linear system is measured by proper biasing of the test signal. A method to check whether quasi-stationary conditions were maintained is presented in section 2.7.

2.2 Nonlinearity

Many electrochemical and physical processes are non-linear. For electrical systems this means that the voltage is a non-linear function of the current, or vice versa. A typical example in electrochemistry is the Butler-Volmer characteristic of the charge transfer reaction, depicted in figure 2.2 with typical values for the positive electrode of a lead-acid battery (cf. section 3.2.3). For large positive (charging) or negative (discharging) currents, the voltage increases logarithmically with current in contrary to a linear (ohmic) resistance, that would be represented by a straight line. Moreover, the current-voltage characteristic is asymmetric, i.e. charging and discharging with the same current results in different absolute values of the overpotentials.

This non-linear relationship requires a refined definition of the resistance. The non-linear small-signal resistance equals the slope of the characteristic curve:

$$R = R(I) = \frac{\mathrm{d}U}{\mathrm{d}I}. \tag{2.1}$$

For non-linear systems the small-signal resistance R differs from the large signal resistance $R_{\mathrm{LS}} = U/I$. The right hand side of figure 2.2 illustrates this difference for the Butler-Volmer characteristic. The small-signal or differential resistance of the charge

[1] For non-linear systems the transfer function in some cases may not be one-to-one and thus not invertible. Grid corrosion in lead-acid batteries for example shows a pronounced maximum of the corrosion rate and the corresponding current at a certain electrode potential; the current is uniquely defined by the potential, but not vice versa [138].

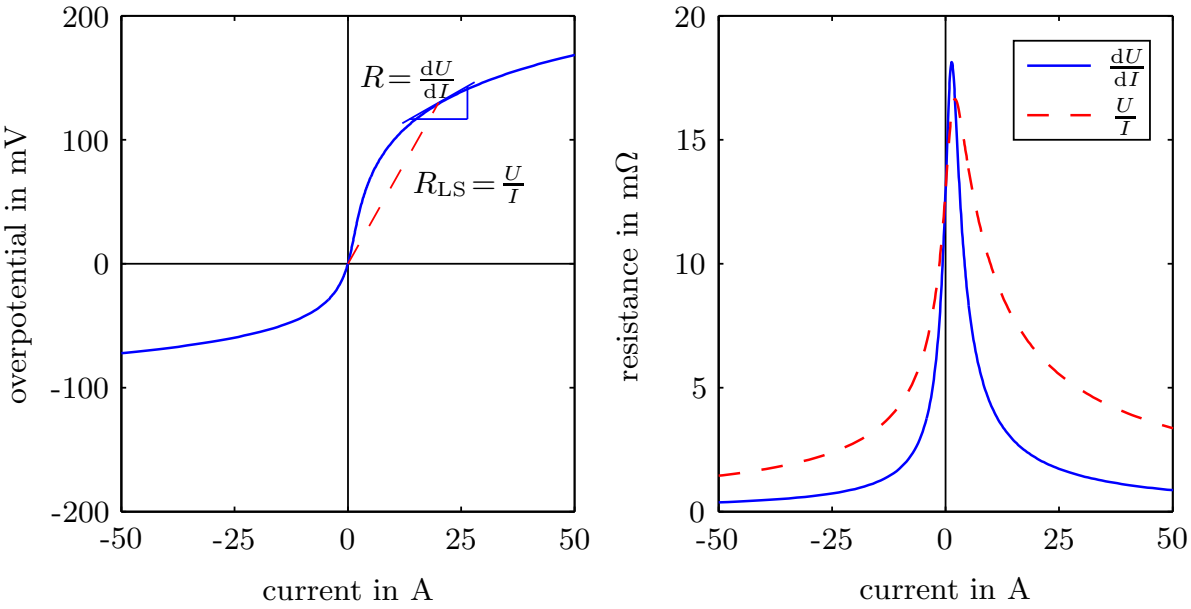

Figure 2.2: Non-linear current-voltage-characteristic (left), small-signal and large-signal resistance (right) according to the Butler-Volmer-equation ($j_0 = 2\,\mathrm{mA/m^2}$, $\alpha = 0.3$, $A_{\mathrm{eff}} = 500\,\mathrm{m}^2$, n = 2, cf. section 3.2.3).

transfer reaction was obtained by differentiating the current-voltage characteristic numerically with respect to I, the large-signal $R_{\mathrm{LS}} = U/I$ resistance is the pure ratio of voltage and current.

The voltage across a non-linear resistance element for a given direct current I_{DC} can then be re-obtained by integrating along the current:

$$U(I_{\mathrm{DC}}) = \int_0^{I_{\mathrm{DC}}} R(I)\,\mathrm{d}I. \tag{2.2}$$

Similar results can be obtained for a non-linear capacitance that can be observed e.g. if the equivalent thickness of the electrochemical double-layer, which determines the capacitance, varies with the potential drop across the double-layer (cf. section 3.1). While for a linear capacitor the voltage increases linearly with the amount of charge stored in the capacitor, a non-linear capacitance leads to a non-linear increase of the voltage if the capacitor is charged with a constant current. Non-linear inductances are of minor interest for the analysis of most electrochemical systems, they are however common in transformers and electric machines.

As a consequence, the result of an impedance measurement on a non-linear system depends on the amplitude of the excitation signal. The complex frequency dependent impedance is strictly spoken not defined for non-linear systems, since the Fourier-transform requires linearity. Yet, a small-signal impedance can be defined that equals the differential impedance at a certain operating point, i.e. a superimposed direct current or voltage.

The true small signal impedance can theoretically only be measured with an infinitesimal small excitation, which conflicts with a strong measurement signal and a

good signal-to-noise ratio required for practical measurements. A good compromise can be found if the signal is small enough that the non-linear behaviour can be linearised in the vicinity of an operating point. For most electrochemical systems this is the case if the amplitude of the voltage response is significantly smaller than the thermal voltage of about 26 mV at room temperature [93]. Accurate impedance spectrometers allow measurements with a voltage amplitude of 3 mV, thus satisfying the requirements on quasi-linearity for most measurements [78]. If the voltage or current amplitude of the excitation signal is too large, the result of the impedance measurement does not correspond to the true small-signal impedance but deviates depending on the shape of the non-linearity, the amplitude of the excitation signal and the operating point.

Another effect of the non-linearity is dispersion, i.e. the response of the system contains harmonics of the excitation frequency.[2] If the processing of the measurement data includes a Fourier analysis, the harmonic content can be eliminated. In the following, it is assumed that the impedance $\underline{Z}$ corresponds to the small signal impedance that was measured with a sufficiently small excitation signal.

The voltage response of a non-linear impedance cannot be analytically calculated, since the back-transformation into the time-domain is not defined for non-linear systems. Yet the non-linear characteristic of the components of an electrical equivalent circuit can be determined from impedance measurements. Impedance based simulations solve discrete lumped element models directly in the time domain [78].

For impedance based battery diagnosis, an understanding of the non-linear processes and the effect of the necessary linearisation is essential. Disregarding the differences between the small and large-signal impedance can lead to misinterpretations and parameterisation errors, as will be discussed in section 5.2 for the pulse-power performance of lead-acid batteries.

2.3 Spectral analysis

For an ideal linear system, measurement of the system response on a sinusoidal excitation signal would be sufficient for the determination of the impedance at the respective frequency. However, some sort of spectral decomposition of the signal is generally involved in an impedance measurement.

Even if the excitation signal is purely sinusoidal, the measured system response has signal contents of other than the fundamental frequencies. Firstly, non-linearity of the measured system creates harmonics of the measurement frequency that would distort the result if they were not excluded from the calculation of the impedance. Secondly, noise is always present in the measured signal, as well from the measurement system itself (inherent noise of resistors and amplifiers), the device under test (e.g. voltage fluctuations due to gassing in a lead-acid battery) or signals from external sources of noise such as the line frequency that couples into the measurement chain. Harmonics can be eliminated and the influence of measurement noise can be drastically reduced, if

[2] The occurrence of harmonics is in conflict with the concept of impedance. An impedance spectrum can be understood as the quotient of a voltage and a current spectrum. In a non-linear system, a sinusoidal current signal causes harmonics, i.e. the voltage spectrum has a finite amplitude at frequencies, where the current spectrum is zero, the quotient of both is thus undefined.

only the harmonic is extracted from the measured signal response. This task is normally achieved by a discrete Fourier transform (DFT).

If the excitation itself is not sinusoidal, a frequency decomposition of both the excitation as well as the response signal is inevitable. Excitation signals that are deliberately composed of several frequencies or even consist of broad-band noise are used in some impedance spectrometers in order to measure the complete spectrum at the same time instead of consecutively [8]. Another reason for a non-sinusoidal excitation signal is the use of a simple electronic switch as a cheap excitation source that can produce only a square-wave signal.

For passive impedance measurements that use the signals available in the system, the excitation signal is a priori unknown. For a fundamental study Robinson [127] used a standard laboratory spectrum analyser, yet for a commercial monitoring systems more cost-efficient solutions have to be found. In the passive impedance measurement method presented in section 6.2, the frequency decomposition is therefore accomplished by efficient digital filters that can be implemented on a microcontroller.

Since the digital Fourier analysis is in a way the competitor of the method proposed in section 6.2, it is described in more detail in the following section.

2.3.1 Discrete Fourier analysis

The classical method to derive impedance information from non-sinusoidal signals is the decomposition of the current and voltage signals with respect to frequency by means of a Fourier analysis. The Fourier analysis yields the amplitude and phase angle – or the real and imaginary part of the amplitude, which is equivalent – of both signals as a function of frequency. The complex impedance $\underline{Z}$ is the quotient of the voltage and current spectrum:

$$\underline{Z}(\omega) = \frac{\underline{U}(\omega)}{\underline{I}(\omega)} = \frac{\mathcal{F}\{u(t)\}}{\mathcal{F}\{i(t)\}} \tag{2.3}$$

with the angular frequency $\omega = 2\pi f$ as the parameter. The Fourier transform of variable $x(t)$ is defined as

$$\underline{X}(\omega) = \mathcal{F}\{x(t)\} = \int_{-\infty}^{+\infty} x(t) \cdot e^{-j\omega t}\,\mathrm{d}t. \tag{2.4}$$

Numerically, the continuous Fourier transform cannot be calculated, since the integration limits are infinite and first of all because the variable $x(t)$ can only be measured at discrete time instances. Generally, a periodic sampling of x with the sampling frequency $f_\mathrm{s} = 1/\Delta t$ is assumed, which yields a series x_n, with $n = 0, 1, 2 \ldots N$ which is equal to $x(t)$ at times $t = 0, \Delta t, 2\Delta t \ldots N\Delta t$. For such a series a discrete Fourier transform (DFT) can be calculated according to [116]

$$\underline{X}_k = \sum_{n=0}^{N-1} x_n \cdot e^{-j\frac{2\pi}{N}kn} \qquad \text{for} \qquad k = 0, 1, 2 \ldots N-1. \tag{2.5}$$

The discrete Fourier transform is calculated over a limited time interval $0 \leq t \leq (N-1)\cdot t$ which has two main consequences. First, the Nyquist-Shannon theorem limits

the maximum frequency to $f < f_s/2$, thus only values of $k < N/2$ yield non-redundant information. Second, the DFT implicitly assumes periodicity with Δt in the time and f_s in the frequency domain, respectively. The results of the discrete Fourier transform are therefore equal to the corresponding continuous transform at the discrete frequencies

$$\underline{X}_k = \underline{X}(\omega = 2\pi \frac{k f_s}{N}) \qquad \text{for} \qquad k = 0, 1, 2 \ldots, k < N/2. \tag{2.6}$$

For the calculation of the DFT methods were developed, that are much more efficient with respect to computation effort than the direct form of equation 2.5 suggests. However, these Fast Fourier Transforms (FFT) still require the storage of the complete data series x_n.

An application of the FFT for impedance spectroscopy is the use of white noise as a test signal. White noise is a random signal with a flat spectrum, i.e. it contains all frequencies with the same amplitude[3]. By means of a complete DFT of both the excitation signal and the system response the complete impedance spectrum can be derived from one measurement [93]. Though this type of measurement may seem attractive due to the shorter measurement time, it implies many difficulties in practice. Apart from the computational effort for the FFT, the signal power for each frequency is low and the amplitude of the excitation signal cannot be easily adapted to the impedance, which is a standard technique of modern impedance spectroscopes [8].

If not a complete spectrum has to be calculated but merely a few, well defined frequencies, a single point DFT for each frequency employing the direct method according to equation 2.5 may be the most efficient choice. Since the sums for each frequency can be updated in real time, the storage of the complete time series data is not necessary, which is often more crucial for embedded systems.

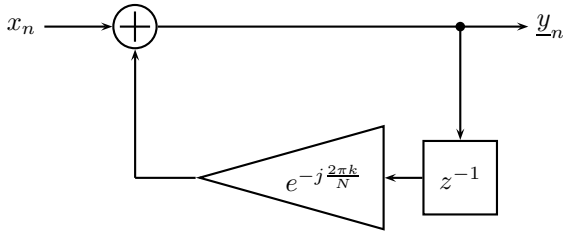

Figure 2.3: Block diagram of a recursive DFT implementation.

A single point DFT as a method to determine the real and imaginary part of a signal of a certain frequency is useful if the current and voltage spectra show peaks at distinct and constant frequencies, such as harmonics in a grid-coupled device.

Instead of using the direct method (cf. equation 2.5), a discrete Fourier transform (DFT) can efficiently be performed using recursive algorithms [116]. Figure 2.3 shows a simple recursive system as a block diagram, composed of the three elements addition $\bigoplus$, multiplication with a constant $\triangleright$ and a unit delay memory $\boxed{z^{-1}}$. The element z^{-1} can also be interpreted as a storage cell that delays the propagation of the signal by one

[3]True white noise cannot be realised by any technical system, at least the maximum frequency is limited by the bandwidth of the system. In practical band limited white noise shows a flat spectrum within a given frequency range.

time step, its initial value is zero. Thus the output $\underline{y}_n$ is fed back to the input with a complex factor of $e^{-j\frac{2\pi k}{N}}$. The output of the system thus is

$$\begin{aligned}
\underline{y}_0 &= x_0 \\
\underline{y}_1 &= x_1 + x_0 \cdot e^{-j\frac{2\pi k}{N}} \\
\underline{y}_2 &= x_2 + x_1 \cdot e^{-j\frac{2\pi k}{N}} + x_0 \cdot e^{\left(-j\frac{2\pi k}{N}\right)^2} \\
&\vdots \\
\underline{y}_{N-1} &= x_{N-1} + x_{N-2} \cdot e^{-j\frac{2\pi k}{N}} + \cdots + x_0 \cdot e^{\left(-j\frac{2\pi k}{N}\right)^{N-1}}.
\end{aligned} \tag{2.7}$$

The closed expression for time step $(N-1)$ is

$$\underline{y}_{N-1} = \sum_{n=0}^{N-1} x_{(N-1)-n} \cdot e^{\left(-j\frac{2\pi k}{N}\right)^n}. \tag{2.8}$$

This is equal to the definition of the DFT in equation 2.5, except that the series x_n is run through in reverse order, which does not affect the result. Due to the multiplication with the complex number $e^{-j\frac{2\pi k}{N}}$, this algorithm still requires four real additions and four real multiplications per time step.

2.3.2 The Goertzel algorithm

An even more efficient DFT method was developed by G. Goertzel in the 1950s. In [55] he presented a recursive algorithm for the calculation of a single point DFT that reduces the number of mathematical operations to a minimum. The discrete transfer function of the system of figure 2.3 is

$$\frac{\underline{y}_n}{x_n} = \frac{1}{1 - e^{-j\frac{2\pi k}{N}} z^{-1}}. \tag{2.9}$$

The nominator defines the recursive part of the algorithm, a multiplication with the complex conjugate $1 - e^{+j\frac{2\pi k}{N}}$ of both the denominator and the numerator yields an expression which is equivalent, but with a purely real denominator.

$$\begin{aligned}
\frac{\underline{y}_n}{x_n} &= \frac{1 - e^{+j\frac{2\pi k}{N}} z^{-1}}{(1 - e^{+j\frac{2\pi k}{N}} z^{-1}) \cdot (1 - e^{-j\frac{2\pi k}{N}} z^{-1})} \\
&= \frac{1 - e^{+j\frac{2\pi k}{N}} z^{-1}}{1 - 2\cos(2\pi k/N) z^{-1} + z^{-2}}.
\end{aligned} \tag{2.10}$$

The corresponding block diagram is shown in figure 2.4. The feed-forward part still contains a complex operation, but since only the result at $N = N - 1$ is of interest, this operation has only to be carried out once at the end of the computation. Only the recursive part of the Goertzel algorithm, which corresponds to the left part of figure 2.4, has to be carried out at each time step. The final result can be calculated from the last

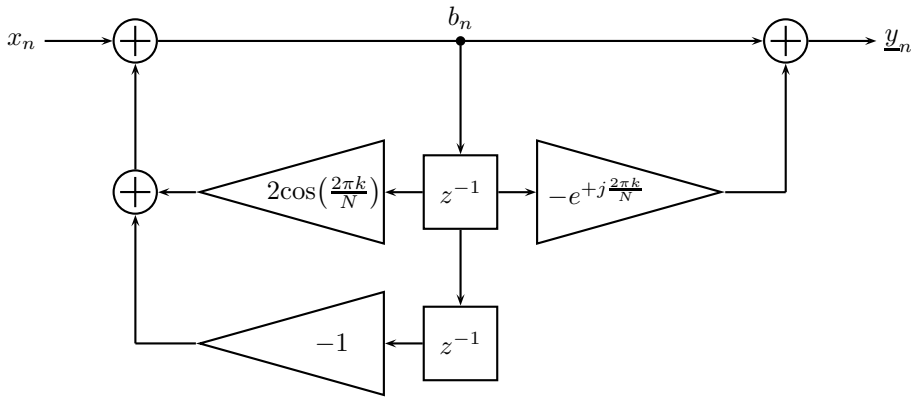

Figure 2.4: Block diagram chart of the Goertzel algorithm.

two values of the auxiliary variable b_n according to $\underline{X}_k = \underline{y}_{N-1} = b_{N-1} - b_{N-2} \cdot e^{-j2\pi k/N}$. The real and imaginary part can thus be calculated as

$$X'_k = b_{N-1} - b_{N-2} \cdot \cos(2\pi k/N) \tag{2.11}$$

$$X''_k = b_{N-1} + b_{N-2} \cdot \sin(2\pi k/N). \tag{2.12}$$

It should be pointed out, that the expression $2\cos(2\pi k/N)$ is a real constant for a given frequency $f_k = f_s \cdot k/N$.

The recursive nature of the Goertzel algorithm is both its strength and weakness. It makes the algorithm highly efficient with respect to computation time and memory requirements, but makes it also sensitive to numerical instabilities since small rounding or truncation errors accumulate.

The direct implementation of the DFT according to equation 2.5 can be used in impedance spectroscopes for the calculation of the fundamental frequency. Since the measurement frequency is known, the coefficients can be calculated beforehand and only the sum of the DFT terms has to be stored, which leads to an efficient implementation. The computational effort can in principle be further reduced using the recursive algorithms presented above, provided that the numerical issues are considered. If the exact measurement frequency is not known beforehand, as for passive impedance measurements, other methods are more apt. If sufficient memory and computational power is available, the spectrum can be calculated at many frequencies using Fast Fourier Transform algorithms. A different approach that allows measuring in a limited frequency range and determining the effective measurement frequency afterwards is presented in section 6.2.

2.4 Measurement instrumentation

The impedance spectroscope that was used for the measurement presented in this thesis is the EISmeter, a measurement device developed specially for measurements on batteries, double-layer capacitors and fuel cells at the Institute for Power Electronics and Electrical Drives (ISEA) of RWTH Aachen University [15, 16, 78]. The EISmeter operates in galvanostatic mode, i.e. it imposes a sinusoidal current on the device under test and measures its voltage response. By controlling the current, the state of charge of a

battery or capacitor can be kept constant, which is important for steady state operation especially at low frequencies. In order to operate at the best compromise between high measurement signal strength and low non-linear distortion, the current amplitude is controlled in such a way as to maintain a predefined amplitude of the voltage response for each measurement [78].

Seven measurement channels are available that allow for simultaneous measurements of up to seven series connected devices. Four DC current and four AC current modules can be connected to obtain a current range of up to 40 A DC and 4 A AC excitation [15, 16]. For higher DC currents external test benches can be connected in parallel to the EISmeter. Measurement frequencies between 7.5 kHz and 1 nHz can be measured, the latter being a rather theoretical limit since the measurement at such a low frequency would most likely exceed the lifetime of both the instrument and its operator [78]. The error limits of the EISmeter are less than 0.1 % of modulus and 1 ° of phase with respect to a calibration resistor for an impedance range of 500 μΩ to 4 Ω [133].

An important feature of the EISmeter for impedance spectroscopy on batteries or similar devices is the drift compensation that mathematically eliminates the effect of a linear change of the open circuit voltage that occurs if the battery is charged or discharged during the impedance measurement. Moreover, standard battery testing procedures such as constant voltage charging can be performed with the EISmeter; hence battery preconditioning and the impedance measurements can be combined in a test program that runs automatically without user intervention [16].

2.5 Measurement procedure

The measurement procedure for electrochemical impedance spectroscopy consists of two main parts: the adjustment of a quasi stationary condition at the operating point and the actual impedance measurement. The first is generally the most difficult and time consuming task and has a crucial impact on the quality of the measurement.

The adjustment of the condition for a battery includes the heating or cooling to test temperature and the setting of the state of charge by charging or discharging. A stable condition, however, can only be achieved if the system is allowed to settle after charging or discharging. Directly after the current is switched off, concentration gradients of the ionic charge carriers alter the battery behaviour. These gradients are reduced by diffusion processes; the necessary time depends strongly on temperature.

For the setting of the operating point, a constant DC current is imposed on the battery[4]. The definition of an operating point by means of a DC current is necessary to measure the non-linear impedance of electrochemical systems correctly (cf. section 2.2.). Imposing a DC current on the system though violates the requirement of stationarity by changing the state of charge of a battery or capacitor. The duration of the measurement is therefore limited by the amount of charge that can be charged to or discharged from

[4] A direct current is imposed in the case of galvanostatic measurements where an AC signal is used as excitation. For potentiostatic measurements an alternating voltage is superimposed onto a DC voltage.

the device without changing its behaviour significantly[5]. The available measurement time defines a lower limit to the frequency range for the measurement; for high DC current the measurement time is shorter and the lowest possible measurement frequency consequently higher [29, 168].

The measurement of the impedance spectrum is performed automatically by the spectrometer sequentially for each frequency, starting with the highest frequency and decreasing the frequency logarithmically for each measurement. A typical division is eight to ten frequencies per decade. Each frequency measurement is performed over at least three periods. The measured voltage response is converted by a digital Fourier transform and only the real and imaginary part of the signal at the fundamental frequency are used together with the known current amplitude to calculate the impedance.

2.6 Visualization of the measurement results

Two types of diagrams are most often used to present impedance data: semi-logarithmic presentation of the real and imaginary part of the impedance and the Nyquist diagram. Figure 2.5 shows an example of the semi-logarithmic representation of an impedance spectrum of a lithium-ion battery. This type of diagram allows a direct correlation of an impedance value with the corresponding frequency as well as, for example, the reading of the transition frequency where the imaginary part of the impedance becomes zero.

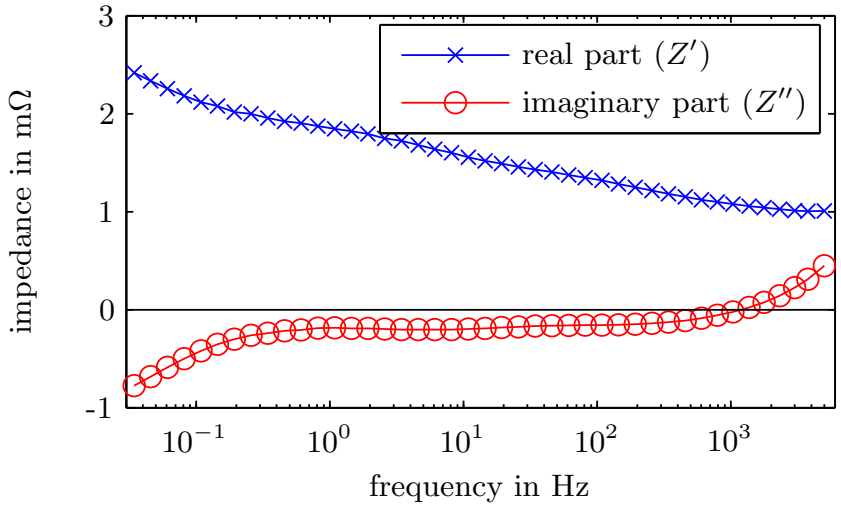

Figure 2.5: Semi-logarithmic representation of the impedance spectrum of a lithium-ion battery.

More common in electrochemistry is the Nyquist diagram that shows the impedance values in a coordinate system of the real and imaginary part. The real part of the impedance is plotted along the x-axis while the imaginary part is plotted along the y-axis in reverse direction, i.e. with the negative values above the origin. The latter takes

[5]As a rule of thumb a change of 5% state of charge during the measurement of one impedance spectrum can be accepted. However, especially at high and low states of charge, the battery behaviour is much more sensitive to charging and discharging, respectively, than at intermediate state of charge levels and thus much shorter measurement times may be necessary.

the fact into account, that the impedance of electrochemical systems is capacitive and thus negative over most of the frequency range of interest. Figure 2.6 shows an example for such a Nyquist diagram, presenting the same data as figure 2.5. The advantage of the Nyquist diagram is that typical patterns such as a semicircle – which corresponds to a parallel RC-circuit in a lumped element model – can be recognised easily if the axes are scaled equally. The disadvantage of the Nyquist plot is the lack of the frequency information, which can be compensated for to some extent by the labelling of data points, as in figure 2.6. Moreover, characteristic values such as the transition frequency $f_{\pm}$, the frequency where the imaginary part passes from positive no negative values, can be marked in the diagram. There are many more possible presentations of impedance data. Several types of 3D-plots are presented by J. R. Macdonald in [8]. These plots may give a better overview on the complex data; a quantitative reading from the diagrams is yet difficult.

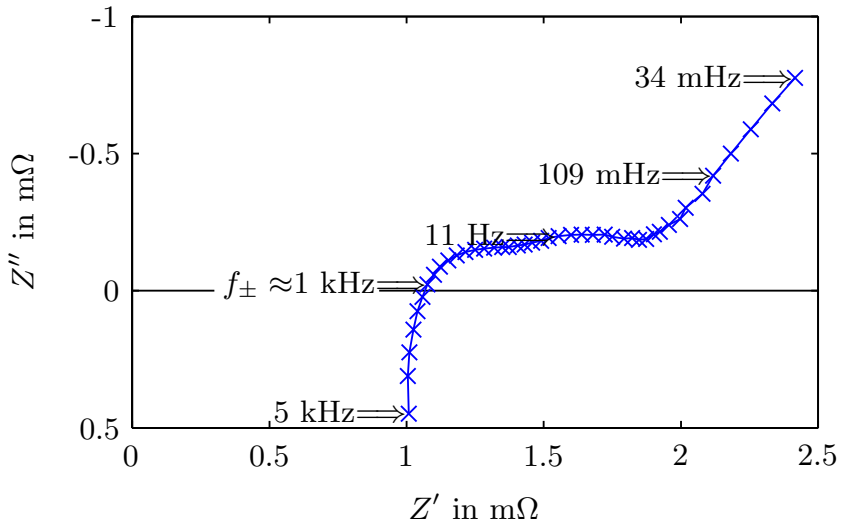

Figure 2.6: Nyquist diagram of the impedance spectrum of a lithium-ion battery.

2.7 Validation of the measurement

As discussed before, impedance measurements yield reasonable results only if certain requirements are met. These are especially linearity and stability of the system under investigation. However, the shape of the spectrum does not necessarily indicate deviations from these conditions. One possibility to check the validity of impedance measurements is the use of Hilbert (HIT) or Kramers-Kronig (KK) transforms [8, 116]. Real and imaginary part or modulus and phase of a complex spectrum are not independent from each other, if the system is a causal, linear, time invariant minimal phase system with a finite magnitude for $\omega \to \infty$ and $\omega = 0$. In this case, the imaginary part of the impedance can be calculated from the real part using the Hilbert transformation, or vice versa. The same is possible for modulus and phase [28].

Electrochemical systems are always causal minimum phase systems with a finite magnitude. A series inductance and a blocking electrode or series capacitance formally

cause infinite imaginary parts of the impedance at $\omega \to \infty$ and $\omega = 0$, respectively. However, physical systems always have a limited DC resistance that shunts the capacitor as well as a parasitic capacitance that compensates the inductive behaviour at very high frequencies. Only linearity and time invariance thus have to be tested.

The basic idea of validation methods employing one of these transformations is to determine one value from its counterpart and to compare this with the measurement. If the system has the properties mentioned above, the result of the transformation should be equal to the corresponding measurement values; if not, one or more of the requirements were violated.

The Kramers-Kronig transformations, that were proposed for the validation of impedance spectra by several authors [8, 28, 93, 175, 182] are given by the pair of equations

$$\begin{aligned} Z''(\omega) &= \frac{2\omega}{\pi} \int_0^\infty \frac{Z'(\nu) - Z'(\omega)}{\nu^2 - \omega^2} \, \mathrm{d}\nu \\ Z'(\omega) &= Z'(\omega \to \infty) + \frac{2\omega}{\pi} \int_0^\infty \frac{\nu Z''(\nu) - \omega Z''(\omega)}{\nu^2 - \omega^2} \, \mathrm{d}\nu \end{aligned} \tag{2.13}$$

that link the real part Z' and imaginary part Z'' of the impedance; ν is the integration variable of the angular frequency ω [28]. The main problem using the Hilbert and the Kramers-Kronig transformations is that they require an integration over the complete frequency range from 0 to ∞, while the measured spectrum is only available for a limited frequency range. Moreover, extrapolation of the measured spectrum over the complete frequency range can lead to erroneous results.

A method that addresses this problem was proposed by C. A. Schiller et al. [146, 147] under the name Z-HIT. The Z-HIT transform was deduced from the logarithmic Hilbert transform with a restriction to systems that show two-pole behaviour[6]. According to [146], the Z-HIT transform that delivers an estimate for the modulus of the impedance from the phase ϕ is given by

$$\ln\left(\frac{|Z_{\mathrm{ZHIT}}(\omega)|}{|Z(0)|}\right) = \frac{2}{\pi} \int_{\omega_\mathrm{s}}^{\omega} \phi(\nu) \, \mathrm{d}\ln\nu + \sum_{k \geq 1, k \text{ odd}} \gamma_k \frac{\mathrm{d}^k \phi(\omega)}{(\mathrm{d}\ln\nu)^k}. \tag{2.14}$$

The first term of the right hand side expression delivers the main contribution to the result and equals the logarithmic Hilbert transform. The angular frequency ω_s is the start frequency for the integration and normally equal to the maximum angular frequency of the measurement. The angular frequency ω is varied between the start frequency ω_s and the end frequency ω_e, which is the lowest angular frequency of the measured spectrum. The second term is a correction that compensates for the limited frequency range of the Z-HIT, a weighted summation of the odd derivatives of the phase with respect to angular frequency. The weighting factor γ_k is given by [146]

$$\gamma_k = \frac{2}{\pi} \zeta(k+1) 2^{-k} \quad \text{for} \quad k = 1, 3, 5, \ldots \tag{2.15}$$

[6] A two-pole shows no signal propagation delay between excitation signal and system response. Electrochemical systems show two-pole behaviour with respect to current and voltage.

where k is the order of the derivative and ζ is the Riemann Zeta function defined as

$$\zeta(x) = \sum_{n=1}^{\infty} n^{-x}. \tag{2.16}$$

The constant term $\ln|Z(0)|$ cannot be determined from the measurement data since impedance measurements are restricted to the frequency range above zero. However, comparison of the measured impedance modulus $|Z|$ and the results of the Z-HIT $|Z_{\mathrm{ZHIT}}|$ is still possible by choosing this constant in such a way that the difference of both curves is minimal and comparing the shape of the spectra. This can be accomplished by a linear regression that minimizes the sum of the squares of the differences between $|Z|$ and $|Z_{\mathrm{ZHIT}}|$.

Figure 2.7 shows an example for the Z-HIT validation. The left hand figure shows a successful reconstruction of the impedance spectrum, while the right hand figure shows a noticeable deviation for low frequencies. Both spectra were measured on a lithium-ion battery (Saft VL7P, 6.8 Ah, 3.6 V) with a superimposed DC discharge current of 6.5 A at room temperature, the left spectrum at approx. 5-10 % state of charge, the right spectrum near the completely discharged state. Analysis of the DC voltage during the measurement revealed that the battery voltage during the measurement of the left spectrum changed virtually linearly by 80 mV. The stability criterion was sufficiently fulfilled, the linear voltage change could be compensated by the measurement instrumentation[7]. During measurement of the right spectrum, the battery voltage changed by nearly 300 mV with an increasing gradient towards the end of the measurement. The battery behaviour close to its discharged state changes much faster and more non-linear than at higher states of charge, a quasi-stationary state was thus not obtained during this measurement.

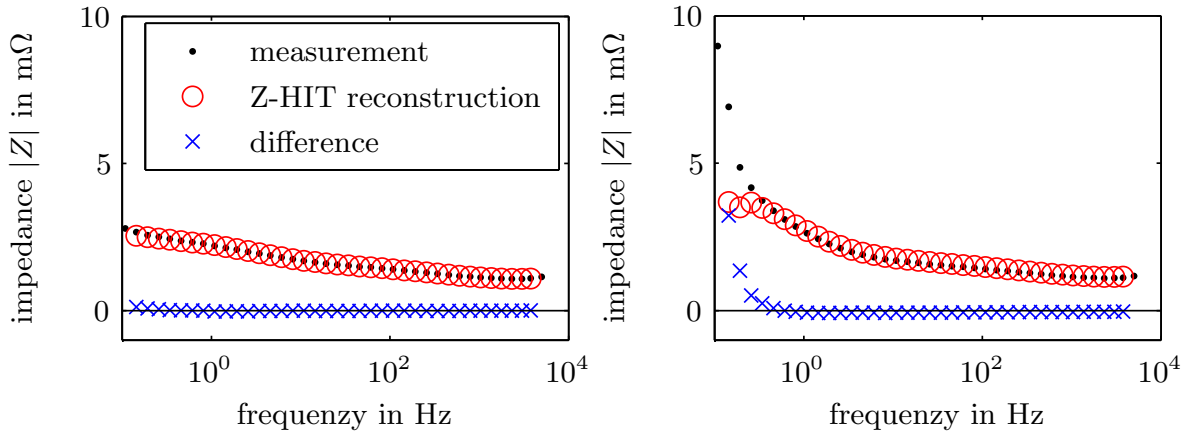

Figure 2.7: Example of the Z-HIT validation for impedance measurements for a quasi-stationary measurement (left) and a non-stationary measurement (right).

The validation of impedance spectra by Z-HIT or related procedures may reveal inconsistencies in the measurements that are not as easy to detect as in the example

[7]The impedance spectroscope (*ISEA EISmeter*) provides a so called drift compensation that corrects for errors caused by a linearly changing DC voltage (cf. section 2.4).

presented above. However, the procedure provides a necessary but not sufficient testing condition; the fact that the impedance modulus can be reconstructed from the phase does not guarantee correct measurement results.

2.8 Impedance models

An essential benefit of the characterisation of batteries and other electrochemical storage devices by impedance spectroscopy is the fact, that it allows both the derivation of the structure of impedance models and their parameterisation. Generally, an impedance model is the complex transfer function that links the current and voltage spectrum for frequencies $> 0\,\mathrm{Hz}$, as described in subsection 2.1. Most often, however, the term impedance model is used for lumped element models, i.e. models that can be described as an electric circuit diagram. With a model consisting of the basic elements resistor, inductor and capacitor virtually any measured impedance spectrum can be modelled.

A generic model, which is a good first attempt for most batteries, is shown in figure 2.8. The inductance L_s represents the inductive behaviour of the conductors and electrodes, the series resistance R_s subsumes the ohmic resistances of conductors, electrodes and also the electrolyte. The semicircles in the complex plane of the Nyquist diagram, which are typical for electrochemical storage devices, are caused by the electrochemical reactions and transport processes (cf. section 3.2.4). These can be modelled with a number of parallel RC-circuits connected in series.

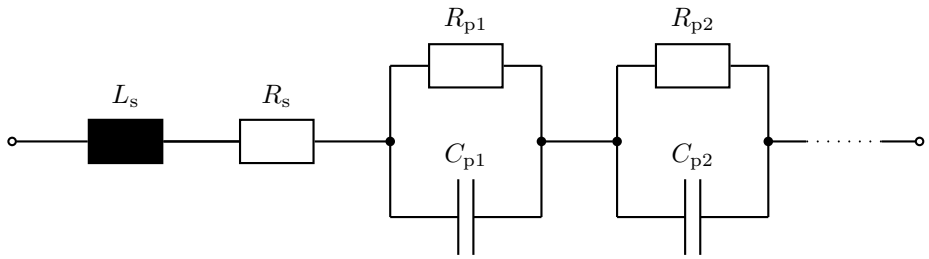

Figure 2.8: Generic impedance model.

The impedance can be expressed analytically as

$$\underline{Z} = j\omega L_\mathrm{s} + R_\mathrm{s} + \frac{R_{\mathrm{p1}}}{1 + j\omega R_{\mathrm{p1}} C_{\mathrm{p1}}} + \frac{R_{\mathrm{p2}}}{1 + j\omega R_{\mathrm{p2}} C_{\mathrm{p2}}} + \ldots + \frac{R_{\mathrm{p}n}}{1 + j\omega R_{\mathrm{p}n} C_{\mathrm{p}n}}, \qquad (2.17)$$

where n is the number of RC-circuits.

With the model described by figure 2.8 and equation 2.17, the dynamic overpotential of a battery can be simulated. For a model of the cell voltage, a voltage source has to be connected in series that represents the open circuit voltage, which is a function of state of charge and temperature[8] [78]. Moreover, for the modelling of self discharge and other charge consuming side reactions, a current path in parallel to the voltage source might be added to the model [29, 168].

[8]For some electrochemical systems, such as NiMH, the open circuit voltage also shows a path dependent hysteresis [159, 162, 167].

Figure 2.9 shows impedance data measured on a lead-acid starter-battery. The generic model with two RC-circuits has been fitted numerically to the data in a frequency range from 47 mHz to 2 kHz. The series resistance causes a frequency-independent offset of the real part of the impedance. The high frequency region, in this case above a transition frequency of $f_{\pm} \approx 200\,\mathrm{Hz}$, is dominated by the inductance. The first arc of the spectrum is modelled by an RC-circuit with a time constant $\tau_1 = R_{\mathrm{p1}} \cdot C_{\mathrm{p1}} \approx 6\,\mathrm{ms}$. For frequencies above 1 Hz (for this spectrum), the simplest model with one RC-circuit would have been sufficient. For an approximation of the low frequency branch, however, a second RC-circuit with a time constant $\tau_2 = R_{\mathrm{p2}} \cdot C_{\mathrm{p2}} \approx 6\,\mathrm{s}$ was necessary.

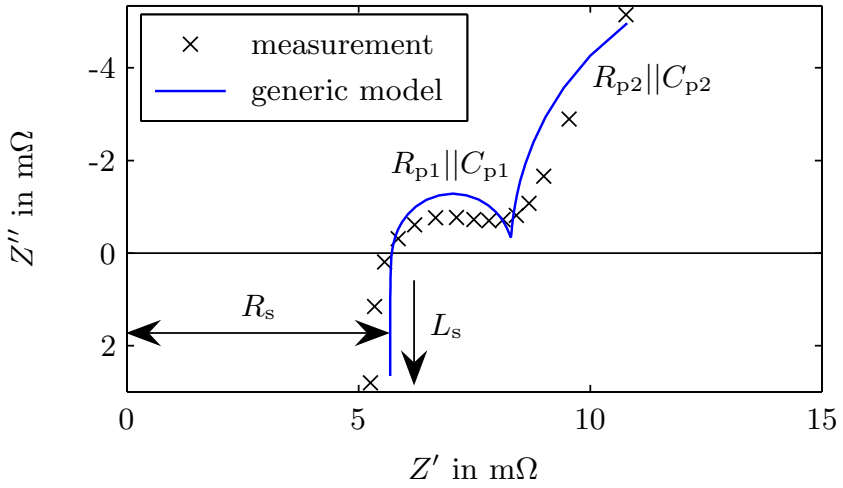

Figure 2.9: Spectrum of the generic impedance model with two RC-circuits fitted to impedance data measured on a lead-acid starter battery.

Figure 2.9 illustrates that the general form of a battery impedance spectrum can be approximated by a very simple model. Yet, it also shows that for a good match of measurement and model some improvements of the model are necessary (the first semicircle is considerably depressed and the low frequency arc is not represented very well by the second semicircle of the model).

Thus, based on this generic model numerous extensions and refinements have been developed. The stock of basic elements can be complemented by special elements. For the example above, the depressed semicircle could be modelled by a so-called ZARC-element, the low frequency branch by a Warburg-impedance (cf. section 3.2.4). A further example is the pore impedance introduced in section 3.1.3. These elements allow describing certain components of the transfer function with very few parameters instead of the large number of basic elements that would otherwise be necessary for a good approximation.

While the generic model mentioned above is heuristic, in analytical impedance spectroscopy the elements and parameters of the model are ascribed to chemical and physical processes. In this context, the model elements are assigned to the functional part of the system, such as the positive and negative electrode, the electrolyte and the conductors. This approach can be extended to a spatially resolved model. This spatial resolution requires special measurement techniques. A common method is the usage of reference

electrode which allows measuring two impedance spectra at the same time, one for the negative and one for the positive electrode.

The approach of a spatial resolution is not followed in this thesis, since the focus is on monitoring of commercial storage devices in technical systems, which normally does not allow for the insertion of reference electrodes.

Irrespective of the model structure, one of the main challenges for a good simulation model is the parametrisation of the model. For most electrochemical systems, the parameters depend on temperature, state of charge, state of health, cell (or half-cell) potential and current rate, the last two introducing a non-linearity, which is not inherent to the lumped element models [29, 78, 79, 93]. For an off-line simulation, these characteristics have to be described analytically or have to be stored in multi-dimensional look-up-tables. For monitoring systems, it is often sufficient to determine these parameters at the current state of the battery (cf. section 7.2), or to adapt the characteristics by learning algorithms during operation (cf. section 6.3).

2.9 Determination of model parameters

Analysis of impedance spectra generally means determining parameters of a model from the measured data. The standard procedure for this task is the least squares method. However, fitting of impedance spectra should be done for the imaginary and real part of the data simultaneously. This can be achieved by complex non-linear least squares (CNLS) fitting, which is basically a generalisation of the standard least squares method.

For a set of N experimental data points $Z'_{\mathrm{e},k}$ and $Z''_{\mathrm{e},k}$ measured at the frequencies ω_k, the model provides the data points $Z'_{\mathrm{m},k}(\omega_k, \mathbf{P})$ and $Z''_{\mathrm{m},k}(\omega_k, \mathbf{P})$, calculated at the corresponding frequencies ω_k and with a given set of parameters $\mathbf{P}$. The objective function to be minimised by a set of adequate model parameters is the sum of the squares of the distance of corresponding measurement and model data points in the complex plane [8, 28]:

$$S = \sum_{k=1}^{N} \left[w'_k \left(Z'_{\mathrm{e},k} - Z'_{\mathrm{m},k}(\omega_k, \mathbf{P}) \right)^2 + w''_k \left(Z''_{\mathrm{e},k} - Z''_{\mathrm{m},k}(\omega_k, \mathbf{P}) \right)^2 \right]. \tag{2.18}$$

The factors w'_k and w''_k were introduced to allow weighting of the data points. If the model describes the measured impedance spectrum well, good results can be achieved without weighting, i.e. with unity factors w'_k and w''_k. However, weighting can improve the results of fitting especially if the model describes the impedance spectrum only approximately and if the values of $Z'_{\mathrm{e},k}$ and $Z''_{\mathrm{e},k}$ exhibit large variation. Especially in the latter case weighting with $w'_k = (Z'_{\mathrm{e},k})^{-2}$ and $w''_k = (Z''_{\mathrm{e},k})^{-2}$, which assigns an equal influence to each data point irrespective of its absolute value, can improve the results [8, 94].

The determination of the parameter set $\mathbf{P}$ that yields a minimum of the objective function S is an optimization problem that can be solved in principal with a multiplicity of algorithms. Data fitting presented in this thesis was performed with the mathematical software *Matlab* using constrained non-linear optimization based on the Nelder-Mead simplex algorithm[9] [83, 97]. General purpose non-linear optimization algorithms such as

[9] The function *easyfit* [45] was used, that provides an interface to the built-in function *fminsearch* [97].

the Nelder-Mead algorithm may however find only local minima, sensible initial guesses and adequate bounds for the model parameters are therefore essential.

For relatively simple models it is often possible to acquire the parameters directly from basic geometric rules. The series resistance can often be estimated by the real part of the impedance at high frequencies, i.e. the offset of the graph with respect to the real axis. If a distinct semicircle is present in a Nyquist plot, which can be modelled by a parallel RC-circuit, the corresponding resistance equals the diameter of the semicircle and the topmost data point was measured at the characteristic angular frequency $\omega_0 = (RC)^{-1}$. This direct parameter estimation is less accurate than CNLS, but it can be used to find initial values for a fitting procedure [8]. Direct parameter estimation can also be employed where the computational effort involved with CNLS has to be avoided, as for the implementation of a real-time diagnosis system implemented on a microcontroller. An example of direct parameter estimation with focus on the resulting inaccuracies is discussed in section 5.1.3.

Chapter 3

Electrochemical storage devices

Impedance-based methods can be applied to virtually any electrochemical storage technology. In this section two storage technologies that have been analysed experimentally in the scope of this thesis will be introduced briefly. These two technologies are the electrochemical double layer capacitor (EDLC) and the lead-acid battery.

3.1 Electrochemical double-layer capacitor

Electrochemical double layer capacitors (EDLCs) - often informally called supercapacitors or ultracapacitors - are storage devices that have a structure similar to batteries, with two electrodes, electrolyte and a separator, but without a chemical reaction that converts electrical energy into chemical. Instead, the energy is stored solely in the electric field at the phase boundary between electrolyte and electrode[1], the electrochemical double layer. This fact is responsible for three main differences compared with batteries:

Low energy density Energy storage in an electric field has a relatively low energy density compared to energy stored in chemical bonds.

High power density No reaction kinetic limits the current flow. Additionally, the absence of active material allows for a more extensive optimisation of the electrodes with respect to internal surface and conductivity than in batteries.

High cycle life The chemical composition and morphology of neither the electrodes nor the electrolyte is changed by charging or discharging, thus imposing virtually no cycling stress on the EDLC. Deterioration of EDLCs is mainly caused by inevitable side reactions that depend almost only on temperature and cell voltage.

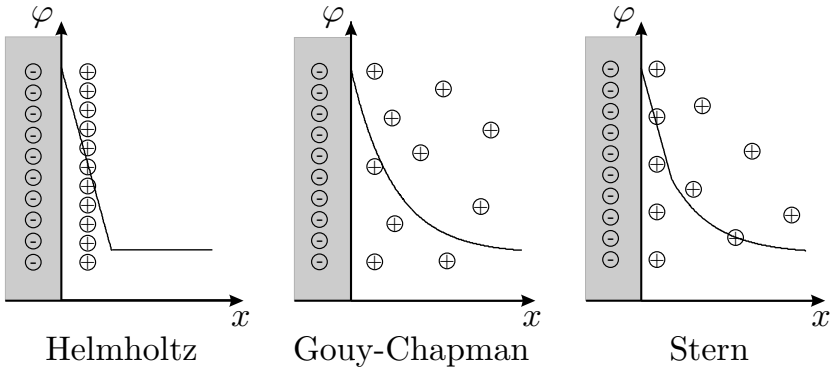

Figure 3.1: Electrochemical double layer and the corresponding potential according to the Helmholtz , Gouy-Chapman and Stern model (from [37, 89]).

3.1.1 The electrochemical double layer

The electrochemical double layer is formed at the interface between the electrolyte and the electrode if a voltage is applied to the EDLC. The excess charge at the surface of the electrode is balanced by ions of the electrolyte in the vicinity of the solid-electrolyte interface. The charge carriers of opposite polarity attract each other. However since no electrochemical reaction takes place, electrons may not cross the boundary and compensate the excess charge. Moreover, charge carriers inside the electrode and the ions in the solution keep a certain distance from each other resulting in an effective capacitance.

Several phenomena contribute to the double layer capacitance, the two predominant effects can be subsumed to the compact and the diffuse layer. The compact layer was first described by Helmholtz. The basic idea of the Helmholtz model is a compact layer of ions at the surface of the electrode, the thickness of the Helmholtz layer is thus determined by the effective ion radius.

A second contribution to the double layer is the diffuse layer described by the Guoy-Chapman model that takes the thermal fluctuation of charge carriers into account. The model was derived from Boltzman's energy distribution and Poisson's equation of the electrostatic field and results in a charge density that decreases exponentially with the distance from the electrode surface. The contribution to the double layer described by the Gouy-Chapman model is therefore referred to as the "diffuse" layer in contrast to the "compact" Helmholtz layer (cf. figure 3.1). A comprehensive theory of the double layer that takes the finite ion radius as well as the thermodynamics into account is the Stern theory, which describes both the compact and the diffuse layer [37, 149].

The effective thickness of the diffuse layer and thus its effective capacitance depends significantly on temperature and ion concentration. However, its contribution to the overall double layer capacitance is small in electrolytes with a high ion concentration, as in the case of EDLCs. The compact layer also shows a dependency on temperature

[1]Depending on the materials used, additional effects such as adsorption or intercalation contribute to energy storage. The resulting charge-voltage characteristic is often non-linear and thus called pseudo-capacitive. From a technology point of view these pseudo-capacitors are between capacitors and batteries. Their energy density is higher and power density is lower, compared to "true" supercapacitors. Cycle life for these types of devices is still uncertain [34].

and potential, yet less pronounced [37].

The typical effective thickness of the double layer in an EDLC is in the range of 5-10 Å, resulting in a specific capacitance of 10-30 $\mu F/cm^2$, depending on electrolyte and electrode material [33, 81].

3.1.2 EDLC design

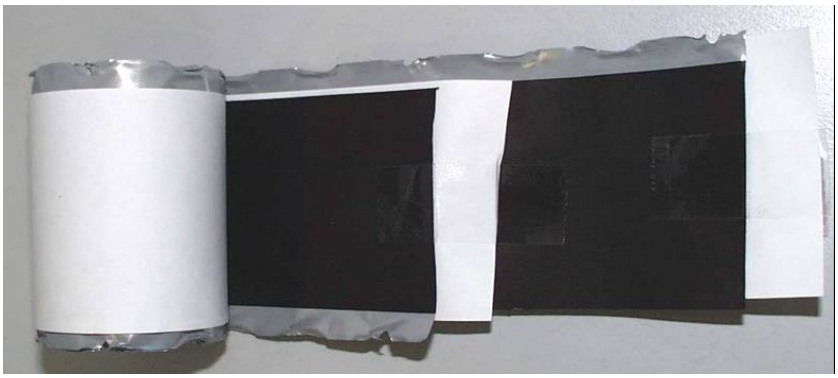

Figure 3.2: Structure of a cylindrical EDLC [160].

The basic construction of an EDLC is rather simple. A thin metal foil, usually aluminium, acts as electronic conductor and support for the porous electrode material. The electrode material in the vast majority of commercially available supercapacitors is activated carbon, which is a relatively good conductor, electrochemically stable and allows for internal surface areas of up to 2000 m^2/g. EDLCs with activated carbon at both electrodes are referred to as carbon/carbon devices. The activated carbon powder is mixed with a binder such as PTFE, with carbon black that facilitates the conductivity between the activated carbon particles, and with a solvent. This paste is literally painted on the aluminium foils. A separator that is an electronic isolator, but allows ions of the electrolyte to pass, is inserted between the electrodes to avoid short circuits. The electrodes can be wound to a cylinder as shown in figure 3.2 or folded to fit into a prismatic casing.

The electrolyte used in most EDLCs is acetonitrile, an organic electrolyte, with conducting salts[2]. Propylene carbonate is used as an alternative for the electrolyte solvent; it is less toxic but provides lower conductivities at low temperatures [91, 160]. Aqueous electrolytes such as KOH_{aq} or sulphuric acid allow for significantly higher ionic conductivities, but limit the maximum voltage of the EDLCs to about 1 V in order to avoid electrolysis of water, while organic electrolytes can be used up to approximately 3 V. Since the energy stored in a capacitor scales with the voltage squared, the higher operation voltage yields a significant gain in energy density.

Commercial carbon/carbon devices currently have energy densities between 3.5 and

[2] E.g. tetraethylammonium tetrafluoroborate or methyltriethylammonium tetrafluoroborate [160]

4.5 $^{\mathrm{Wh}}/_{\mathrm{kg}}$. The corresponding power densities for a 95% efficiency discharge[3] is between 800 and 1200 $^{\mathrm{W}}/_{\mathrm{kg}}$ [34].

3.1.3 Impedance model of an EDLC

The electrical behaviour of EDLCs can be described well by impedance based models. Very basic capacitor models comprising an ideal capacitor in series with an internal resistance yield reasonable results for many applications [95], but fail to describe the dynamic behaviour precisely. These models can be extended by a series inductance to represent the stray inductance of the electrodes and connectors and a resistance in parallel to the capacitance as a first order approximation for the leakage current [47].

Standard pore impedance

The most important improvement to this simple, linear model is the introduction of a pore impedance [79]. Porous electrodes show a behaviour that deviates noticeably from that of flat electrodes. The ion conducting path from the bulk electrolyte towards a section of the double layer deep inside the pores of the electrode is longer than the path towards a section near the pore mouth. Thus, the series resistance varies depending on where the corresponding part of the double layer is inside the pore. The macroscopic effect of this spatially distributed impedance was described by de Levie [43].

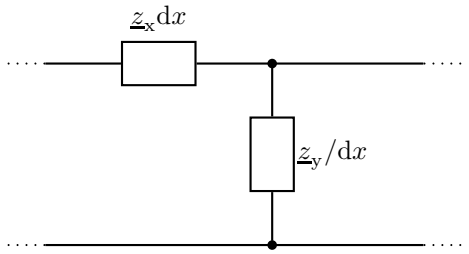

Figure 3.3: Equivalent circuit of an infinitesimal pore section.

Figure 3.3 shows an equivalent circuit of an infinitesimal fraction of the pore length. $\underline{z}_{\mathrm{x}}$ and $\underline{z}_{\mathrm{y}}$ are the impedance values per unit length of the pore along the pore axis (x) (assumed as perpendicular to the current collector) and perpendicular to the pore axis (y), respectively. As a first approach, the impedance along the pore axis is exclusively determined by the electrolyte conductivity $\underline{z}_{\mathrm{x}}\mathrm{d}x = \mathrm{d}R_{\mathrm{el}}$, while the impedance perpendicular to the pore axis and the pore walls is solely caused by the double layer capacitance $\underline{z}_{\mathrm{y}}^{-1}\mathrm{d}x = j\omega\mathrm{d}C_{\mathrm{dl}}$. From the model shown in figure 3.3 the differential equations for current and voltage can be derived:

$$\frac{\mathrm{d}\underline{u}}{\mathrm{d}x} + \underline{i}\underline{z}_x = 0 \qquad \text{and} \qquad \frac{\mathrm{d}\underline{i}}{\mathrm{d}x} + \frac{\underline{u}}{\underline{z}_y} = 0. \tag{3.1}$$

[3]The maximum discharge power of a supercapacitor is in principal only limited by its internal resistance. The maximum power is available if discharged to a matched impedance, however at the cost of a 50% power loss, which is far from an efficient use of the device. A practical measure of the maximum power can therefore be defined as the power at which the discharge efficiency is 95% [34].

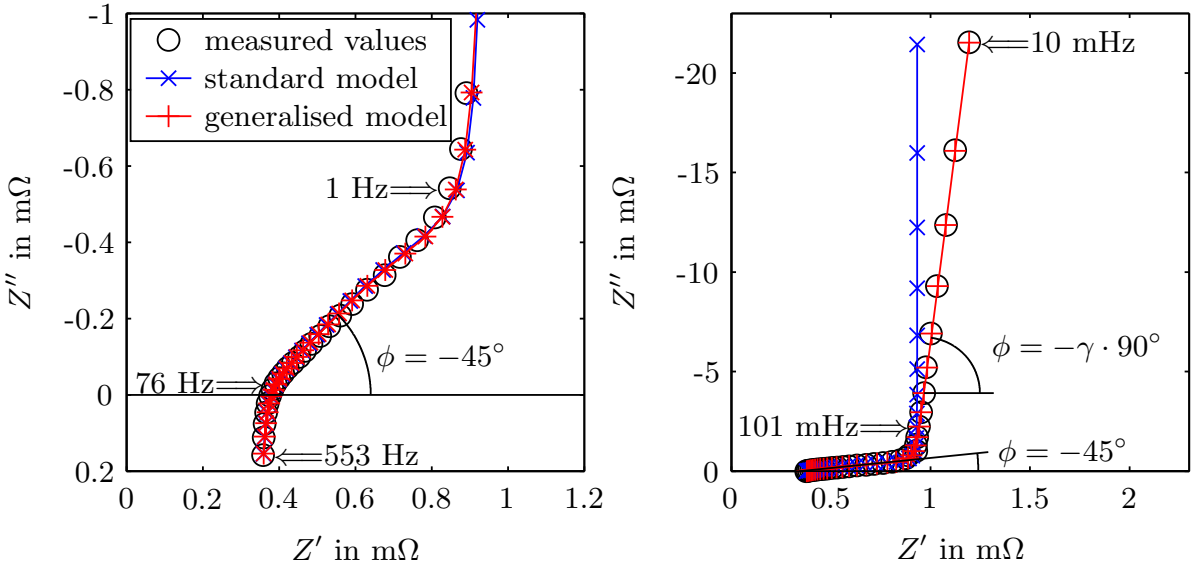

Figure 3.4: Measured impedance spectrum (EPCOS 600 F, 25 °C, 2.7 V_{DC}) and fitted spectra for the standard and generalised pore model, as described by equations 3.8 and 3.13, respectively. The corresponding model parameters are given in table 3.1. The aspect ratio of the right Nyquist plot was changed to 1:10 in order to emphasise the deviation from true capacitive behaviour in the low frequency region.

Combining these equations yields the steady state differential equations for a transmission line:

$$\frac{\mathrm{d}^2\underline{i}}{\mathrm{d}x^2} - \frac{\underline{z}_x}{\underline{z}_y} = 0 \qquad \text{and} \qquad \frac{\mathrm{d}^2\underline{u}}{\mathrm{d}x^2} - \frac{\underline{z}_x}{\underline{z}_y} = 0. \tag{3.2}$$

These equations can be solved for a pore of finite length l with the boundary conditions $\underline{i}(x = 0) = \underline{i}_0$ (excitation current at the pore mouth) and $\underline{i}(x = l) = 0$ (open circuit at the pore end). The solution for the voltage at the pore mouth is

$$\underline{u}_0 = \underline{u}(x = 0) = \underline{i}_0 \sqrt{\underline{z}_x \underline{z}_y} \coth\left(l\sqrt{\underline{z}_x \underline{z}_y^{-1}}\right). \tag{3.3}$$

Assuming an even distribution of the electrolyte resistance and the double layer capacitance along the pore

$$\underline{z}_x = \frac{R_{\mathrm{el}}}{l} \qquad \text{and} \qquad \underline{z}_y = \frac{l}{j\omega C_{\mathrm{dl}}}, \tag{3.4}$$

the analytic expression of the pore impedance can be derived [42, 43, 78]:

$$\underline{Z}_{\mathrm{p}} = \frac{\underline{u}_0}{\underline{i}_0} = \sqrt{\frac{R_{\mathrm{el}}}{j\omega C_{\mathrm{dl}}}} \cdot \coth\sqrt{j\omega R_{\mathrm{el}} C_{\mathrm{dl}}}. \tag{3.5}$$

For a uniform, long cylindrical cell, the values of R_{el} and C_{dl} can be calculated analytically from the geometry of the pore, the electrolyte conductivity and the properties of

the double layer [43,78]. Equation 3.5 can be approximated for high and low frequencies by

$$\underline{Z}_{\mathrm{p}}(\omega \to \infty) \approx \sqrt{\frac{R_{\mathrm{el}}}{j\omega C_{\mathrm{dl}}}} \tag{3.6}$$

and

$$\underline{Z}_{\mathrm{p}}(\omega \to 0) \approx \frac{R_{\mathrm{el}}}{3} + \frac{1}{j\omega C_{\mathrm{dl}}}, \tag{3.7}$$

respectively. Equation 3.6 describes the typical branch with a constant phase angle of $\pi/4$, that can be seen in figure 3.4, left graph. The impedance for low frequencies equals that of an ideal capacitor with a series resistance, which reflects the fact that after a potential was applied to the pore impedance for a sufficiently long time, the current distributes equally on all capacitors $\mathrm{d}C_{dl}$ and the corresponding resistors $\mathrm{d}R_{\mathrm{el}}$. One practical benefit of this pore model is that it can be approximated by finite ladder networks which can easily be implemented as a simulation model [30, 31, 79, 87, 110]. A good approximation can be already achieved with less than ten RC-elements if the resistance values are determined by a least squares fit procedure from appropriate measurements [89]. Another simplification can be achieved by replacing the ladder network by a series connection of parallel RC-circuits [30, 126].

An impedance model that accurately describes the behaviour of an EDLC over a wide frequency range can be achieved by extending this pore impedance with a series resistor R_{s} that models the ohmic resistance of conductors and the bulk electrolyte and an inductor representing the stray inductance of the device, as shown in figure 3.5 [29, 30, 89]. The impedance of this standard model of an EDLC can be expressed as

$$\begin{aligned} \underline{Z}_{\mathrm{EDLC,std}} &= R_{\mathrm{s}} + j\omega L_{\mathrm{s}} \\ &+ \sqrt{\frac{R_{\mathrm{el}}}{j\omega C_{\mathrm{dl}}}} \cdot \coth \sqrt{j\omega R_{\mathrm{el}} C_{\mathrm{dl}}}. \end{aligned} \tag{3.8}$$

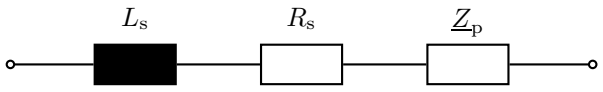

Figure 3.5: Equivalent circuit of an EDLC.

Figure 3.4 shows the impedance spectrum of this standard model that was fitted to the measured impedance spectrum of a commercial EDLC (EPCOS 600 F, 25 °C, 2.7 $\mathrm{V_{DC}}$). The left figure shows a Nyquist plot of the high and medium frequency range. The standard model describes the real behaviour in the frequency range above approximately 1 Hz very well. The main contribution to the impedance branch that describes a 45° angle to the real axis originates from the pore impedance $\underline{Z}_{\mathrm{p}}$. The inductive behaviour dominates at frequencies above approx. 100 Hz. The real part of the impedance at high frequencies is caused by the ohmic resistance and corresponds to the model parameter R_{s}.

Generalised pore impedance

However, a close observation of the low frequency branch of the impedance spectrum (figure 3.4, right part) reveals that the spectrum does not approach the behaviour of an ideal capacitor, as predicted by the standard pore model. Instead, the spectrum in this frequency range is a straight line with a constant phase angle not equal to 90°. This characteristic is called a constant phase behaviour [8]. It can be observed at EDLCs and other electrochemical systems and may arise from surface roughness [44], non-uniformity of the double layer thickness [96], a distribution in microscopic charge transfer rates or adsorption processes [37, 81]. Pajkossy [118] and Kerner [80] have experimentally shown, that even surface roughness on an atomic scale can produce such constant phase behaviour. It is however not the scope of this thesis to analyse these chemical processes in detail, but to develop mathematical models that describe the observed behaviour sufficiently.

Table 3.1: Example parameters of the impedance model (eq. 3.8 and 3.13) for a commercial EDLC (cf. figure 3.4).

model	R_s in mΩ	R_el in mΩ	L_s in nH	A_dl in $\mathrm{F/s}^{(1-\gamma)}$	γ
generalised	0.34	1.77	51	729	0.992
standard[a]	0.34	1.74	50	709	1.000

a) For the determination of R_s, R_el and L_s the frequency range was restricted to $< 100\,\mathrm{mHz}$.

Kötz et al. propose to replace the frequency dependent terms $(j\omega)$ in the expression for the pore impedance (eq. 3.5) by a constant phase term in the form $(j\omega)^\gamma$ with $0 < \gamma \leq 1$ [81]. The generalized expression for the pore impedance [24] is

$$\underline{Z}_\mathrm{pg} = \sqrt{\frac{R_\mathrm{el}}{(j\omega)^\gamma A_\mathrm{dl}}} \cdot \coth \sqrt{(j\omega)^\gamma R_\mathrm{el} A_\mathrm{dl}}. \tag{3.9}$$

C_dl in equation 3.5 was replaced by the term A_dl, the magnitude of the constant phase element (CPE)[4]. Purely capacitive behaviour as in the standard pore model corresponds to $\gamma = 1$, $\gamma = 0.5$ would result in a -45° branch and $\gamma = 0$ describes purely resistive behaviour. The term $(j\omega)^\gamma A_\mathrm{dl}$ is composed of a real part $\cos(\gamma\pi/2)\omega^\gamma A_\mathrm{dl}$ and an imaginary part $\sin(\gamma\pi/2)\omega^\gamma A_\mathrm{dl}$. In order to retrieve the true double layer capacitance, one can formally set $\omega C_\mathrm{dl} = \sin(\gamma\pi/2)\omega^\gamma A_\mathrm{dl}$. Unfortunately, the result is a frequency dependent term:

$$C_\mathrm{dl} = A_\mathrm{dl} \cdot \omega^{\gamma-1} \sin(\gamma\pi/2). \tag{3.10}$$

However, for an EDLC, γ is very close to one, and for the relevant frequency range[5] the term $\omega^{\gamma-1}\sin(\gamma\pi/2) \approx 1$, thus the numerical values of C_dl and A_dl are nearly identical.

[4] The unit of A_dl formally is $[A_\mathrm{dl}] = \mathrm{s}^\gamma/\Omega = \mathrm{F/s}^{(1-\gamma)}$. A physical meaning can yet only be assigned to the product $[\omega^\gamma A_\mathrm{dl}] = 1/\Omega$.

[5] For frequencies above 10 Hz the contribution of the pore impedance to the total impedance is small. Frequencies below 10 mHz are of minor interest for the dynamic modelling of EDLCs. For significantly lower frequencies additional effects such as self discharge are predominant.

The approximations for high and low frequencies are similar to those of the standard pore model but include the CPE exponent γ:

$$\underline{Z}_{\mathrm{pg}}(\omega \to \infty) \approx \sqrt{\frac{R_{\mathrm{el}}}{(j\omega)^{\gamma} A_{\mathrm{dl}}}}. \tag{3.11}$$

and

$$\underline{Z}_{\mathrm{pg}}(\omega \to 0) \approx \frac{R_{\mathrm{el}}}{3} + \frac{1}{(j\omega)^{\gamma} A_{\mathrm{dl}}}. \tag{3.12}$$

The complete impedance model for an EDLC including series resistance and inductance can be expressed in a closed expression:

$$\begin{aligned} \underline{Z}_{\mathrm{EDLC}} &= R_{\mathrm{s}} + j\omega L_{\mathrm{s}} \\ &+ \sqrt{\frac{R_{\mathrm{el}}}{(j\omega)^{\gamma} A_{\mathrm{dl}}}} \cdot \coth \sqrt{(j\omega)^{\gamma} R_{\mathrm{el}} A_{\mathrm{dl}}}. \end{aligned} \tag{3.13}$$

This generalized model can be fitted very well to the measured spectrum of a real EDLC over the complete measured frequency range, as can be seen in figure 3.4. The model parameters for this example are given in table 3.1.

3.1.4 Self discharge

Self discharge of EDLCs is a very slow process that cannot be adequately determined by impedance measurements. Instead, the progression of the open circuit voltage (OCV) after a full charge of the EDLC can be analysed, which shows a quasi-exponential decrease. The time constant of this discharge depends on several parameters, first of all temperature, but also on the initial open circuit potential, and changes significantly during the first hours [112, 125].

If the capacitance of the EDLC is known, the leakage current as a function of voltage can be calculated from the slope of the voltage curve:

$$i_{\mathrm{leak}} = -C_{\mathrm{dl}} \frac{\mathrm{d}U}{\mathrm{d}t}. \tag{3.14}$$

The underlying assumption is that for time constants in the range of hours and days the pore impedance can be modelled as an ideal capacitor (cf. eq. 3.7). [6]

Figure 3.6 shows a semi-logarithmic plot of the leakage current determined at three different temperatures for a commercial EDLC. The leakage current varies over more than two decades in a small voltage window; self discharge can thus not be adequately modelled by a linear parallel resistor but shows approximately an exponential behaviour [24]. A measured self discharge characteristic can be introduced in an impedance model as a voltage dependent current source, which corresponds to a non-linear resistor, in parallel to the pore impedance.

[6] Ongoing measurements indicate that the self discharge of EDLCs is also influenced by transient processes that exhibit time constants of several hours to days [144]. The physical origin of this effect has not been explained yet. If these findings are confirmed, the modelling of self discharge processes will have to be refined.

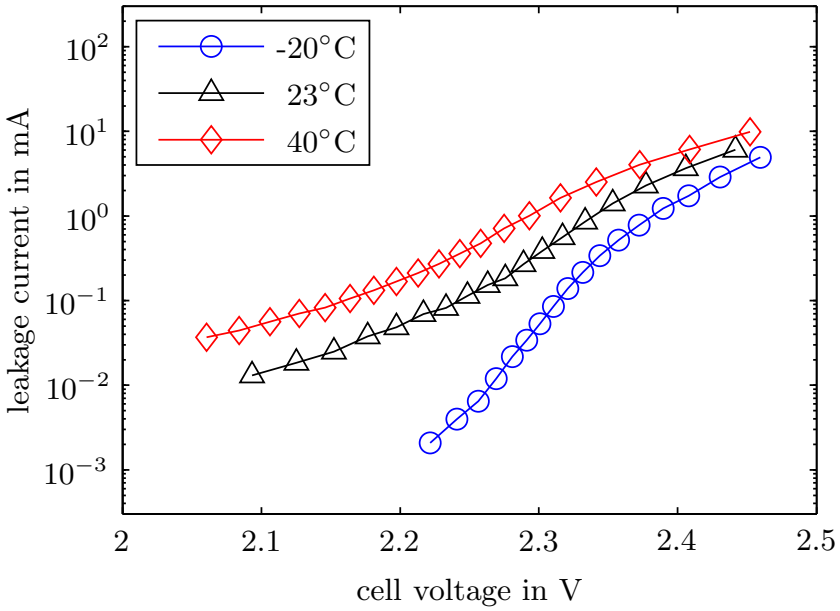

Figure 3.6: Self discharge current determined for EDLCs of type C (cf. table 5.1) at different temperatures according to equation 3.14.

The impedance model for EDLCs with the generalised pore impedance is used as a basis for the development of an ageing model in section 5.1. Self discharge in EDLCs is of secondary importance for dynamic applications; yet, for simulation models that combine impedance and ageing models an cover long time periods (cf. [25]) it has to be considered.

3.2 Lead-acid battery

The most common battery for automotive and stationary applications is by far the lead-acid battery. This is mainly due to its low cost; its robustness, good performance at low temperatures and easy recyclability are further benefits of this technology.

The basic cell of a lead-acid battery consists of two electrodes, aqueous sulphuric acid (H_2SO_4) as electrolyte and a separator. The electrodes are made of porous active material pasted on a grid made of lead. The positive active material is lead-dioxide (PbO_2), the negative is lead (Pb). The separator is a thin sheet of porous plastic that allows the ionic current to pass, but impedes electric short circuits between the electrodes.

The cell is held by a plastic case only penetrated by the battery poles or inter-cell-connectors and a venting. Figure 3.7 shows the schematic design of such a cell.

Two main types of lead-acid batteries can be distinguished: the flooded and the sealed type. The flooded lead-acid battery has – as the name suggests – a liquid electrolyte. Its battery case is vented, hydrogen and oxygen gas that emerge during overcharge escape and lead to a gradual dry-out of the cell. Sealed or valve regulated lead-acid (VRLA) batteries in contrary have a closed case, the gasses recombine in the cell and only under severe overcharge a relevant amount of gas is released through

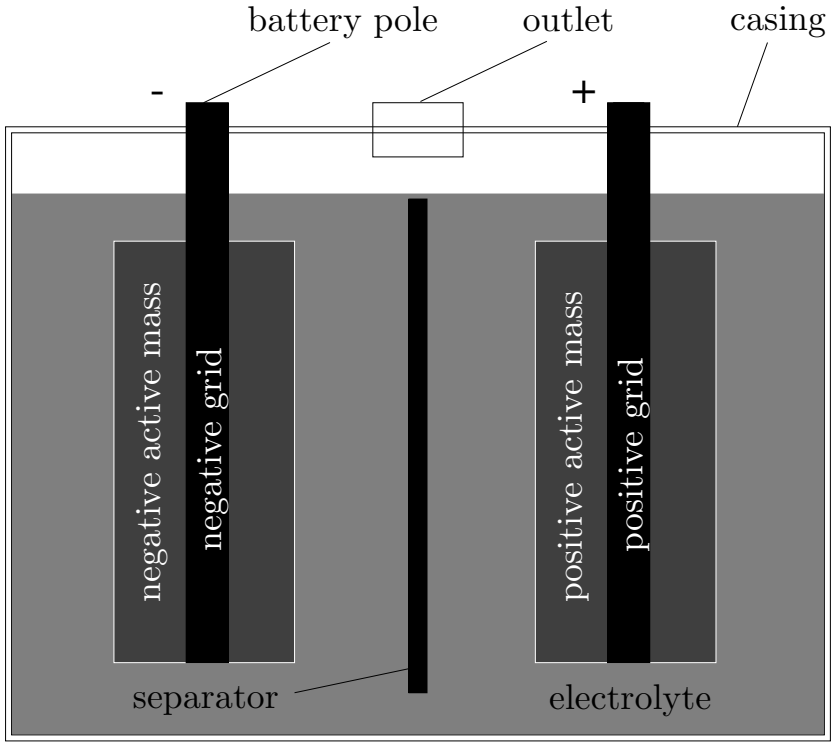

Figure 3.7: Schematic design of a flooded lead-acid battery cell (modified from [138]).

safety valves. The electrolyte in sealed lead-acid batteries is either absorbed in a fleece (absorbed glass mat - AGM) or immobilised by means of a gelling agent [12].

3.2.1 Chemistry of the lead-acid battery

The electrode reaction of a lead-acid cell takes place at the phase interface of the active material and the electrolyte. Inside the electrodes and in the electric circuit, electrons are the charge carriers, while ionic current flows in the electrolyte.

During discharge, metallic lead is being oxidised and electrons are released at the negative electrode, lead-dioxide is being reduced and electrons are accepted at the positive electrode. In contrary to most other battery technologies the electrolyte itself is involved in the reaction, sulphuric acid is consumed and forms lead-sulphate at both electrodes during discharge. Equations 3.15 show the chemical main reaction of the lead-acid battery at the electrodes and the total cell reaction [13, 88].

$$\begin{array}{lrcl} \text{pos.} & PbO_2 + 3H^+ + HSO_4^- + 2e^- & \rightleftharpoons & PbSO_4 + 2H_2O \\ \text{neg.} & Pb + HSO_4^- & \rightleftharpoons & PbSO_4 + H^+ + 2e^- \\ \hline \text{cell:} & Pb + PbO_2 + 2H^+ + 2HSO_4^- & \rightleftharpoons & 2PbSO_4 + 2H_2O \end{array} \tag{3.15}$$

The most important side reaction is the decomposition of water to hydrogen and oxygen[7]. This electrolysis is driven by the cell potential. At the positive electrode,

[7]Grid corrosion at the positive electrode and hydrogen evolution at the negative electrode form an additional pair of side-reactions, which causes permanent hydrogen loss, however at a rate much lower than the gassing reaction in flooded lead-acid batteries.

electrons and protons are separated from the water molecule, the protons are solved in the electrolyte while the electrons pass the phase interface into the electrode and oxygen emerges as gas. At the negative electrode the protons are being reduced by electrons from the electrode and form hydrogen gas.

$$\begin{array}{lrcl} \text{pos.} & H_2O & \Rightarrow & \frac{1}{2}O_2 + 2H^+ + 2e^- \\ \text{neg.} & 2H^+ + 2e^- & \Rightarrow & H_2 \\ \hline \text{cell:} & H_2O & \Rightarrow & H_2 + \frac{1}{2}O_2 \end{array} \tag{3.16}$$

In sealed lead-acid batteries the oxygen produced at the positive electrode can reach the negative electrode in gaseous form through pores in the immobilised electrolyte, where it is reduced with protons from the electrolyte to water. Due to this internal recombination process virtually no gas leaves the cell during normal operation. Yet, the energy that was necessary for the hydrolysis of water at the positive electrode can not, in contrast to flooded batteries, leave the cell with the gas, but is set free as heat at the negative electrode. This makes the sealed lead-acid battery more sensitive to overcharging [12, 88].

3.2.2 Potential in thermodynamic equilibrium

The amount of energy converted in an electrochemical reaction, the change of molar enthalpy ΔH, is composed of the molar Gibbs free energy ΔG and the product of absolute temperature T and the molar entropy of the reaction ΔS. Only the Gibbs free energy can be converted to electrical energy[8]:

$$\Delta G = \Delta H - T\Delta S. \tag{3.17}$$

In a solvent, the Gibbs free energy changes depending on the activities of the reactants according to:

$$\Delta G = \Delta G_\mathrm{S} - R_\mathrm{m} \cdot T \cdot \sum_i \ln\left[(a_i)^{j_i}\right], \tag{3.18}$$

where ΔG_S is the Gibbs free energy under standard conditions, R_m is the universal gas constant, T the absolute temperature, a_i the activity[9] of reactant i and j_i the number of equivalents of one reactant involved in the reaction.

The electric energy is equal to the product of the converted amount of charge and the cell voltage. For the amount of electric energy converted for one mole of substance in the electrochemical reaction the following equation can be set up:

$$nF\,U_0 = \Delta G, \tag{3.19}$$

[8] The energy associated with the entropy corresponds to reversible heat. In the case of lead-acid batteries, reversible heat is accepted during discharge and emitted during charge.

[9] The activity is the effective concentration $a = c \cdot f_a$, where c is the concentration and f_a the activity coefficient. This relation is non-linear and a varies itself with concentration, for a limited concentration range it can however be linearised.

where n is the number of electrons involved in the reaction and F is the Faraday number ($F \approx 96500\,{}^{\mathrm{As}}/_{\mathrm{mol}}$). ΔG is the difference of the enthalpies of the starting materials and the products of the reaction:

$$\Delta G = \sum \Delta G_{\mathrm{start}} - \sum \Delta G_{\mathrm{end}}, \tag{3.20}$$

these values are tabulated for standard conditions, e.g. in [13]). Equation 3.19 thus allows calculating the equilibrium potential of the cell:

$$U_0 = -\frac{\Delta G}{n \cdot F} = \frac{\sum \Delta G_{\mathrm{end}} - \sum \Delta G_{\mathrm{start}}}{n \cdot F}. \tag{3.21}$$

For the main reaction of the lead-acid battery given in equation 3.15, a potential of $U_{0,\mathrm{S}} = 1.928\,\mathrm{V}$ can be calculated for standard conditions (all activities $a_i = 1$). The nominal cell voltage of a lead-acid battery is defined internationally as $U_{\mathrm{N}} = 2\,\mathrm{V}$. By inserting equation 3.18 in 3.21 the dependency of the equilibrium potential on the activities of the reactants can be calculated. The expression

$$U_0 = U_{0,\mathrm{S}} + \frac{R \cdot T}{n \cdot F} \cdot \left(\sum_{i_{\mathrm{start}}} \ln \left[(a_{i_{\mathrm{start}}})^{j_{i_{\mathrm{start}}}} \right] - \sum_{i_{\mathrm{end}}} \ln \left[(a_{i_{\mathrm{end}}})^{j_{i_{\mathrm{end}}}} \right] \right) \tag{3.22}$$

is known as the Nernst equation. For the lead-acid cell according to the chemical reaction of equation 3.15 the Nernst equation yields [10]

$$U_0 = U_{0,\mathrm{S}} + \frac{R \cdot T}{n \cdot F} \cdot \left(\ln a^2_{HSO_4^-} + \ln a^2_{H^+} - \ln a^2_{H_2O} \right). \tag{3.23}$$

The activities of the solid reactants are equal to unity per definition, the potential therefore depends only on the acid concentration [138]. The open circuit voltage that can be measured at the terminals of a battery is not identical with the equilibrium potential, but is a mixed potential of the main reaction and the side reactions. Since the kinetics of the side reactions are much slower, their influence is small. In practice, inhomogeneous acid concentration within the cell and the active material cause much more deviation of the measured open circuit voltage from the equilibrium potential corresponding to the average electrolyte concentration of the cell.

3.2.3 Dynamic cell voltage

The voltage of a lead-acid cell during charging or discharging differs from the equilibrium potential, this voltage difference is termed overpotential, irrespective of its sign. The cell voltage equals the sum of the equilibrium potential and the overpotentials:

$$U(t) = U_0 + \Delta U_{\mathrm{s}} + \Delta U_{\mathrm{ct}} + \Delta U_{\mathrm{con}} + \Delta U_{\mathrm{dif}}. \tag{3.24}$$

The ohmic voltage drop ΔU_{s}, the charge-transfer overpotential ΔU_{ct}, the concentration overpotential ΔU_{con} and the diffusion overpotential ΔU_{dif} are briefly discussed in the following paragraphs.

[10] To a certain extent also the second stage of dissociation $H_2SO_4 \Rightarrow SO_4^{2-}$ occurs. The enthalpies for the reactants differ slightly from those of equation 3.15, which leads to an equilibrium potential of 2.046 V, the true cell potential is a mixed potential of these two voltages [13].

Resistance As for all electrochemical storage devices the metallic connectors and the metallic grid cause an ohmic voltage drop. The resistance R_m is generally linear and relatively insensitive to temperature and state of charge. Metallic conductors show a small positive temperature coefficient of resistance.

At the interface of the lead grid and the positive active material a corrosion and passivation layer is formed, which consists mainly of low conductive materials and contributes to the electrode resistance [138]. The growth of this layer due to corrosion directly affects the internal resistance of a lead-acid battery in two ways. Firstly, the resistance of the layer growth and secondly the cross sectional area of the grid is reduced.

The active masses contribute little to the cell resistance due to their high conductivity compared to the electrolyte. However, the resistance of the active masses R_am depends significantly on the state of charge and grows with proceeding discharge as more and more of the conductive lead and lead-dioxide is converted to lead-sulphate, which is an electric isolator. Structural changes in the active material caused by the different densities of the charged and discharged material may contribute to this effect [138].

The electrolyte contributes significantly to the resistance of the lead-acid cell, the electrolyte resistance R_el is highly sensitive to temperature and electrolyte concentration and consequently to the state of charge. Figure 3.8 shows how the conductivity of sulphuric acid depends on temperature and concentration. Obviously, for very low concentrations the electrolyte passes into pure water and the conductivity approaches very low values. For high concentrations the conductivity decreases again; the nominal electrolyte concentration of lead-acid batteries is close to the maximum of the conductivity.

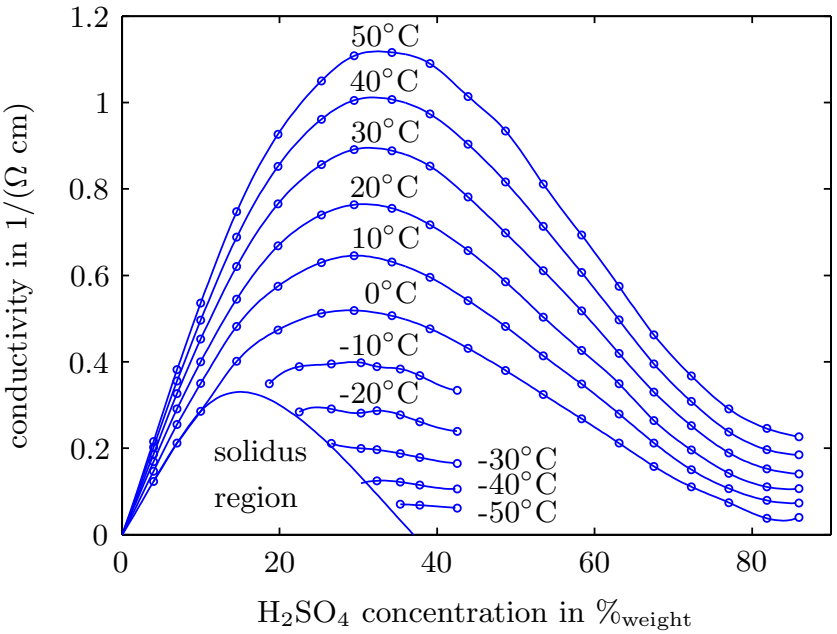

Figure 3.8: Specific conductivity of aqueous sulphuric acid as a function of voltage and temperature (data from [17]).

A significant amount of the electrolyte in the main current path is inside the pores of the active masses and the separator. The porous structure causes a reduced active cross

sectional area and a longer path through the non-uniform pores, compared to the outer geometric dimensions. Additionally, during operation the acid concentration in the pores may differ significantly from the average concentration. The acid consumed or produced time interval at the inner surface of the active mass is directly proportional to the average current during that interval, the equalisation of the different concentrations by diffusion is relatively slow. During discharge with a high current the acid concentration in the vicinity of the active surface decreases significantly, which leads both to a local reduction of the equilibrium potential and to an increase of the effective electrolyte resistance[11]. Both effects lead to an increasing overpotential and are particularly pronounced at low states of charge and low temperatures. At low states of charge the acid is already diluted and the concentration can easily approach values where conductivity and potential drop disproportionally fast. Moreover, at low states of charge the pore volume is already reduced, which impedes the supply of "fresh" acid from the bulk. Low temperatures mainly influence the diffusion rate. Moreover, at temperatures below zero the electrolyte concentration can locally fall below the critical value and ice crystals are formed in the pores, which electrically deactivates the affected parts.

From measurements on the complete cell, the contributions of conductors, active mass and electrolyte can hardly be distinguished and are therefore mostly subsumed to an internal series resistance $R_\mathrm{s} = R_\mathrm{m} + R_\mathrm{am} + R_\mathrm{el}$. The overpotential due to R_s is

$$\Delta U_\mathrm{s} = R_\mathrm{s} \cdot I, \tag{3.25}$$

where I is the battery current.

Charge transfer Another important overpotential is contributed by the potential drop related to the charge transfer process at the solid electrolyte interface. At this interface a continuous exchange of charge carriers takes place. In equilibrium the same amount of ions is reduced and oxidised at both electrodes and the total current is zero. If the potential is shifted, one of the reactions prevails and causes an overall current.

To surmount the potential barrier represented by the interface, the charge carriers need activation energy. During charging the activation energy is increased proportionally to the overpotential ΔU_ct; during discharge it is decreased accordingly. The correlation of the current density j and the corresponding overpotential ΔU_ct is given by the Butler-Volmer equation [17]:

$$j = j_0 \left[\mathrm{e}^{\frac{\alpha n N_\mathrm{A} e}{R_\mathrm{m} T} \Delta U_\mathrm{ct}} - \mathrm{e}^{-\frac{(1-\alpha) n N_\mathrm{A} e}{R_\mathrm{m} T} \Delta U_\mathrm{ct}} \right]. \tag{3.26}$$

A positive current density corresponds to charging, a negative to discharging. The factor j_0 is the exchange current density, n is the number of electrons involved in the chemical reaction, N_A is the Avogadro number, e is the elementary charge, R_m is the universal gas constant, T is the absolute temperature and α is a factor that defines the asymmetry with respect to charging and discharging. The exchange current density j_0 is a function of the concentrations of the reactants [149], equation 3.26 is therefore only valid if the concentration of the ions which take part in the reaction is equal to the equilibrium condition. This is however not the case during charging or discharging of the battery

[11] The reduced acid concentration also influences the charge transfer resistance (see below).

due to transport or dissolution limitations (see **concentration** and **diffusion** below). During charging the Pb^{2+}-concentration is lower than in equilibrium, which reduces the exchange current at both the positive and negative electrode. During discharging the depletion of the sulphuric acid causes a reduction of the exchange currents, thus in both cases the absolute value of the charge transfer overpotential for a given current is increased compared to the simplified assumptions of equation 3.26. An explicit model of the charge transfer process that takes the dependence on the local ion concentration into account is described in [138]. The dependency on the local concentrations is however often neglected for a simplified discussion of the charge-transfer characteristic.

Multiplying equation 3.26 with the effective internal surface A_{eff} of the electrodes yields the equation for the cell current $I = j \cdot A_{\text{eff}}$ and the exchange current $I_0 = j_0 \cdot A_{\text{eff}}$. The reduction of the inner surface during constant current discharge consequently leads to an increase of the charge transfer overpotential ΔU_{ct}.

The Butler-Volmer equation cannot be solved explicitly to yield the ΔU_{ct} as a function of j or the current I. Therefore, two approximations are commonly used, that allow for an inversion. For high overpotentials one of the exponential terms can be neglected and equation 3.26 becomes a simple exponential function that can be solved to

$$\begin{aligned} \Delta U_{\text{ct}} &\approx \frac{R_{\text{m}}T}{\alpha n F} \cdot \ln \frac{I}{I_0} \qquad \text{for} \quad I \gg I_0 \\ \Delta U_{\text{ct}} &\approx -\frac{R_{\text{m}}T}{(1-\alpha) n F} \cdot \ln \frac{I}{I_0} \qquad \text{for} \quad I \ll -I_0 \end{aligned} \tag{3.27}$$

with the Faraday number $F = N_{\text{A}} \cdot e$. This approximation is known as the Tafel equation [17, 149]. For small overpotentials a linear approximation can be derived from equation 3.26 by a Taylor series:

$$\Delta U_{\text{ct}} \approx \frac{R_{\text{m}}T}{n F\, I_0} \cdot I = R_{\text{ct},0} \cdot I. \tag{3.28}$$

The factor $R_{\text{ct},0}$ is the charge transfer resistance for $I \approx 0$. The effective charge transfer resistance at larger overpotentials can only be calculated from the non-linear Butler-Volmer equation. The non-linear Butler-Volmer impedance is discussed in section 2.2.

Double-layer capacitance An electrochemical double-layer[12] is formed at the solid-electrolyte interface. From the electrical point of view, the double-layer capacitance is in parallel to the charge transfer resistance and thus influences the transient behaviour of the reaction overpotential. In concentrated electrolytes the effect of the Helmoltz layer prevails and the diffuse layer can be neglected [17]. The double-layer is formed at both electrodes, the specific capacitance at the positive PbO_2-electrode was calculated by Karden [78] to be 720 to 7200 F per 100 Ah and 40 to 100 F per 100 Ah for the negative Pb-electrode. The double-layer capacitance shows a significant dependency on the state of charge of a battery. The decrease of the active surface with proceeding discharge is the main reason for corresponding decrease of the double-layer capacitance. Buller measured a certain non-linearity of impedance parameters closely related to the double-layer capacitance, the effect however is significantly less pronounced than the non-linearity of the charge-transfer reaction [29].

[12] The electrochemical double-layer has already been discussed in connexion with the EDLC in section 3.1. In contrast to EDLCs the double layer in batteries is formed irrespective of an externally applied potential.

Concentration The dependency of the equilibrium voltage on the acid concentration can be described by the Nernst equation (cf. eq. 3.22). Similarly, any deviation of the ion concentration involved in the electrochemical reaction from the equilibrium causes an overpotential that can be calculated according to the Nernst equation. The ion concentration is different from the equilibrium, if the chemical or physical process that precedes the electrochemical reaction is rate limiting, i.e. the supply of the reactants is slower than the reaction itself. Two important mechanisms play the role of the rate limiting processes, dissolution and diffusion.

The dissolution of lead-sulphate during charging is the main limiting process for the Pb^{2+}-ions, that are oxidised at the positive electrode and reduced at the negative electrode[13]. Especially at high charging currents the Pb^{2+}-ions are consumed faster than the dissolution provides replenishment until a stable situation is reached at which the concentration of Pb^{2+} is below the equilibrium concentration. The overpotential that results from this concentration $c_{\mathrm{pos}}(Pb^{2+})$ at the positive and $c_{\mathrm{neg}}(Pb^{2+})$ at the negative electrode with respect to the corresponding equilibrium concentrations $c_{\mathrm{pos},0}(Pb^{2+})$ and $c_{\mathrm{neg},0}(Pb^{2+})$ is

$$\Delta U_{\mathrm{con}} = -\frac{R_{\mathrm{m}}T}{nF} \cdot \ln\left(\frac{c_{\mathrm{pos}}(Pb^{2+})}{c_{\mathrm{pos},0}(Pb^{2+})} \cdot \frac{c_{\mathrm{neg}}(Pb^{2+})}{c_{\mathrm{neg},0}(Pb^{2+})}\right) \tag{3.29}$$

according to the Nernst equation [138].

The opposite effect of crystal growth during discharge is principally the same with an opposite sign, though less pronounced. However, if the sulphate crystals have been entirely solved after a full charge of a battery, at the start of the following discharge the lack of seed crystals causes the concentration of Pb^{2+} to exceed the equilibrium potential. At a certain excess concentration, seed crystals start to form and the concentration is decreased close to equilibrium. The overpotential that corresponds to this concentration development is known as the 'coup de fouet', a voltage sag typical for the beginning of the discharge of a fully charged lead-acid battery.

Diffusion While the lead ions have to travel only a short way between the active mass, the solution in the vicinity of the surface and the sulphate crystals at the inner surface of the active mass, the H_2SO_4-ions have to travel much further between the bulk electrolyte and the reaction locus in the depth of the porous active material. This diffusion transport is driven by the concentration gradient.

The concentration gradient in the active mass is mainly perpendicular to the electrode surface, for a one-dimensional diffusion Fick's first law yields

$$\frac{\mathrm{d}\nu}{\mathrm{d}t} = -D\frac{\mathrm{d}c}{\mathrm{d}x} \approx -D\frac{c_2 - c_1}{l}, \tag{3.30}$$

where ν is the number of moles of ions, D is the diffusion constant, c is the concentration of ions in the electrolyte and l is the length of the diffusion path. For the approximate total gradient c_1 can be chosen as the concentration in the active mass where the reaction takes place and c_2 as the concentration of the bulk electrolyte.

[13] Transport of the ions from the place of dissolution to the place of the reaction by diffusion is a second limiting process, the influence is however significantly smaller due to the short path length.

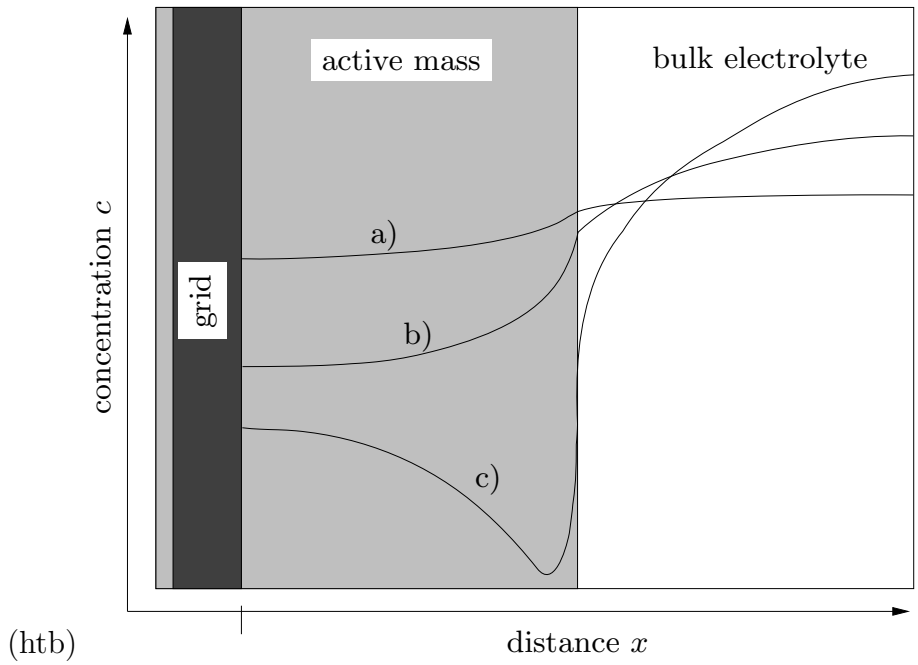

Figure 3.9: Qualitative shape of the ion concentration in the bulk electrolyte and in the porous active mass during discharge with I_{20} (a), 20 I_{20} (b) and 200 I_{20} (c) [78]. (I_{20} is the current that discharges the battery within 20 hours, e.g. 5 A for a 100 Ah-battery.)

Figure 3.9 shows schematic concentration profiles for different discharge current rates according to Karden [78], which develop in the electrolyte in the pores of the active mass. The concentration gradient increases for higher current rates; moreover, at very high discharge rates the reaction takes place mainly at the part of the active mass that is in direct contact with the bulk electrolyte, which results in a concentration profile that has a local minimum (cf. curve c in figure 3.9). The concentration gradient also increases if the diffusion rate is low at low temperatures.

The change of the concentration at the solid electrolyte interface depends on the generation or consumption of the HSO_4^--ions, which is directly proportional to the current. The ionic equalisation current is determined by the concentration gradient and the diffusion constant D[14] and depends on the porosity of the active material and the effective pore length. A porosity factor and a factor that describes the tortuosity of the pores can be introduced in equation 3.30 [138]. The porosity decreases with progressing discharge, since the reaction product $PbSO_4$ has a lower density and thus a higher specific volume than the starting materials Pb and PbO_2.

The diffusion overpotential originates from concentration differences of the ions at different loci in the pore volume of the active mass. From the Nernst equation (eq. 3.22)

[14]The diffusion constant is a function of temperature and concentration [17, 78]. The dependency on concentration introduces non-linearity into the effect of the diffusion overpotential.

the diffusion overpotential can be calculated from [15] [13, 17]:

$$\Delta U_{\mathrm{dif}} = \frac{R_{\mathrm{m}} T}{nF} \ln \frac{c_1}{c_2}. \tag{3.31}$$

The diffusion overpotential is only indirectly linked to the current by the change of the local concentration at the place of the reaction. The ion transport driven by diffusion has an effect similar to a lowpass. An instant change of the current therefore has no direct effect on the diffusion overpotential, but only after a certain time a new concentration profile develops. For the same reason the concentration overpotential is still present if the battery current is switched off and it significantly influences the measurable open circuit voltage. The reduction of the concentration gradients after a standard charge of a lead-acid battery takes several hours even at room temperature.

A concentration gradient in the active material has a second influence on the cell voltage that interferes with the diffusion overpotential. At each point in the active mass the local acid concentration causes a local equilibrium voltage; what can be measured at the terminals is a mixed potential that differs from the potential that would correspond to the concentration of the bulk electrolyte or the average acid concentration of the complete electrolyte volume[16].

Discharge characteristics Figure 3.10 shows the battery voltage of a typical starter battery during discharge with different current rates. It can be seen, that the higher the current is, the lower is the voltage curve. The voltage difference between the curves is not constant, it increases towards low states of charge, which indicates that the effective resistance increases, too. This increase can be explained to some extent by the decrease of the active surface, moreover the decrease of the pore diameter due to the formation of lead sulphate leads to a stronger inhibition of ion transport and consequently increases the concentration and diffusion overpotentials.

Inhomogeneity The electrical, electrochemical and physical properties of an electrochemical cell are not homogeneously distributed over the volume. Horizontal concentration gradients also cause a horizontal distribution of the lead-sulphate and the porosity.

Additionally, vertical inhomogeneities can be observed. Typically the electrode plates are connected on top, the path for the current through the lower part of the plates is longer than through the upper part, which causes a vertical inhomogeneous distribution of the current density. This in turn causes different local states of charge of the active material. An important phenomenon associated with vertical inhomogeneity is acid stratification. During charging more sulphuric acid is produced in the upper part of the plates, which leads to a higher concentration and density. The denser electrolyte however is driven downwards by gravity. Acid stratification is therefore pronounced in flooded lead-acid batteries and scarcely observable in sealed batteries with an immobilised electrolyte.

[15] Concentrations have been used here under the simplified assumption that the activity coefficients are constant in the concentration range c_1 to c_2.

[16] Migration, i.e. the movement of ions under the influence of an electric field, also contributes to the ion transport [17].

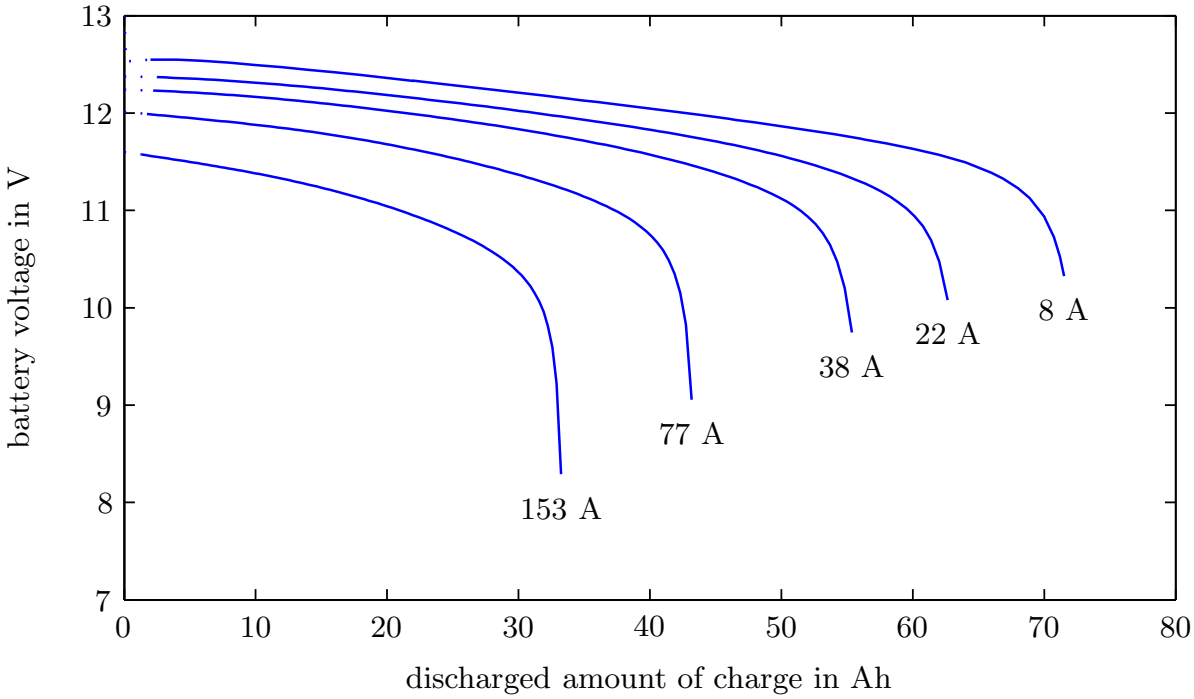

Figure 3.10: Typical voltage curves of an SLI battery (MOLL Kamina) measured during discharge with different current rates. The nominal capacity of the battery is 70 Ah. (The region of the coup de fouet at the beginning of the discharge was removed from the data.)

The complex interactions of acid stratification, local current, local state of charge and temperature have a significant influence on battery performance and ageing processes [107,137,138]. Any inference on the state of the battery only from cell voltage and current necessarily reduces the complexity of a spatial distribution to average values. This fact limits the accuracy of one-dimensional models and the description of the battery by scalar state variables.

The performance of a lead-acid battery depends on its current state, which is strongly influenced by its medium and long-term history. The characteristic of a lead-acid battery can therefore not be described by static characteristics. Deriving the battery performance from observations of the history of the battery would require simulation models that are far too complex to be implemented on a monitoring system. The precise modelling of ageing processes is currently not possible even with complex simulation models.

It is therefore necessary to determine the actual state of function of the battery continuously. The passive impedance measurement method described in section 6.2 can be used for a continuous parameterisation of an impedance model, as described in section 5.2. This method can be complemented by characteristic maps that have the ability to adapt automatically to the changing battery performance. Algorithms for self-adaptation of characteristic maps are presented in section 6.3.

3.2.4 Impedance model of the lead-acid battery

One of the first attempts to model the dynamic voltage behaviour of an electrochemical cell was proposed by Randles in 1947 [123]. The electrical equivalent circuit of an electrochemical cell widely known as "Randles circuit" is shown in figure 3.11. The series resistance R_s describes the quasi-ohmic resistance of the electrolyte, C_dl is the double layer capacitance and R_ct is the reaction or charge transfer resistance.

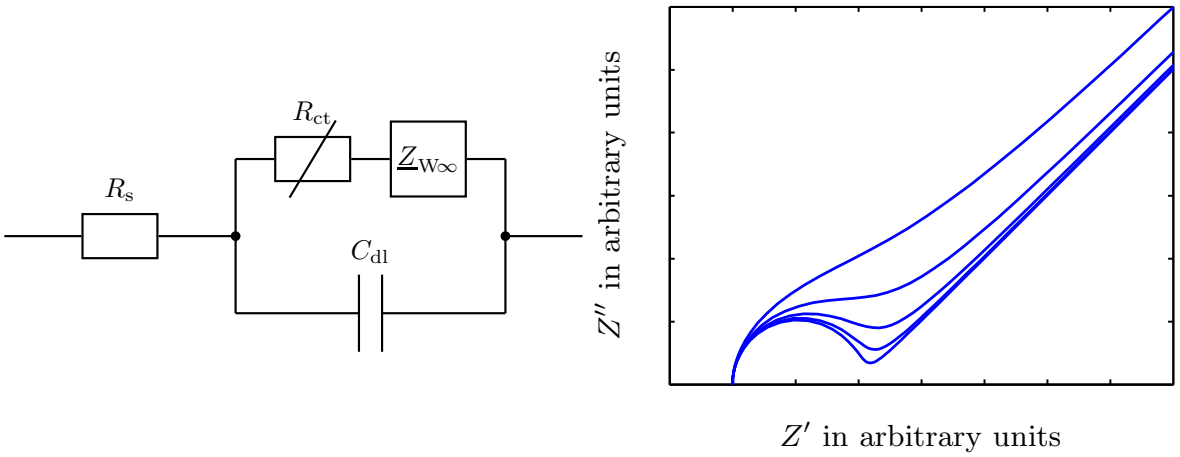

Figure 3.11: Randles equivalent circuit of an electrochemical cell (left) [123] and the corresponding Nyquist plot (right) [78]. The Nyquist plots correspond to five sets of parameters that differ only in the diffusion constant.

The element $\underline{Z}_\mathrm{w}$ is an element that describes the influence of the diffusion overpotential. $\underline{Z}_\mathrm{w}$ is known as the Warburg impedance and is the solution of the differential equation of diffusion. Depending on the boundary conditions, different expressions for $\underline{Z}_\mathrm{w}$ can be derived. For the one-dimensional case with a sink or source of ions at $x = 0$ and a constant concentration c_0 (in mole per litre) at $x \to \infty$, the Warburg impedance is [78]

$$\underline{Z}_{\mathrm{w}\infty} = \frac{RT}{c_0 n^2 F^2 A_\mathrm{eff}} \frac{1}{\sqrt{j\omega D}}. \tag{3.32}$$

$\underline{Z}_{\mathrm{w}\infty}$ describes a straight line with a -45° angle in the complex plane.

Two other boundary conditions are of interest. The first is an ideal reservoir with a constant concentration at a finite distance, which is generally a better assumption for the lead-acid battery. The resulting Nyquist plot is a -45° branch that bends down to a semicircle towards low frequencies. The second boundary condition is that of a non-permeable wall at finite distance, which describes the impedance of a porous blocking electrode and yields the expression that has already been discussed for the electrochemical double layer capacitor (eq. 3.5 in section 3.1).[17]

[17]Strictly spoken the derivation of the Warburg diffusion expressions is only valid for supported electrolytes, i.e. for electrolytes that are not involved in the chemical reaction [8]. This is surely not true for the lead-acid battery (cf. sec. 3.2.1), however, the Warburg impedance has been successfully used to describe diffusion phenomena even in lead-acid batteries [78].

The difference between these impedance terms, however, is only visible at very low frequencies in the μHz range [8]. Karden [78] estimated the Warburg impedance of a 100 Ah lead-acid battery cell to be about 1 μΩ at 10 Hz and 0.1 mΩ at 1 mHz. Though these are only rough estimates, it makes clear that the Warburg impedance has only a small influence on the dynamic performance of a battery. Only for low temperatures and low states of charge diffusion is so slow that the effect is clearly visible in the frequency range between 1 mHz and 1 Hz [78].

Based on Randles circuit, more complex and more accurate impedance models of the lead-acid battery were developed. The spatial distribution of the reaction in the porous active masses leads to a dispersion of the time constants [8]. This can be modelled by distributing the Randles circuit in a ladder network similar to that described for the EDLC (cf. sec. 3.1). The resulting impedance can be described by replacing the double layer capacitance by a constant phase element (CPE) [8].

For simplicity of the model, the Warburg impedance is often neglected or connected in series to the parallel RC-circuit. If the capacitance in a simple parallel RC-circuit is replaced by a CPE, the resulting circuit can be subsumed to a so-called ZARC-element with the analytic expression:

$$\underline{Z}_{\mathrm{ZARC}} = \frac{R_{\mathrm{ct}}}{1 + (j\omega)^{\gamma} R_{\mathrm{ct}} A_{\mathrm{dl}}}. \tag{3.33}$$

The exponent γ and the magnitude A_{dl} of the CPE-element have been introduced in section 3.1.3 for the electrochemical double-layer capacitor. The effect of the CPE-element can be interpreted as a dispersion of the time constant of the original RC-element. In the Nyquist diagram, this effect is visible as a depression of the semicircle, as shown in figure 3.12.

A close observation of impedance spectra measured on half cells[18] reveals that the spectrum of each electrode is composed of one or several processes with different time constants. Consequently, the impedance model can be split into several modules connected in series.

Karden developed an impedance model of a lead-acid cell for charge-discharge operation that consists of one Randles circuit with CPE and Warburg impedance for the positive electrode and three simplified Randles circuits without diffusion elements for the negative electrode, two of those with a CPE element instead of the capacitances. The complete model that includes series resistances and inductances for each electrode has 14 parameters, most of them depend on temperature, current and state of charge.

Such complex impedance models require extensive measurements and data analysis for parameterisation but allow describing the dynamic behaviour over a wide operating range. Yet, many effects that influence the voltage response of a lead-acid battery cannot be modelled adequately by impedance models because they are not accessible by impedance measurements. Processes that exhibit strong non-linear behaviour and have very low time constants would require long measurements with the superposition of a bias current, yet these measurements would violate the necessary (quasi-)stationarity (cf. sec. 2.2) [166].

[18] A half-cell measurement is the measurement of each electrode separately with respect to a common potential defined by a reference electrode immersed in the electrolyte.

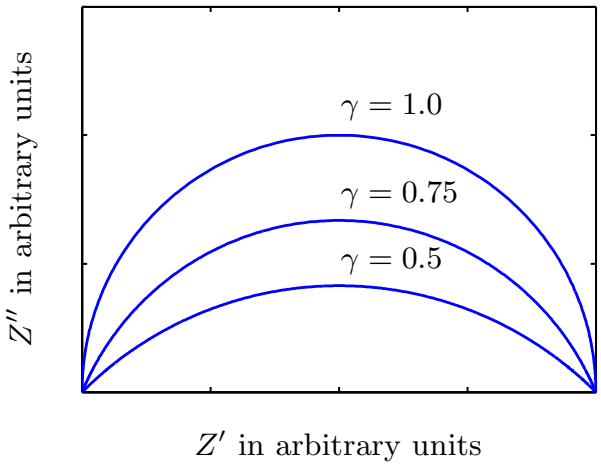

Figure 3.12: Nyquist plot of the impedance spectrum of a ZARC-element for different values of the CPE-exponent γ [78].

An approach to solve this problem is the development of hybrid models, that extend impedance-based models by simplified physical models such as an electrolyte transport model [168], a gassing model [169] and models that describe the overcharging behaviour [170].

A different approach has been chosen for the pulse power prediction presented in section 5.2. Here, the validity range of the model has been limited; within this validity range a model with only few elements yields good results. The modelling of long-term effects is not necessary, if the parameters of the model can be continuously updated.

Chapter 4

Battery diagnostic and monitoring

In this chapter, the concepts of battery diagnosis, monitoring and management as well as different state variables of a battery will be explained. In section 4.2 common methods for battery monitoring will be briefly presented and in section 4.3 an extensive literature survey gives an overview on prior attempts to use impedance measurements for the determination of the state of the battery.

4.1 Definitions

The terms battery diagnostic, monitoring, management and energy management are often used ambiguously. A concise definition of these terms is given in the following:

Battery diagnostic is the determination of the state of the battery in general. It can be applied in a laboratory environment to determine the battery performance in the scope of accelerated ageing tests, the development of new materials or testing the voltage or resistance of a SLI battery in a car repair shop.

Battery monitoring is the continuous determination of the state of the battery during operation. Battery monitoring systems observe the battery in an application and report the data to a user or a control system or even store the data for later analysis. Moreover, battery monitoring combines the results from battery diagnostics and the requirements of the system to determine the state of function (cf. section 4.2.3) of the battery.

Battery management reacts on the information from battery monitoring and determines which measures have to be taken to keep the battery in an optimal operating range. It determines the necessary charging voltage, temperature and may demand switching off non-essential electrical loads to prevent the battery from deep discharge. Most often the battery monitoring systems may not execute these actions directly but give mere recommendations to an energy management system.

Energy management is the top level control system that has to take into account not only the needs of the battery but of the whole system. It decides e.g. which loads may be switched off or how much and how fast the charging voltage may be changed

without negative impact on other electric systems. The energy management may even decide to operate the battery temporarily in a suboptimal condition during safety critical events such as electric steering or braking[1].

Within this chapter, methods will be discussed that allow determining the battery state. The fundamental principles can be applied both to battery diagnostics and monitoring. Whether a method is suitable for real-time monitoring or not depends mainly on the measurement and computation requirements, a strict differentiation is thus not possible.

Battery and energy management are – except for their diagnostic features – out of the scope of this thesis and thus only discussed briefly. Their concept is closely related to the application of the complete system.

A battery management system for an uninterruptible power supply (UPS) with sealed lead-acid batteries is described in [92]. The main requirements on such a system are enhancement of battery life and reliability, user information and improved charging strategies that permit optimal system efficiency. The main task of the battery monitoring in this system is the prediction of the bridge-time and fault detection.

A battery management system for photovoltaic power supplies was described by Kaiser [77]. The requirements are similar to those of a UPS, yet the mode of operation is different. While UPS batteries are fully charged during most of the time and only infrequently discharged with a relatively constant load, batteries in many photovoltaic systems are virtually never fully charged [138] and the room for charging strategies is restricted by the stochastic nature of the primary power source sunshine. The primary and most difficult task for battery diagnosis in such a system is the determination of the state of charge and state of health.

Schöpe gives a good overview on a system for an electric vehicle (EV) in [154]. Similar to UPS systems, the battery is frequently fully charged and the main task is to determine the actual battery capacity for a reliable prediction of the remaining driving distance. Since the battery is connected to a charger most of the time, optimized charging strategies can be efficiently applied.

Many publications address battery management systems in standard automotive applications and the large scale introduction of battery management systems for SLI batteries has already begun [19, 61, 64, 100, 104, 139] . In automotive systems often a strict separation of battery monitoring and energy management exists. This may even be a hardware separation, with a battery sensor acquiring the data transmitting the information about the battery state via CAN or LIN bus to a central controller unit [114]. The measures, which the controller can take, are restricted to changing the alternator output voltage in certain limits and a load management. Apart from state of charge and state of health information about the pulse power or cranking capability is essential for an automotive battery management. For hybrid electric vehicles (HEV) battery monitoring and management is mandatory. Their state has to be controlled actively in order to assure as well long life expectancy as high performance in any situation. Typically batteries in HEVs are operated at an intermediate state of charge

[1]Battery and energy management are however often subsumed to energy management, regarding the battery as one of many subsystems to be managed [139]

that allows for both delivery of power during acceleration as charge acceptance during regenerative braking. Moreover, charge/discharge cycles are restricted to a relatively narrow state-of-charge region in order to minimize harmful stress.

4.2 Battery state

The physical state of a battery could be described by a multitude of parameters such as the concentration and conductivity of the electrolyte or the crystal structure of the electrode material. Additionally, most parameters vary depending on the geometrical position in the device. For battery diagnosis however, none of these parameters is directly accessible by measurement but only the current and voltage at the battery poles. Often temperature at the surface of the device is also measured. These are the primary variables from which the internal state can be estimated.

For battery diagnosis, physical and electrochemical parameters are rarely used to describe the state of the battery but condensed parameters. The state parameters most often used are the capacity and the state of charge, which will be discussed briefly in the following sections. Another way to describe the state of the battery is by models and their parameters. The most basic model is that of a voltage source and a series resistor, the open circuit voltage and the internal resistance being the corresponding parameters.

4.2.1 Battery capacity

The battery capacity is the amount of charge that can be discharged from a fully charged battery until a certain cut-off voltage is reached. The unit of capacity is ampere hours. It depends not only on the individual battery but also on the discharge rate (cf. figure 3.10), temperature and the state of health (SOH) of the battery [13, 88]. The actual battery capacity is also influenced by how the battery is discharged (continuously or with pauses), how it has been charged before and by effects that influence the behaviour of the battery such as acid stratification in lead-acid batteries [107].

Information about the capacity as a function of the discharge rate and temperature can often be found in data sheets. An empiric formula that describes the dependency of battery capacity on the discharge rate was proposed by Peukert [13, 17, 88]. The parameters of these formulas however vary for different battery types. The discharge current is generally given relative to the battery capacity and with respect to discharge time. As an example, with the current I_{20} a fully charged battery with the capacity C_{20} is discharged in 20 hours. Yet this definition is recursive which makes the exact determination difficult. Another convention is the so called “C-rate”, which corresponds to the rated capacity divided by one hour, i.e. for a 100 Ah battery the C-rate is 100 A, 0.5 C-rate corresponds to 50 A etc.

The following capacity definitions are used within this thesis:

$C(I, T)$ is the actual capacity, which is the capacity that the battery has after a full charge when it is discharged at a given temperature T and current I.

C_{av} is the actual available capacity, which is the capacity that the battery has after a full charge when it is discharged with nominal current I_{N} ($C_{\mathrm{av}} = C(I_{\mathrm{N}}, T_{\mathrm{N}})$) at

nominal temperature T_N .

$C_\mathrm{OP}(I,T)$ is the operational capacity, which is the capacity that the battery has after it has been charged under operational conditions and discharged at a given temperature T and current I.

C_OPav is the available operational capacity, which is the capacity that the battery has after it has been charged under operational conditions and discharged at nominal temperature T_N and with nominal current I_N ($C_\mathrm{OPav} = C_\mathrm{OP}(I_\mathrm{N}, T_\mathrm{N})$).

C_N is the rated or nameplate capacity, which is the capacity that a new battery *should* have after a full charge and discharged at nominal temperature and with nominal current.

The available operational capacity C_OPav in a photovoltaic system or in a motor vehicle may be significantly lower than C_av since the battery is virtually never charged to "electrochemically full".

The rated capacity C_N is a fixed value that might however never be identical with the real capacity. The actual capacities C_av and C_OPav change during the lifetime of a battery. While C_av always decreases with the lifetime of the battery due to ageing processes, C_OPav may vary and recover after the battery has been charged properly[2].

The definitions above also hold for electrochemical double layer capacitors, however they are rarely used. Instead, the capacitance in Farad is frequently used to characterise the devices.

The exact actual battery capacity can only be determined by a complete discharge of the battery. Naturally, this is a very unsuitable procedure for battery monitoring in most applications. For the estimation of the battery capacity from the characteristic of the battery during normal operation different approaches are necessary. An estimation of the capacity from a partial discharge with the normal fluctuating load profile was proposed for photovoltaic systems [18, 77]. Methods that evaluate the internal resistance for the estimation of battery capacity will be discussed in section 4.3.

4.2.2 State of charge

The state of charge (SOC) is the "electric fill level" of the battery. For the definition of the SOC two concurring concepts exist, which define either the fully charged or the fully discharged state as a reference point. The latter definition is common, since the SOC is directly linked to the amount of charge that can be discharged from the battery at its current state without prior charging.

From an electrochemical point of view this definition is however unfavourable, since the discharged state of the battery is poorly defined. As an example, if the cut off voltage is reached during discharge, the voltage will re-raise after the current is switched off. After a certain time the discharge can be re-started and some more charge can be drawn from the battery until it reaches the cut-off voltage again.

[2]The difference between the capacity after an operational charge and a full charge is especially pronounced in lead-acid batteries, where the lack of extensive charging leads to large crystal sulphates that can only be dissolved by charging at elevated temperatures for several hours or even days [142].

Therefore the fully charged state will be used here as the reference point at 100 % SOC. The amount of charge Q_{dch} discharged from the full state of charge divided by the battery capacity is called the depth of discharge (DOD). The SOC thus can be calculated as

$$SOC = 1 - DOD = 1 - \frac{Q_{\mathrm{dch}}}{C}. \tag{4.1}$$

The influence of temperature and current on the discharge characteristic and thus on the SOC are basically the same as for the determination of the capacity. For a valid definition, both Q_{dch} and C have to be specified, the following definitions are used according to the definitions of the capacity:

$SOC(I,T)$ refers to $Q_{\mathrm{dch}}(I,T)$ discharged at a given temperature T and current I and the actual capacity $C(I,T)$, where T and I are kept constant during the discharge.

SOC_{av} refers to $Q_{\mathrm{dch,av}} = Q_{\mathrm{dch}}(I_{\mathrm{N}}, T_{\mathrm{N}})$ discharged at nominal temperature T_{N} and with nominal current I_{N} and to the actual capacity at nominal conditions $C(I_{\mathrm{N}}, T_{\mathrm{N}})$.

$SOC_{\mathrm{OP}}(I,T)$ refers to $Q_{\mathrm{dch}}(I,T)$ discharged at a given temperature T and current I and to the operational capacity C_{OP}.

SOC_{OPav} refers to $Q_{\mathrm{dch,av}} = Q_{\mathrm{dch}}(I_{\mathrm{N}}, T_{\mathrm{N}})$ discharged at nominal temperature T_{N} and with nominal current I_{N} and to the operational capacity at nominal conditions C_{OPav}.

SOC_N refers to $Q_{\mathrm{dch,av}}$ discharged at nominal temperature T_{N} and with nominal current I_{N} and to the rated capacity C_{N}.

$SOC_{\mathrm{OP}}(I,T)$ always has a range from 0 % to 100 % if T is the actual temperature. Yet, for an aged battery 30 % $SOC(I,T)$ corresponds to a smaller amount of charge and energy content than the same value for a new battery. The same is true for SOC_{av} and $SOC(I,T)$ except that on this scale the battery might never reach 100 %.

SOC_N is most frequently used since it has a fixed scale, each percent SOC_N corresponds to a certain amount of charge irrespective of battery age, temperature etc. However, a battery may be completely discharged above 0 % if it is cold, aged or discharged with a current higher than the nominal value, or it may even be discharged below 0 % if the actual capacity is larger than the rated capacity.

A comprehensive overview on the different definitions and ranges of SOC is given in [140], yet with a different nomenclature[3].

Different definitions for the state of charge can be found in literature [20, 103, 141], more often the term SOC is used without an explicit definition.

The state of charge can be determined by a complete discharged, followed by charging (either full or operational, depending on the definition) and a capacity test. For the determination of the state of charge by a battery monitoring system during normal

[3] In [140] the variables that refer to the operational charge are named without the identifier "OP", instead the fully charged state, which can be achieved by a standardised charging procedure is labelled "EN".

operation and without the need for discharging the battery, a wide variety of methods have been proposed.

The most common is charge balancing. Charge balancing is basically current integration to measure the amount of charge that has been charged in or discharged from the battery in a certain period. For systems that are fully charged regularly, as in a UPS or an electric vehicle, this method is straight forward and reliable, provided that the impact of temperature and current rate is modelled correctly and that the battery capacity was determined accurately. Whenever the battery reaches the fully charged state, integration errors can be reset.

In all other cases a pure Ah-balance will fail sooner or later because measurement errors accumulate and charge-balancing will loose precision if it is not supported by other methods. Even the most accurate current measurement would not help, because side reactions, especially gassing, create a leakage current, which is therefore not available for the main reaction[4].

An approach to describe this gassing current is presented in [27,121].The main parameter of the model, however, is strongly dependent on battery technology and design and changes significantly during deterioration of the battery. Therefore, this parameter has to be estimated and adapted during operation. This can be done, if the SOC from charge-balancing is frequently corrected by other methods.

The classical supporting method is the evaluation of the open circuit voltage (OCV). The equilibrium voltage is correlated to the depth of discharge of the active materials or in the special case of lead-acid batteries to the concentration of the electrolyte. For many lithium-ion batteries the evaluation of the OCV yields reliable and good results, for EDLCs it is very straight-forward. For many battery technologies, however, the correlation of the open circuit-voltage with the state of charge is much more difficult. As an example, lithium batteries with $LiFePO_4$ as cathode material show a nearly flat OCV over most of the SOC range [117], hence the smallest measurement error would lead to large errors in the determination of the SOC. In nickel-cadmium (NiCd) and nickel-metal-hydride (NiMH) the open circuit voltage exhibits a pronounced hysteresis that depends on whether the battery has been charged or discharged before [119, 159, 162, 176, 180]. In lead-acid batteries horizontal and vertical gradients (stratification) of the acid concentration cause deviations of the measured OCV compared to the OCV that corresponds to the average acid concentration [107, 138]. Moreover, at very low temperatures even a small quiescent current can depress the battery voltage to several 10 mV below equilibrium, because diffusion is very slow and creates large overvoltages. The main problem however is battery deterioration. The ageing mechanisms related with sulfation, corrosion, loss of active mass and loss of water have completely different impacts on the correlation of acid concentration, OCV and remaining amount of charge [13, 17, 22, 138].

The open circuit voltage can only be measured if the system has been at rest for a sufficient long time, often several hours. Algorithms based on voltage characteristics

[4]Gassing currents that are relevant for the Ah-balance occur in batteries with aqueous electrolytes, such as the lead-acid battery and the nickel-cadmium and nickel-metal-hydride battery. Side reactions in lithium-ion batteries and double-layer capacitors with organic electrolytes are normally so slow that the associated leakage currents are negligible for current integration.

of the battery during charging and discharging could provide information at any time. These methods require large sets of characteristics for all relevant current rates and temperatures and need algorithms that translate the behaviour under dynamic load conditions to a static charge or discharge curve. Due to transient overpotentials (cf. section 3.2.3), the battery voltage does not depend solely on the present current and temperature, which can lead to large inaccuracies. Furthermore, static characteristics provide erroneous information if the battery is aged. Self-adapting characteristic maps that "learn" these changes can be a solution to this [20, 22], algorithms for such a self-adaptation are presented in section 6.3.

A very robust method for an SOC-estimation is a rule-based expert system. A battery expert, given a plot of battery current, voltage and temperature over a certain time interval, will be able to give reliable information about the battery state in terms like "the battery is nearly full" or "this battery is almost empty". These statements are too fuzzy to be used for exact determination of the SOC, but they can be immensely helpful to prevent other algorithms from going completely off course. In order to evaluate the expert knowledge automatically, it has to be translated into a set of rules. Fuzzy logic supplies the mathematical tools to describe expressions like high SOC and to combine the results of several rules that may be valid at the same time [77]. One drawback of these sets of rules is that they generally describe well the boundaries of the operation range, i.e. full charge or deep discharge of a battery. States of charge between 40 % and 80 % are difficult to evaluate, since battery behaviour changes very little at moderate SOCs. Therefore, an expert system allows reliable information on the SOC during all operation modes only in combination with other methods.

A different approach is the use of battery models that are continuously synchronised with the real battery by means of a state observer such as a Kalman filter [121, 161]. From the internal state variables of the battery model the state of charge and other battery state variables can be derived. These methods depend strongly on the quality of the battery model. A battery model, especially if it has to be easy enough to run on a microcontroller, will rarely describe the battery accurately, a state-of-charge algorithm based on Kalman-filtering may therefore require additional correcting models [153]. Similar to characteristic maps, the parameters of a model have to be adapted if the battery ages. A method that combines Kalman-filtering and parameter estimation is described in [135].

A good overview on existing methods for state-of-charge estimation can be found in several reviews [20,66,121,122,129,130]. Methods that make use of impedance measurements are discussed in section 4.3.

4.2.3 State of function

The state of function (SOF) is defined as the capability of the storage device to fulfil a certain task. The task is typically defined by the energy management system; it is not battery specific but load specific. A battery management system has to bring together the information about the state of the battery and the requirements of the energy management to determine the SOF.

A general exact definition of the SOF is difficult since it depends strongly on the requirements and the application. A possible definition is a simple fail/pass criterion.

However, this does not provide the necessary information that allows taking early measures to prevent critical states of the battery.

Meissner and Richter proposed a continuous definition in [103]:

$$SOF = \frac{U_{\min} - U_{\text{low}}}{U_{\text{fresh}} - U_{\text{low}}}, \tag{4.2}$$

where $U_{\min}$ is the lowest voltage reached during the discharge load profile, U_{low} is a lower voltage limit defined by the energy management system and U_{fresh} is the lowest voltage during the discharge load profile that a fresh battery would have. This definition allows a scaling similar to that of the state of charge, however it is restricted to a certain type of load profile and situations limited by a lower voltage boundary.

Other possible definitions evaluate the maximum current or power or the time for which a certain load may be supplied.

Cranking capability The cranking capability or pulse power performance is a special SOF. It describes the capability of the storage device to deliver a certain high power or high current pulse for a duration of several seconds. Typical applications that require information about the pulse power performance is the cranking of a conventional motor vehicle, a boost period of a hybrid electric vehicle or the load characteristic of electrohydraulic brakes.

The load case is defined by a time dependent discharge current profile, which generally reflects the worst-case scenario. The essential information of the voltage response is the lowest battery voltage during the load case, the corresponding SOF_{CC} can be calculated according to equation 4.2. If the voltage drops below the voltage threshold, the energy management will rate the SOF_{CC} as zero, i.e. the operation – cranking, braking or whatever demands power from the battery – will fail. For a more detailed analysis, the voltage at a certain time after the beginning of the load pulse can be evaluated in addition to the minimum voltage.

In [63, 102], methods are proposed that determine a cranking SOF from the observation of the voltage during cranking, which allows detecting a critical state of the battery. In [102, 152] it is also claimed that a functional dependency of the cranking capability on state of charge and temperature is stored, which allows a prediction of SOF_{CC} at a battery state different from the present. During ageing of the battery, this dependency will change, a stationary characteristic will therefore fail to predict the cranking capability of an aged battery or of a battery for which it has not been parameterised. In order to overcome this disadvantage, a method for the self-adaptation of characteristic maps was developed, that is described in section 6.3.

In [86] the ratio of the voltage drop and the current during cranking is analysed, which can be interpreted as an effective non-stationary resistance. Since the pulse power performance of a battery is closely linked to its internal resistance, analysis of the battery impedance for the prognosis of the cranking capability is a promising approach; an impedance based cranking capability prognosis is therefore presented in section 7.2.

4.2.4 State of health

One of the major problems of electrochemical energy storage devices is their loss in performance and finally in functionality due to ageing processes. Especially for batteries, the end of life is in most cases reached much earlier than that of all other parts of the system, causing a contribution to life-cycle costs for replacement and maintenance that may exceed the initial investment costs dramatically. In many applications, the energy storage device has a safety-critical function. Lead-acid batteries in UPS systems for nuclear power plants, lithium batteries in hybrid electric vehicles and EDLCs for the door-opener in a plane's emergency exit [98] are just three examples amongst many.

Though a battery failure may appear to be a sudden event, the device has in most cases already been deteriorated, which could have been detected by an adequate monitoring system beforehand. Moreover, many ageing processes have a self-accelerating nature; adapting the operating strategy to the altered behaviour of the device can decelerate the ageing process. Finally, knowledge about the state of ageing or state of health can help to decide when to replace a battery or supercapacitor, thereby reducing both unnecessary routine replacements and unexpected failures.

Ageing processes as well as their effect on the performance are manifold. It is therefore difficult to find a universal definition for the state of health (SOH) of an electrochemical storage device. Generally, SOH describes the ratio of a state or SOF-parameter of an aged and a new device. A definition of SOH that refers to the battery voltage for a certain load application is proposed by Meissner and Richter [103, 104], other authors define the SOH as the remaining number of charge-discharge cycles of a battery [158] or relate it vaguely to battery impedance [58, 85]. For batteries, the SOH is often defined exclusively with respect to the capacity, i.e. the amount of charge that can be drawn from a fully charged battery [20, 66]. For supercapacitors, the capacitance (in F) or the internal resistance is more suitable as an indicator for the state of health [82, 151].

State of health in this thesis will be used as a generic term describing how a property of a storage device that describes or influences its performance has changed compared to its initial value.

4.3 Literature survey on impedance-based battery monitoring

Impedance spectroscopy is a well established analysis technique for electrochemical systems under laboratory conditions. It has been successfully employed in fundamental research, the spectra yield valuable information that allows to draw conclusions about the electrochemical processes that are not easily accessible by other means.

Impedance spectra measured on batteries at different conditions – temperature, state of charge, state of health different charging and discharging currents – show different shapes, which suggests the possibility to use impedance spectra for battery diagnosis.

Typically not a complete impedance spectrum measured over a wide frequency range is evaluated but the information is condensed into few significant parameters. These parameters can be determined in different ways. Two main attempts can be distinguished:

direct parameters such as real or imaginary part, modulus or phase angle of the impedance at a certain frequency

model parameters such as the charge transfer resistance, the double layer capacitance or a characteristic time constant

The use of direct parameters typically requires only one measurement for each parameter, mostly at a fixed frequency. The measurement procedures can thus be optimised and specialised, less expensive measurement hardware can be employed. The direct impedance parameter most frequently mentioned is the internal resistance. The term is not well defined and can refer to either the modulus or the real part of the impedance, typically measured at frequencies in the range of 100 Hz and above.

The ohmic resistance, which can be measured as the real part of the impedance at sufficiently high frequencies, is mainly determined by the resistance of the conductors, the active masses and the electrolyte. For lead-acid batteries the electrolyte conductivity varies with the acid concentration and – since the sulphuric acid takes part in the main reaction – with the state of charge (cf. section 3.2.3).

Barton et al. [9] claim to have identified the ohmic resistance as an ideal parameter for the determination of the state of charge of lead-acid batteries. The shape of the characteristic, however, shows a significant slope only for low states of charge and is relatively flat over a wide impedance range. Huet et al. [68] observed a slight bath-tube shape that can be explained by the characteristic of the electrolyte conductivity having a maximum at a concentration that is typical for a state of charge around 70-90 % (cf. figure 3.8). Huet concludes consequently that the high frequency ohmic resistance is not suitable for SOC determination except for deep discharge detection. The different characteristics and interpretations are due to different lead-acid battery technologies and mainly due to different operating modes. The characteristic of the ohmic resistance during a discharge, at charge and at open circuit differs significantly. Moreover, temperature, acid stratification and battery age influence the absolute value as well as the characteristic.

A correlation of the ohmic resistance with the state of charge can also be found for other battery chemistries. Lahav and Appelbaum [84] found a linear correlation of the modulus of the impedance measured at 90, 190 and 570 Hz for 7 Ah NiCd batteries, yet without a physical interpretation. The sensitivity on state of charge, however, is low, the impedance changes only approximately 0.07 % per 1 % SOC change, the sensitivity on temperature is approximately 0.5 % impedance change per degree Kelvin.

Instead of using the impedance at a certain frequency defined in advance, some authors propose to use the real part $R_\pm$ of the impedance at the transition frequency $f_\pm$ where the imaginary part of the impedance equals zero [57, 67]. The value of $R_\pm$ is very similar to the ohmic resistance, however it should be noted that it is also slightly influenced by the inductance, and the RC-circuit with the lowest time constant in the impedance model[5]. The inductance is typically a constant for a given battery, the con-

[5]For the generic impedance model of a battery described in section 2.8, $f_\pm$ and $R_\pm$ can be calculated analytically. The impedance of the model with one RC-circuit is $\underline{Z} = R_\mathrm{s} + j\omega L_\mathrm{s} + \frac{R_\mathrm{p}}{(1+j\omega R_\mathrm{p} C_\mathrm{p})}$. By setting the imaginary part of the impedance to zero and solving the expression with respect to frequency one obtains: $f_\pm = \frac{1}{2\pi}\sqrt{\frac{1}{C_\mathrm{p} L_\mathrm{s}} - \frac{1}{R_\mathrm{p}^2 C_\mathrm{p}^2}}$. For the impedance at $f_\pm$ follows $R_\pm = R_\mathrm{s} + \frac{L_\mathrm{s}}{R_\mathrm{p} C_\mathrm{p}}$.

tribution of the first RC-circuit however may be beneficial for state-of-charge estimation since the charge transfer resistance and double layer capacitance, which are the physical correspondents in many cases[6], are both influenced by the state of charge.

Hammouche [57] proposed to use the transition frequency itself to detect the state of charge, because the characteristic of $f_{\pm}$ with SOC measured on NiCd, NiMH and lead-acid batteries [15] shows a monotonic decrease with state of charge. Nonetheless the shape of this characteristic depends similarly on the charge or discharge current rate and profile, on state of health and on temperature as the ohmic resistance itself [15]. The determination of $f_{\pm}$ is somewhat more intricate than a single frequency impedance measurement, it requires a variation of the measurement frequency, yet an active and passive measurement procedure suitable for battery monitoring is patented [41].

The ohmic resistance has also been employed for SOH monitoring. In UPS applications, where lead-acid batteries are constantly held at a voltage above equilibrium, the so-called float charge, the predominant ageing process is corrosion[7]. Corrosion leads to an increase of the ohmic resistance which can be detected by a single frequency measurement. The increased resistance and the local insulation of the active masses from the grid by the corrosion layer causes capacity loss, which explains the good correlation of the ohmic resistance and the capacity found by Feder, Hlavac et al. both in laboratory and in extensive field tests with battery monitoring systems from Midtronics [49–52, 65]. Similar results were reported by Nagashima et al. [106]. Whether a good correlation can be found for batteries where the main ageing process is different and more complex than in UPS applications is questionable. Yet, a correlation of the high frequency ohmic resistance and capacity was also found for other battery technologies. Takeno et al. describe the result of an extensive study on 800 lithium-ion batteries (10 different types in fresh and deteriorated condition) that shows a good correlation of the modulus of the impedance measured at 1 kHz[8] and battery capacity [165].

Typically, the low frequency part of the impedance spectrum of lead-acid [78], lithium [128], NiCd and NiMH batteries [57] shows a more pronounced variation with SOC than the ohmic resistance. Blanchard [14] found a correlation of the modulus of the impedance at 1 Hz and the state of charge for small sealed NiCd-batteries. The correlation is however ambiguous if the cell is overcharged.

A correlation of the phase angle and the equivalent parallel and series resistance[9] determined at frequencies between 10 Hz and 100 Hz with state of charge is described for lead-acid [56] and NiCd batteries [136] by Gopikanth and Sathyanarayana.

[6] For lithium batteries, the first semicircle may also be caused by the resistance and capacitance of the solid-electrolyte interface [155].

[7] For sealed lead-acid batteries dry-out of the electrolyte can also contribute significantly to an increasing series resistance.

[8] The measurement frequency of 1 kHz was close to the transition frequency $f_{\pm}$, where the imaginary part of the impedance for this type of battery passes through zero.

[9] The concept of parallel and serial resistance and capacitance assumes two equivalent circuits, namely a parallel connection $\underline{Z}_{\mathrm{RCp}} = \frac{R_{\mathrm{p}}}{1+j\omega R_{\mathrm{p}} C_{\mathrm{p}}}$ and a series connection $\underline{Z}_{\mathrm{RCs}} = R_{\mathrm{s}} + \frac{1}{j\omega C_{\mathrm{s}}}$ of a resistor and a capacitance. For each of theses two models the parameters R_{p} and C_{p} or R_{s} and C_{s} can be determined analytically from the real and imaginary part of one impedance measurement. However it is not a real model based approach, since none of the two models describes the battery impedance well if the model parameters are determined as a function of frequency. It is thus merely a different representation of the measured impedance.

If more than one impedance parameter is used for the estimation of a single state variable such as state of charge or capacity, these have to be combined in an appropriate way. One possibility to do this is fuzzy logic, which was applied to different storage systems and applications by Salkind, Singh et al. [109, 131, 156–158, 183][10]. From the analysis of impedance spectra a set of suitable parameters is chosen and a fuzzy system maps the impedance values on the desired output state variable. Rules are formed in a linguistic way that assigning a certain membership of input and output variables to a so called fuzzy set. Fuzzy logic is the mathematical tool that allows to combine these memberships and rules and finally to defuzzify the result in a single-valued variable [131,157]. This method also allows combining impedance values with other measurement data such as temperature, voltage and current [173].

A different approach to estimate a battery state from several input variables is the use of artificial neural networks (ANN). A method for the estimation of SOC from temperature, voltage, current and impedance values is presented in [181], however without a clear definition of the measured impedance. The benefit of using an ANN model is, that no knowledge or assumptions regarding the system – in this case the battery – are necessary. Simple ANNs map a linear combination of the input variables on the output. A generic network can be *trained* with a reference data set. Training in this context means that the weights are determined by an optimization procedure in such a way that the error for the training set is minimal.

Both ANN modelling and fuzzy-logic methods are a heuristic mapping of measurement values on state variables of the battery. This concept has two main disadvantages. Firstly, a trained ANN is only optimal for the training data set. Similarly a set of fuzzy rules is derived from a limited set of measurements. If the training data does not represent the real operating mode accurately or if the data set is too small, the ANN or the set of fuzzy rules may produce wrong results in the final application. Secondly, the ANN or the fuzzy rules have to be trained separately for each type of battery and may produce wrong results for aged devices.

Bundy et al. [32] describe the usage of partial least squares (PLS) analysis of a whole impedance data set to determine the SOC of NiMH batteries. The advantages and disadvantages of the method are basically the same as for ANNs, moreover the relatively high requirements on measurement, computation and data storage are disadvantageous for an implementation in low-cost battery monitoring systems.

Instead correlating impedance values directly to battery state variables impedance measurements can be used to parameterise a battery model and derive the battery state from the value of the model parameters. If the model describes the battery behaviour well and especially if the parameters of the model have a physical meaning, this procedure allows a more reliable and stable state estimation. The classical and most accurate way to determine the model parameters is by a least square fit procedure as described in section 5. However, this procedure requires extensive measurements and computations. For relatively simple equivalent circuit models the impedance term can be solved in such a way that each model parameter can be determined directly from a number of nodes, i.e. sparse impedance values measured at a few selected frequencies. From measurements at n frequencies a model with $2n$ parameters can be parameterised, since

[10] More detailed information can be found in table 1 in the appendix.

each measurement yields a pair of real and imaginary values. This method is however much more sensitive to measurement errors and model inaccuracies than fitting a model to a large number of data points. A method for the determination of parameters for battery models comprised of resistors, capacitors and inductors is described in detail in US patent US6037777 by Champlin [36]; a variant for a model with a CPE element is presented by Nelatury and Singh [108].

Most battery impedance models used are variations of Randle's circuit (cf. section 3.2.4 and figure 3.11). A series resistance is present in virtually any model, its significance for battery state estimation has been discussed in the scope of the ohmic or high frequency resistance above. The true series resistance can yet be determined more accurately by a model based approach (cf. footnote 9).

A simplified version of Randle's circuit is a resistance in series with an RC parallel-circuit. Blanchard [14] found that for NiCd batteries the elements of the RC parallel-circuit vary both as a function of the state of charge and of the applied current while the series resistance does not vary sufficiently. Hughes et al. [69] used a more complex model that includes a Randle's circuit and found a good correlation of the characteristic time constant with SOC. Models comprised of a series resistance and two RC parallel-circuits were used by several authors [35, 53, 58] for different types of batteries, Champlin found a correlation of the capacitance of the first RC-circuit and the conductance of the second RC-circuit with state of charge of lead-acid batteries. With reference to Randle's model, the capacitor of RC parallel-circuits can be interpreted as the double layer capacitance and the resistor as the charge transfer resistance. Both are directly correlated to the active surface of the active mass, ideally the double layer capacitance should be proportional to the active surface and the resistance proportional to the inverse of the active mass. At least for lead-acid batteries the active surface decreases during discharge because lead-sulphate is formed at the surface of the electrodes. However, Hughes et al. [69] found a correlation of the product of double layer capacitance and charge transfer resistance with SOC for lead-acid cells, which indicates that the correlation is more complex.

If more than one parameter of the impedance model is evaluated, the same methods as for direct impedance parameters – namely fuzzy logic, artificial neural networks and partial least squares analysis – can be employed. A generic modelling approach is described by Tinnemeyer [174], and is implemented in a commercial device (*Cadex Spectro*). The algorithm fits spectra to several models and selects valid models depending on the quality of the fit. The model parameters are then combined in a "data fusion algorithm" [174] and mapped onto state of charge and cranking capability. The parameters for the data fusion and mapping are stored in an internal library.

More examples of direct impedance data and model parameters used for battery state estimation can be found in table 1 and 2, respectively, in the appendix. An overview on impedance based methods for battery state estimation is also given in review articles of Huet [66], Rodrigues [129], Blanke et. al. [15] and Pop et al. [122] and in the PhD thesis of Tröltzsch [175].

The general concepts for the use of impedance data for battery monitoring are independent of the battery technology. The characteristics, however, depend on the chemistry and to some extent also on the design of the devices.

Lead-acid batteries show a special dependence of the electrolyte resistance on the state of charge, because unlike in other battery types the electrolyte takes part in the main reaction. For sealed lead-acid batteries also dry-out of the electrolyte causes a typical increase of the series resistance. The complex chemical and physical mechanisms in lead-acid batteries produce a pronounced dependency of the impedance spectra on battery state, but at the same time cause ambiguity that makes a unique interpretation difficult or even impossible.

Nickel-based systems show a significantly less pronounced characteristic change of the series resistance with SOC, here the evaluation of lower frequencies seems to be necessary. Monitoring of ageing effects on the other hand are simplified by the lower impact of SOC.

Lithium-ion batteries are available in a wide variety of material combinations that are still under development. A general trend is to have a performance as constant as possible over a wide SOC range. This implies a low sensitivity of the impedance spectra on the state of charge. Typical ageing phenomena such as an increase of the solid-electrolyte interface are though easily detectable wit impedance spectroscopy.

On impedance-based monitoring of EDLCs little is published yet. The SOC can be easily determined from the cell voltage, thus no need for other methods exists. Monitoring the state of health of EDLCs is discussed in detail in section 5.1.

Chapter 5

Lab-based impedance analysis

In this chapter two examples of impedance analysis and modelling of electrochemical storage systems are presented. In section 5.1 an impedance-based ageing model for electrochemical double-layer capacitors (EDLCs) is presented. Different types of commercially available EDLCs were analysed in accelerated ageing tests by impedance spectroscopy. From these measurements, the parameters of an impedance model were determined. Based on the experimental results a heuristic ageing model for EDLCs was developed, that describes the changes of these model parameters as a function of the voltage and temperature stress of the devices.

In section 5.2 an impedance model for lead-acid batteries is developed, that allows modelling the voltage response of the battery on short high-current discharge pulses. The parameterisation of the model from impedance measurements and the validity range of the model are discussed.

The analysis methods and experimental results presented in this chapter are based on measurements under laboratory conditions. The models developed here are – combined with the passive impedance measurement technique of chapter 6 – applied to on-board monitoring in chapter 7.

5.1 Monitoring state of health of EDLCs

Different types of commercially available electrochemical double-layer capacitors were analysed in accelerated ageing tests by impedance spectroscopy. From these measurements, the parameters of the impedance model introduced in section 3.1.3 were determined and the characteristic change of these impedance parameters is analysed in section 5.1.1. Based on these results an ageing model for EDLCs was developed that is presented in section 5.1.2. For monitoring systems, the parameters cannot be determined from complete impedance spectra, but from sparse measurements, this issue is addressed in section 5.1.3.

5.1.1 Experimental study of EDLC ageing

Even though energy storage in EDLCs is predominantly electrostatic[1], parasitic electrochemical reactions limit the life expectancy of these devices. Decomposition of the electrolyte is one predominant factor; the composition of the electrode material has a strong impact on deterioration processes. Taberna et. al. state that functional groups at the surface of the carbon electrode cause instability during ageing under floating at high potentials [163].

The two predominant factors that influence ageing in EDLCs are temperature and voltage. Both, increased voltage and temperature exponentially accelerate electrochemical reactions. The effect of this degradation is generally described as an increase of the internal resistance and a decrease of the capacitance of the devices [82, 89, 151].

In order to quantify these effects and to analyse the effect of ageing on the parameters of the impedance model introduced in section 3.1.3, three types of commercially available EDLCs from different manufacturers were analysed with respect to their ageing behaviour. Table 5.1 gives an overview of the devices under test.

Table 5.1: Supercaps used in the accelerated ageing tests (all devices purchased in July and August 2004).

type	manufacturer	capacity	rated voltage	geometry	datasheet
A	Epcos	600 F	2.5 V	cylindrical	[48]
B	Nesscap	600 F	2.7 V	prismatic	[111]
C	Maxwell	350 F	2.5 V	cylindrical	[99]

Since the life expectancy of EDLCs under normal conditions, i.e. at voltages below the rated maximum voltage and at room temperature, is in the order of at least ten to twenty years, ageing was accelerated by increasing voltage and temperature during the tests. According to a rule of thumb, the ageing rate doubles if either the cell voltage is increased by 100 mV or the temperature is increased by 10 K [90]. This was taken into account for the design of the tests[2].

For each of the capacitor types, two test conditions were chosen that should increase the ageing rate by a factor of approximately 64 by either increasing the temperature by 40 K above the nominal temperature of 25 °C (≈298 K) and the voltage by 200 mV above the rated voltage, or by an increase of 20 K and 400 mV, respectively. Thus, devices with a life expectancy of 15 years should reach their end of life within three month of test duration. Two additional tests were defined for types A (U_r + 400 mV, T_r + 40 K) and B (U_r + 200 mV, T_r + 20 K) in order to compare these devices at the same conditions,

[1] Surface functional groups which are in general present on activated carbons account for a certain non-linear pseudocapacitance. The contribution in organic electrolytes, as for the devices tested in this study, is however small [81]. Pseudocapacitance is not incorporated explicitly in the models presented here, yet the impedance model allows a voltage dependent parameterisation of the capacitance, which can be interpreted as the macroscopic effect of pseudocapacitance.

[2] Strictly exponential behaviour is always an approximation for a limited temperature and voltage range. In general, the activation energy itself is a function of temperature and especially high temperatures may introduce new chemical processes.

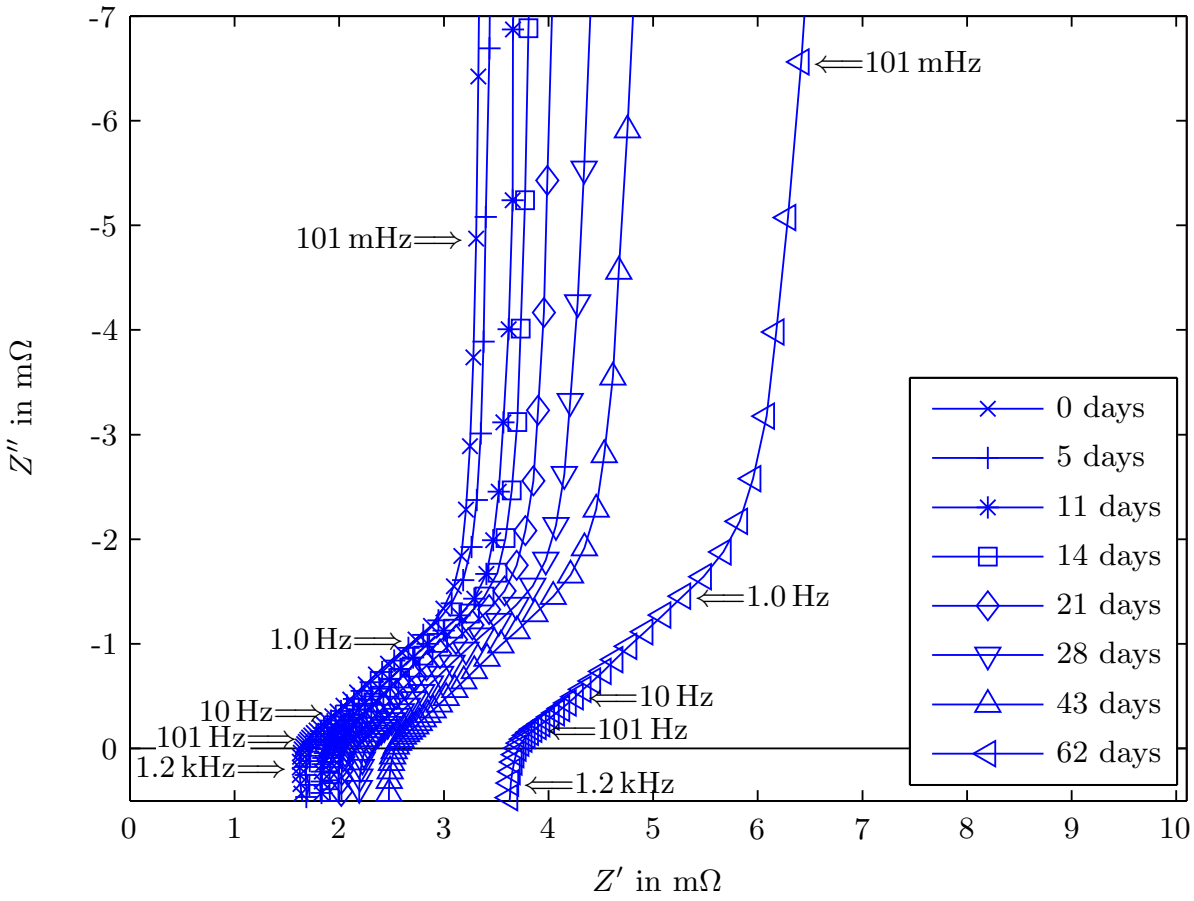

Figure 5.1: Impedance spectra during progress of ageing for EDLC type C, test conditions: 65 °C, 2.7 V (U_r+200 mV, T_r+40 K). Each spectrum was measured after a certain ageing duration; the respective number of days under accelerated ageing conditions is given in the legend.

irrespective of their different voltage ratings (cf. table 5.1). Table 5.2 summarises the test conditions for the three types of EDLCs.

Table 5.2: Configuration for the ageing tests, voltages and temperatures with respect to rated voltage U_r (cf. table 5.1) and rated temperature $T_r = 25\,°C$ ($\approx 298\,K$), respectively.

	U_r + 200 mV	U_r + 400 mV
T_r + 20 K	B	A, B, C
T_r + 40 K	A, B, C	A

The choice of voltage and temperature levels is crucial because values that differ too much from typical operating conditions could activate new electrochemical processes and cause atypical ageing behaviour. The temperature and voltage levels chosen for the tests are a compromise between this requirement and adequate test durations.

Two devices at a time were tested at the same conditions to avoid misinterpretation due to outliers. The devices were connected to a power supply in fully charged state at different test voltages and were held at constant ambient temperature in tempera-

ture chambers. The devices were only disconnected from the power supplies for regular impedance measurements and capacity tests and were immediately recharged and reconnected afterwards. These performance tests were done to track the gradual change of the electrical behaviour during the ageing process. The impedance measurements were performed with the EISmeter, a multi-channel galvanostatic impedance spectrometer [15]. The measurements were conducted at the test voltages and test temperatures (cf. table 5.2) in open circuit mode, i.e. without bias current, and in a frequency range from 5.25 kHz to 5.67 mHz.

Figure 5.1 shows the development of the impedance spectra measured on a device of type A at 40 K above rated temperature and 200 mV above rated voltage with proceeding test duration. Some typical effects of the ageing process can be deduced directly from the spectra. The most prominent effect is a shift of the spectra along the real axis, corresponding to an increase of the internal resistance. It can also be seen, that this process is fairly continuous during most of the test duration, but accelerates towards the end of the test. The last spectrum of the test is not shown in figure 5.1, its real part of the impedance is above 15 mΩ, indicating that the device is already severely damaged. All devices that reached this state during the tests, showed a similar acceleration of ageing after a certain level of degradation had been exceeded. However, the formal end of life, defined by an increase of the equivalent series resistance by a factor of two, was always reached during the continuous ageing period.

Comparing measurement points at the same frequency in the capacitive branch in figure 5.1 shows that the imaginary part of the impedance at low frequencies also increases. Thus, the effective capacitance of the device decreases due to the ageing process. Both, the increase of the resistance and the decrease of the capacitance are in accordance with results from independent experimental analysis [82, 151].

For a more detailed analysis of the ageing behaviour, the impedance model introduced in section 3.1.3 was fitted to the measured impedance spectra[3]. The model consists of a series resistance R_s, a stray inductance L and a generalised pore impedance Z_pg:

$$\underline{Z}_\mathrm{EDLC} = R_\mathrm{s} + j\omega L_\mathrm{s}\underline{Z}_\mathrm{pg}. \tag{5.1}$$

The generalised pore impedance was introduced in equation 3.9:

$$\underline{Z}_\mathrm{pg} = \sqrt{\frac{R_\mathrm{el}}{(j\omega)^\gamma A_\mathrm{dl}}} \cdot \coth\sqrt{(j\omega)^\gamma R_\mathrm{el} A_\mathrm{dl}}. \tag{5.2}$$

It is defined by three parameters, the pore electrolyte resistance R_el, the magnitude A_dl of the constant phase element (CPE) and the CPE exponent γ. For an easier physical interpretation, the parameter A_dl was equated with the double layer capacitance C_dl, as discussed in section 3.1.3.

The result of the fitting procedure is a set of model parameters for each device and for each step of ageing. Spectra that showed extreme deterioration of the device (R_s increased by more than a factor of five) were excluded from analysis. Plotting the values along the test time axis allows analysing the effect of ageing on the model

[3]The curve fitting was carried out with the mathematical software *Matlab*, using the function *easyfit* (cf. section 2.9). The measurement data was tested for stationarity with the *Z-HIT* procedure presented in section 2.7.

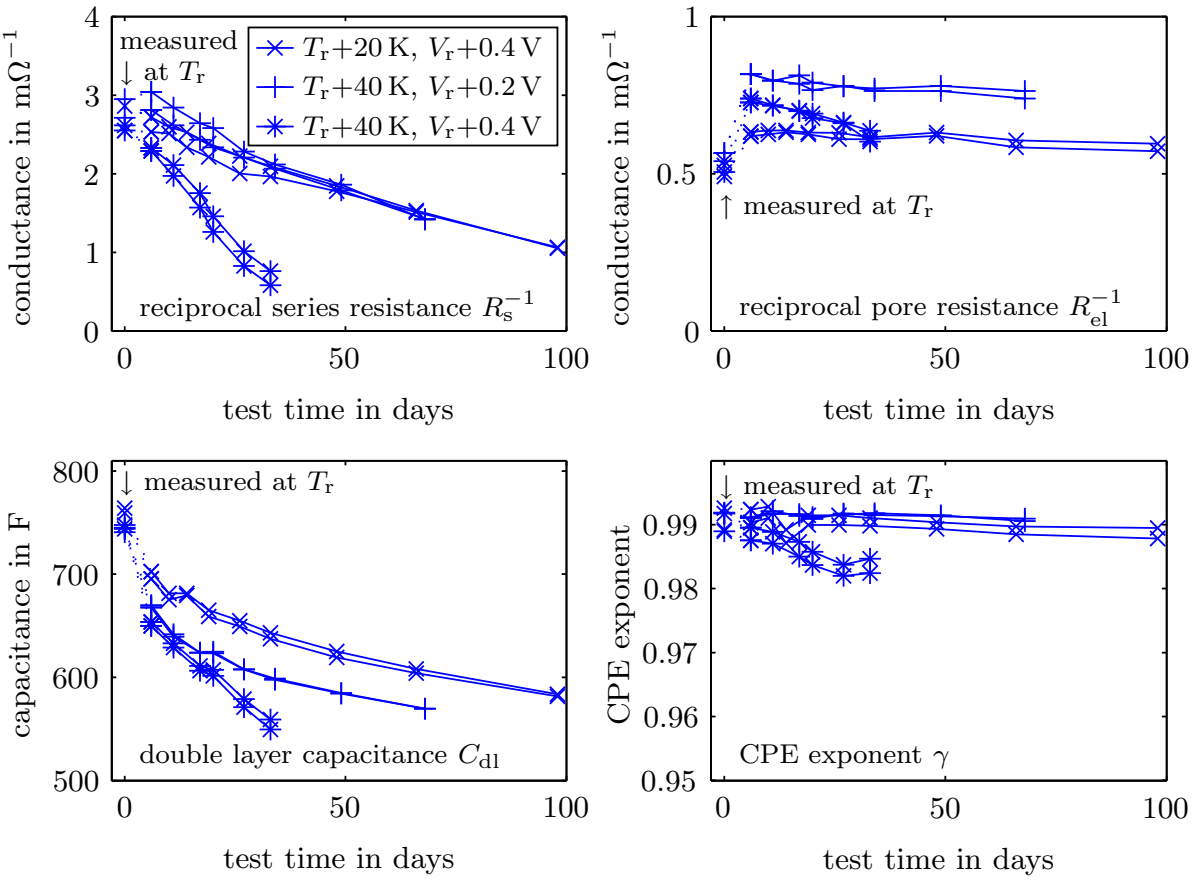

Figure 5.2: Model parameters during accelerated ageing test for ageing, EDLC type A. For an easier physical interpretation, C_{dl} is shown instead of A_{dl}. C_{dl} has been calculated according to eq. 3.10 for $f = 10\,\text{mHz}$. Numerical values of A_{dl} an C_{dl} are nearly identical. Note that the first measurement (before ageing) was conducted at rated temperature T_r and rated voltage U_r.

parameters. Figure 5.2 shows the development of the model parameters with the progress of ageing for EDLCs of type A. The parameters prior to the ageing experiment (day zero) were determined at rated temperature T_r and rated voltage U_r for all devices, all other impedance measurements were carried out at the respective test temperature and voltage.

The two top figures show the reciprocal values of the series and pore electrolyte resistance. It was found that the conductances decrease nearly linearly with ageing time. The series conductance R_s^{-1} shows a pronounced trend while the pore electrolyte conductance R_{el}^{-1} is less sensitive to ageing. The double layer capacitance C_{dl} also shows a noticeable decline of up to 20 %. The CPE exponent that is correlated to the slope of the low frequency impedance branch, changes only little due to ageing. The series inductance (not shown in figure 5.2) showed relatively strong scattering but no clear trend. The inductance is mainly determined by the geometric design of the device, thus no ageing effect on L_s is expected. Since the geometric inductance of EDLCs is very low (cf. table 3.1), the inductance of the measurement cables contributes significantly to the measurement result and varies from test to test [145], but is not sensitive to ageing.

The parallel development of the model parameters obtained at T_r + 20 °C / U_r + 400 mV and at T_r + 40 °C / U_r + 200 mV corroborates the assumption, that 10 K temperature rise and a voltage increase of 100 mV have virtually the same effect on the ageing behaviour of an EDLC.

A validated explanation of the ageing effects would require detailed electrochemical analysis that is beyond the scope of this work. A possible explanation for the fading of the double layer capacitance is a decrease of the active surface. Qualitatively the linear decrease of the conductance could also be assigned to a reduced cross-sectional surface, though the different slopes of R_s and C_dl prove that other effects contribute to the degradation. Weighing of the devices at the start and the end of the ageing test revealed that electrolyte was lost through the safety vents, which might have additional effects besides decomposition of the electrolyte.

5.1.2 Heuristic ageing model

As a working hypothesis for a heuristic ageing model, the following assumptions were made:

- At constant voltage and temperature, the capacitance and the conductance parameters decrease linearly with time[4].
- The rate of degradation accelerates exponentially with temperature and voltage[5].

The change of a model parameter a[6] compared to its initial value a_init can thus be described by

$$a(t, T, U) = a_\mathrm{init} \cdot (1 + c_\mathrm{a} \cdot t_\mathrm{eq}) \,, \tag{5.3}$$

where t_eq is the equivalent ageing time defined by

$$t_\mathrm{eq} = t \cdot c_\mathrm{T}^{\frac{T-T_0}{\Delta T}} \cdot c_\mathrm{U}^{\frac{U-U_0}{\Delta U}} \,. \tag{5.4}$$

The constants T_0, U_0, ΔT and ΔU can be chosen arbitrarily. If T_0 and U_0 are set to rated temperature and voltage of the device, respectively, t_eq equals the real time at nominal conditions and c_a is the relative ageing rate at nominal conditions. For the results presented in the following, T_0 and U_0 were set to the rated values according to table 5.1, ΔT to 10 °C and ΔU to 100 mV.

To determine the ageing model parameters c_a, c_T and c_U, the model parameters that were obtained from the impedance spectra were fitted to the formula given in equation 5.3. Wherever possible, all parameters were left free for the regression analysis. Since

[4] A linear change was also assumed for the CPE exponent and the inductance in order to test for a correlation with ageing.

[5] The exponential dependency on the voltage is in good accordance with the Butler-Volmer equation. The reaction rate as it is described by Butler-Volmer or the basic Arrhenius equation increases exponentially with the negative inverse of the absolute temperature ($k \propto \mathrm{e}^{-E_\mathrm{a}/T}$), where E_a is the activation energy. However, for a limited temperature range this can be approximated by an expression increasing directly exponentially with temperature.

[6] a stands for one of the model parameters R_s, R_el, A_dl and γ.

Table 5.3: Parameters of the ageing model for an EDLC.

type	parameter	c_a in $\%/\mathrm{year}$	c_T	c_U	R^2	σ_err
A	R_s^{-1}	-6.94	1.98	1.75	0.98	0.033
	R_el^{-1}	-0.26	2.84	1.83	0.85	0.016
	A_dl	-6.81	1.66	1.44	0.93	0.018
	γ	-0.02	2.0[a]	2.0[a]	0.56	0.001
B	R_s^{-1}	-8.79	2.22	2.06	0.90	0.072
	R_el^{-1}	-4.60	2.0[a]	2.0[a]	0.51	0.145
	A_dl	-5.57	1.88	1.98	0.96	0.017
	γ	-0.42	2.0[a]	2.0[a]	0.42	0.012
C	R_s^{-1}	-5.20	2.0[a]	1.92	0.99	0.022
	R_el^{-1}	-3.83	2.0[a]	1.89	0.96	0.027
	A_dl	-2.03	2.0[a]	1.94	0.98	0.015
	γ	-0.19	2.0[a]	2.05	0.83	0.005

[a] Coefficient fixed during regression.

Table 5.4: Parameters of the simplified ageing model for an EDLC.

type	parameter	c_a in $\%/\mathrm{year}$	R^2	σ_err
A	R_s^{-1}	-4.11	0.96	0.089
	R_el^{-1}	-0.63	0.71	0.023
	A_dl	-1.12	0.80	0.031
B	R_s^{-1}	-12.07	0.90	0.151
	R_el^{-1}	-4.61	0.51	0.379
	A_dl	-4.69	0.96	0.023
C	R_s^{-1}	-4.54	0.99	0.052
	R_el^{-1}	-3.15	0.96	0.043
	A_dl	-1.83	0.98	0.017

the devices of type C were only tested at two operating points, c_T and c_U cannot be determined independently, c_T was therefore fixed to a value of two. Moreover, both c_T and c_U were set to a value of two, where the regression did not converge or the correlation was too weak to produce reliable results for these parameters.

The results of the regression for all EDLCs in the ageing test are summarised in table 5.3. As a measure for the quality of fitting, the coefficient of correlation R^2 and the standard deviation of the errors σ_err are included. The results for the inductance were omitted due to the high scattering of the data and the very low correlation ($R^2 \ll 1$). The correlation for γ is low for types A and B, the sensitivity to ageing is however very small, as can be seen from the values of c_a. The correlation for the inverse of the series resistance (which is the parameter that influences the dynamic performance of an EDLC most) is good. Similarly, the correlation for the linear decrease of the capacitance, expressed by the model parameter A_dl.

The fact that the influence of voltage and temperature on the deterioration rate can be described well by the exponential ageing model can also be interpreted as an

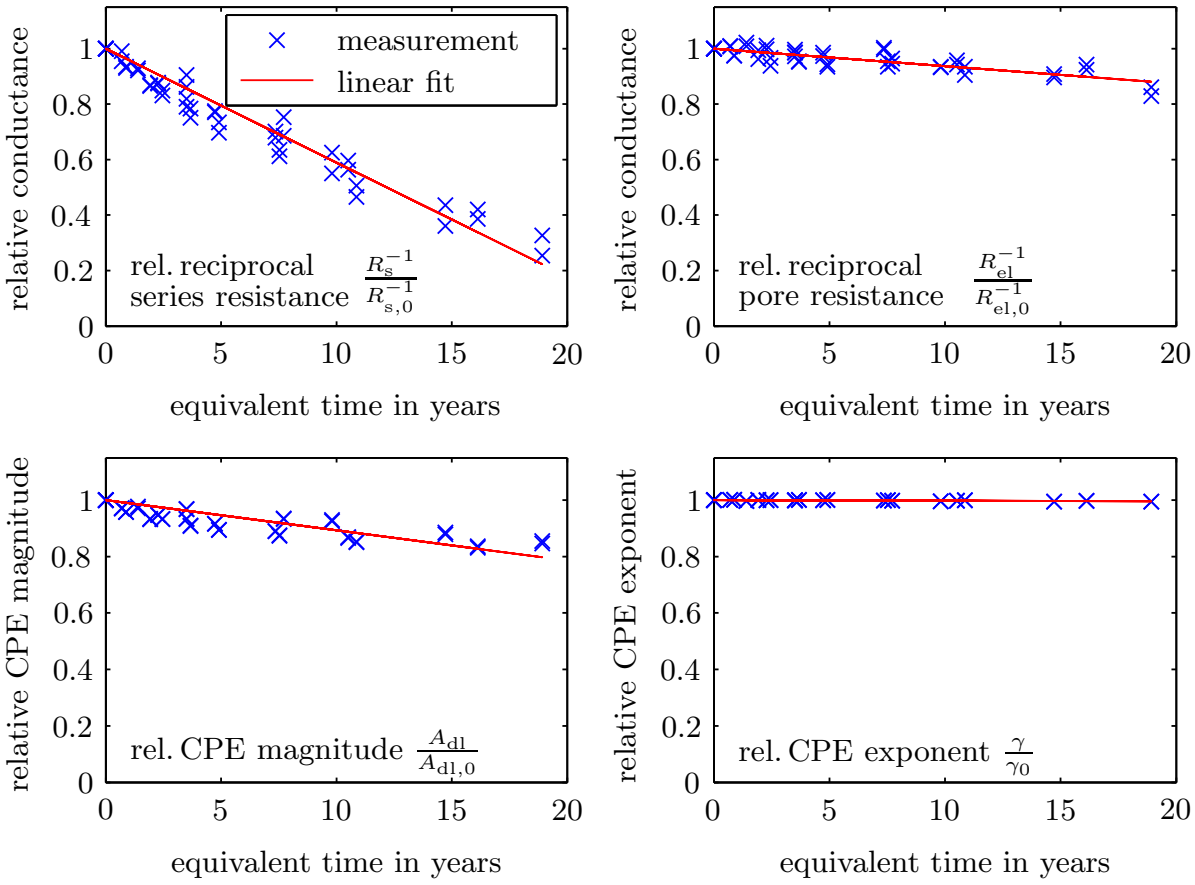

Figure 5.3: Relative parameters for ageing, EDLC type A.

indication that no new electrochemical processes have been activated.

The coefficients c_T and c_U are mostly close to a value of two, as expected from the rule of thumb mentioned above. However, they vary not only from one EDLC type to another, but also for the different model parameters. In order to achieve a more simplified but also more consistent ageing model, all coefficients c_T and c_U were set equal to two, which is close to the average of the regression results. Results of a regression with only c_a as a free parameter are presented in table 5.4. Except for type A the correlation coefficients are very close to those in table 5.3. However, even for type A the simplified model describes the impact of ageing on the impedance parameters adequately, as can be seen in figure 5.3. The measurement points are the same as in figure 5.2 but normalized to the initial values of the new devices and plotted against the equivalent time t_{eq}. The lines mark the development described by the simplified ageing model with the parameters shown in table 5.4.

For the interpretation of tables 5.3 and 5.4, it should be kept in mind that type B has a rated voltage of 2.7 V, while that of the other two devices is only 2.5 V. This leads to ageing rates of type B that seem significantly higher than the others. However, if U_0 for type B was set to 2.5 V, c_a would be approximately one fourth of the value presented here. Thus, type B would age slightly slower if operated at the same conditions as type A and C. It appears that its rated voltage was set too high.

The development of commercial EDLCs is still a dynamic process, it is very likely that products available today show ageing rates different from the devices used in the tests, yet the dependency on temperature and voltage will be close to those presented here.

5.1.3 Direct parameter estimation

For a real-time monitoring of the ageing effects of EDLCs, it would be too expensive to measure complete impedance spectra and to determine the model parameters by a least square error fitting procedure. It is therefore necessary to identify direct impedance values that can be easily measured and allow a good estimation of the model parameters. In section 6.2, a real-time measurement method will be proposed that allows the determination of the modulus, real and imaginary part of the impedance, however with a certain frequency blurring. The identification of a suitable frequency range for the measurements is therefore a key issue.[7]

The three model parameters that describe most of the electrical behaviour of an EDLC are the series resistance R_s, the double layer capacitance C_dl and the electrolyte resistance R_el. The inductance L_s has only little influence on the electrical behaviour except for high frequencies and is superimposed by the inductance of the feed cables, cell connectors etc. The CPE exponent on the other hand is mostly so close to one that it is hard to identify with the limited measurement accuracy of passive impedance measurements used for real time diagnosis. Furthermore, its influence on the electrical behaviour is small and limited to very low frequencies or long time constants.

A review of the standard model of an EDLC (eq. 3.8) and the asymptotes of the pore impedance given in equations 3.6 and 3.7 allow deriving simple rules for the estimation of the model parameters from single impedance measurements.

R_s can be obtained from the real part of the impedance at high frequencies since the pore impedance vanishes:

$$R_\mathrm{s} = \lim_{\omega\to\infty} Z'_\mathrm{EDLC}$$

R_el cannot be directly measured, only by means of the sum of the electrode and series resistance. Only for the standard model, i.e. for $\gamma = 1$, R_el can be determined from a consideration of limit values. According to equations 3.7 and 3.8 the real part of the impedance of an EDLC for low frequencies approaches the value $R_\mathrm{s} + {}^1\!/_3 R_\mathrm{el}$. Using the above mentioned estimate for R_s the pore resistance can be calculated:

$$R_\mathrm{el} = 3 \cdot \left(\lim_{\omega\to 0} Z'_\mathrm{EDLC} - \lim_{\omega\to\infty} Z'_\mathrm{EDLC} \right) \quad \text{for} \quad \gamma = 1$$

C_dl can be calculated from the imaginary part of the impedance at low frequencies. The influence of the inductance can be neglected for low frequencies, thus only the term $\lim_{\omega\to 0} Z''_\mathrm{EDLC} = -(\omega C_\mathrm{dl})^{-1}$ remains and the double layer capacitance according to the standard model can be determined:

[7] A different approach would be the estimation of the model parameters with classical parameter estimation methods. This approach is not followed in this thesis, a brief discussion on the topic can be found in section 6.2.8.

$$C_{\mathrm{dl}} = -\left(\omega \lim_{\omega\to 0} Z''_{\mathrm{EDLC}}\right)^{-1} \quad \text{for} \quad \gamma = 1.$$

For the determination of the model parameters according to the standard model ($\gamma = 1$), only two impedance measurements, one at the highest possible and one at the lowest possible frequency, would be necessary. However, for a real EDLC the low frequency impedance does not fit into that of an ideal capacitor. This behaviour has been discussed in section 3.1 and can be modelled with a generalized pore impedance (cf. equations 3.9 and 3.13).

The impedance can be described analytically by an impedance model, the error that is made if the model parameters are directly estimated from the real or imaginary part of the impedance can therefore be calculated as a function of frequency. Finding the frequency where the error is minimal or equals zero yields the optimal measurement frequency for the estimation of a certain parameter.

In order to calculate the errors, the complex impedance of the EDLC and especially the generalised pore impedance $\underline{Z}_{pg}$ (cf. section 3.1.3, eq. 3.9) have to be separated into its real and imaginary part. The complete calculations shall be abandoned here, the main steps are the separation of the terms

$$\sqrt{(j\omega)^{\gamma}} = \cos(\gamma\pi/4) + j\sin(\gamma\pi/4) \tag{5.5}$$

and

$$\coth(x_1 + jx_2) = \frac{\sinh 2x_1 - j\sin 2x_2}{\cosh 2x_1 - j\cos 2x_2}, \tag{5.6}$$

x_1 and x_2 are arbitrary real arguments.

For $\underline{Z}_{pg}$ follows:

$$Z'_{pg} = R_{\mathrm{el}} \cdot \frac{\sinh(2\sqrt{\Omega^{\gamma}}\cos\phi)\cos\phi - \sin(2\sqrt{\Omega^{\gamma}}\sin\phi)\sin\phi}{\sqrt{\Omega^{\gamma}} \cdot \left(\cosh(2\sqrt{\Omega^{\gamma}}\cos\phi) - \cos(2\sqrt{\Omega^{\gamma}}\sin\phi)\right)} \tag{5.7}$$

$$Z''_{pg} = -R_{\mathrm{el}} \cdot \frac{\sinh(2\sqrt{\Omega^{\gamma}}\cos\phi)\sin\phi + \sin(2\sqrt{\Omega^{\gamma}}\sin\phi)\cos\phi}{\sqrt{\Omega^{\gamma}} \cdot \left(\cosh(2\sqrt{\Omega^{\gamma}}\cos\phi) - \cos(2\sqrt{\Omega^{\gamma}}\sin\phi)\right)} \tag{5.8}$$

with the substitutions $\Omega = \omega(R_{\mathrm{el}}A_{\mathrm{dl}})^{1/\gamma}$ and $\phi = \gamma\pi/4$. The relative error for the direct parameter estimation of R_{s}, R_{el} and C_{dl} can now be calculated. For R_{s} the corresponding error is

$$r_{Rs} = \frac{Z'_{\mathrm{EDLC}} - R_{\mathrm{s}}}{R_{\mathrm{s}}} = \frac{Z'_{\mathrm{p}}}{R_{\mathrm{s}}} \tag{5.9}$$

$$= \frac{R_{\mathrm{el}}}{R_{\mathrm{s}}} \cdot \frac{\sinh(2\sqrt{\Omega^{\gamma}}\cos\phi)\cos\phi - \sin(2\sqrt{\Omega^{\gamma}}\sin\phi)\sin\phi}{\sqrt{\Omega^{\gamma}} \cdot \left(\cosh(2\sqrt{\Omega^{\gamma}}\cos\phi) - \cos(2\sqrt{\Omega^{\gamma}}\sin\phi)\right)}.$$

The error is proportional to the ratio of the series and the pore resistance and decreases towards higher frequencies. Equation 5.10 can be simplified by replacing the generalised pore impedance by the standard pore impedance. This approximation is justified by the

fact that at higher frequencies the impedance spectra of the standard and the generalised model are virtually indistinguishable. For the pore impedance the high frequency approximation $\underline{Z}_\mathrm{p} \approx \sqrt{\frac{R_\mathrm{el}}{j\omega C_\mathrm{dl}}}$ (eq. 3.6) can be used and separated into real and imaginary part employing the identity $\sqrt{j} = \frac{1+j}{\sqrt{2}}$, thus resulting in an approximation of the relative error

$$r_{R\mathrm{s}} = \frac{Z'_\mathrm{EDLC} - R_\mathrm{s}}{R_\mathrm{s}} = \frac{Z'_\mathrm{p}}{R_\mathrm{s}} \approx \frac{R_\mathrm{el}}{R_\mathrm{s}} \cdot \frac{1}{\sqrt{2\omega R_\mathrm{el} C_\mathrm{dl}}}. \tag{5.10}$$

The relative error of the pore resistance

$$\begin{aligned} r_{R\mathrm{el}} &= \frac{3 \cdot (Z'_\mathrm{EDLC} - R_\mathrm{s}) - R_\mathrm{el}}{R_\mathrm{el}} = \frac{3 \cdot Z'_\mathrm{pg}}{R_\mathrm{el}} - 1 \qquad (5.11) \\ &= 3 \cdot \frac{\sinh(2\sqrt{\Omega^\gamma}\cos\phi)\cos\phi - \sin(2\sqrt{\Omega^\gamma}\sin\phi)\sin\phi}{\sqrt{\Omega^\gamma} \cdot \Big(\cosh(2\sqrt{\Omega^\gamma}\cos\phi) - \cos(2\sqrt{\Omega^\gamma}\sin\phi)\Big)} - 1 \end{aligned}$$

depends only on Ω and ϕ, i.e. on the product $R_\mathrm{el}A_\mathrm{dl}$ and the CPE exponent γ. A similar simplification as for R_s is not possible for $r_{R\mathrm{el}}$. Within the frequency ranges that are suitable for the estimation of the corresponding parameters neither high nor low frequency behaviour can be neglected and γ has a significant influence on the characteristic.

The correlation $C_\mathrm{dl} = A_\mathrm{dl} \cdot \omega^{\gamma-1}\sin(\gamma\pi/2)$ (cf. equation 3.10) allows to calculate the relative error of C_dl as a function of the model parameters R_el, A_dl and γ:

$$\begin{aligned} r_{C\mathrm{dl}} &= \frac{-\left(\omega Z''_\mathrm{EDLC}\right)^{-1} - C_\mathrm{dl}}{C_\mathrm{dl}} = \frac{-1}{\omega C_\mathrm{dl} Z''_\mathrm{EDLC}} - 1 \qquad (5.12) \\ &= \frac{-1}{\omega A_\mathrm{dl}\omega^{1-\gamma}\sin(\gamma\pi/2)Z''_\mathrm{EDLC}} - 1 \\ &= \frac{-1}{\omega^\gamma A_\mathrm{dl}\sin(2\phi)\left(\omega L - R_\mathrm{el}\frac{\sinh(2\sqrt{\Omega^\gamma}\cos\phi)\sin\phi + \sin(2\sqrt{\Omega^\gamma}\sin\phi)\cos\phi}{\sqrt{\Omega^\gamma}\cdot\left(\cosh(2\sqrt{\Omega^\gamma}\cos\phi) - \cos(2\sqrt{\Omega^\gamma}\sin\phi)\right)}\right)} - 1. \end{aligned}$$

The influence of the inductance can be neglected for the relevant frequency range $f \ll R_\mathrm{el}/(2\pi L)$, which again leads to an expression that depends only on Ω and ϕ.

$$\begin{aligned} r_{C\mathrm{dl}} &\approx \frac{1}{\sin(2\phi)\omega^\gamma C_\mathrm{dl} R_\mathrm{el}} \qquad (5.13) \\ &\quad \cdot \frac{\sqrt{\Omega^\gamma}\cdot\left(\cosh(2\sqrt{\Omega^\gamma}\cos\phi) - \cos(2\sqrt{\Omega^\gamma}\sin\phi)\right)}{\sinh(2\sqrt{\Omega^\gamma}\cos\phi)\sin\phi + \sin(2\sqrt{\Omega^\gamma}\sin\phi)\cos\phi} - 1 \\ &= \frac{1}{\sin(2\phi)\sqrt{\Omega^\gamma}} \\ &\quad \cdot \frac{\cosh(2\sqrt{\Omega^\gamma}\cos\phi) - \cos(2\sqrt{\Omega^\gamma}\sin\phi)}{\sinh(2\sqrt{\Omega^\gamma}\cos\phi)\sin\phi + \sin(2\sqrt{\Omega^\gamma}\sin\phi)\cos\phi} - 1. \end{aligned}$$

The relative error $r_{C\mathrm{dl}}$ converges[8] to $\cot^2(2\phi)$, which has values well below 1 % for typical

[8] This expression can be derived by replacing each sin, sinh, cos and cosh expression that have $\sqrt{\Omega^\gamma}$ as an argument by their Taylor series approximation.

values of γ.

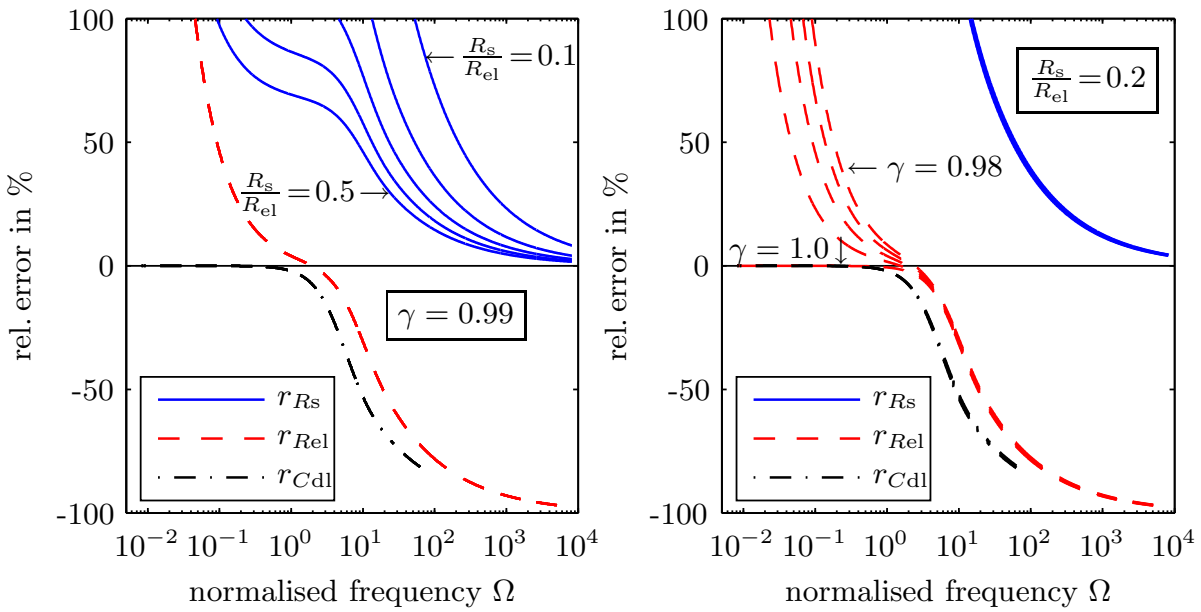

Figure 5.4: Development of the relative errors for an estimation of the model parameters from a single impedance measurement as a function of the standardised frequency $\Omega = \omega(R_{el}A_{dl})^{1/\gamma}$ for different ratios $\frac{R_s}{R_{el}}$ and fixed γ (left) and for a fixed ratio $\frac{R_s}{R_{el}}$ and variable values of γ (right).

Figure 5.4 shows the relative error of the estimation of the model parameters R_s, R_{el} and C_{dl} as a function of the standardised frequency $\Omega = \omega(R_{el}A_{dl})^{1/\gamma}$ for different sets of parameters. The left figure shows the relative errors for a fixed CPE exponent $\gamma = 0.99$ and different ratios of the series and pore electrolyte resistance, the right figure shows the development of the errors for a variation of γ.

To identify the optimal frequency for the estimation of each parameter, the minimum of the respective error has to be found. The relative error r_{Rel} is always positive and converges towards zero with increasing frequency without a local minimum. The optimal frequency would therefore theoretically be as high as possible. In practice the maximum frequency is limited by the measurement equipment, first of all by the maximum sample rate. For the model parameters R_{el} and C_{dl} the errors do not converge to zero for high or low frequencies, yet there is an optimal frequency where the errors cross zero. This transition frequency depends on the characteristic of the EDLC, i.e. on the model parameters, specifically the product $R_{el} \cdot A_{dl}$ and the CPE exponent γ. Equations 5.12 and 5.13 can be solved numerically for a given set of model parameters.

Figure 5.5 shows the optimal frequencies determined numerically for the parameters of an EDLC during ageing. The initial values for a fresh EDLC of type B were taken from table 3.1, the change of the parameters was calculated according to the ageing model described by equation 5.3 with the coefficients from table 5.3. The dashed line represents the optimal frequency for the determination of the respective model parameter. For R_s no optimal frequency exists, since the error never approaches zero. The calculations were also carried out for an acceptable error of $\pm 10\,\%$, which results in a frequency

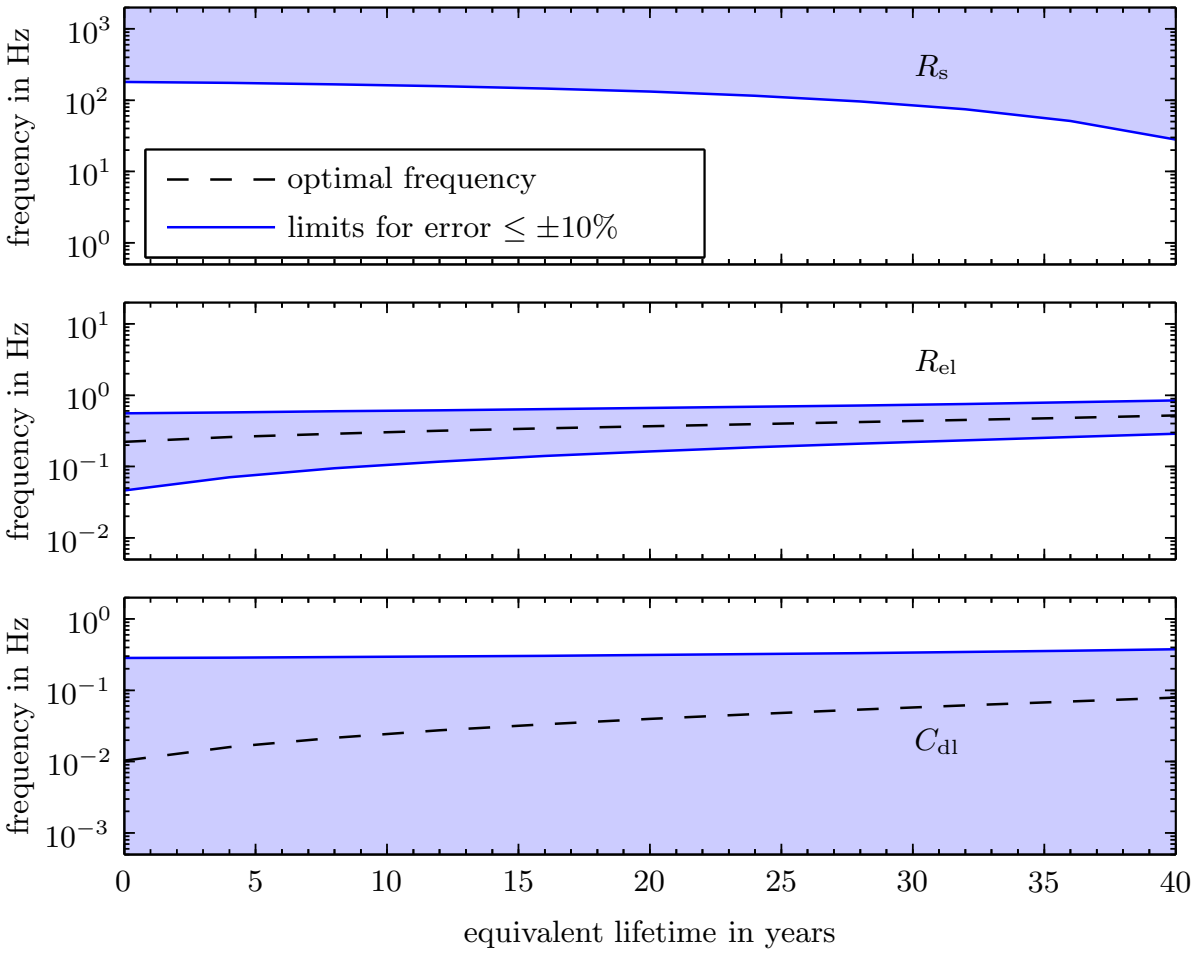

Figure 5.5: Optimal frequencies for the direct estimation of model parameters as a function of the equivalent life time (cf. eq. 5.4). Shaded areas denote the frequency ranges for an acceptable error of ±10 %. The values have been calculated exemplary for an EDLC of type B (initial model parameters according to table 3.1, variation during ageing according to equation 5.3 and table 5.3).

range that can be used for the parameter estimation, the results are represented as shaded areas in figure 5.5. For the determination of R_{el} a relative narrow frequency band is available that becomes narrower as the EDLC deteriorates. For R_s and C_{dl} only a lower and upper frequency limit, respectively, exists, the measurement frequency can be chosen much more freely. The frequency ranges for R_{el} and C_{dl} overlap, so in this case one measurement at about 0.3 Hz would be sufficient for the determination of both parameters, if a relative error of ±10 % can be accepted. In practice, variations in the parameters due to manufacturing tolerances and the dependency of the parameters on temperature and voltage are further sources of error and influence the optimal frequency.

The determination of the modulus of the impedance is easier than the determination of the real part of the impedance, since the information about the phase is not evaluated (cf. section 7.1.2). It would therefore be desirable to replace the real part of the impedance for the model parameter identification with the modulus. The additional relative error for the determination of R_s and R_{el} is determined by the phase angle of

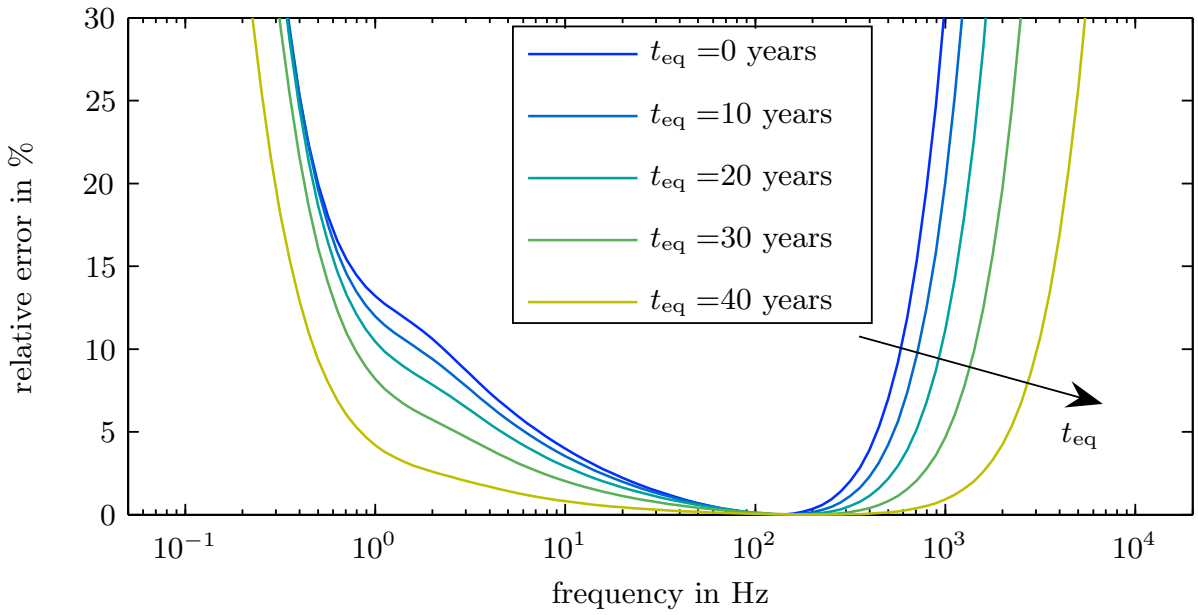

Figure 5.6: Relative error for the determination of R_s and R_{el}, which would occur if the measurement value of real part of the impedance was replaced by the modulus, as a function of frequency for different ageing states. The values have been calculated exemplary for an EDLC of type B (initial model parameters according to table 3.1, variation during ageing according to equation 5.3 and table 5.3).

.

the impedance:

$$r_{R,|Z|} = \frac{|Z| - Z'}{Z'} = \frac{1 - \cos(\phi)}{\cos(\phi)}. \tag{5.14}$$

For $\phi = 0$ $|Z|$ and Z' are identical, for both increasing inductive and capacitive impedance values the error increases.

Figure 5.6 shows the development of $r_{R,|Z|}$ with frequency for an EDLC at different stages of ageing. In a frequency region around 100 Hz the error amounts to only a few percent, which might be acceptable for the monitoring of the series resistance R_s. During ageing the acceptable frequency range becomes broader, mainly because the real part of the impedance increases significantly while the imaginary part of the impedance in this frequency range is less sensitive to ageing.

For frequencies below 1 Hz the error increases considerably, a replacement of the real part by the modulus of the impedance for the determination of the electrolyte resistance R_{el} is therefore not possible with adequate accuracy.

For monitoring systems that employ passive impedance measurements, normally only impedance values at one or very few frequencies can be determined. Moreover, the measurement frequency is only known in certain limits, for reasons that will be explained in section 6.2. With the error analysis described above, the optimal frequency range for such a passive impedance measurement can be determined, if the model parameters of the EDLC are known. If the parameters of the ageing model are also known – generally from accelerated ageing tests – the error can be predicted for the lifetime of the device.

Using the analytic expressions above for a correction of the model parameters determined by a monitoring system in real-time is possible only in a limited scale, since error terms depend on the parameters themselves.

5.2 Pulse power performance of lead-acid batteries

In some situations a battery has to provide a high power for short durations. One of the most common applications for this is the cranking of an automotive engine (the process of cranking itself is discussed in detail in section A.2). With the increasing electrification of modern motorcars, more electric loads have temporary power demands, which cannot be supplied by the generator but have to be buffered by the battery. Electric or electro-hydraulic brakes and electric steering assist are two examples.

Impedance models of the lead-acid battery for discharge pulses are presented in section 5.2.1, the parameterisation of this model is discussed in section 5.2.2. Moreover, an impedance based approach for a prognosis of the batteries power capability without an explicit battery model is presented in section 5.2.3.

5.2.1 Battery impedance model for discharge pulses

To predict the voltage during a given current profile, a battery model is necessary. This model has to take into account the special boundary conditions of the application, i.e. the high discharge current rate and the short duration. For implementation in a battery monitoring system, it should be simple enough to be implemented on a low-cost microcontroller.

Figure 5.7 shows the voltage development of a starter battery that is initially at rest and is at $t = 0$ loaded with a high rate constant current discharge for a duration of five seconds. The voltage drop can be subdivided into two parts, an instantaneous drop and

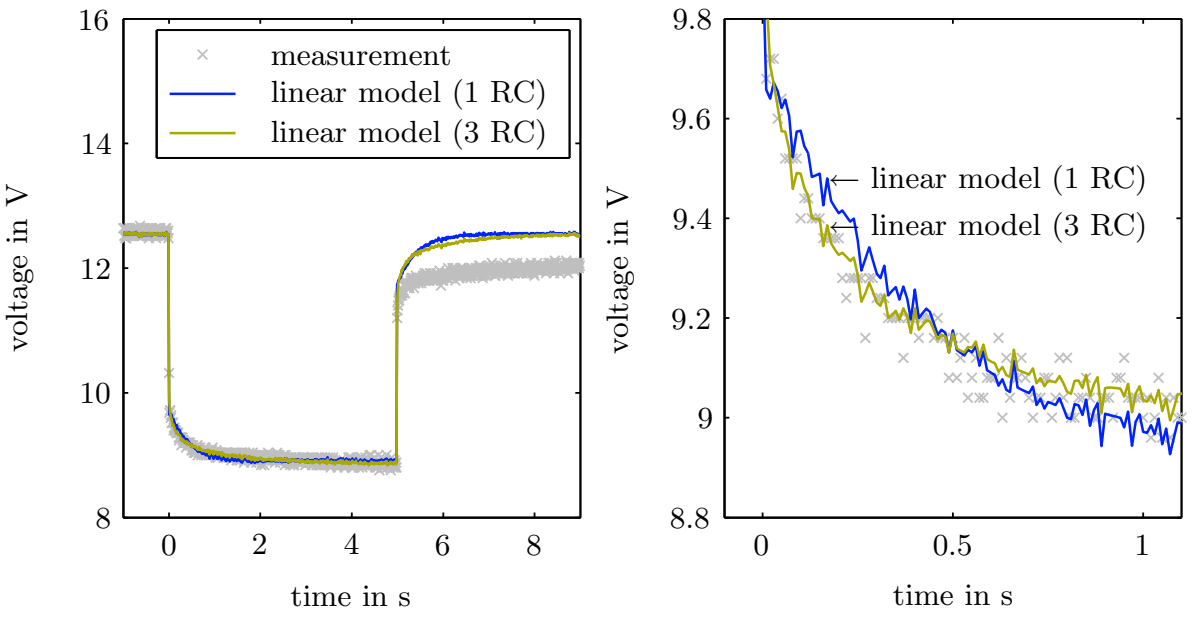

Figure 5.7: Voltage response of a starter battery (Moll Kamina 70 Ah at -18 °C and 85 % SOC) during a constant current discharge ($I = 100\,\mathrm{I}_{20} = 350\,\mathrm{A}$) in comparison to simulation results of two different linear impedance models ('1 RC': series resistance plus one parallel RC-circuit, '3 RC': series resistance plus three RC-circuits). Simulations have been carried out with the measured current profile.

a transient part. The instantaneous voltage drop is caused by the series resistance R_s of the battery, it can be calculated as

$$\Delta U_{inst} = R_s \cdot I. \tag{5.15}$$

The initial voltage drop makes up the predominant part of the total voltage drop, an impedance model that consist only of a series resistance will therefore produce acceptable results for very short high current pulses.

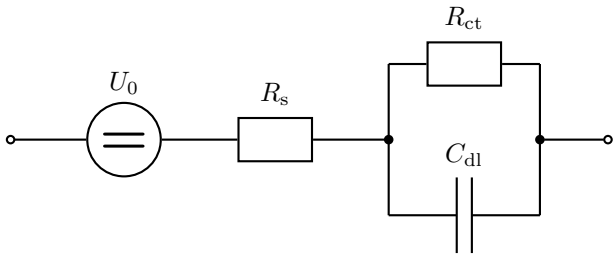

Figure 5.8: Generic impedance model for pulse power performance of batteries.

The shape of the transient voltage drop resembles an exponential decrease as one would anticipate from a parallel RC-circuit. This leads to a linear impedance model as shown in figure 5.8, which corresponds to the generic model[9] introduced in section 2.8. This model can also be derived from the original Randle's circuit presented in section 3.2.4, by neglecting the Warburg diffusion element and linearising the charge transfer resistance. The neglect of the Warburg impedance may be justified by the fact that diffusion in lead-acid batteries has typically time constants that are significantly larger than the typical pulse duration of a cranking pulse [78]. Transport processes can however have a significant influence on the overpotential, which will be discussed below. These processes are indirectly linked to diffusion and cannot be modelled adequately by the Warburg impedance.

Figure 5.7 shows a comparison of the measured voltage during a constant current discharge with the voltage progression for a linear model according to figure 5.8. The parameters of the model have been determined by a least squares fit over the duration of the discharge pulse. Model and measurement show good accordance, however during the first second of the discharge pulse a deviation of the shape of the curves can be observed. This deviation can be explained by the fact that the time constants of the electrical and electrochemical processes in a battery are not single-valued but dispersed due to the spatial distribution of the processes. This dispersion can be modelled by replacing the capacitor in a parallel RC-circuit by a constant phase element (CPE, cf. section 3.1.3), which leads to a so-called ZARC-element [8, 78]. There is no direct representation of a ZARC-element in the time domain, yet it can be approximated by a finite number of parallel RC-circuits connected in series. Buller has proposed an approximation of a ZARC-element with three RC circuits

$$R_1 = R_2 = R_3 \quad \text{and} \quad C_1 = \frac{C_2}{k_\gamma}, C_3 = C_2 \cdot k_\gamma, \tag{5.16}$$

[9]The series inductance has been neglected, since its influence on the voltage response in the time domain is negligible for the very most applications.

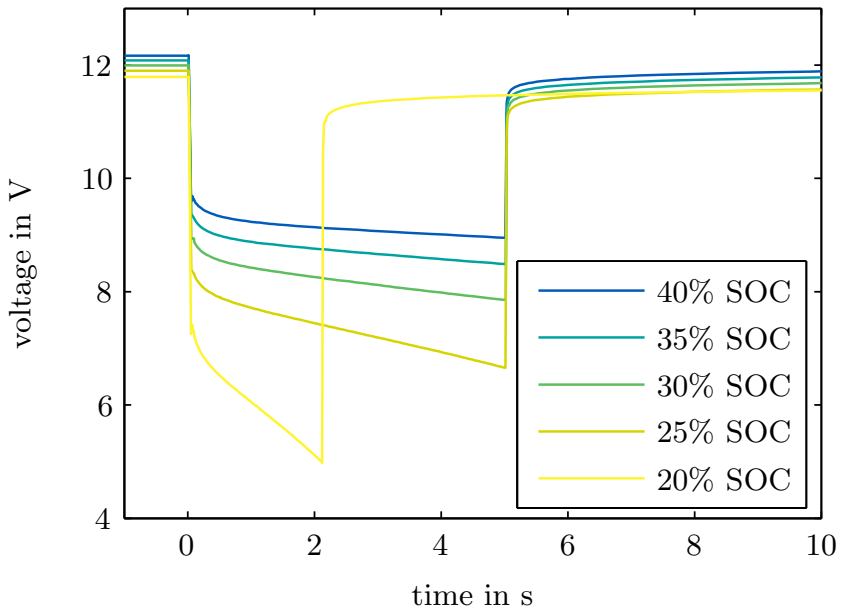

Figure 5.9: Voltage response of a starter battery (Moll Kamina 70 Ah at 10 °C) on a high rate constant current discharge ($I = 100\,\mathrm{I}_{20} = 350\,\mathrm{A}$) for different states of charge.

where $R_{1...3}$ and $C_{1...3}$ are the elements of the RC-circuits and k_γ is an optimization factor, that depends on the CPE exponent γ [29].

Figure 5.7 also shows the result of a simulation with a model comprised of three RC circuits. The parameters R_2, C_2 and k_γ were determined by a least squares fit, the remaining parameters where calculated according to equation 5.16. The agreement of measurement and model for the given experiment is excellent, the deviation during the relaxation after the current has been switched off however indicates that the validity range of the model is limited.

Figure 5.9 shows the voltage response of batteries to the same current profile as in figure 5.7, yet the batteries are in a more critical state, namely at low states of charge. The proposed linear model will fail to describe the voltage behaviour over the pulse duration. Physically, the linear or even progressive decrease of the voltage can be explained by a depletion of the electrolyte in the vicinity of the active surface in the pores. This depletion corresponds to a discharge of the sulphuric acid in a volume much smaller than the total electrolyte volume. The transport of ions into the depleted region by diffusion is too slow to compensate for the consumption of ions if the current rate is very high and the pulse duration is short. The decrease of the concentration of the electrolyte in the vicinity of the active surface has two effects: both the local equilibrium potential and the conductance of the electrolyte fall. The decrease of the conductance in turn causes a growing voltage drop. The two effects can be distinguished by observing the relaxation of the voltage at the point where the current is switched off. If the conductance has decreased during the discharge, the voltage drop at switch-off will be larger than at switch-on of the current. A change in the equilibrium potential in contrast will lead to a reduced open circuit voltage after the pulse compared to the voltage before.

Figure 5.9 shows the voltage response of a starter battery at 10 °C for different states

of charge. Towards low states of charge not only the initial voltage drop becomes larger due to the decreased electrolyte conductivity, but also the slope of the voltage during the discharge becomes steeper. The change of the state of charge for the whole pulse is less than 1 %, the voltage decrease can thus only be explained by a local acid depletion. Figure 5.9 shows clearly that voltage difference before and directly after the discharge pulse is nearly identical, the increase of the voltage drop can therefore be assigned mainly to an increase of the electrolyte resistance.

The change of the equilibrium potential due to the depletion of the electrolyte can be approximated by a series capacitor C_s. This capacitor causes a voltage drop proportional to the amount of charge withdrawn from the battery. The capacitance C_s cannot be derived directly from the open circuit voltage characteristic of the battery, since only a small part of the total electrolyte volume is influenced by the high rate discharge.

The change of the electrolyte conductivity cannot be modelled with a linear impedance model. An impedance element that produces the desired behaviour is a resistance that grows linearly with the discharged amount of charge:

$$R_\mathrm{k} = -k \cdot \int_0^t i(t)\,\mathrm{d}\tau, \tag{5.17}$$

where k is a constant that determines the slope of the resistance increase[10]

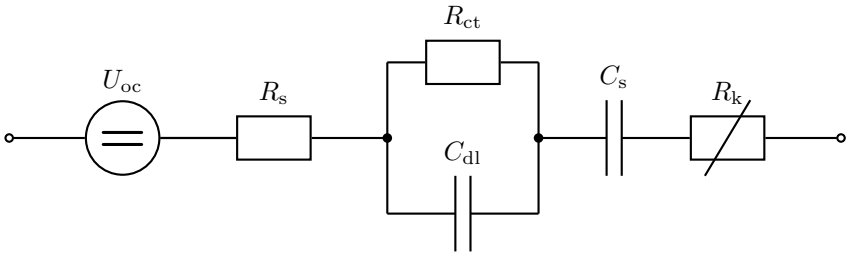

Figure 5.10: Non-linear impedance model for pulse power performance of lead-acid batteries.

Figure 5.10 shows the proposed model for the pulse power performance of lead-acid batteries consisting of the open circuit voltage U_oc, a series resistance R_s, a parallel RC-circuit with R_ct and C_dl[11], the series capacitance C_s that models the decrease of the open circuit potential and the non-linear resistance R_k that simulates the increase of the electrolyte resistance.

Both the series capacitance C_s and the non-linear resistance R_k would cause a voltage drop that exceeds all physically sensible limits, if the model was used for discharge or charge periods longer than a few seconds. This limitation is due to the fact that the underlying assumption of the model is the discharge of a small electrolyte volume without any supply of charge carriers from the bulk electrolyte. For a more general model, charge transport processes cannot be neglected [138, 168]. However, the voltage

[10] The minus sign has to be introduced since discharge currents are by definition negative.

[11] The notations for charge transfer ('ct') and double layer ('dl') have been kept for easier interpretation. The model however is heuristic and not detailed enough to relate these model parameters clearly to the physical processes at the electrodes.

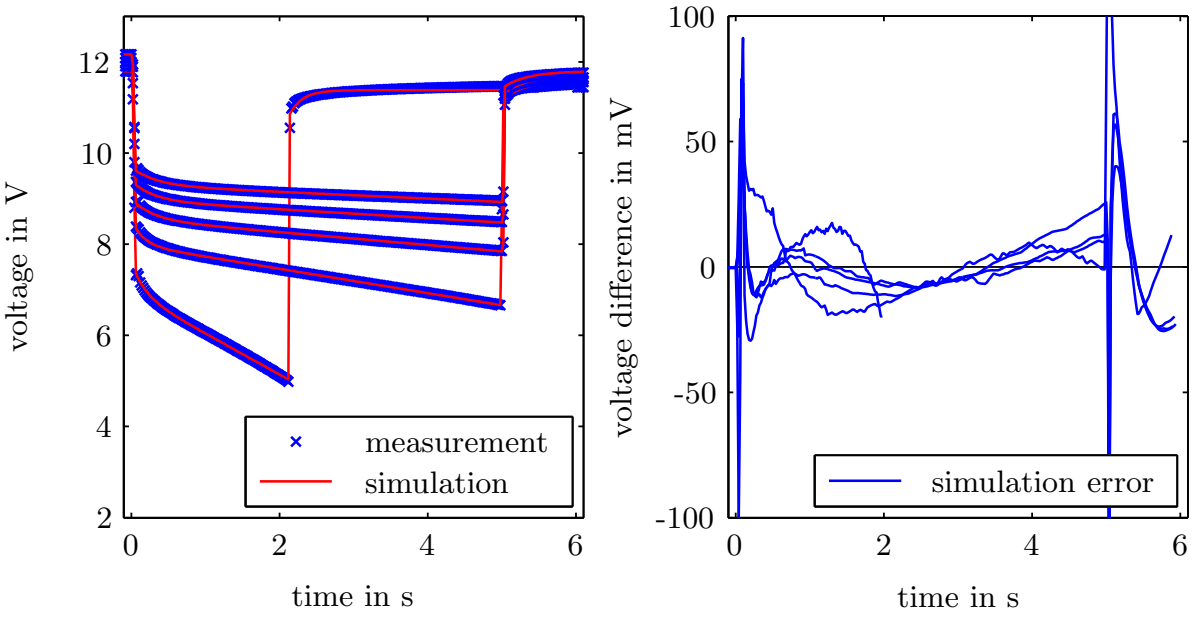

Figure 5.11: Comparison of simulation results with the measured voltage curves from figure 5.9 (left) and deviations of measurement and simulation (right).

curves that can be obtained with this simulation model show very good accordance with measurements. Figure 5.11 (left) shows a comparison of the battery voltage during a high current discharge pulse with the voltage curves that have been obtained with the model of figure 5.10. The model parameters have been obtained by numerically fitting the voltage curves for the respective current profiles. The corresponding model parameters for the different states of charge are presented in table 5.5.

Figure 5.11 (right) shows the deviations of measurement and simulation. The deviations during the first few hundred milliseconds after the beginning and the end of the current pulse are mainly due to the fact that the single RC-circuit of the model does not reproduce the voltage transient correctly. This could be improved by a CPE element. The small deviations, however, scarcely justify the increased model complexity. The simulation error shows a systematic shape during the discharge pulse, since C_s and R_k produce only a linear voltage slope, which is only a first order approximation of the real characteristics of the equilibrium potential and the electrolyte resistance.

The applicability of the model for realistic current profiles is demonstrated in figure 5.12. The left figure shows a comparison of voltage profile measured during the cranking of a combustion engine in a motorcar with a voltage curve simulated with the model of figure 5.10 and the measured cranking current. The parameters of the model have been determined by a least squares regression for the corresponding current profile. The deviations between measurement and simulation are shown in the right figure. For comparison, the simulation of the voltage has also been carried out for a simplified model that consists only of the series resistance and the linear RC-circuit ('R-RC') and with the simplest possible battery model comprised only of the series resistance ('R'). The deviation of the purely resistive model is large. The deviation of the R-RC-model is moderate in this example, yet for critical battery states the non-linear voltage drop due

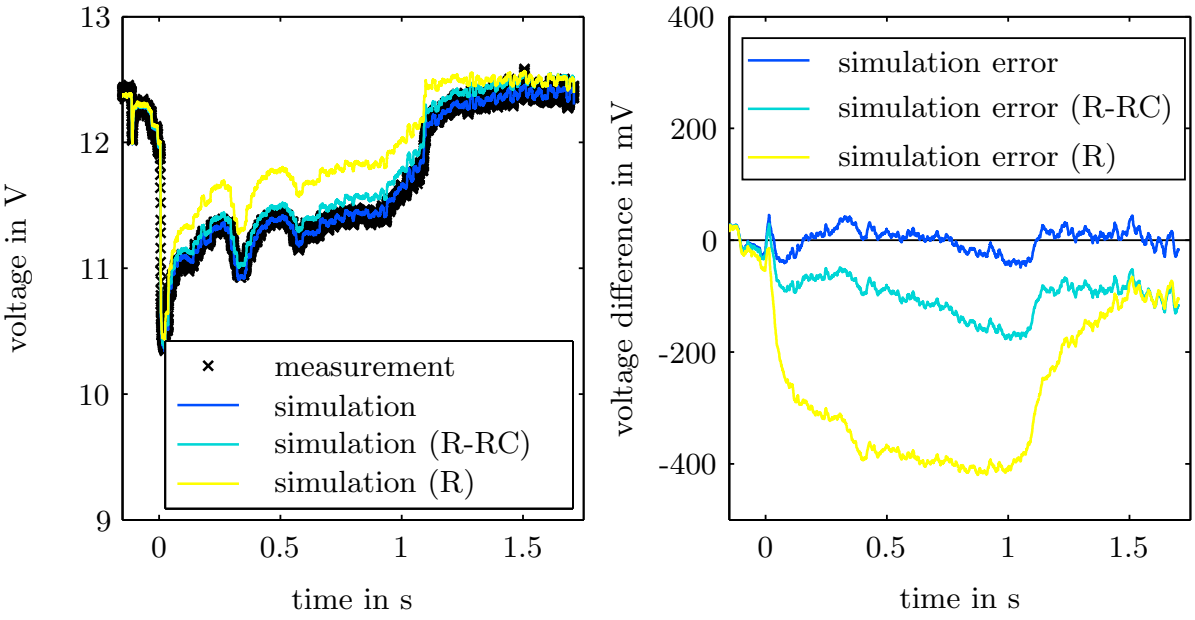

Figure 5.12: Voltage response of a starter battery (Moll Kamina 70 Ah at room temperature) on a cranking current profile (peak current 335 A) compared to simulation results for the model according to fig. 5.10 (left) and deviations between measurement and simulation (right). 'R-RC' denotes a model comprised only of R_s, R_{ct} and C_{dl}, 'R' a model with only the series resistance R_s.

to local electrolyte depletion can be significantly larger (cf. figure 5.9).

Table 5.5: Parameters for the impedance model (fig. 5.10) for the discharge pulses shown in figure 5.11.

SOC in %	U_{oc} in V	R_s in mΩ	R_{ct} in mΩ	C_{dl} in F	k in $^{m\Omega}/_{As}$	C_s in F
20	11.79	12.84	1.53	112	6100	1745
25	11.90	10.34	1.19	132	1597	4114
30	12.00	9.05	1.11	257	507	4123
35	12.08	8.12	1.07	267	151	4250
40	12.16	7.47	0.98	328	0	4606

5.2.2 Parameterisation of the impedance model

In section 5.2.1 an impedance model has been developed that allows simulating the voltage of the battery during a discharge with a high current for a time range of up to several seconds. To demonstrate the capability of the model to describe the behaviour of the battery, the model parameters were determined from the measured battery voltage during the discharge pulse. Yet, for a prediction of the pulse power performance, these parameters have to be known beforehand.

Two fundamentally different methods can provide this information: on-board impedance measurements and self-adapting characteristics.

The determination of impedance parameters in real time during operation from small signal measurements allows tracking changes in the cranking capability directly and independent from the monitoring of other battery state variables such as state of charge and temperature. This method does, however, not provide any information about the battery performance at a situation that differs from the current state of the battery, e.g. for the cranking capability of the battery after a long parking period when state of charge and ambient temperature have changed. In addition to that, the estimation of the model parameters for a high discharge current from impedance values from small signal measurements and at a different operating point involves inaccuracies due to the non-linear nature of the battery.

For a prognosis of the battery behaviour at other states, the parameters can be stored in look-up tables as a function of other battery state variables, namely the state of charge and the battery temperature. Static characteristics will though always fail as the battery behaviour varies from one battery type to another and changes slowly due to ageing processes. This problem can be overcome by using self-adaptation methods that evaluate the battery behaviour during normal operation and change the characteristics accordingly.

These two methods are not concurring, but have each their strengths and weaknesses in different situations and should be combined for a stable and reliable prognosis. A method for the self-adaptation of characteristics is proposed in section 6.3. The parameterisation from impedance measurements is discussed below; a passive impedance measurement procedure for battery monitoring systems is presented in section 6.2.

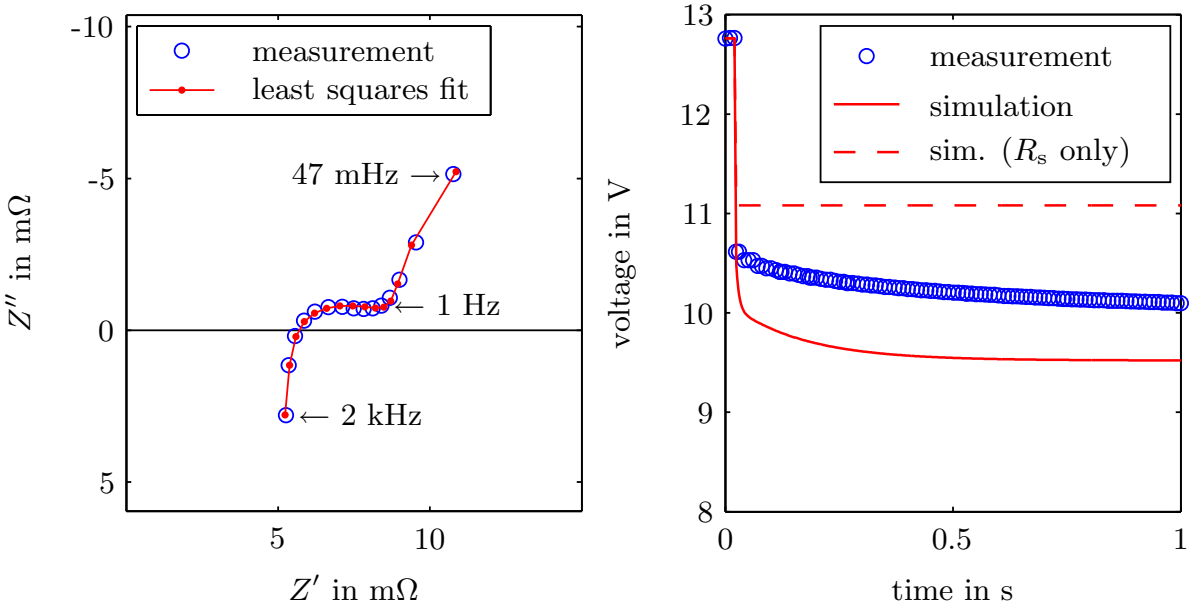

Figure 5.13: Impedance spectrum of a starter battery (Moll Kamina 70 Ah at 76 % SOC and room temperature, DC bias current 3.5 A) and simulation result with a fitted impedance model (left). Measured voltage progression during a 350 A discharge and simulation result with the same impedance model. The dashed line shows the simulation result with only the series resistance parameterised from the impedance spectrum.

Figure 5.13 (left) shows the impedance spectrum of a starter battery (Moll Kamina 70 Ah at 76 % SOC and room temperature), measured with a superimposed discharge current of 3.5 A[12]. The spectra were fitted with a generic battery model that consists of a series inductance and two ZARC elements (cf. section 3.2.4). The first ZARC element represents the left, depressed semicircle in the figure 5.13 (left), other impedance measurements on lead-acid batteries with a reference electrode show, that this part of the spectrum can be assigned to the positive electrode [78]. The second semicircle with a significantly lower time constant is also modelled by a ZARC-element to improve the quality of the fit; measurements with significantly lower frequencies would be necessary to determine its shape and model parameters accurately [31, 78, 168]. The spectra calculated by the impedance model show good accordance with the measurements. In figure 5.13 (right) the results of a simulation with the impedance model[13] for a discharge pulse of 350 A are compared with the battery voltage for this current profile. The discharge pulse has been measured approximately one hour after the impedance measurements were finished. The shape of the discharge curve during the first 200 ms is represented well by the simulation, the absolute voltage drop, however, has been significantly over-estimated. This effect can be attributed to the non-linearity of the Butler-Volmer equation (eq. 3.26). The corresponding charge-transfer resistance decreases for higher direct currents, as can be seen in figure 2.2. Moreover, impedance spectroscopy yields the differential or small-signal resistance, while in the time domain the large-signal resistance is observed (cf. section 2.2).

In order to distinguish the influence of the different parts of the model, the voltage curve simulated for a model with only a series resistance R_s is also given in figure 5.13 (right). The voltage drop during the first second, which is the most significant time range for a real start of a combustion engine, is mainly determined by the ZARC element. Still, the voltage drop is significantly too large. This effect can be understood by the strong non-linear behaviour of the battery. The impedance measurement yields the differential impedance measured at a certain direct current I_DC, while the voltage drop is determined by the absolute impedance at a discharge current I_DCH, which is generally significantly higher than I_DC. In the example shown in figure 5.13 the ratio of I_DCH and I_DC is 100. Moreover, for a passive impedance in a vehicle I_DC is often a positive (charging) current, while I_DCH is always negative.

The non-linear over-potential can be approximated by the simplified Butler-Volmer equation discussed in section 3.2.3. For a large discharge current, the Butler-Volmer equation can be approximated by the Tafel equation (eq. 3.27):

$$\Delta U_\mathrm{ct,DCH} \approx -\frac{R_\mathrm{m} T}{(1-\alpha) n F} \cdot \ln \frac{I_\mathrm{DCH}}{I_0}, \tag{5.18}$$

[12]The spectra were measured during "microcycle operation", i.e. three spectra during charging and three spectra during discharging have been measured alternately. This procedure assures reproducible conditions by eliminating the pre-history of the battery; only the third charge and discharge spectrum is used for analysis [78].

[13]The ZARC element does not have an exact representation for a time-domain model, it has therefore been approximated by a series connection of three RC-circuits, as proposed by Buller [29].

the corresponding absolute charge transfer resistance is

$$R_{\mathrm{ct,DCH}} \approx -\frac{R_{\mathrm{m}}T}{(1-\alpha)nF} \cdot \frac{\ln I_{\mathrm{DCH}} - \ln I_0}{I_{\mathrm{DCH}}}. \tag{5.19}$$

The constants R_{m}, n and F are known, temperature T and the discharge current I_{DCH} can be measured and the symmetry factor α is very similar for all lead-acid batteries [78]. What remains for the determination of $R_{\mathrm{ct,DCH}}$ is the exchange current I_0, which is sensitive to the state of charge, temperature and the composition of the active materials. If the impedance measurement is carried out at a relatively large charging current, the differential resistance can be derived from the Tafel-approximation (eq. 3.27):

$$\mathrm{d}R_{\mathrm{ct,DCH}} \approx \frac{\mathrm{d}}{\mathrm{d}I}\left(\frac{-R_{\mathrm{m}}T}{(1-\alpha)nF} \cdot \ln\frac{I_{\mathrm{DCH}}}{I_0}\right) = \frac{-R_{\mathrm{m}}T}{(1-\alpha)nF} \cdot \frac{1}{I_{\mathrm{DCH}}}, \tag{5.20}$$

which does not contain information about the exchange current I_0. The same is true for an impedance measurement with a large discharge current.

Yet, I_0 can be determined by an impedance measurement with only a small direct current close to zero. The respective approximation of the Butler-Volmer equation is given by equation 3.28, the absolute and the differential charge transfer resistance for this linear approximation are identical:

$$\mathrm{d}R_{\mathrm{ct},0} = R_{\mathrm{ct},0} \approx \frac{R_{\mathrm{m}}T}{nF\,I_0}. \tag{5.21}$$

If the impedance spectrum has been measured at a significant number of frequencies, a least-squares fit is the most accurate procedure to determine the model parameters. If a passive impedance measurement as the one proposed in section 6.2 is used, only very few frequencies points can be measured due to the low frequency resolution. In this case, a direct determination of the parameters is more apt.

A method that allows the determination of the impedance parameters of a model that consists of a series resistance and a ZARC element from impedance measurements at three frequencies has been described by Nelatury and Singh [108]. The proposed method does not include the determination of an inductance, it is therefore required that the three measurements are conducted in a frequency range where the battery impedance is capacitive. If necessary, the inductance can be easily determined by measuring the impedance at a high frequency f_{h} of several 100 Hz, where the inductive behaviour dominates the impedance [109]:

$$L \approx \frac{Z''(f_{\mathrm{h}})}{2\pi f_{\mathrm{h}}}. \tag{5.22}$$

The inductive behaviour does not influence the voltage response of the battery during a cranking pulse significantly, but if the value of the inductance is known, the measured impedance values for the determination of the remaining model parameters can be compensated for the inductive contribution by subtracting ωL from the imaginary part in order to improve the accuracy.

5.2.3 Simplified prognosis for discharge pulses

The parameterisation of an equivalent circuit model for a voltage prognosis during a pulse discharge requires some computational effort, the accuracy yet is still limited due to the fact that some assumptions about the non-linearity of the battery impedance have to be made and that an equivalent circuit model for the time domain[14] can only approximate the real behaviour.

A considerably simplified method has therefore been developed and implemented for an automotive battery monitoring system [20, 21, 23]. The idea of this approach is based on the fact that the real part of the impedance grows continuously with decreasing frequency and that the voltage drop for a constant current discharge growth with time. For each pulse duration Δt_p, there is a corresponding frequency f_p, where the real part of the impedance equals the "effective" resistance defined by the voltage drop and the pulse current:

$$\frac{u(t_\mathrm{p}) - u(0)}{i(t_\mathrm{p})} = Z'(f_\mathrm{p}), \tag{5.23}$$

where $u(0)$ is the battery voltage immediately before the pulse.

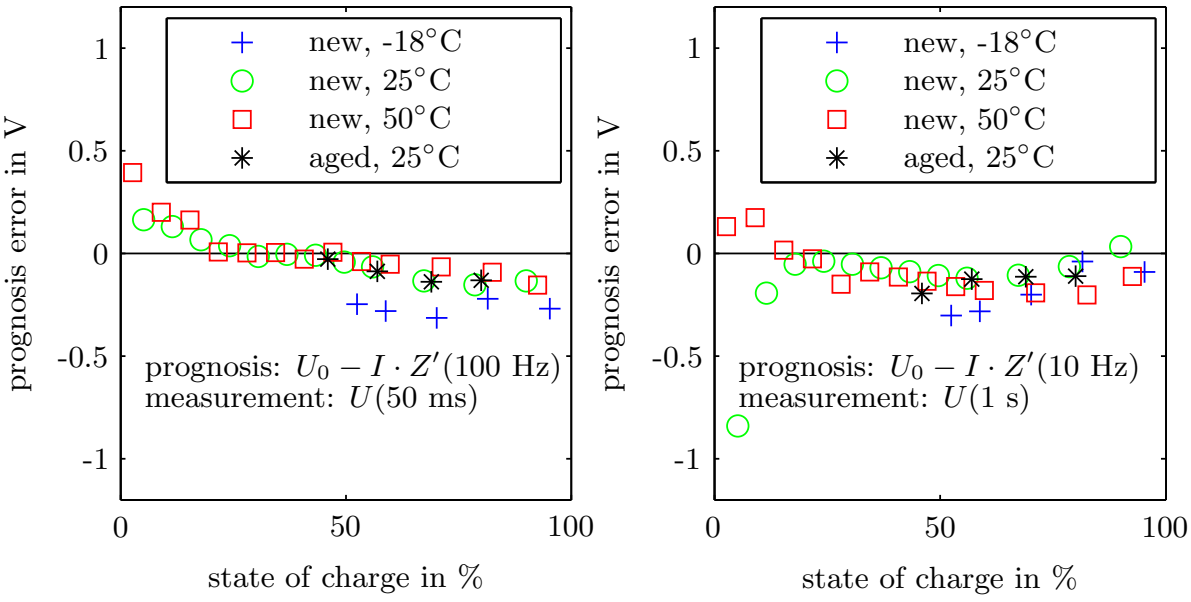

Figure 5.14: Difference of the predicted and the measured voltage drop for the simplified cranking prognosis for a pulse duration of 50 ms (left) and 1 s (right). Positive values imply, that the measured voltage was higher than the prognosis.

The mapping of a pulse duration to a single corresponding frequency cannot be derived analytically for a non-linear impedance (cf. section 2.2) and even for a linear impedance, integration along the complete frequency range would be necessary.

Yet, for a given battery characteristic and discharge current rate the mapping is unique and can be determined experimentally. For practical use, it is essential that this

[14] The CPE behaviour can be described in the frequency domain by a closed expression, for a representation in the time domain it has to be approximated by one ore more RC-circuits.

characteristic is relatively insensitive to temperature, discharge current rate and battery state. For starter batteries the frequency-time pairs

$$f = 100\,\mathrm{Hz} \Leftrightarrow t = 50\,\mathrm{ms} \quad \text{and} \quad f = 10\,\mathrm{Hz} \Leftrightarrow t = 1\,\mathrm{s} \tag{5.24}$$

have been identified experimentally to yield good results. For this purpose, impedance spectra have been measured at different batteries, temperatures and states of charge, and the predicted voltage drop for a predefined discharge pulse have been compared with the measured voltage drop.

The impedance spectra have been measured with the EISmeter, an impedance spectrometer for laboratory use [16] with a superimposed direct current of -3.5 A (discharge). After each impedance measurement the battery was at rest for approximately one hour followed by the discharge pulse of 350 A for 10 seconds.

Figure 5.14 shows the difference of the predicted and the measured voltage drop for a pulse duration of 50 ms (left) and one second (right) as a function of state of charge for a new battery (Moll Kamina 70 Ah) at three different temperatures and for an aged battery (Moll Kamina, nominal capacity 70 Ah, measured capacity after cyclic ageing 45 Ah). Both figures show that the error has a systematic component, however all deviations – except for extremely low states of charge – are in a range of $\pm 300\,\mathrm{mV}$ for a battery with a nominal voltage of 12 V.

Chapter 6

Algorithms for on-board monitoring

This chapter focuses on measurement techniques and algorithms that are necessary for the application of impedance-based diagnostics in battery monitoring systems. An introduction to typical applications and to state-of-the-art measurement hardware suitable for commercial real time applications is given in section 6.1.

In section 6.2 a novel method for passive impedance measurements based on RMS-values is presented. The mathematical foundation of this method as well as the different factors influencing its accuracy are discussed in detail and compared with standard methods. In addition, a passive measurement technique is presented that determines the effective frequency of the passive impedance measurement.

As a complement to impedance measurements, which provide information only about the current state of the battery, algorithms for self-adapting characteristic maps are presented in section 6.3. These algorithms allow describing the properties of storage systems by means of characteristic maps even for systems that change slowly due to ageing processes.

6.1 Requirements and environment

Large rechargeable batteries are used in all kinds of technical systems and environments, in autonomous power supplies, safety systems, uninterruptible power supplies or in conventional automotives and hybrid electric vehicles. The specific requirements on battery monitoring systems are different for diverse applications but have some things in common:

Robustness Battery monitoring systems may be exposed to wide temperature ranges, climatic influences, vibration and the like. Moreover, electromagnetic as well as grid-bounded noise disturbs the measurement. These environmental conditions demand not only a robust hardware but also robust and fault-tolerant algorithms.

Low cost A battery monitoring system should not contribute significantly to the total cost of the system, since it is generally not recognized by the user as an additional benefit.

These two requirements are probably most pronounced in the automotive sector, where cost pressure is very high, the hardware may be located under the engine bonnet

and the electric surrounding is extremely noisy due to the alternator ripple and dozens of switched loads in the power system.

6.1.1 Signals and noise

Figure 6.1 (left) shows the voltage ripple measured across the battery of a modern automobile driving in city traffic. The right side of figure 6.1 shows a section of the amplitude spectrum of the voltage signal determined by a discrete Fourier transform (DFT). Two distinct peaks can be identified in the frequency range between 30 and 100 Hz, that are also visible as the 'slow' ripple in the time domain. The characteristic frequency of the alternator is visible at about 2 kHz. Despite these distinct frequencies some noise is present over virtually the whole spectrum.

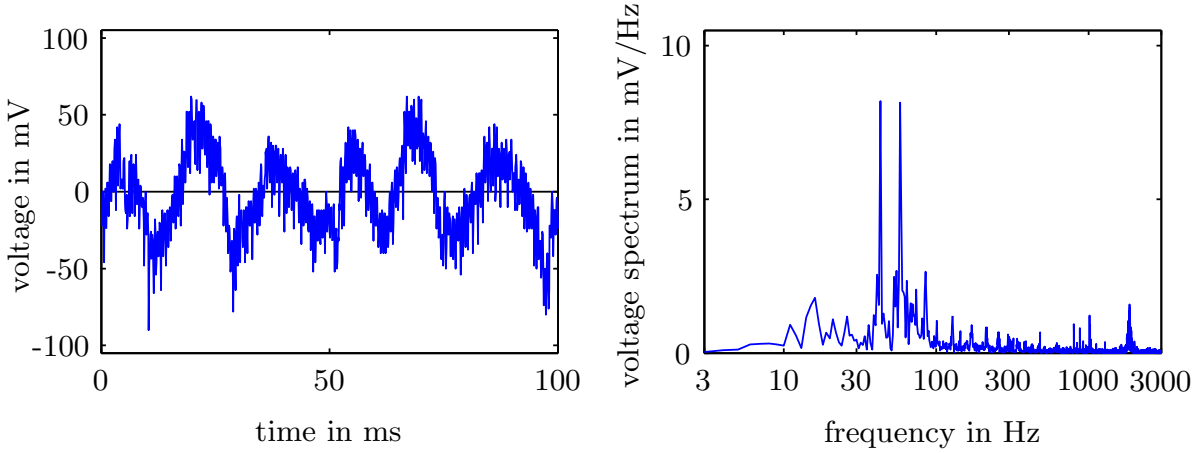

Figure 6.1: Ripple voltage across battery terminals in a modern vehicle (Audi A4) in city traffic (sample rate: 10 kHz).

A much longer data series is shown in figure 6.2, measured on a VW Golf V with a sample rate of 1 kHz over 10 minutes. During the first two minutes the car is active, but the engine is not running. The current is negative because the battery supplies various loads. After the cranking pulse with a peak current of more than 900 A, the motor accelerates and runs at idle speed for the rest of the profile. The spectrum shows large amplitudes in the low frequency range. However these are almost solely caused by the cranking pulse. A spectrum calculated exclusively for the time where the engine is running shows much lower amplitudes for frequencies below 10 Hz. Several spikes that correspond to distinct signals can be seen in the upper part of the spectrum.

A more detailed look at the development of the spectrum over time is shown in figure 6.3 as a spectrogram. The logarithmic amplitude normalized to full scale (dBFS) of the spectrum is represented as a colour value of each data point. The data was produced by a short-time FFT with a Hanning-window (cf. [97,115]) over intervals of one second, the resulting spectrum is plotted along the y-axis. This representation of the data allows drawing conclusions regarding the nature of the signal components. Straight lines at about 100, 200, 300 and 400 Hz are clearly produced by a switching electronic device, their is frequency sharply defined and constant in the course of time. Other signals show

a variation in time that indicates that the signal source is coupled to the engine speed. Pulses create a broadband excitation that expands along the frequency axis and create a vertical line, most pronounced during the cranking pulse at $t \approx 110\,\mathrm{s}$.

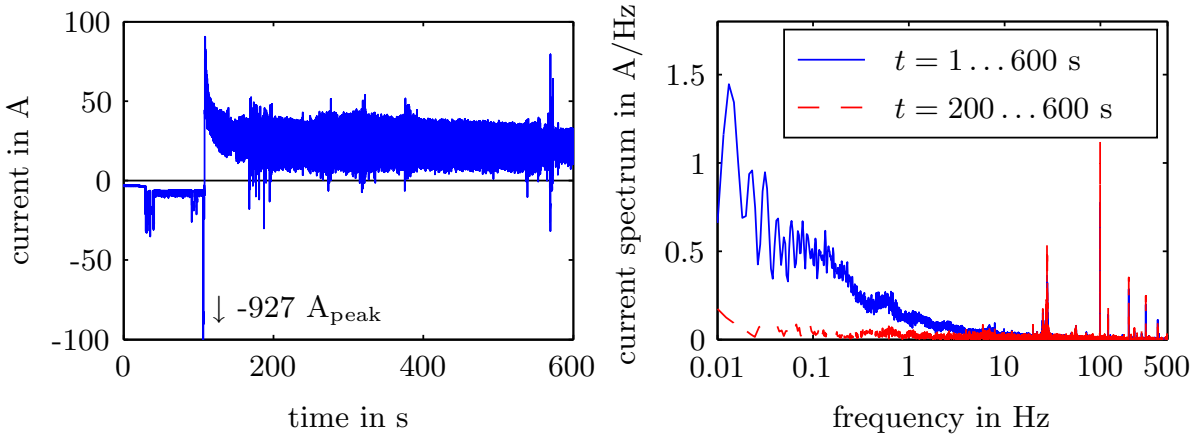

Figure 6.2: Battery current during stop mode, cranking and idle motor speed measured in a VW Golf V (sample rate: 1 kHz).

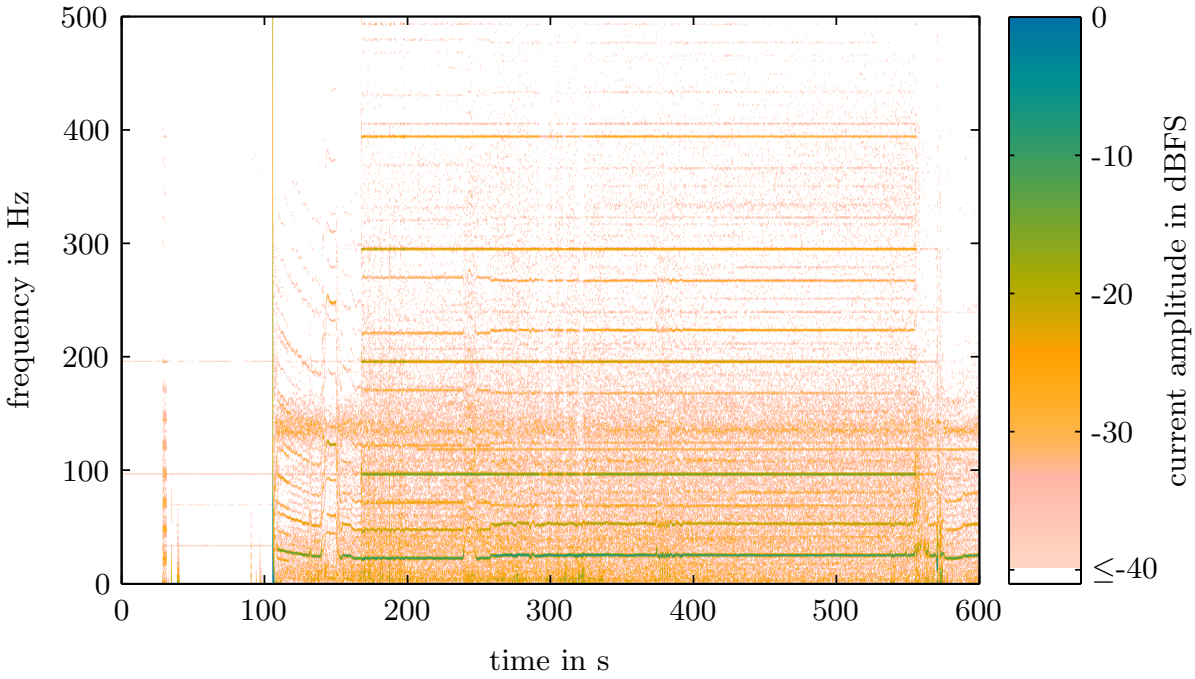

Figure 6.3: Spectrogram of the battery current shown in figure 6.2.

Figure 6.4 (left) shows a typical current profile in a hybrid electric vehicle (Toyota Prius NHW20). Its shape is directly determined by the driving of the vehicle and is thus a stochastic process. This is reflected in the spectrum (figure 6.4, right), which shows no distinct peaks that correspond to a strong signal at a single frequency. However, the current profile leads to strong signals in the low frequency region below 1 Hz.

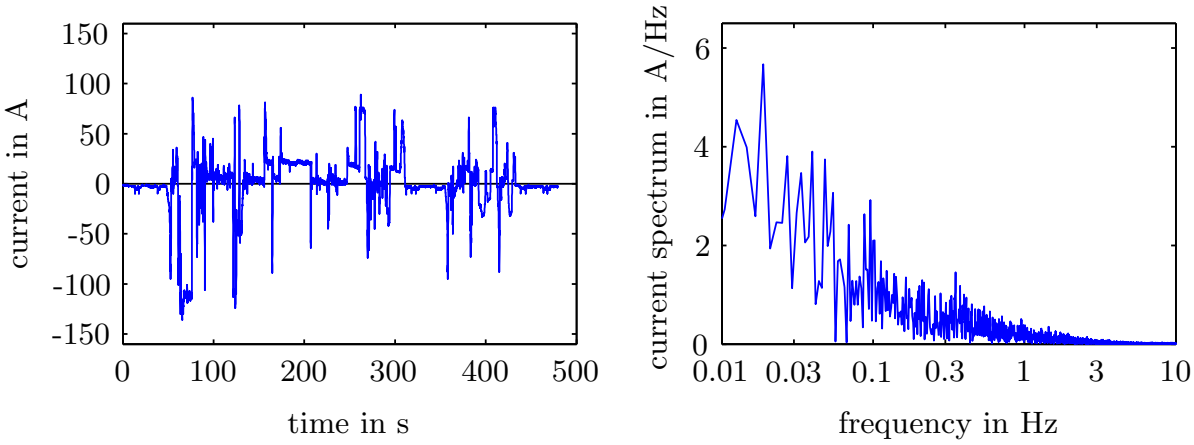

Figure 6.4: Current profile in a commercial hybrid electric vehicle (Toyota Prius) (sample rate: 25 Hz).

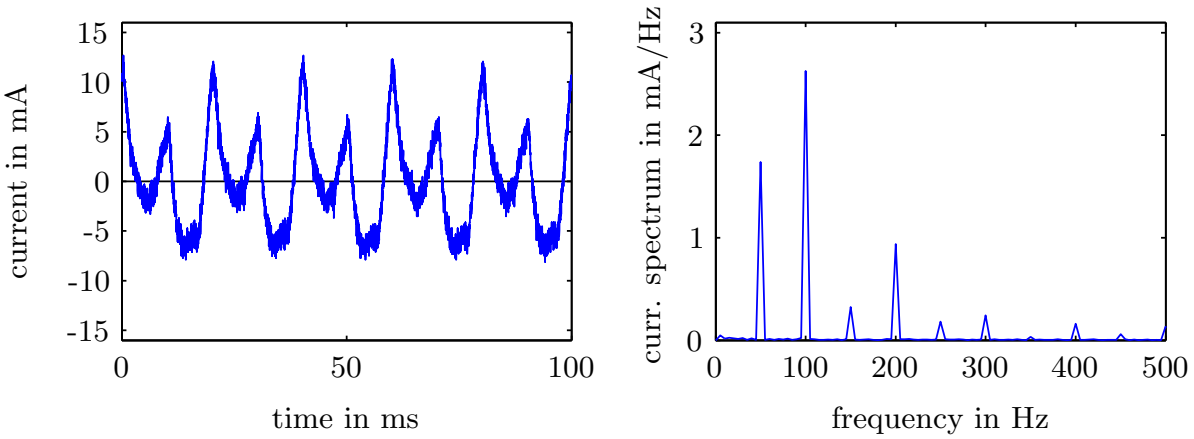

Figure 6.5: Ripple current in a commercial UPS for personal computers during charging (sample rate: 50 kHz).

In contrast to the preceding examples, the current and voltage waveforms in grid-connected devices generally only contain harmonics of the line frequency. The ripple current in an uninterruptible power supply (UPS) as well as its spectrum are depicted in figure 6.5. The predominant part of the signal power is concentrated in the fundamental frequency – which is 50 Hz in the European grid – and the first and third harmonic at 100 and 200 Hz.

The current signals that originate from the electric system of which the battery is a part of can be interpreted as noise that complicates accurate measurements. However, they can as well serve as the necessary excitation signal for impedance measurements. The measurement method and the data analysis, however, have to be adapted to the special conditions. In the case of a UPS, the grid serves as a current source with an accurate and stable frequency. Here conventional methods such as DFT can be used and optimised for real-time applications (cf. section 2.3.1). Similar conditions exist where loads are switched on and off with a well defined rate, if the switching frequency is in a range where useful impedance information can be gained.

The situation is different for systems where no fixed frequency can be observed. The spectrum of the voltage ripple in a conventional vehicle contains narrow peaks at distinct frequencies, as shown in figure 6.1, but these frequencies are often correlated to the engine speed, which is not constant at all, and are hence not steady. In systems where stochastic loads dominate the spectrum, as shown in figure 6.4 for a hybrid electric vehicle, the spectrum is rather blurred. In both cases the signal power at a single frequency – or, to be exact, in a very narrow frequency band – may be too low to permit accurate measurements in the presence of broadband noise. A measurement method that allows to extract impedance information from such blurred or fluctuating current and voltage spectra is presented and discussed in detail in section 6.2.

6.1.2 Measurement instrumentation

Battery monitoring systems generally consist of measurement instrumentation for voltage and current, a digital processor and some interface to the user or other systems. The highest integration density of such systems can be found for consumer electronics, where such a systems consists merely of one integrated circuit. However, these systems are limited to relatively small batteries and low power. Monitoring systems for stationary batteries are not yet sold in very high volume, the measurement hardware is thus mostly a standard printed circuit board layout.

Measurement hardware for battery monitoring in automotive vehicles has experienced a rapid development towards highly integrated, cost-effective mass market products. Intensive development of battery monitoring hardware started in the 1990s for automobiles of the so-called premium segment. First series implementation of battery monitoring systems from Bosch in the Mercedes-Benz SL, Maybach and VW Phaeton started at the beginning of this century [64, 100]. The hardware was bulky and expensive and thus not economically sound for middle class vehicles. Especially a precise current measurement over a dynamic range of a few milliamps stand-by current up to several hundred amps during cranking was the chief cause for high costs of early battery monitoring hardware. For that reason, battery diagnosis algorithms that work without current measurement or with low resolution current measurement were under investigation [143]. These developments were more or less discontinued when application specific integrated circuits (ASIC) especially designed for current measurement with a precision measurement resistor became available. The German company Isabellenhütte developed the IHM-A-1500 ASIC that was presented in 2002. A similar device from Analog Devices followed a few years later [6, 71]. These ASICs include the analogue circuitry as well as microcontrollers for data acquisition and pre-conditioning and can be mounted on a small PCB directly on the measurement resistor, which allows small packaging and provides minimal sensitivity to induced noise [73].

This development lead to the pole-niche battery sensors which are currently becoming a standard for automotive batteries [60, 64, 100, 139]. A simplified functional block diagram of such a sensor is shown in 6.6.

The battery voltage is directly measured across the terminals and adjusted to the voltage input range of the differential buffer (BUF) and analogue to digital converter (ADC) by means of a voltage divider. The battery current (IB) is measured as the voltage across the shunt resistor (RS). This voltage signal is amplified by a differential

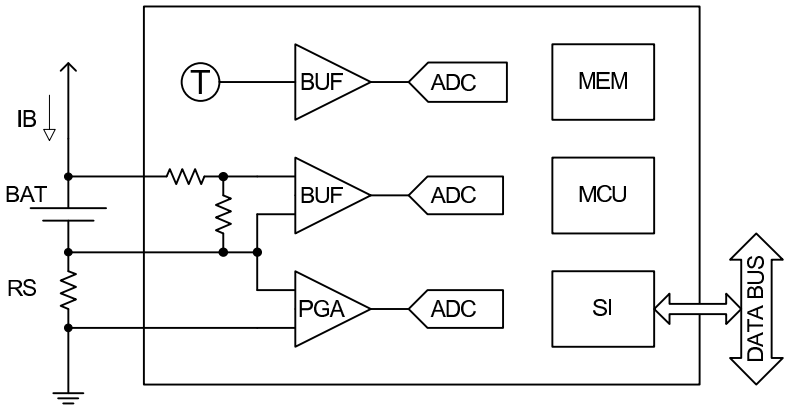

Figure 6.6: Battery sensor integrated circuit.

programmable gain amplifier (PGA) which dynamically matches the signal to the input range of the ADC. Temperature ϑ is measured using external or on-chip sensors, sample rate and resolution are generally lower than for the current and voltage signals.

The data acquired by the ADCs is processed in the microcontroller unit (MCU). A limited amount of data and the program code are stored in the memory (MEM). Depending on the performance of the MCU, battery diagnosis algorithms or merely data pre-processing is performed locally on the battery sensor. In the latter case, the more complex algorithms are located in a central processing unit together with the vehicle energy management. Communication with central or distributed processing units is realised via a serial interface (SI) to a data bus such as LIN or CAN.

Details of the electrical implementation of the measurement instrumentation vary. Battery voltage, current and temperature channel, or only two of them, may share the same ADC and be sampled alternately in order to reduce costs for the ADCs. However, the resolution of the ADCs, sampling rate, memory size and the clock frequency of the microcontroller unit (MCU) are likely to increase with technical progress.

Current devices such as the ADuC7030 employ ADCs with a resolution of 16 bit and are equipped with an ARM7TDMI MCU that operates at 10 MHz and provide 32 kBytes Flash as well as 4 kBytes SRAM memory. A module consisting of the IHM-A-1500 ASIC assembled on a 100 $\mu\Omega$ shunt resistor is rated with an accuracy of 0.5 % for voltage and current measurement at an effective sample rate of 1 kHz[1] [72].

6.1.3 Impedance measurements in automotive monitoring systems

Battery monitoring systems are not yet widespread in the automotive industry, consequently very few is reported on automotive monitoring systems that employ impedance measurements.

In [54] Gallego e.a. report impedance measurements with a device that actively

[1]The accuracy of the current measurement depends on the current range, 0.5 % is specified for a current range of ±300 A. The actual sample rate of the controller is 16 kHz, internal averaging and downsampling yields effective sample rates between 2 Hz and 16 kHz.

measures the complex impedance of the battery at a given frequency. The impedance measurement is reported to be used for SOC and SOH monitoring, yet without further detailed explanation. The measurement hardware described in [54] and in US patent US6876174B1 [132] consists of a current source that creates a sine wave signal and analogue measurement instrumentation comprised of high-pass filters, synchronising circuits and rectifiers.

The company Midtronics describes in several publications [38–40] a battery monitoring system that used conductance measurements. The information on the measurement procedure is limited to mentioning that a low-level AC signal is imposed on the battery [38]. No information about differentiation between real and imaginary part of the impedance is provided.

6.2 Passive impedance measurement technique

In this section, a mathematical method is presented that allows determining the modulus, real part and – indirectly – the imaginary part of the impedance of a system from arbitrary excitation signals. In contrast to methods employing a Fourier transform, the frequency segmentation is separated in an independent procedure and accomplished by digital filters. This allows operating with somewhat fuzzy frequency information, which is beneficial if the excitation signal is blurred or time-variant with respect to frequency, such as many signals in an automotive on-board power system.

A measurement procedure for the real part of the impedance from current noise as a signal source based on rms-values was first described by Walter et al. [179]. This method is further developed within this thesis. Important extensions are the use of digital filters that allow to choose the frequency ranges for the measurement easily, methods for the determination of the modulus and the imaginary part of the impedance and a measurement procedure to determine the equivalent frequency of the excitation frequency. The latter is of special importance: by regaining the frequency information from an arbitrary signal, the frequency resolution of the measurement can be drastically enhanced. In addition to this, the following sections for the first time provide a comprehensive theoretical derivation of the method and an analysis of its accuracy.

6.2.1 Measurement principle

Figure 6.7 shows a brief overview of the method. The algorithm can be separated in three main stages. The first stage comprises digital bandpass filters that limit the measured current and voltage signal to a certain frequency range. In the second stage, the mean square values of these band limited signals $\tilde{u}$ and $\tilde{i}$ and the effective power $\tilde{p}$ are calculated. From these values the square of the modulus and the real part of the impedance, $|\widetilde{Z}|^2$ and $\widetilde{Z}'$, respectively, are determined. The mathematical operations in the first two stages have to be executed in real time with the sample rate of the analogue to digital conversion. However, they consist only of a few additions and multiplications which can be computed very fast on a digital controller. The divisions in the third stage and further processing of the data that may include the calculation of the modulus

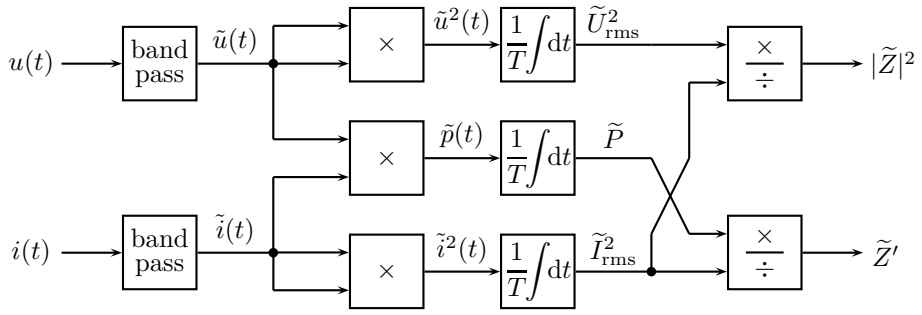

Figure 6.7: Overview on the passive impedance measurement method based on RMS-values.

(unsquared) and the imaginary part of the impedance are calculated after the summation over a large number of samples and are thus not time-critical.

In the following pages the mathematical method for the determination of the impedance from measured time series of voltage and current will be discussed in detail. The method will be derived first for sinusoidal signals and generalized to arbitrary signals in a second step.

The impedance $\underline{Z}$ is assumed to be linear or linearised in the operating point[2].

For a sinusoidal current signal

$$i(\omega, t) = \widehat{i} \cdot \sin(\omega t + \varphi) \tag{6.1}$$

with the angular frequency $\omega = 2\pi f$, the phase shift φ and the amplitude $\widehat{i}$, the voltage across the complex impedance

$$\underline{Z}(\omega) = Z'(\omega) + jZ''(\omega) \tag{6.2}$$

can be written as

$$u(\omega, t) = \widehat{i} \cdot (Z'(\omega) \cdot \sin(\omega t + \varphi) + Z''(\omega) \cdot \cos(\omega t + \varphi)) \tag{6.3}$$

or

$$u(\omega, t) = \widehat{i} \cdot |Z(\omega)| \cdot \sin(\omega t + \varphi + \phi), \tag{6.4}$$

with the phase angle of the impedance

$$\phi = \arg(\underline{Z}(\omega)). \tag{6.5}$$

Three characteristic quantities that are necessary for the determination of the complex impedance can be calculated from the current and voltage signals: the rms-values of current and voltage and the average effective power.

$$I_{\mathrm{rms}}^2 = \frac{1}{T} \int_0^T i^2(t)\,\mathrm{d}t \tag{6.6}$$

[2]This is a necessary assumption, the impedance of a system that cannot be linearised in the vicinity of the operating point is not defined. The problem of non-linearity is discussed in section 2.2. As long as the system can be treated as linear, galvanostatic and potentiostatic mode, i.e. the excitation with a sinusoidal current and voltage signal, respectively, yields the same results.

and

$$U_{\mathrm{rms}}^2 = \frac{1}{T}\int_0^T u^2(t)\,\mathrm{d}t \tag{6.7}$$

are the mean square values[3] of current and voltage, respectively. T is the time period over which the averaging is performed. The mean effective power can be calculated similarly as the algebraic average of the instantaneous power:

$$\overline{P} = \frac{1}{T}\int_0^T p(t)\,\mathrm{d}t = \frac{1}{T}\int_0^T i(t)\cdot u(t)\,\mathrm{d}t. \tag{6.8}$$

Calculating these three values for the signals $u(\omega,t)$ and $i(\omega,t)$ introduced above, one obtains the expressions

$$I_{\mathrm{rms}}^2(\omega) = \frac{\widehat{i}^{\,2}}{2} \cdot \left(1 - \frac{\sin(2\omega T + 2\varphi) - \sin(2\varphi)}{2\omega T}\right), \tag{6.9}$$

$$\begin{aligned} U_{\mathrm{rms}}^2(\omega) &= \frac{\widehat{i}^{\,2}}{2}\cdot|\underline{Z}(\omega)|^2\cdot\Bigg(1 \\ &- \frac{\sin(2\omega T + 2\varphi + 2\phi) - \sin(2\varphi + 2\phi)}{2\omega T}\Bigg) \end{aligned} \tag{6.10}$$

and

$$\begin{aligned} \overline{P}(\omega) &= \frac{\widehat{i}^{\,2}}{2}\cdot Z'(\omega)\cdot\Bigg(1 - \frac{\sin(2\omega T + 2\varphi) - \sin(2\varphi)}{2\omega T} \\ &- \frac{Z''(\omega)}{Z'(\omega)}\cdot\frac{\cos(2\omega T + 2\varphi) - \cos(2\varphi)}{2\omega T}\Bigg). \end{aligned} \tag{6.11}$$

The term in brackets for each of the equations above equals one if T is an integer multiple of the fundamental time constant $\frac{2\pi}{\omega}$ and converges to one for $T \to \infty$. The influence of the integration time on the accuracy will be discussed in 6.2.6, for further discussion let us assume that T is sufficiently large and thus:

$$I_{\mathrm{rms}}^2(\omega) \approx \frac{\widehat{i}^{\,2}}{2} \tag{6.12}$$

$$U_{\mathrm{rms}}^2(\omega) \approx \frac{\widehat{i}^{\,2}}{2}\cdot|\underline{Z}(\omega)|^2 \tag{6.13}$$

$$\overline{P}(\omega) \approx \frac{\widehat{i}^{\,2}}{2}\cdot Z'(\omega). \tag{6.14}$$

[3]The square root of these values are the effective or root mean square (rms) values of current and voltage.

Equation 6.14 and 6.13 can be combined to calculate the real part of the complex impedance $\underline{Z}(\omega)$:

$$Z'(\omega) = \frac{\overline{P}(\omega)}{I^2_{\mathrm{rms}}(\omega)}. \tag{6.15}$$

Similarly, the modulus of $\underline{Z}(\omega)$ can be calculated from the rms-values of voltage and current

$$|\underline{Z}(\omega)| = \sqrt{\frac{U^2_{\mathrm{rms}}(\omega)}{I^2_{\mathrm{rms}}(\omega)}}. \tag{6.16}$$

The imaginary part of the impedance cannot be calculated directly by a combination of equations 6.13 to 6.14. However, the absolute value of Z'' is given by the Pythagorean theorem

$$|Z''(\omega)| = \sqrt{|Z(\omega)|^2 - Z'^2(\omega)}. \tag{6.17}$$

The derivation for these quantities can be generalised for arbitrary signals[4] by means of the Fourier integral. The current signal from equation 6.1 can be rewritten as the inverse Fourier transform of the Fourier spectrum $\underline{I}(\omega)$ [10]:

$$i(t) = \frac{1}{2\pi} \int_{-\infty}^{\infty} \underline{I}(\omega) \cdot \mathrm{e}^{j\omega t}\, \mathrm{d}\omega. \tag{6.18}$$

The resulting voltage drop across the frequency dependent impedance $\underline{Z}(\omega)$ is

$$u(t) = \frac{1}{2\pi} \int_{-\infty}^{\infty} \underline{I}(\omega) \cdot \underline{Z}(\omega) \cdot \mathrm{e}^{j\omega t}\, \mathrm{d}\omega. \tag{6.19}$$

The relation between the mean square values of the signals and the spectra can be obtained by the generalized Parseval theorem [113]

$$\int_{-\infty}^{\infty} x(t) \cdot y(t)\, \mathrm{d}t = \frac{1}{2\pi} \int_{-\infty}^{\infty} \underline{X}(\omega) \cdot \underline{Y}^*(\omega)\, \mathrm{d}\omega. \tag{6.20}$$

$x(t)$ and $y(t)$ are signals in the time domain, while $\underline{X}(\omega)$ and $\underline{Y}(\omega)$ are their Fourier transforms, $\underline{Y}^*(\omega)$ is the complex conjugate of $\underline{Y}(\omega)$. Equation 6.20 is defined for signals with finite signal energy. However, it can be modified for the average signal power:

$$\frac{1}{T} \int_{0}^{T} x(t) \cdot y(t)\, \mathrm{d}t = \frac{1}{2\pi T} \int_{-\infty}^{\infty} \underline{X}(\omega) \cdot \underline{Y}^*(\omega)\, \mathrm{d}\omega. \tag{6.21}$$

[4]The Fourier transform $\underline{I}(\omega)$ exists, if the Dirichlet criterion $\int_{-\infty}^{\infty} |i(t)|\, \mathrm{d}t < \infty$ is fulfilled [10]. Here and further on only physical signals that are limited to the time interval $[0, T]$ are regarded, which fulfil this criterion.

Thus, equations 6.13 to 6.14 can be generalized to

$$\begin{aligned} I_{\mathrm{rms}}^2 &= \frac{1}{2\pi T}\int_{-\infty}^{\infty} |\underline{I}(\omega)|^2\,\mathrm{d}\omega \\ U_{\mathrm{rms}}^2 &= \frac{1}{2\pi T}\int_{-\infty}^{\infty} |\underline{U}(\omega)|^2\,\mathrm{d}\omega = \frac{1}{2\pi T}\int_{-\infty}^{\infty} |\underline{I}(\omega)|^2\cdot|\underline{Z}(\omega)|^2\,\mathrm{d}\omega \\ \overline{P} &= \frac{1}{2\pi T}\int_{-\infty}^{\infty} \underline{I}(\omega)\cdot\underline{U}^*(\omega)\,\mathrm{d}\omega = \frac{1}{2\pi T}\int_{-\infty}^{\infty} |\underline{I}(\omega)|^2\cdot Z'(\omega)\,\mathrm{d}\omega^5. \end{aligned} \tag{6.22}$$

The real part and the impedance modulus squared, which can be derived from these quantities, are

$$\widetilde{Z}' = \frac{\overline{P}}{I_{\mathrm{rms}}^2} = \frac{\int_{-\infty}^{\infty} |\underline{I}(\omega)|^2\cdot Z'(\omega)\,\mathrm{d}\omega}{\int_{-\infty}^{\infty} |\underline{I}(\omega)|^2\,\mathrm{d}\omega} \tag{6.23}$$

and

$$\widetilde{Z}^2 = \frac{U_{\mathrm{rms}}^2}{I_{\mathrm{rms}}^2} = \frac{\int_{-\infty}^{\infty} |\underline{I}(\omega)|^2\cdot|\underline{Z}(\omega)|^2\,\mathrm{d}\omega}{\int_{-\infty}^{\infty} |\underline{I}(\omega)|^2\,\mathrm{d}\omega}. \tag{6.24}$$

Equation 6.23 and 6.24 can be interpreted as a weighted average of the real part and modulus squared, respectively, with the power spectrum $|\underline{I}(\omega)|^2$ of the current signal as the weighting function.

Obviously, if $\underline{I}(\omega)$ is completely unknown, these results are meaningless with respect to impedance measurements. However, if the signals have a limited bandwidth which is sufficiently small and the impedance within this frequency range changes only little, the values determined with the proposed method are a good approximation of the impedance at the centre of the frequency band. Such band limited signals can be extracted from arbitrary signals by means of bandpass filters, which will be discussed briefly in section 6.2.4.

6.2.2 Influence of the spectrum of the input signal

For practical reasons, it is often not advantageous to have a very narrow frequency band. For these cases it is clear from equations 6.23 and 6.24 that the estimated value of the real part and impedance modulus, respectively, depends not only on the impedance, but also on the spectrum of the excitation signal. Certain assumptions about the spectrum $\underline{I}(\omega)$ are necessary to give $\widetilde{Z}'$ and $\widetilde{Z}^2$ a practical meaning. First we will assume that the spectrum $\underline{I}(\omega)$ is band limited, i.e. that

$$\underline{I}(\omega) = 0 \quad \text{for} \quad \omega < \omega_{\mathrm{l}} \quad \text{and} \quad \omega > \omega_{\mathrm{u}}, \tag{6.25}$$

[5] The imaginary part of $\underline{Z}(\omega)$ is an odd function of ω and therefore vanishes when integrated from $-\infty$ to ∞ [113].

where ω_l and ω_u are the lower and upper boundary of the angular frequency, respectively. The value of $\widetilde{Z}'$ and $\widetilde{Z}^2$ is then also restricted to the range of the impedance within this frequency band by the inequations:

$$\begin{array}{rcccl} \min(Z'(\omega)) & \leq & \widetilde{Z}' & \leq & \max(Z'(\omega)) \\ \min(|\underline{Z}(\omega)|^2) & \leq & \widetilde{Z}^2 & \leq & \max(|\underline{Z}(\omega)|^2) \end{array} \quad \text{for} \quad \omega_\mathrm{l} \leq \omega \leq \omega_\mathrm{u}. \tag{6.26}$$

Since $Z'(\omega)$ and $|\underline{Z}(\omega)|^2$ are continuous for physical systems, there will always be a frequency $\widetilde{\omega}$, where the impedance is identical with the estimated value, i.e.

$$Z'(\widetilde{\omega}) = \widetilde{Z}' \;\text{ and }\; |\underline{Z}(\widetilde{\omega})|^2 = \widetilde{Z}^2. \tag{6.27}$$

An expression for the effective frequency $\widetilde{\omega}$ can be derived from equation 6.27 if the structure of $Z'(\omega)$ is known. We will therefore as a first attempt assume that $Z'(\omega)$ can be approximated by a linear function within the frequency band:

$$Z'(\omega) \approx a'_\mathrm{lin} + b'_\mathrm{lin} \cdot \omega \;\text{ for }\; \omega_\mathrm{l} \leq \omega \leq \omega_\mathrm{u}. \tag{6.28}$$

a'_lin and b'_lin are constants. Inserting equation 6.28 and 6.23 into 6.27 yields

$$\widetilde{\omega}_\mathrm{lin} = \frac{\int\limits_{\omega_\mathrm{l}}^{\omega_\mathrm{u}} |\underline{I}(\omega)|^2 \cdot \omega \,\mathrm{d}\omega}{\int\limits_{\omega_\mathrm{l}}^{\omega_\mathrm{u}} |\underline{I}(\omega)|^2 \,\mathrm{d}\omega}. \tag{6.29}$$

The same expression for $\widetilde{\omega}_\mathrm{lin}$ can be derived for $|\underline{Z}(\omega)|^2$ with the linear approximation[6] $|\underline{Z}(\omega)|^2 \approx a_\mathrm{lin} + b_\mathrm{lin} \cdot \omega$. Other definitions can be derived for higher order approximations that contain only one frequency term. A definition of $\widetilde{\omega}$ for polynomial expressions, which would allow a general approach using Taylor series, is not unambiguous.

6.2.3 Determination of the effective frequency

Impedance measurements aim to determine the impedance $\underline{Z}$ at a certain angular frequency ω. If for a passive measurement the frequency cannot be controlled, it would nevertheless be beneficial to determine the frequency that corresponds to the measured impedance value. In the following a method will be derived that allows to estimate this excitation frequency; figure 6.8 shows the basic concept of the algorithm.

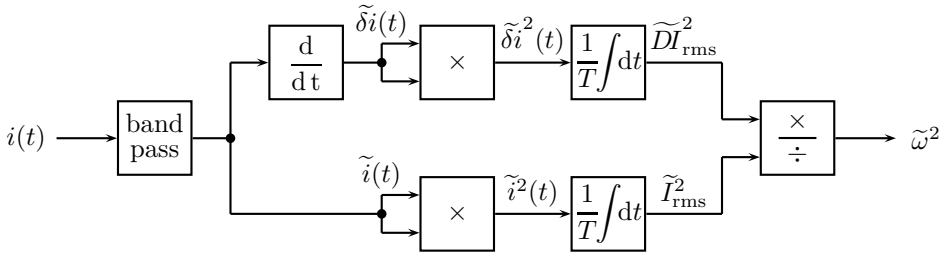

Figure 6.8: Overview of the method for the determination of the effective frequency.

[6] a_lin and b_lin have different units compared to a'_lin and b'_lin.

The derivative of the current signal defined in equation 6.1

$$\delta i(f,t) \equiv \frac{\mathrm{d}i(\omega,t)}{\mathrm{dt}} = \widehat{i} \cdot \omega \cdot \cos(\omega t + \varphi) \tag{6.30}$$

is proportional to the frequency. Consequently, the mean square value

$$DI^2_{\mathrm{rms}}(\omega) \equiv \frac{1}{T} \int_0^T \delta i^2(\omega,t)\,\mathrm{d}t \tag{6.31}$$

is proportional to the angular frequency squared and has a similar structure as the mean square of the current signal from equation 6.9

$$DI^2_{\mathrm{rms}}(\omega) = \frac{\widehat{i}^{\,2}}{2}\omega^2 \cdot \left(1 \; + \frac{\sin(2\omega T + 2\varphi) - \sin(2\varphi)}{2\omega T}\right). \tag{6.32}$$

The quotient

$$\frac{DI^2_{\mathrm{rms}}(\omega)}{I^2_{\mathrm{rms}}(\omega)} = \omega^2 \cdot \left(1 + \frac{2(\sin(2\omega T + 2\varphi) - \sin(2\varphi))}{2\omega T - (\sin(2\omega T + 2\varphi) - \sin(2\varphi))}\right) \tag{6.33}$$

therefore yields an expression proportional to the square of the excitation frequency. The second term in brackets converges to zero for large T, so

$$\lim_{t\to\infty} \frac{DI^2_{\mathrm{rms}}(\omega)}{I^2_{\mathrm{rms}}(\omega)} = \omega^2. \tag{6.34}$$

The quotient of DI^2_{rms} and the definition of I^2_{rms} from equation 6.22 results in the expression

$$\widetilde{\omega}^2_{\mathrm{sqr}} \approx \frac{DI^2_{\mathrm{rms}}}{I^2_{\mathrm{rms}}} = \frac{\int_0^T \delta i^2(t)\,\mathrm{d}t}{\int_0^T i^2(t)\,\mathrm{d}t} = \frac{\int_{-\infty}^{\infty} |\underline{I}(\omega)|^2 \cdot \omega^2\,\mathrm{d}\omega}{\int_{-\infty}^{\infty} |\underline{I}(\omega)|^2\,\mathrm{d}\omega}. \tag{6.35}$$

Even for a band limited signal the effective frequency $\widetilde{\omega}_{\mathrm{sqr}}$ is not equal to the frequency $\widetilde{\omega}^2_{\mathrm{lin}}$ of equation 6.29, which has been derived from a linear approximation of the impedance characteristic within a frequency band. For practical applications, however, the difference is small, as can be seen in figure 6.9.

The effective frequency $\widetilde{\omega}_{\mathrm{sqr}}$ is slightly higher, since the weighting with the square of the frequency favours signals at higher frequencies. For a sharp peak in the spectrum, $\widetilde{\omega}_{\mathrm{sqr}}$ and $\widetilde{\omega}_{\mathrm{lin}}$ are virtually identical, the difference is maximum for signal amplitude that is constant in the complete frequency range. For this case ($\underline{I}(\omega) = \text{const.}$), the quotient of the two frequency terms can be calculated analytically:

$$\frac{\widetilde{\omega}_{\mathrm{sqr}}}{\widetilde{\omega}_{\mathrm{lin}}} = \frac{\int_{\omega_{\mathrm{l}}}^{\omega_{\mathrm{u}}} \mathrm{d}\omega}{\int_{\omega_{\mathrm{l}}}^{\omega_{\mathrm{u}}} \omega\,\mathrm{d}\omega} \cdot \sqrt{\frac{\int_{\omega_{\mathrm{l}}}^{\omega_{\mathrm{u}}} \mathrm{d}\omega}{\int_{\omega_{\mathrm{l}}}^{\omega_{\mathrm{u}}} \omega^2\,\mathrm{d}\omega}} = \sqrt{\frac{4}{3} \cdot \frac{\left(\frac{\omega_{\mathrm{u}}}{\omega_{\mathrm{l}}}\right)^3 - 1}{\left(\frac{\omega_{\mathrm{u}}}{\omega_{\mathrm{l}}}\right)^3 + \left(\frac{\omega_{\mathrm{u}}}{\omega_{\mathrm{l}}}\right)^2 - \left(\frac{\omega_{\mathrm{u}}}{\omega_{\mathrm{l}}}\right) - 1}}. \tag{6.36}$$

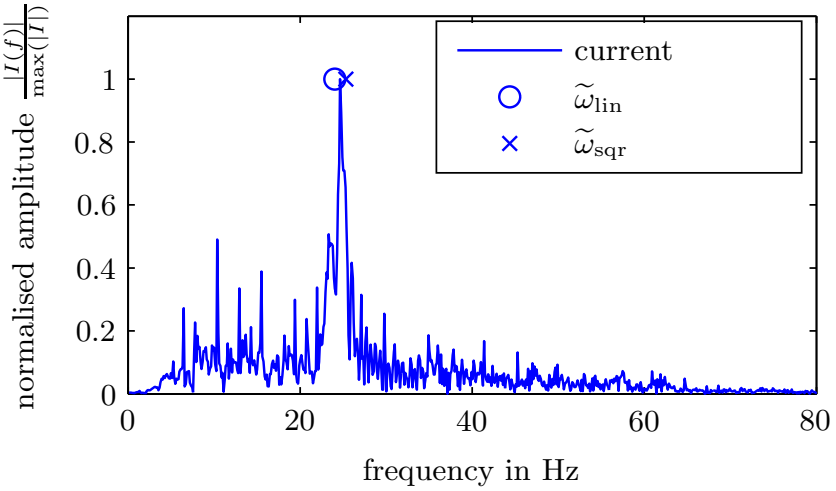

Figure 6.9: Current spectrum measured during driving in a compact class car, band-limited by a 4^{th} order Butterworth filter with corner frequencies at 10 Hz and 50 Hz. The circle and the cross denote the effective frequencies determined according to equations 6.29 and 6.35, respectively.

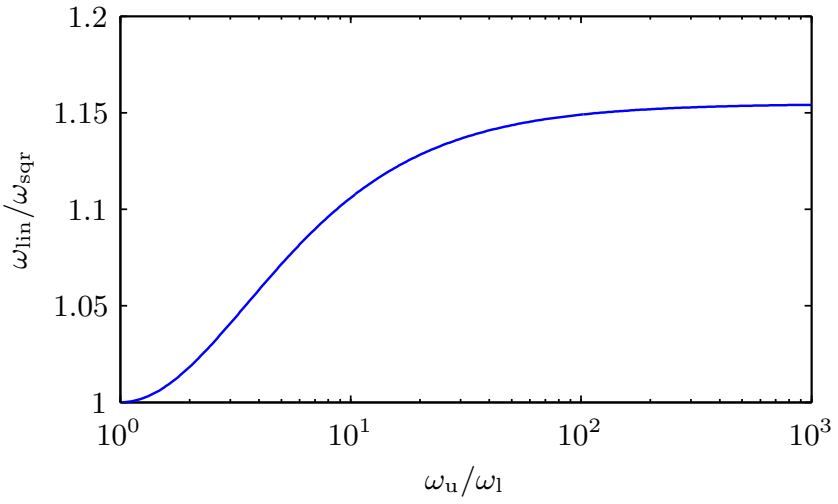

Figure 6.10: Quotient of the effective frequency ω_{sqr}, which can be measured, and the frequency ω_{sqr}, which corresponds to a linear approximation of the impedance characteristic, as a function of the frequency interval $\omega_{\mathrm{l}} \ldots \omega_{\mathrm{u}}$.

The term depends only on the quotient of the upper and lower frequency limit, figure 6.10 shows the quotient of the two frequency terms as a function of the quotient of the upper and lower frequency limit. If, for example, the frequency interval is limited to $\omega_\mathrm{l} = 2\pi \cdot 10\,\mathrm{Hz}$ and $\omega_\mathrm{u} = 2\pi \cdot 30\,\mathrm{Hz}$, the deviation of ω_sqr and ω_lin is always smaller than 5 %, irrespective of the shape of the spectrum.

6.2.4 Filtering

Influence of a filter on the impedance measurement

As mentioned before, filtering of the measured signals is necessary in order to limit the frequency range to a relatively narrow band around the frequency, for which the impedance shall be determined. Further filtering may be necessary in the process of the data acquisition and digitisation. At least an analogue lowpass that damps signal contents above the Nyquist frequency to avoid aliasing will generally be part of the measurement system.

A filter can be described entirely by its complex transfer function $\underline{H}(\omega)$. In the frequency domain, the effect of the filter is a multiplication with the Fourier transform of the input signal. If $\underline{H}_I(\omega)$ and $\underline{H}_U(\omega)$ are filters for the current and voltage signal, respectively, the expression for the real part of the impedance (eq. 6.23) with filtered current and voltage signals becomes

$$\begin{aligned}\widetilde{Z}' \approx \frac{\overline{P}}{I_\mathrm{rms}^2} &= \frac{\int_{-\infty}^{\infty} (\underline{H}_I(\omega) \cdot \underline{I}(\omega)) \cdot (\underline{H}_U^*(\omega) \cdot \underline{U}^*(\omega))\,\mathrm{d}\omega}{\int_{-\infty}^{\infty} |\underline{H}_I(\omega) \cdot \underline{I}(\omega)|^2\,\mathrm{d}\omega} \\ &= \frac{\int_{-\infty}^{\infty} (\underline{H}_I(\omega) \cdot \underline{H}_U^*(\omega)) \cdot |\underline{I}(\omega)|^2 \cdot Z'(\omega)\,\mathrm{d}\omega}{\int_{-\infty}^{\infty} |\underline{H}_I(\omega)|^2 \cdot |\underline{I}(\omega)|^2\,\mathrm{d}\omega}. \end{aligned} \tag{6.37}$$

If the filters for current and voltage have different transfer functions, the value of $\widetilde{Z}'$ will be distorted.[7] The same is true for the impedance modulus (cf. eq. 6.24).

However, for identical filters $\underline{H}_I(\omega) = \underline{H}_U(\omega) = \underline{H}(\omega)$, the modulus squared of the transfer function acts as an additional weighting function, the distortion of the phase angle by the filter does not affect the impedance measurement:

$$\widetilde{Z}' \approx \frac{\overline{P}}{I_\mathrm{rms}^2} = \frac{\int_{-\infty}^{\infty} |\underline{H}(\omega)|^2 \cdot |\underline{I}(\omega)|^2 \cdot Z'(\omega)\,\mathrm{d}\omega}{\int_{-\infty}^{\infty} |\underline{H}(\omega)|^2 \cdot |\underline{I}(\omega)|^2\,\mathrm{d}\omega}. \tag{6.38}$$

[7] Only if the exact transfer functions of both filters are known, this distortion can be corrected for analytically.

$$\widetilde{Z}^2 \approx \frac{U_{\mathrm{rms}}^2}{I_{\mathrm{rms}}^2} = \frac{\int_{-\infty}^{\infty} |\underline{H}(\omega)|^2 \cdot |\underline{I}(\omega)|^2 \cdot |\underline{Z}(\omega)|^2 \,\mathrm{d}\omega}{\int_{-\infty}^{\infty} |\underline{H}(\omega)|^2 \cdot |\underline{I}(\omega)|^2 \,\mathrm{d}\omega}. \tag{6.39}$$

Analogue filters

Analogue filters are used to shape the signals directly in the analogue measurement chain. Basic lowpass characteristic can be achieved by passive RC network, however, this provides a load to the signal. Active analogue filters that provide a high input impedance for the measured signals can be built with operational amplifiers, resistors and capacitors [172]. Their bandwidth is high since it is limited only by the characteristics of the devices whereas digital filters are limited by the sample rate.

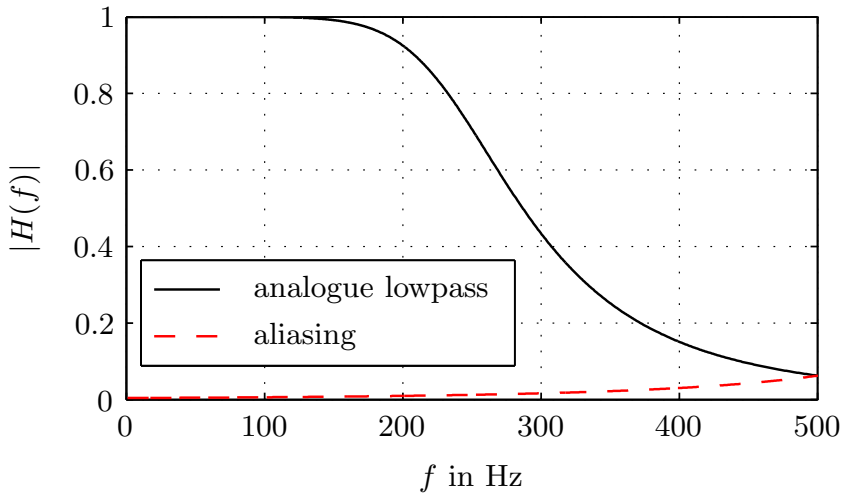

Figure 6.11: Magnitude characteristic of a 4th order Butterworth lowpass filter with a corner frequency of $f_{\mathrm{c}} = 250\,\mathrm{Hz}$.

For digital signal processing, at least one analogue lowpass filter per channel is necessary to avoid aliasing. Aliasing occurs during the analogue to digital conversion if the analogue signal contains frequencies higher than the Nyquist frequency, i.e. half of the sampling frequency. Parts of the spectrum above the Nyquist frequency are "mirrored" into the region below the Nyquist frequency and distort the original signal [115]. The analogue signal therefore has to be band-limited by an analogue lowpass before the conversion[8].

Depending on the requirements different filter types can be used. The most common is the Butterworth filter that provides a smooth characteristic and a flat response in the pass band. Chebychev and elliptical filters provide a steeper roll-off at the cost of pass band ripple [171]. As an example for an adequate anti-aliasing filter for a system with a sample rate of 1 kHz figure 6.11 shows the characteristic of a fourth order Butterworth lowpass with the corner frequency $f_{\mathrm{c}} = 250\,\mathrm{Hz}$. This corner frequency

[8]Digital filters operate at the discretised signals and can thus not prevent aliasing.

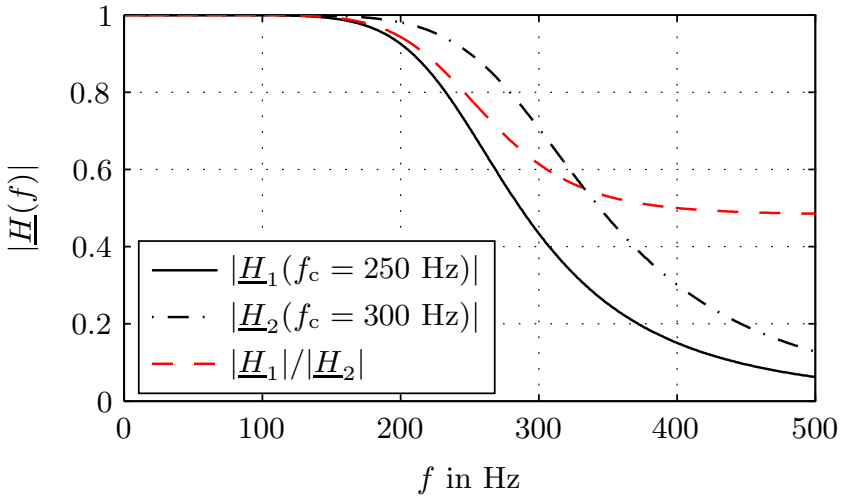

Figure 6.12: Transfer functions of two 4th order lowpass filters, which differ only in their corner frequencies f_c. The quotient of the magnitudes differs significantly from unity for $f > f_c$, which causes a corresponding error in the impedance measurement.

provides a compromise between sufficient damping at the Nyquist frequency and low influence on the lower frequency range. The filter does not avoid aliasing completely, figure 6.11 also shows the overlap of the aliasing spectrum. This overlap could be reduced either by lowering the corner frequency at the cost of a smaller usable frequency range or by increasing the filter order, which requires a higher complexity of the filter.

Another problem with analogue filters occurs if two signals such as the current and voltage signal pass two analogue filters. Even if the characteristics of the two filters are very similar with respect to magnitude and shape, the corner frequencies will often be slightly different due to tolerances of the resistors and the capacitors that are part of virtually any analogue filter. Especially for high order filters this causes noticeably different damping of signals within the frequency range of the falling edges of the filters. Figure 6.12 illustrates this effect. A fourth order analogue filter may contain four capacitors with a tolerance of 5% resulting in a tolerance of the corner frequency of 20%. Comparing the characteristic of the original filter ($f_c = 250\,\text{Hz}$) with a second filter with a 20% higher corner frequency shows a ratio of the damping of two filters of less than 0.5 in the transition region. This ratio would severely distort the impedance measurement according to 6.37 for signals with a frequency above 150 Hz, in this example.

Digital filters by contrast are numerical algorithms and can therefore be designed perfectly identical for both signals[9]. They should therefore be used primarily to select the frequency range for the passive impedance measurement, the use of analogue filters should be restricted to anti-aliasing.

Digital filters

A digital band-pass filter is necessary for the pre-processing of the current and voltage signals in order to limit the frequency range. Digital filters are numerical algorithms,

[9]For implementations on a microcontroller it is often advantageous to use even the same part of code for filtering of current and voltage signals.

that are fed with an input sequence of discrete values x_n and produce an output sequence y_n. A digital filter can have an influence on the input sequence similar to that of an analogue filter on a continuous system. The correlation of the output and input sequence can be described by a discrete transfer function $H(z)$, where z is the variable of the z-transform. The right-sided z-transform is defined as

$$\underline{X}(z) = \sum_{n=0}^{+\infty} x_n \cdot z^{-n} \quad \text{with} \quad z = e^{(\sigma+j\omega)T}, \tag{6.40}$$

where σ is a real constant and T is the time between two sampled values [115]. The z-transform plays a similar role for discrete sequences as the Fourier transform does for continuous signals[10]. For the further discussion it is sufficient to note that z^{-n} can be interpreted as an operator that corresponds to a time delay of n sample intervals T. The transfer function of a digital filter has the general form

$$\underline{H}(z) = \frac{\underline{Y}(z)}{\underline{X}(z)} = \frac{b_0 + b_1 z^{-1} + \ldots + b_k z^{-k}}{1 + a_1 z^{-1} + \ldots + a_l z^{-l}}. \tag{6.41}$$

The order of a digital filter is defined by the larger of the two integer parameters k and l and also defines the minimal required number of storage cells. The difference equation that corresponds to the transfer function $H(z)$ is

$$y_n + a_1 y_{n-1} + \ldots + a_l y_{n-l} = b_0 x_n + b_1 x_{n-1} + \ldots + b_k x_{n-k}. \tag{6.42}$$

Here x_n is the n^{th} sample of the input signal and y_n the n^{th} sample of the output signal. Equation 6.42 can be solved with respect to the output y_n, which depends not only on the input sequence x but also on the output values of the preceding steps. Such a structure with a time-delayed feedback of the output is called a recursive or infinite impulse response (IIR) filter. Filters without feedback of the output, i.e. with all coefficients $a_{1\ldots l} = 0$, are called finite impulse response (FIR) or window filters.

The latter have advantages with regard to stability and can be designed to have a linear phase but require significantly more memory and computational operations.

Recursive filters by contrast can be implemented very efficiently on a microcontroller or digital signal processor with very few data storage and are therefore the best choice for the applications described in this thesis. However, certain design criteria have to be regarded in order to assure stability and avoid oscillations [148].

A convenient way to describe a digital filter and to illustrate equation 6.42 is the use of block diagrams introduced in section 2.3.1. These are composed of the three elements that are necessary to implement a digital filter: addition $\bigoplus$, multiplication with a constant $\triangleright$ and a unit delay memory $\boxed{z^{-1}}$.

The same transfer function can be represented by different filter structures that are analytically identical, but can have different numerical properties [148]. Figure 6.13 shows the so called direct form II of a second order IIR filter. This structure is widely used because it has the lowest possible complexity in terms of memory and arithmetical operations [148].

[10] For $\sigma = 0$ equation 6.40 is formally identical with the Fourier transform. However, this equivalency is only valid if the Fourier sum converges for all frequencies ω. The z-transform is discussed in detail in [115].

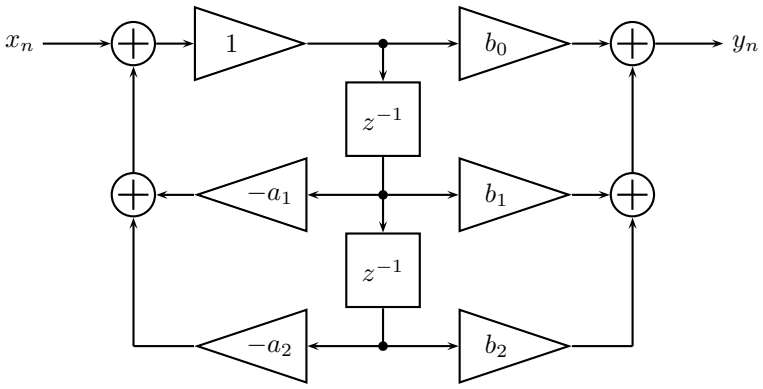

Figure 6.13: Block diagram of a second order IIR filter.

Arbitrary filter characteristics such as low-pass, high-pass, band-pass or band-stop can be designed with this structure or cascades of such second order sections by choosing the adequate set of filter coefficients. The filter coefficients also determine if the filter characteristic is of a Bessel or a Chebychev type and the like. The higher the filter order, the steeper are the edges of the magnitude characteristic, if the same filter type is used. A high filter order yet requires more memory and more arithmetical operations per time step. These operations have to be carried out each time step, the time required for this may therefore limit the possible sampling rate.

The variety of filter types that could be implemented for the necessary band-limiting of the voltage and current signals is large. As an example for a digital filter design a fourth order Butterworth IIR-filter will be discussed in the following. This filter was chosen because it has a number of properties that fit well to the application of a passive impedance measurement implemented on highly integrated and low-cost measurement hardware.

A Butterworth filter has a smooth transfer function, the gain in the passband is very close to unity and has in contrast to Chebychev filters no ripple. Thereby it is guaranteed that the signal in the middle of the frequency band is never weighted less then at the edges, which eases the interpretation of the impedance results. A characteristic that is beneficial for the implementation is that the zeros of the denominator of $H(z)$ are placed at $z = \pm 1$ which leads to coefficients for a second order filter of $b_0 = 1$, $b_1 = 0$ and $b_2 = -1$. To achieve unity gain in the pass band, a scaling coefficient s has to be introduced, which leads to a filter structure as in figure 6.14 that requires only three additions/subtractions and three multiplications.

coefficient	first section	second section
s	0.0456	0.0456
a_1	-1.8925	-1.9667
a_2	0.9042	0.9680

Table 6.1: Coefficients of a 4th order Butterworth bandpass filter with edge frequencies at 5 and 20 Hz.

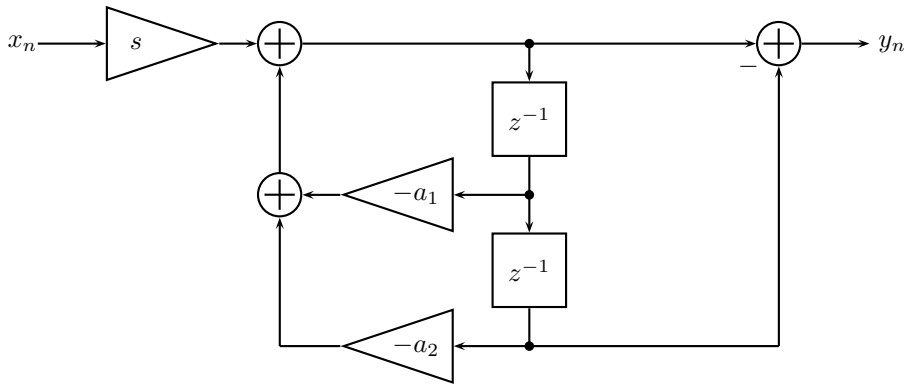

Figure 6.14: Simplified block diagram of a second order section of a digital Butterworth filter.

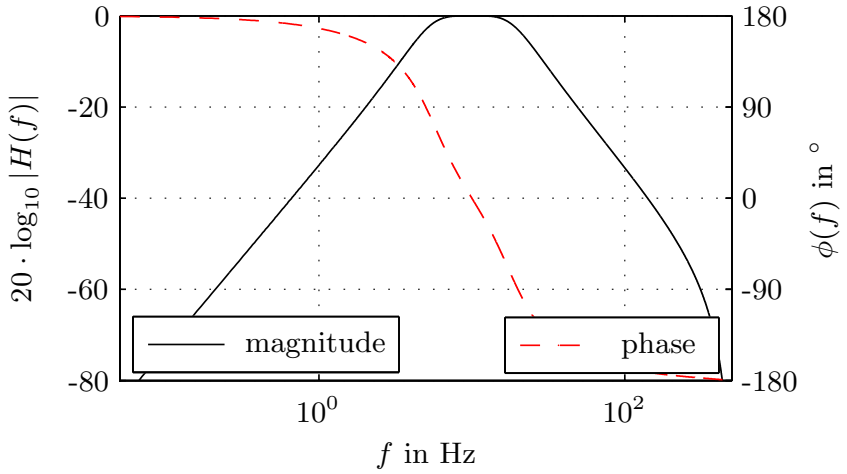

Figure 6.15: Magnitude and phase characteristic of a 4th order Butterworth bandpass filter with edge frequencies at 5 and 20 Hz.

A fourth order filter can be designed as a cascade of two second order sections that have a structure as shown in figure 6.14. For the determination of the filter coefficients various methods can be found in literature [115, 120, 148]. However, many software tools exist that design a digital filter from a few specifications set by the user. As an example, table 6.1 shows the set of filter coefficients that were determined with the *Matlab Filter Realization Wizard* [97] for a fourth order Butterworth bandpass filter realised as a cascade of two second order sections. The filter is specified by the two edge frequencies at 5 and 20 Hz and the sample frequency $f_s = 1\,\text{kHz}$[11]. Figure 6.15 shows the corresponding filter characteristic as a Bode diagram. The filter gain at the edge frequencies is -3 dB and decreases with approximately -20 dB per decade towards lower and higher frequencies. The phase angle shows the typical sharp decrease within the pass band region. Since the filter is applied to both the current and the voltage signal for the impedance measurement, only the magnitude but not the phase angle influences the result (cf. eq. 6.38 and 6.39).

[11]These parameters have been used for a filter in the cranking prognosis algorithm, cf. section 7.2)

6.2.5 Example

As an example demonstrating the passive impedance measurement the battery current and voltage measurements in a VW Golf that have already been presented in section 6.1 are shown in figure 6.16. Both battery voltage and current were measured with a battery monitoring system at a sample rate of 1 kHz over a period of ten minutes. During the first 106 seconds of the measurement the engine was at standstill and the electric loads discharged the battery. Cranking of the car occurs at $t \approx 106\,\mathrm{s}$ indicated by the high discharge current pulse. After cranking, the engine runs in idle mode and charges the battery. The charging current is superimposed by a strong ripple current.

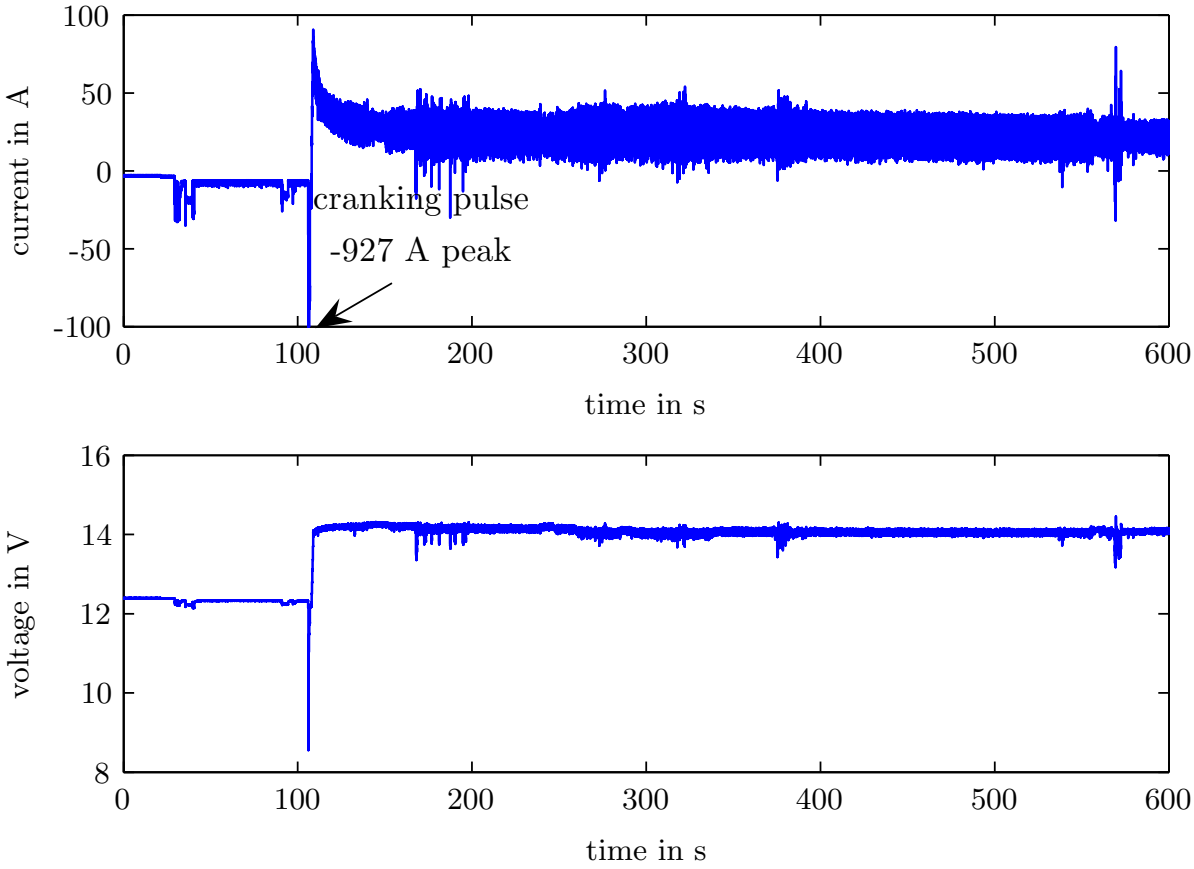

Figure 6.16: Battery current and voltage measured in a VW Golf (cf. figure 6.2).

To determine the battery impedance at about 25 Hz a fourth order band pass filter with edge frequencies at 20 and 30 Hz (cf. section 6.2.4) was applied to the current and voltage signal. Figure 6.17 illustrates the result of the filtering for the current signal. The two graphs on the left show the amplitude spectrum of the raw and filtered current signal computed for the time interval $300\,\mathrm{s} \leq t \leq 310\,\mathrm{s}$. The two plots on the right show the spectrograms of the raw and filtered signals. The signal component that falls into the pass band of the bandpass filter is hardly altered while the lower and higher frequency range was significantly damped. The strong signal at 100 Hz, for example, is still visible in the lower spectrogram, but its amplitude is by 40 dB smaller than the signal in the pass band.

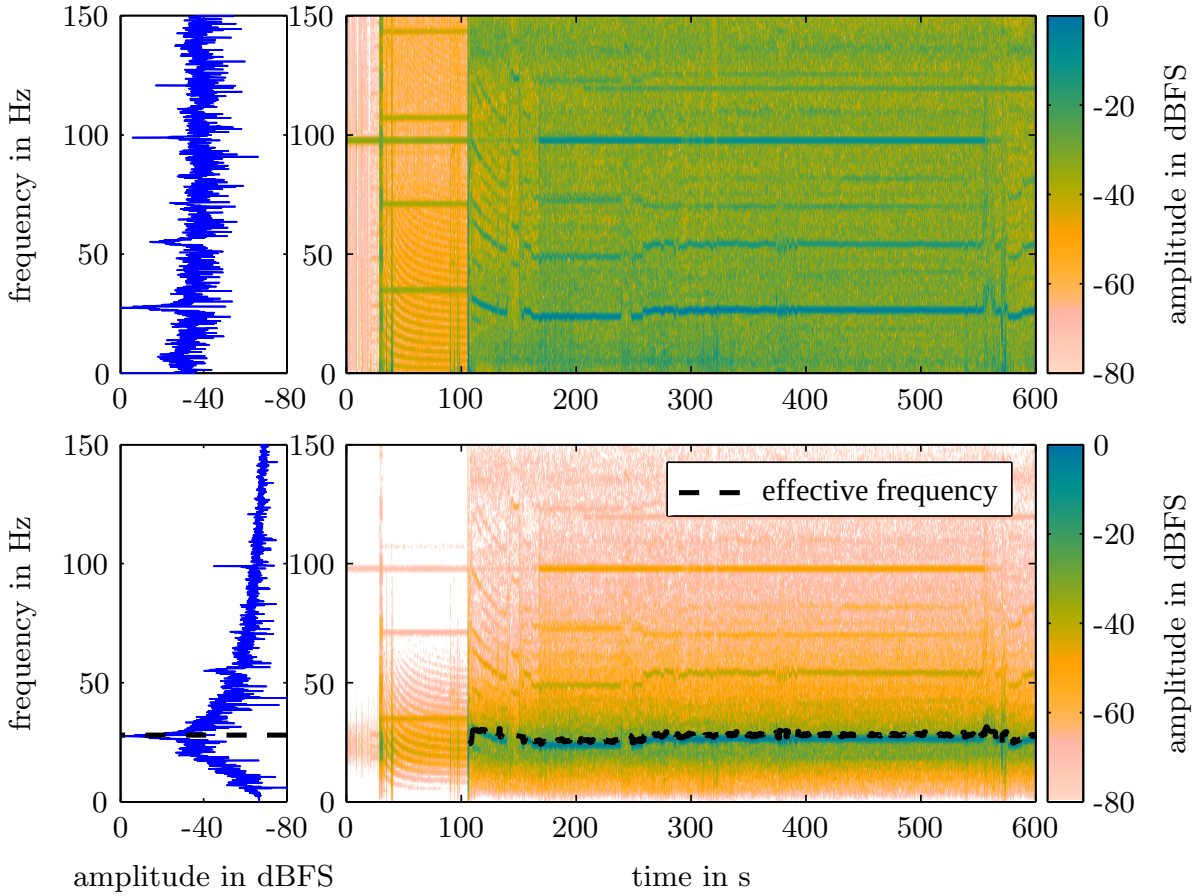

Figure 6.17: Spectrum (top left) and spectrogram (top right) of the measured current signal shown in figure 6.16 (top). The bottom part of the figure shows the spectrum (bottom left) and spectrogram (bottom right) of the current signal that has been filtered by a fourth order Butterworth bandpass filter with edge frequencies at 20 and 30 Hz. The effective frequency has been calculated from the filtered signal according to the method explained in section 6.2.3.

To illustrate the meaning of the effective frequency, introduced in section 6.2.3, the calculation according to equation 6.35 was applied to the filtered current signal. The result is plotted in the lower spectrogram, it closely follows the progress of the strongest signal component.

The raw and filtered current signals are also displayed in figure 6.18 (top). The amplitude of the filtered and thus average free current $\tilde{i}$ indicates the signal strength, which is low while the engine is not running and shows three short pauses during the further progress. The root mean square value of the filtered current signal provides a quantitative measure for the signal and varies over nearly three orders of magnitude depending on the mode of operation. The mean square values of current and voltage and the mean power were calculated according to equations 6.22. Using these quantities, the real part, modulus and imaginary part of the impedance according to equations 6.15, 6.16 and 6.17. The development of these three impedance values is shown in figure 6.18 (bottom).

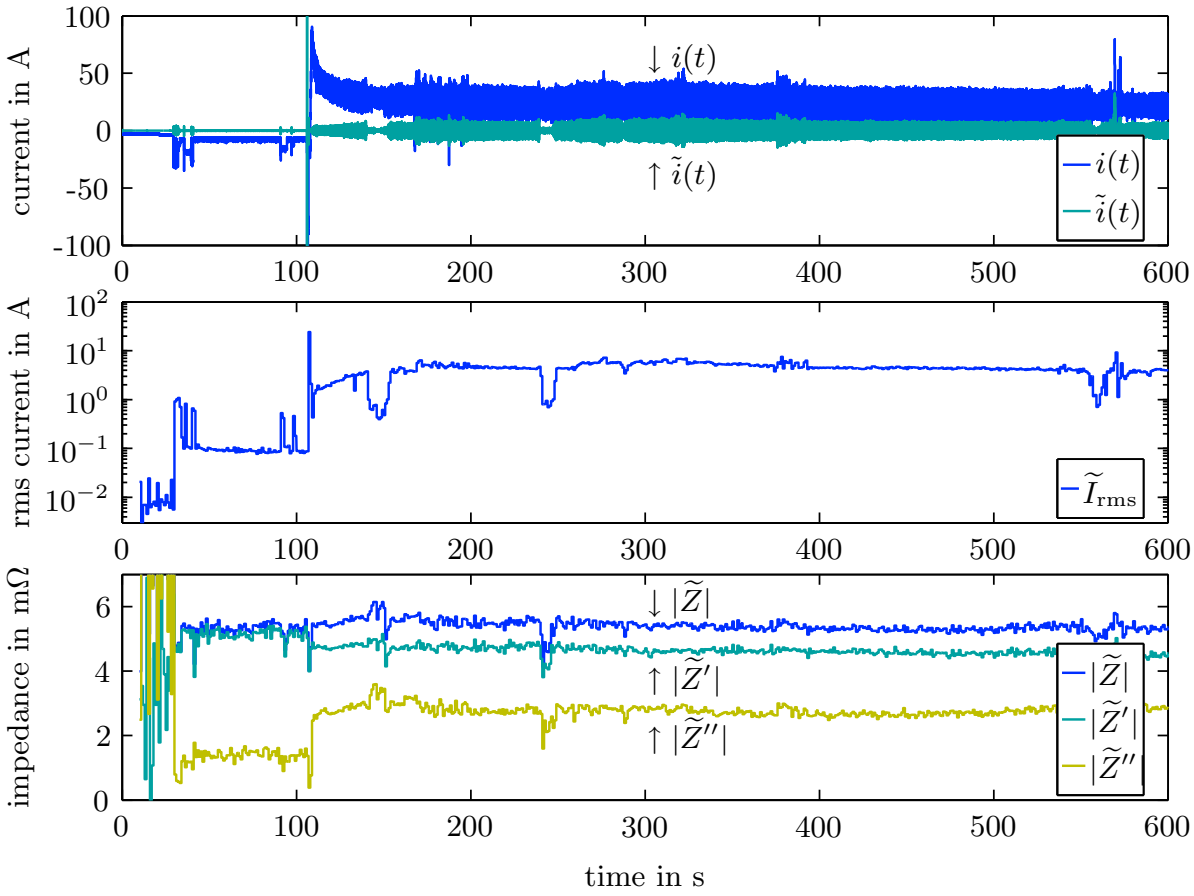

Figure 6.18: Results of the proposed passive impedance measurement applied to the measurement on a VW Golf battery. Raw and filtered current signal (top) and rms value of the filtered battery current (middle). The signal $\tilde{i}$ has been filtered by a 4th order bandpass filter with corner frequencies at 20 and 30 Hz. The real part ($|\widetilde{Z}'|$), modulus ($|\widetilde{Z}|$) and imaginary part ($|\widetilde{Z}''|$) of the battery impedance (bottom) have been calculated according to the procedure explained in section 6.2.1.

The comparison of the rms current and the impedance values shows that the impedance values determined by the proposed method are relatively stable throughout the second part of the measurement, where the engine is running and the signal strength within the pass band range of the bandpass is high. However, it can also be seen that no stable results can be achieved if the signal is very low, as for the very beginning of the measurement, and that the low signal strength causes a systematic error. The latter can be seen best at the dip of the rms current at $t \approx 240\,\mathrm{s}$. This dip can also be found in the impedance values, though the battery impedance is very unlikely to change within such a very short period of time and without a change in the direct current.[12]

The influence of the signal strength on the impedance measurement can be explained by the impact of noise. As a first approximation noise is independent from the measured signal, thus the signal-to-noise-ratio is proportional to the amplitude of the measured

[12]The difference of the impedance values before and after the cranking are mainly caused by the different operating point, i.e. the direct current changing from discharging to charging.

signal. Lower signal strength results in a lower SNR and thus to a higher error (cf. 6.2.6, equations 6.82, 6.83 and 6.85).

To obtain useful information from a passive impedance measurement, the factors that influence the measurement and its accuracy have to be understood. These are therefore discussed in section 6.2.6. In section 6.2.7 guidelines are presented on how to separate "good" from distorted measurements.

6.2.6 Accuracy

Influence of the integration period

In section 6.2.1 the mean square values and the average power was derived for a sinusoidal current and voltage signal. Equations 6.9 and 6.10 include terms that describe the relative calculation error with respect to the ideal values that would be obtained if the integration time T is infinite.

Equation 6.9 can be rewritten as

$$I^2_{\mathrm{rms}}(\omega, T) = \lim_{T\to\infty} I^2_{\mathrm{rms}}(\omega, T) \quad \cdot \quad \left(1 - \frac{\sin(2\omega T + 2\varphi) - \sin(2\varphi)}{2\omega T}\right). \tag{6.43}$$

The relative error of the mean square current caused by the finite integration time thus is

$$r_{TI^2} = -\frac{\sin(2\omega T + 2\varphi) - \sin(2\varphi)}{2\omega T}. \tag{6.44}$$

it depends on the integration period T, the phase angle φ at the start of the integration and on the angular frequency ω of the measurement signal. For a passive impedance measurement T and φ are unknown.

A worst case estimation can yet be obtained for r_{TI^2}: the numerator is a difference of two sinusoidal signals, it always has a value between -2 and 2. The absolute value of the relative error is

$$|r_{TI^2}| \leq \frac{1}{\omega T}, \tag{6.45}$$

it decreases proportional to the reciprocal integration time. If ω is not exactly known, the lowest frequency in a frequency band has to be chosen for a worst case estimation.

The relative error of the mean square voltage is

$$r_{TU^2} = -\frac{\sin(2\omega T + 2\varphi + 2\phi) - \sin(2\varphi + 2\phi)}{2\omega T}, \tag{6.46}$$

it additionally depends on the phase angle ϕ of the impedance. However, with the same reasoning as above, error limits can be determined:

$$|r_{TU^2}| \leq \frac{1}{\omega T}. \tag{6.47}$$

The relative error of the average power given in equation 6.11 is

$$r_{TP} = - \frac{\sin(2\omega T + 2\varphi) - \sin(2\varphi)}{2\omega T} \tag{6.48}$$

$$- \frac{Z''(\omega)}{Z'(\omega)} \cdot \frac{\cos(2\omega T + 2\varphi) - \cos(2\varphi)}{2\omega T}, \tag{6.49}$$

due to the factor $\frac{Z''(\omega)}{Z'(\omega)}$ of the second term it can become large if the impedance is mainly capacitive or inductive.

The relative error of the modulus of the impedance squared can be determined from the mean square values of voltage and current by means of linear error propagation rules including the total differential [10]

$$r_{TZ^2} \approx \frac{1}{|\underline{Z}(\omega)|} \cdot \left(\frac{\mathrm{d}Z^2}{\mathrm{d}U^2_{\mathrm{rms}}} \cdot r_{TU^2} U^2_{\mathrm{rms}} + \frac{\mathrm{d}Z^2}{\mathrm{d}I^2_{\mathrm{rms}}} \cdot r_{TI^2} I^2_{\mathrm{rms}} \right) \tag{6.50}$$

$$= r_{TU^2} - r_{TI^2}. \tag{6.51}$$

The error r_{TZ^2} depends on the impedance; if $Z''(\omega) = 0$, i.e. if the impedance is purely real, $r_{TU^2} = r_{TI^2}$ and the relative error vanishes. If the impedance is purely capacitive or inductive, then r_{TU^2} and r_{TI^2} have opposite signs, the error is therefore always smaller than twice the error of mean square voltage or current:

$$|r_{TZ^2}| \leq \frac{2}{\omega T}. \tag{6.52}$$

The relative error is approximately halved if the root of the expression is calculated[13], the relative error of the modulus of the impedance thus is

$$|r_{T|Z|}| \leq \frac{1}{\omega T}. \tag{6.53}$$

The relative error of the real part of the impedance can be calculated from $\overline{P}(\omega)$ and $I^2_{\mathrm{rms}}(\omega)$ analogical to r_{Z^2}:

$$r_{TZ'} \approx r_{TP} - r_{TI^2} = -\frac{Z''(\omega)}{Z'(\omega)} \cdot \frac{\cos(2\omega T + 2\varphi) - \cos(2\varphi)}{2\omega T}. \tag{6.54}$$

The error limit is

$$|r_{TZ'}| \leq \left| \frac{Z''(\omega)}{Z'(\omega)} \right| \cdot \frac{1}{\omega T}, \tag{6.55}$$

the relative error of the real part of the impedance becomes large, if $|Z''(\omega)| \gg |Z'(\omega)|$[14]. The relative error of the imaginary part of the impedance can be estimated by inserting

[13] For $y(x) = \sqrt{x}$ the relative error according to linear error propagation can be calculated as $\frac{\Delta y}{y} = \frac{\mathrm{d}y}{\mathrm{d}x} \cdot \Delta x \cdot \frac{1}{y} = \frac{1}{2\sqrt{x}} \cdot \Delta x \cdot \frac{1}{\sqrt{x}} = \frac{1}{2} \frac{\Delta x}{x}$.

[14] The relative error of Z' with respect to $|Z|$ however is $|r_{TZ'} \frac{Z'}{|Z|}| \leq \frac{1}{\omega T}$.

the expressions 6.9, 6.10 and 6.11 into 6.17 and by neglecting all error terms that decrease with $(\omega T)^{-2}$:

$$r_{TZ''} \approx \frac{\sin(2\omega T + 2\varphi) - \sin(2\varphi)}{2\omega T}. \tag{6.56}$$

The limit of the relative error is

$$|r_{TZ''}| \leq \frac{1}{\omega T}. \tag{6.57}$$

For most electrochemical storage systems, the phase angle of the impedance is in the range of $\pm 45°$ for the relevant frequency range, in this case the relative error of the impedance measurement can be summarised to be $|r_{TZ}| \leq \frac{1}{\omega T}$. For measurements of the real part of the impedance at high or low phase angles – the inductive branch of a battery at very high frequencies or the impedance of a EDLC at very low frequencies – a more detailed analysis according to equation 6.51 and 6.54 is necessary.

The relative error of the effective frequency can be derived from equation 6.33 analogue to the discussions above. For the square of the effective angular frequency the relative error is

$$r_{T\widetilde{\omega}^2_{\mathrm{sqr}}} = \frac{2(\sin(2\omega T + 2\varphi) - \sin(2\varphi))}{2\omega T - (\sin(2\omega T + 2\varphi) - \sin(2\varphi))}. \tag{6.58}$$

The difference of the trigonometric terms is always smaller than two, thus for $\omega T > 1$ the error limit is

$$|r_{T\widetilde{\omega}^2_{\mathrm{sqr}}}| \leq \frac{2}{\omega T - 1}. \tag{6.59}$$

The relative error of the effective frequency $\widetilde{\omega}_{\mathrm{sqr}} = \sqrt{\widetilde{\omega}^2_{\mathrm{sqr}}}$ is

$$|r_{T\widetilde{\omega}_{\mathrm{sqr}}}| \leq \frac{1}{\omega T - 1}. \tag{6.60}$$

Influence of different measurement errors

Any real measurement involves errors and inaccuracies to a certain degree. Designing the measurement system and the data processing algorithms for best performance is often a compromise between different technological and economical constraints. Knowledge about the influence of different types of errors therefore is the basic requirement for an optimised design.

Measurement errors can be differentiated into the groups of systematic and stochastic errors. A systematic error always shows the same magnitude and direction under identical measurement conditions while a stochastic error is random and unpredictable and has an expectation value of zero. Differentiating between these two types can sometimes be difficult, the input voltage offset of an operational amplifier may scatter around zero for a large number of devices due to tolerances in the production process; the error caused by a certain device in a circuit however is systematic. In the following discussion only measurement noise will be regarded as a stochastic error source, all other influences that do not show stochastic behaviour within a typical measurement period of a few seconds are regarded as systematic.

Offset errors The impedance can only be determined from signals with an average value of zero. By using a digital bandpass filter this is secured even if the raw measurement signals have a significant offset. If however the current or voltage signal used for the calculation of the impedance values has an offset, e.g. if the integration time had been chosen too small with respect to the lower edge frequency of the bandpass, the measurement will be distorted.

For a distorted current signal $i(t)_{\mathrm{err}} = \tilde{i}(t) + \overline{I}$ and voltage signal $u(t)_{\mathrm{err}} = \tilde{u}(t) + \overline{U}$, where $\tilde{i}(t)$ and $\tilde{u}(t)$ are the average-free parts of the signals and $\overline{I}$ and $\overline{U}$ are the averages, one can determine the mean square values and the effective power:

$$U^2_{\mathrm{rms,err}} = \frac{1}{T}\int_0^T \left(\tilde{u}^2(t) + 2\tilde{u}(t)\overline{U} + \overline{U}^2\right) \mathrm{d}t = U^2_{\mathrm{rms}} + \overline{U}^2 \tag{6.61}$$

$$I^2_{\mathrm{rms,err}} = \frac{1}{T}\int_0^T \left(\tilde{i}^2(t) + 2\tilde{i}(t)\overline{I} + \overline{I}^2\right) \mathrm{d}t = I^2_{\mathrm{rms}} + \overline{I}^2 \tag{6.62}$$

$$\overline{P}_{\mathrm{err}} = \frac{1}{T}\int_0^T \left(\tilde{p}(t) + \tilde{u}(t)\overline{I} + \tilde{i}(t)\overline{U} + \overline{U}\cdot\overline{I}\right) \mathrm{d}t = \overline{P} + \overline{I}\cdot\overline{U}. \tag{6.63}$$

All cross-terms in equations 6.61 to 6.63 vanish, because the average over the average-free signals $\tilde{u}(t)$ and $\tilde{i}(t)$ is zero per definition. The errors for the modulus and the real part squared of the impedance consequently are

$$|\underline{Z}^2_{\mathrm{err}}| = \frac{U^2_{\mathrm{rms}} + \overline{U}^2}{I^2_{\mathrm{rms}} + \overline{I}^2} \tag{6.64}$$

$$Z'_{\mathrm{err}} = \frac{\overline{P} + \overline{U}\cdot\overline{I}}{I^2_{\mathrm{rms}} + \overline{I}^2}. \tag{6.65}$$

For small offset errors these expressions can be developed by a Taylor series to an expression that shows the relative errors:

$$|\underline{Z}_{\mathrm{err}}| \approx |\underline{Z}| \cdot \sqrt{1 + \frac{\overline{U}^2}{U^2_{\mathrm{rms}}} - \frac{\overline{I}^2}{I^2_{\mathrm{rms}}}} \tag{6.66}$$

$$Z'_{\mathrm{err}} \approx Z' \cdot \left(1 + \frac{\overline{U}\cdot\overline{I}}{\overline{P}} - \frac{\overline{I}^2}{I^2_{\mathrm{rms}}}\right). \tag{6.67}$$

The most important conclusion from equations 6.61 to 6.63 is that offset errors can easily be eliminated by replacing the calculation of the mean square values and the average power from equations 6.6 to 6.8 by

$$I^2_{\mathrm{rms}} = \frac{1}{T}\int_0^T i^2(t)\,\mathrm{d}t - \left(\frac{1}{T}\int_0^T i(t)\,\mathrm{d}t\right)^2, \tag{6.68}$$

$$U_{\mathrm{rms}}^2 = \frac{1}{T}\int_0^T u^2(t)\,\mathrm{d}t - \left(\frac{1}{T}\int_0^T u(t)\,\mathrm{d}t\right)^2 \tag{6.69}$$

and

$$\overline{P} = \frac{1}{T}\int_0^T i(t)\cdot u(t)\,\mathrm{d}t - \frac{1}{T}\int_0^T i(t)\,\mathrm{d}t \cdot \frac{1}{T}\int_0^T u(t)\,\mathrm{d}t. \tag{6.70}$$

The calculation of the average current and voltage signal can be implemented very easily on a digital system, the correction of the mean square values and average power can be done after the summation and are therefore not time-critical.

Amplification errors Amplification errors are constant relative measurement errors. Current and voltage signals with their afflicted amplification errors r_i and r_u, respectively, can be written as $u_{\mathrm{err}}(t) = u(t)\cdot(1+r_u)$ and $i_{\mathrm{err}}(t) = i(t)\cdot(1+r_i)$. For the calculation of the mean square values, the terms $(1+r_i)$ and $(1+r_u)$ can be factored out:

$$\begin{aligned} U_{\mathrm{rms,err}}^2 &= (1+r_u)^2 \cdot U_{\mathrm{rms}}^2 \approx (1+2r_u)\cdot U_{\mathrm{rms}}^2 \\ I_{\mathrm{rms,err}}^2 &= (1+r_i)^2 \cdot I_{\mathrm{rms}}^2 \approx (1+2r_i)\cdot I_{\mathrm{rms}}^2 \\ \overline{P}_{\mathrm{err}} &= (1+r_i)\cdot(1+r_u)\cdot \overline{P} \approx (1+r_i-r_u)\cdot \overline{P}. \end{aligned} \tag{6.71}$$

The approximations made in equations 6.71 are a first order linearisation, which corresponds to linear error propagation rules[15] [10]. The modulus and the real part of the impedance can now be calculated from these distorted properties:

$$\begin{aligned} |\underline{Z}_{\mathrm{err}}| &= \sqrt{\frac{U_{\mathrm{rms}}^2\cdot(1+r_u)^2}{I_{\mathrm{rms}}^2\cdot(1+r_i)^2}} = |\underline{Z}|\cdot\frac{1+r_u}{1+r_i} \approx |\underline{Z}|\cdot(1+r_u-r_i) \\ Z'_{\mathrm{err}} &\approx \frac{\overline{P}\cdot(1+r_u-r_i)}{I_{\mathrm{rms}}^2\cdot(1+2r_i)} = Z'\cdot\frac{1+r_u+r_i}{1+2r_i} \approx Z'\cdot(1+r_u-r_i). \end{aligned} \tag{6.72}$$

For the calculation of the imaginary part according to equation 6.17 the relative error can also be factored out and is thus the same as for the real part and modulus of the impedance.

Rather coarse amplification errors that could occur e.g. due to mismatched resistors in an operational amplifier circuit can be compensated for by calibration of the measurement system. What remains is a certain tolerance $\pm r$, either due to the limited accuracy of the calibration or as a worst case estimate of a nonlinearity. For a worst case estimation of the error, the tolerances of voltage and current therefore have to be added:

$$\frac{|\underline{Z}_{\mathrm{err}}|}{|\underline{Z}|} = \frac{Z'_{\mathrm{err}}}{Z'} = \frac{|Z''_{\mathrm{err}}|}{|Z''|} = 1 \pm (|r_i| + |r_u|). \tag{6.73}$$

[15] For $y(x_1,x_2) = \frac{x_1}{x_2}$ the propagated error can be calculated by means of the total differential: $\Delta y = \Delta x_1 \frac{\mathrm{d}y}{\mathrm{d}x_1} + \Delta x_2 \frac{\mathrm{d}y}{\mathrm{d}x_2} = \Delta x_1 \frac{1}{x_2} + \Delta x_2 \frac{-x_1}{x_2^2} = \frac{x_1}{x_2}\cdot\left(\frac{\Delta x_1}{x_1} - \frac{\Delta x_2}{x_2}\right)$.

Noise Measurement of current and voltage always involves some noise, especially when signals of small amplitude have to be measured in presence of large signals, such as the voltage drop across battery impedance superimposed by an open circuit voltage of several volts. Noise can couple into the measurement system by external sources or internally generated in the measurement system itself[16].

Typical types of noise involved in the measuring process are thermal and Schottky noise in semiconductor devices and resistors and quantisation noise that is generated by the conversion from analogue to digital. Depending on the underlying process, noise can have different characteristics regarding spectral distribution and correlation. However, many processes can be approximated by zero-mean white noise. White noise is a purely random signal, this implies that cross-correlation of two random noise signals s_1 and s_2 is always zero:

$$\lim_{T\to\infty} \frac{1}{T} \int_0^T s_1(t) \cdot s_2(t-\tau)\,\mathrm{d}t = 0 \quad \forall \quad \tau, \tag{6.74}$$

while the autocorrelation of a noise signal s_1 with itself

$$\lim_{T\to\infty} \frac{1}{T} \int_0^T s_1(t) \cdot s_1(t-\tau)\,\mathrm{d}t = \begin{cases} S_{11}^2 & \text{for} \quad \tau = 0 \\ 0 & \text{for} \quad \tau \neq 0 \end{cases} \tag{6.75}$$

also vanishes for all $\tau \neq 0$. Yet for a time lag $\tau = 0$, the autocorrelation yields the noise power S_{11}^2 [113]. The definition of S_{11}^2 for $\tau = 0$ is identical to the definition of the mean square value introduced in equations 6.6 and 6.7.

For the analysis of the influence of random noise on the determination of the impedance we assume that the current and voltage signal are disturbed by the zero-mean white noise signals $s_i(t)$ and $s_u(t)$, respectively, which are uncorrelated to each other and to the signals $i(t)$ and $u(t)$. The mean square values of the disturbed current signal can be calculated according to equation 6.6

$$\begin{aligned} I_{\mathrm{rms,dist}}^2 &= \lim_{T\to\infty} \frac{1}{T} \int_0^T \left(i(t) + s_i(t)\right)^2 \,\mathrm{d}t \\ &= \lim_{T\to\infty} \frac{1}{T} \int_0^T \left(i^2(t) + 2i(t)s_i(t) + s_i^2(t)\right) \,\mathrm{d}t \\ &= \lim_{T\to\infty} \frac{1}{T} \int_0^T i^2(t)\,\mathrm{d}t + \lim_{T\to\infty} \frac{1}{T} \int_0^T s_i^2(t)\,\mathrm{d}t \\ &= I_{\mathrm{rms}}^2 + S_i^2. \end{aligned} \tag{6.76}$$

The cross term vanishes, because $i(t)$ and $s_i(t)$ are uncorrelated. Thus, the mean square values of signal and noise add together. The same can be shown for the disturbed voltage

[16]The excitation signal for the passive impedance measurement is also referred to as "noise". Here noise means a disturbance in the measurement chain.

signal

$$U_{\mathrm{rms,dist}}^2 = \lim_{T\to\infty} \frac{1}{T} \int_0^T (u(t) + s_u(t))^2 \, \mathrm{d}t = U_{\mathrm{rms}}^2 + S_u^2. \tag{6.77}$$

The calculation of the average power by contrast can be interpreted as a cross correlation with time lag $\tau = 0$, therefore the uncorrelated noise signals vanish while current and voltage are correlated by the impedance:

$$\begin{aligned}
\overline{P}_{\mathrm{dist}} &= \lim_{T\to\infty} \frac{1}{T} \int_0^T (i(t) + s_i(t)) \cdot (u(t) + s_u(t)) \, \mathrm{d}t \\
&= \lim_{T\to\infty} \frac{1}{T} \int_0^T (i(t)u(t) + i(t)s_u(t) + u(t)s_i(t) + s_u(t)s_i(t)) \, \mathrm{d}t \\
&= \lim_{T\to\infty} \frac{1}{T} \int_0^T i^2(t) \, \mathrm{d}t = \overline{P}.
\end{aligned} \tag{6.78}$$

Therefore, the calculation of the mean power is not sensitive to uncorrelated white noise, while the calculation of the mean square values of current and voltage involve the autocorrelation of the corresponding noise signals that yield the signal power of the noise. The determination of the real part and the impedance modulus according to equations 6.15 and 6.16 therefore produces systematically disturbed values:

$$Z'_{\mathrm{dist}} = \frac{\overline{P}_{\mathrm{dist}}}{I_{\mathrm{rms,dist}}^2} = \frac{\overline{P}}{I_{\mathrm{rms}}^2 + S_i^2} \tag{6.79}$$

and

$$|\underline{Z}_{\mathrm{dist}}|^2 = \frac{U_{\mathrm{rms,dist}}^2}{I_{\mathrm{rms,dist}}^2} = \frac{U_{\mathrm{rms}}^2 + S_u^2}{I_{\mathrm{rms}}^2 + S_i^2}. \tag{6.80}$$

By introduction of the signal-to-noise-ratios for voltage and current

$$SNR_u = \frac{U_{\mathrm{rms}}^2}{S_u^2} \quad \text{and} \quad SNR_i = \frac{I_{\mathrm{rms}}^2}{S_i^2} \tag{6.81}$$

and linearization for $S_u^2 \ll U_{\mathrm{rms}}^2$ and $S_i^2 \ll I_{\mathrm{rms}}^2$, the disturbed impedance values can be expressed as

$$Z'_{\mathrm{dist}} \approx Z' \cdot \left(1 - \frac{1}{SNR_i}\right) \tag{6.82}$$

and

$$|\underline{Z}_{\mathrm{dist}}| \approx |\underline{Z}| \cdot \sqrt{1 + \frac{1}{SNR_u} - \frac{1}{SNR_i}}. \tag{6.83}$$

It should be emphasized that the random noise causes a systematic error that cannot be reduced by additional filtering or averaging. The real part of the impedance

determined with the proposed method is always smaller than the actual value. For an error smaller than 1% the signal to noise ratio of the current measurement has to be $SNR_i > 40\,\mathrm{dB}$.

The calculation of the impedance modulus involves both the current and the voltage noise power, thus the disturbed value can be larger or smaller than the actual one, depending on which signal has a better SNR. However, the calculation of the impedance modulus is less sensitive to noise since part of the disturbance cancels out. For equal signal-to-noise-ratios the error nearly vanishes, provided the noise is distinctly smaller than the signals.

The error of the imaginary part of the impedance that is caused by noise can be determined by inserting equations 6.82 and 6.83 into 6.17 with the approximation $Z'^2_{\mathrm{dist}} \approx Z' \cdot \left(1 - 2\frac{1}{SNR_i}\right)$:

$$\begin{aligned} Z''^2_{\mathrm{dist}} &\approx \underline{Z}^2 \cdot \left(1 + \frac{1}{SNR_u} - \frac{1}{SNR_i}\right) - Z'^2 \cdot \left(1 - 2\frac{1}{SNR_i}\right) \qquad (6.84)\\ &= Z'^2 \cdot \left(1 + \frac{1}{SNR_u} - \frac{1}{SNR_i}\right)\\ &\quad + Z''^2 \cdot \left(1 + \frac{1}{SNR_u} - \frac{1}{SNR_i}\right) - Z'^2 \cdot \left(1 - 2\frac{1}{SNR_i}\right)\\ &= Z''^2 \cdot \left(1 + \frac{1}{SNR_u} - \frac{1}{SNR_i}\right) + Z'^2 \cdot \left(\frac{1}{SNR_u} + \frac{1}{SNR_i}\right). \end{aligned}$$

The real part of the impedance can be replaced by the expression $Z' = Z'' \cot\phi$, where $\phi = \arg(\underline{Z})$ of the impedance, which leads to the following expression:

$$Z''_{\mathrm{dist}} \approx Z'' \cdot \left(1 + \frac{1 + \cot^2(\phi)}{SNR_u} - \frac{1 - \cot^2(\phi)}{SNR_i}\right). \qquad (6.85)$$

The error induced by noise on the imaginary part of the impedance thus depends not only on the signal-to-noise-ratios but also on the phase angle. For small ϕ the relative error becomes large, because the true value of Z'' decreases while the errors involved with the determination of Z' and $|\underline{Z}|$ do not vanish.

The relationships of the signal-to-noise ratios and the associated errors can be used to compensate for known sources of noise. An example for noise power that can be obtained analytically is quantisation, which will be briefly discussed in the following section.

Signal digitisation

For the implementation on a digital system the methods for the impedance measurement have to be digitised, they are sampled with a fixed, finite sampling rate and the values are quantised with the resolution of the analogue-to-digital converter (ADC). Two effects

related to a digital implementation will also be discussed in the following, the effect of a finite integration time and the synchrony of current and voltage measurement.

Quantisation Although the quantisation of continuous signals is a strictly deterministic process, it can be described by the same methods as random noise due to its similar spectral distribution. So-called quantisation noise is caused by the finite resolution of analogue-to-digital converters (ADC). The noise power for linear quantisation that is rounded to the nearest integer[17] is

$$S_{\mathrm{Q}}^2 = \frac{\Delta^2}{12}. \tag{6.86}$$

The step size Δ of the quantiser is defined by its maximum input range $A_{\max}$ and the number of bits B, so $\Delta = A_{\max} \cdot 2^{-B}$ [113, 116, 171]. The error caused by quantisation can be calculated by inserting the quantisation noise for the current and voltage channel into 6.79 and 6.80. The relative error is proportional to the reciprocal amplitude of the excitation signal.

Quantisation noise caused solely by the ADC would only be relevant, if the rms-value of the wanted signal is very small compared to the maximum input range of the ADC. The digital bandpass filter however, which is necessary to preserve some frequency information for the passive impedance measurement, contributes to the quantisation noise. Especially in fixed point implementation, intermediate data has to be truncated or rounded after addition and multiplication. Each rounding or truncation acts as an additional source of quantisation error, weighted with the remaining transfer function of the filter from the location of the quantisation to the output. Depending on the word length used for the computation, the order of the filter, the location of the poles and the filter structure, quantisation noise that originates from the digital filters can be significantly higher than that of the ADC. Schlichthärle [148] gives an extensive analytical description of quantization noise in digital filters. A more pragmatic approach is the "experimental" determination of quantization noise by simulation, as proposed by Parks and Burrow [120].

Sampling Digital signal processing theory states that an analogue signal that is digitised with a sample rate more than twice as large as the highest contained frequency can be reconstructed without errors [116]. This Shannon-Nyquist criterion has to be guaranteed by the analogue input filters of the measurement system (cf. section 6.2.4). Prerequisite for the ideal reconstruction of the signal is an infinite number of samples, which corresponds to an infinite time for the integration of the mean square values. In practise only a finite number of samples is used for the calculation. The influence of the number of samples can be analysed by replacing the continuous integration by a summation over sampled data points. For the mean square value of current one obtains

$$I_{\mathrm{eff,d}}^2 = \frac{1}{N} \sum_{k=0}^{N-1} i_k^2 \tag{6.87}$$

[17] A derivation of this expression can be found in [113].

$$= \frac{1}{N}\sum_{k=0}^{N-1}\widehat{i}^2\cdot\sin^2(\omega k\Delta t+\varphi)\,\mathrm{d}t \tag{6.88}$$

$$= \frac{\widehat{i}^2}{2}\cdot\left(1-\frac{1}{N}\sum_{k=0}^{N-1}\cos(2\omega\frac{k}{f_\mathrm{s}}+2\varphi)\right). \tag{6.89}$$

The current values i_k are sampled at the instances $k\Delta t$, the sampling period Δt is defined by the reciprocal sample frequency $\Delta t = 1/f_\mathrm{s}$. For $N\to\infty$, equation 6.89 passes into the continuous expression of equation 6.9. For the evaluation of the error caused by discrete sampling, a situation can be chosen, in which the error of the continuous expression ($N\to\infty$) becomes zero. This is the case for $\varphi = 0$ and $2\omega T = \pi, 3\pi, 5\pi\ldots$, which is also the worst case scenario for the discrete sampling. For $2\omega T = \pi$ over half a period of a cosine function the values at k and $N-k$ compensate, except the value $\cos(2\omega\frac{N}{f_\mathrm{s}}) = -1$ at $k = N$, which is missing. The relative error then is N^{-1}. This result can be generalised as an upper limit of the relative error of the impedance due to discrete sampling:

$$|r_{DZ}| = \frac{1}{N}. \tag{6.90}$$

The relative errors that remain even after a large number of samples are defined by the tolerances determined for the continuous case (equations 6.53, 6.55 and 6.57). Though these errors and r_{DZ} may compensate in certain cases, the maximum error should be estimated as the sum of both. For the modulus of the impedance and for the real part of the impedance under the assumption[18] that $|\phi| < 45°$, the relative error is

$$|r_Z| \le |r_{DZ}| + |r_{TZ}| \le \frac{1}{N} + \frac{1}{\omega T}. \tag{6.91}$$

By replacing the integration time $T = N\Delta t = N/f_\mathrm{s}$, the relative error can be expressed as a function of the number of samples N, the sample frequency f_s and the frequency f of the measured signal:

$$|r_Z| \le \frac{1}{N}\cdot\left(1+\frac{f_\mathrm{s}}{2\pi f}\right). \tag{6.92}$$

If the signal is a mixture of frequencies, the error should be calculated for the lowest frequency, since it causes the largest error.

The use of equation 6.92 for the determination of the necessary number of samples shall be illustrated with an example: The sample frequency be $f_\mathrm{s} = 1\,\mathrm{kHz}$ and the lowest frequency used for the impedance measurement be $f = 30\,\mathrm{Hz}$. If a relative error of $|r_Z| < 1\,\%$ is demanded, the required number of sample points is $N > \frac{1}{1\%}\cdot\left(1+\frac{1\,\mathrm{kHz}}{2\pi\cdot 30\,\mathrm{Hz}}\right) \approx 631$. This estimate does not consider other sources of error. Still, the practical error can be significantly lower as all calculations above are based on worst case estimations.

[18] For situations where the phase angle is not in the range of ±45°, e.g. the measurement at very high frequencies where inductive behaviour is dominant or for measurements on EDLCs at very low frequencies, equation 6.55 has to be considered explicitly.

Synchrony The determination of the real part of the impedance according to equation 6.15 requires the accurate measurement of the mean real power $\overline{P}$. The real power is calculated as the average over the instantaneous power $p(t) = i(t) \cdot u(t)$ (cf. eq. 6.8). Voltage and current have to be measured at exactly the same point in time to obtain the correct value of $\overline{P}$. Especially for low cost measurement instrumentation, different signal channels often share one ADC and are sampled alternately. This time-multiplex mode violates the request for synchrony and adds a time difference Δt to the signals. For the analysis one can assume the current signal to be measured at time t while the voltage is measured at time $t + \Delta t$. This time shift can be expressed as a frequency dependent factor in the Fourier spectrum[19] of the voltage signal:

$$\underline{U}_{\Delta t}(\omega) = \underline{U}(\omega) \cdot e^{j\omega\Delta t}. \tag{6.93}$$

The mean power for arbitrary signals is defined by the integral over the Fourier spectra (eq. 6.22), so the complex factor $e^{j\omega\Delta t}$ leads to

$$\begin{aligned}
\overline{P}_{\Delta t} &= \frac{1}{2\pi T} \int_{-\infty}^{+\infty} \underline{I}(\omega) \cdot \underline{U}^*_{\Delta t}(\omega)\, \mathrm{d}\omega \\
&= \frac{1}{2\pi T} \int_{-\infty}^{+\infty} \underline{I}(\omega) \cdot \underline{U}^*(\omega) \cdot e^{-j\omega\Delta t}\, \mathrm{d}\omega \\
&= \frac{1}{2\pi T} \int_{-\infty}^{+\infty} |\underline{I}(\omega)|^2 \cdot \underline{Z}(\omega) \cdot e^{-j\omega\Delta t}\, \mathrm{d}\omega.
\end{aligned} \tag{6.94}$$

The integration over the whole frequency range lets the imaginary part of the expression vanish, since it is an odd function of ω [113]. However, instead of the real part of the impedance $Z'(\omega)$, the quantity $\Re\left\{\underline{Z}(\omega) \cdot e^{-j\omega\Delta t}\right\}$ is measured for each frequency, so the averaged real part of the impedance $\widetilde{Z}'$ from equation 6.23 becomes

$$\begin{aligned}
\widetilde{Z}'_{\Delta t} = \frac{\overline{P}_{\Delta t}}{I^2_{\mathrm{rms}}} &= \frac{\int_{-\infty}^{\infty} |\underline{I}(\omega)|^2 \cdot \Re\left\{\underline{Z}(\omega) \cdot e^{-j\omega\Delta t}\right\}\, \mathrm{d}\omega}{\int_{-\infty}^{\infty} |\underline{I}(\omega)|^2\, \mathrm{d}\omega} \\
&= \frac{\int_{-\infty}^{\infty} |\underline{I}(\omega)|^2 \cdot |\underline{Z}(\omega)| \cdot \cos\left(\phi - \omega\Delta t\right) \mathrm{d}\omega}{\int_{-\infty}^{\infty} |\underline{I}(\omega)|^2\, \mathrm{d}\omega},
\end{aligned} \tag{6.95}$$

with the phase angle $\phi = \arg(\underline{Z})$ of the impedance. For $\Delta t = 0$ the expression is identical to equation 6.23 with $Z' = |Z| \cdot \cos\phi$. The error caused by the time shift Δt thus depends also on the spectrum of the current signal and on the phase angle of the impedance. For a band-limited signal a worst-case estimation can be made, assuming the signal concentrated at the upper boundary of the frequency interval ω_{u}.

[19] A discussion in the continuous time domain was chosen despite the time discrete nature of the problem, since it allows to discuss a time shift that is not an integer multiple of the sample time.

The relative error then is

$$r_{\Delta t} \leq \frac{Z'_{\Delta t}(\omega_\mathrm{u}) - Z'(\omega_\mathrm{u})}{Z'(\omega_\mathrm{u})} = \frac{\cos(\phi - \omega_\mathrm{u}\Delta t) - \cos\phi}{\cos\phi}. \tag{6.96}$$

The absolute error can be expressed with respect to the modulus of the impedance:

$$|Z'_{\Delta t}(\omega_\mathrm{u}) - Z'(\omega_\mathrm{u})| = |(\cos(\phi - \omega_\mathrm{u}\Delta t) - \cos\phi)| \cdot |\underline{Z}(\omega_\mathrm{u})|. \tag{6.97}$$

For an estimate of the maximum error the maximum of this expression can be determined analytically[20] and simplified by the inequation $|\sin\alpha| < \alpha$:

$$\begin{aligned} |Z'_{\Delta t}(\omega_\mathrm{u}) - Z'(\omega_\mathrm{u})| &= |(\cos(\phi - \omega_\mathrm{u}\Delta t) - \cos\phi)| \cdot |\underline{Z}(\omega_\mathrm{u})| \\ &< 2\left|\sin\left(\omega_\mathrm{u}\frac{\Delta t}{2}\right)\right| \cdot |\underline{Z}(\omega_\mathrm{u})| \\ &< \omega_\mathrm{u}\Delta t \cdot |\underline{Z}(\omega_\mathrm{u})|. \end{aligned} \tag{6.98}$$

The error is thus proportional to the product of the time difference between the current and voltage measurement and the frequency of the measured signal. The absolute value of the impedance is not affected by asynchronous measurement of voltage and current. Since the imaginary part of the impedance is calculated as the difference of absolute value and real part, its error limit is the same as that of the real part.

6.2.7 Validation and selection of measured data

For an accurate measurement, certain criteria regarding the excitation signal, the measurement procedure and the device under test have to be assured. For active impedance measurement with laboratory equipment, these conditions – e.g. the measurement frequency and the amplitude of the alternating and the direct current – can be set by the measurement instrumentation. For passive impedance measurements, this is not possible; naturally, many measurement values are obtained during inadequate measurement conditions and are thus inaccurate or even completely useless. It is therefore necessary to check each measurement[21] and to separate the "good" from the "bad" values.

Important for a good measurement quality is sufficient signal strength. Measurement noise is always present and typically independent of the signal amplitude. Assuming a constant noise power, the signal-to-noise ratio is directly proportional to the rms-values of the current and voltage signal (cf. equation 6.81).

As a consequence, minimum boundary values for the mean square values of current and voltage can be introduced in the calculation:

$$I^2_\mathrm{rms} \overset{!}{>} I^2_\mathrm{rms,min} \quad \text{and} \quad U^2_\mathrm{rms} \overset{!}{>} U^2_\mathrm{rms,min}. \tag{6.99}$$

[20] Setting the first derivative with respect to ϕ equal to zero: $\frac{\mathrm{d}}{\mathrm{d}\phi}(\cos(\phi - \omega\Delta t) - \cos\phi) = \sin\phi - \sin(\phi - \omega\Delta t) \overset{!}{=} 0$ yields $\phi = \pm\frac{\pi}{2} + \frac{\omega\Delta t}{2}$, inserting this into $\cos(\phi - \omega\Delta t) - \cos\phi$ again results in $\pm 2\sin\frac{\omega\Delta t}{2}$.

[21] One "measurement" refers to the measurement of one impedance value, i.e. the integration over a sufficient number of samples. A typical measurement may include 1000 samples measured over a period of one second.

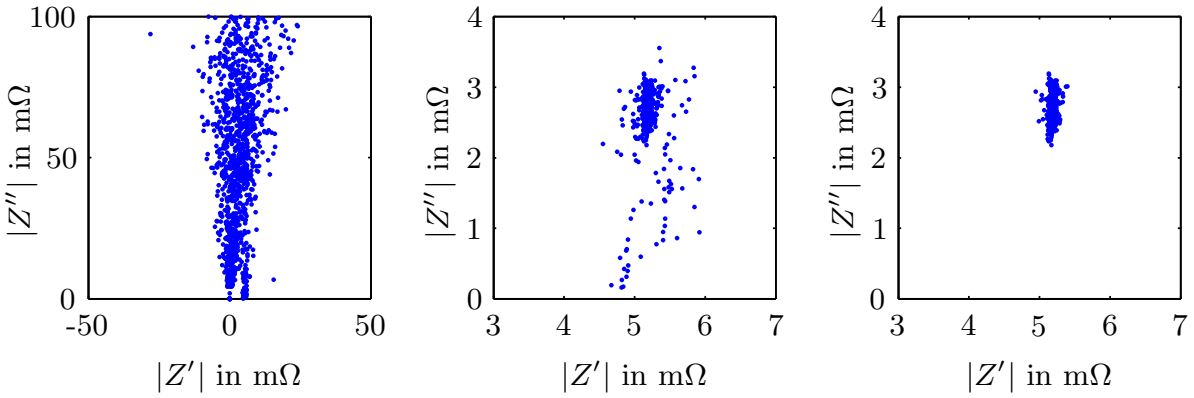

Figure 6.19: Example for the selection of measured impedance values. The raw data (left) shows very strong scattering that was significantly reduced by discarding measurements with low signal strength (centre). Additional elimination of non-stationary measurements yields the final data set (right).

Signals below these boundaries are discarded and not used for the determination of the impedance.[22]

There are, however, more factors that influence the quality of the measurement. Battery impedance is generally non-linear, a certain operating point can therefore be defined by the momentary direct current and voltage:

$$i_{\mathrm{dc,min}} \overset{!}{<} i_{\mathrm{dc}} \overset{!}{<} i_{\mathrm{dc,max}} \quad \text{and} \quad u_{\mathrm{dc,min}} \overset{!}{<} u_{\mathrm{dc}} \overset{!}{<} u_{\mathrm{dc,max}}. \tag{6.100}$$

Both can be measured in parallel to the impedance measurement, if either the direct current or the effective frequency are not within predefined boundaries, the measured impedance value should be discarded.

As discussed in section 2, the system to be measured should be quasi-stationary during the measurement period. One possibility to validate a quasi-stationary measurement condition is to calculate the maximum value of the momentary values $i^2(t)$ over one integration period and compare this to the corresponding average value I^2_{rms}. If the quotient k_I exceeds a certain limit, the excitation signal has changed too much within the measurement period:

$$\frac{\max(i^2(t))}{I^2_{\mathrm{rms}}} = k_I \overset{!}{<} k_{I,\mathrm{max}}. \tag{6.101}$$

Figure 6.19 shows an example for the process of data selection from passive impedance measurements. The current and voltage data has been recorded in a compact car on a lead-acid battery with a commercial battery sensor (cf. section 7.2.3) over a period of approximately three hours with urban traffic, start-stop and parking periods. For the impedance data shown in figure 6.19 the frequency range of the current and voltage signals has been limited by a 4th order digital band-pass filter with corner frequencies at

[22] For measurement systems that switch between different input signal ranges, e.g. by means of a programmable gain amplifier as shown in figure 6.6, these boundaries have to be defined for each range, since noise caused by the analogue instrumentation and by the digital conversion and fixed point arithmetic scale differently.

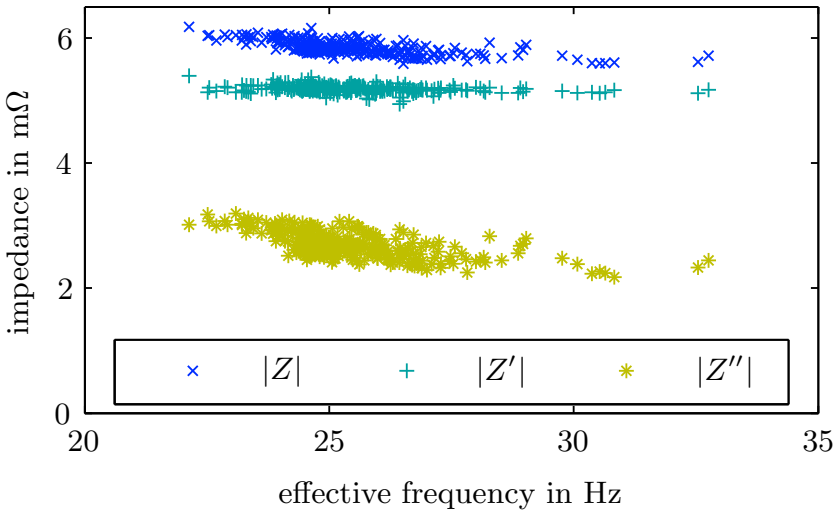

Figure 6.20: Impedance data measured with the passive measurement technique as a function of the effective frequency (same data as in figure 6.19, right).

20 Hz and 30 Hz. The left plot shows the raw impedance data that has been calculated with the proposed method. Most of the data does not contain useful information, mostly because it has been calculated at times where no excitation signal was present. For the centre plot all data was removed, for which either I^2_{rms} or U^2_{rms} were below a certain threshold. The scattering of data points is significantly reduced and most of the data accumulates in a narrow region in the Nyquist plane. For the right plot additionally those measurements have been removed that did not fulfil the requirements defined by equations 6.100 and 6.101. The limits for dc-current and voltage where chosen such that only constant charging periods during driving were evaluated, k_I was limited to $k_{I,\max} = 10$. The selected impedance data in the right plot has standard deviation of $\sigma_{Z'} = 0.05\,\mathrm{m\Omega}$ for the real part and $\sigma_{Z''} = 0.20\,\mathrm{m\Omega}$ for the imaginary part. The larger scattering of the Z''-values can be explained partially by the fact that Z''^2 is calculated as the difference of the directly measured values $|Z'|$ and Z^2, thus the errors of both measurements add up. Moreover, the imaginary part of the impedance changes more distinctly with frequency than the real part in the respective frequency region. Figure 6.20 shows the real and imaginary part as well as the modulus of the impedance data from figure 6.19 (right) as a function of frequency. The frequency has been determined with the procedure described in section 6.2.3. The remaining scattering is not only due to measurement errors but also reflects the change of the impedance with SOC and temperature during the measurement period.

6.2.8 Comparison with other measurement methods

The measurement method proposed in section 6.2.1 has to compete with established methods for determination of the electric impedance. A comparison with the most common measurement methods shall therefore make clear, which specific advantages and disadvantages the measurement based on rms-values has.

For low-cost applications, the internal resistance is often measured as the ratio of

the voltage and current difference from one time step to the next:

$$R_{\Delta u/\Delta i} \approx \frac{\Delta u(t)}{\Delta i(t)} = \frac{u(t+\Delta t) - u(t)}{i(t+\Delta t) - i(t)}. \tag{6.102}$$

Regarding computational effort, this calculation is extremely efficient, since only two subtractions and one division have to be calculate each time step.

For a purely real impedance this method yields good results, yet it produces erroneous results if the measured impedance is complex. This can be easily shown for the sinusoidal test signal introduced in equation 6.1

$$i(\omega, t) = \widehat{i} \cdot \sin(\omega t + \varphi) \tag{6.103}$$

and the voltage response across the impedance $\underline{Z} = Z' + jZ''$ (eq. 6.3):

$$u(\omega, t) = \widehat{i} \cdot (Z'(\omega) \cdot \sin(\omega t + \varphi) + Z''(\omega) \cdot \cos(\omega t + \varphi)) \,. \tag{6.104}$$

For a very small Δt, the finite differences pass into a derivative and $R_{\Delta i/\Delta u}$ can be calculated:

$$\begin{aligned} R_{\Delta u/\Delta i} &\approx R_{\mathrm{d}u/\mathrm{d}i} = \frac{\mathrm{d}u(t)}{\mathrm{d}i(t)} = \frac{\mathrm{d}u(t)}{\mathrm{d}t}\frac{\mathrm{d}t}{\mathrm{d}i(t)} \\ &= \frac{\omega\widehat{i} \cdot (Z'(\omega) \cdot \cos(\omega t + \varphi) - Z''(\omega) \cdot \sin(\omega t + \varphi))}{\omega\widehat{i} \cdot \cos(\omega t + \varphi)} \\ &= Z'(\omega) - Z''(\omega) \cdot \tan(\omega t + \varphi). \end{aligned} \tag{6.105}$$

The measured value thus contains a term that varies with time and distorts the constant value of the real part of the impedance. This result can be generalised for arbitrary signals, which can be decomposed into its sinusoidal components. A second disadvantage of this method is the fact that the measured value depends on the frequency of the excitation signal, which is generally not known for a passive impedance measurement. Moreover, differential methods are inherently sensitive to measurement noise.

There are, however, several reasons, why this measurement method often produces reasonable results:

- The time average of the $\tan(\omega t + \varphi)$ term is zero. The accuracy of the result can therefore be increased by calculating the mean value over several measurements[23].
- The real part of the impedance of a battery is often dominant in a broad frequency range around 100 Hz, the influence of the second term in equation 6.105 may therefore be small.
- The frequency range can be implicitly limited by choosing the time step Δt and by defining thresholds for Δi or Δu. The time step defines the upper limit of the measured frequency range due to the Shannon-Nyquist theorem, provided that higher frequencies are suppressed by an analogue filter (cf. section 6.2.4). Low frequencies cause small changes $\Delta u/\Delta t$ and $\Delta i/\Delta t$, which can be excluded from the calculation.

[23] Yet, the tan-function is discontinuous, thus numerical problems arise if $\tan(\omega t + \varphi) \to \infty$. This problem can be minimized by discarding measurements whenever $\Delta i \approx 0$.

If these requirements are not met and if the limitations of this method are not considered adequately, measuring the internal resistance by the differential method may produce meaningless results. The measurement based on rms-values in contrast allows measuring both the real part and the modulus (and thus the absolute value of the imaginary part) of the impedance, measurement errors are inherently reduced by the integrations. Moreover, the frequency range is explicitly defined by the digital filters.

A measurement methods that provides full access to the information of the complex impedance as a function of frequency is the spectral analysis of the current and voltage signals. The significant disadvantages of full spectral analysis are the high number of computations and especially the demand of memory. Though modern FFT-algorithms are highly efficient, the complete time series of measured voltage and current values have to be stored and processed. The number of data points necessary for one measurement is mainly determined by the required frequency range and resolution. The frequency resolution should not be chosen smaller than the width of distinct peaks in the spectrum, therefore several hundred to thousand data points are often necessary for one measurement.

If the shape of the spectrum is known in advance and if signals at distinct frequencies are present, single point DFT methods can be used. A typical example for a distinct spectrum is shown in figure 6.5 for a UPS system. The spectrum of the current is composed of harmonics of the grid frequency, which is constant within tight limits. The current spectrum measured in a vehicle (cf. figure 6.3) also contains some signals at fixed frequencies, though these depend on the electric components used in each type and brand of vehicle.

If an impedance measurement at a single, fixed frequency is possible and sufficient, the Goertzel algorithm presented in section 2.3.2 is the most efficient way to compute the complex impedance. In contrast to the method based on rms-values, the Goertzel algorithm also provides the information about the sign of the imaginary part. A possible disadvantage is, however, the iterative nature of the algorithm; the new value at each time step is calculated based on the previous result, thus numerical inaccuracies accumulate and may cause stability problems. The main disadvantage is its limitation to single frequency signals, while the method proposed in section 6.2.1 works also with blurred and fluctuating signals.

Table 6.2 summarises the properties of the different methods. The ideal method would have low requirements on computation time and memory and provide high accuracy and robustness against noise and numerical inaccuracies. A high frequency resolution is in principal desirable, the high amount of information that has to be processed may however be problematic for low-cost monitoring systems.

The measurement method based on digital filters and rms-values that is presented in this thesis is the best choice, if the spectra of current and voltage are unknown and non-stationary and if only limited memory and execution time are available on the microcontroller. In contrast to standard spectral analysis, the frequency decomposition and the calculation of the effective values are separated in two steps that can be controlled individually, which allows to adapt the algorithm optimally to the system requirements.

All measurement techniques discussed above determine the impedance of a system irrespective of any underlying model. A different approach is parameter estimation. If an

Table 6.2: Comparison of methods for passive impedance measurements.

method	computation time	memory requirement	accuracy	frequency resolution	robustness
differential ($\Delta u/\Delta i$)	low	low	low	none/low	low
spectral analysis, FFT	high	high	high	high	high
single point DFT	low	low	moderate	high	low
rms with digital filters	moderate	low	high	moderate	high

accurate model of the system – here the battery or double-layer capacitor – exists, parameter estimation allows determining the model parameters directly. A good overview on the theory and methods for direct parameter estimation can be found in publications of R. Isermann [74–76]. Ilangovan [70] proposed a method for the determination of impedance model parameters from galvanostatic discharge curves. This approach requires special test equipment and is thus not apt for passive monitoring systems.

Parameter estimation in combination with a Kalman filter as a state observer has been proposed by Sarfert [134, 135]. While the Kalman filter monitors the changes of state variables, the parameter estimation adapts the model parameters, if these change due to ageing or battery defects. From the respective patents [134,135] it is unfortunately not clear, whether the underlying model is impedance-based or not. Even if an energy storage device can be described by an impedance model, the actual implementation of the model may be different and incorporate non-impedance parameters. As an example, in [95] a double-layer capacitor is modelled by means of an artificial neural network (ANN).

However, for many battery technologies, the models that describe the electric behaviour are either inaccurate or complex with a high number of parameters and thus not suitable for real-time monitoring systems. This thesis focuses on impedance measurements, since the concept of impedance is more general and does not necessarily require a model of the storage device. Nonetheless parameter estimation is an interesting option for devices such as the EDLC that can be accurately described by impedance models.

6.3 Self-adapting characteristic maps

Characteristic maps play an important role in battery monitoring systems. Physical models that could describe the electrical behaviour of a battery in all operating points are generally too complex for an implementation on a cheap microcontroller and require many parameters that are not directly accessible to an electrical measurement.

Examples for a characteristic map in a battery monitoring system are the cranking capability as a function of temperature and open circuit voltage [22] or the capacity as a function of discharge current and temperature. For impedance-based battery monitoring characteristic maps are a means for long-term prognosis. Impedance measurements allow the detection of the current battery state and thus only a prognosis of the battery

behaviour at its current state. For a prognosis for state of charge or temperature different from the current state, impedance values can be stored in a characteristic map.

Yet, the electrical behaviour of batteries and other electrochemical storage devices changes significantly during the lifetime of the device due to ageing processes. A static characteristic map would therefore loose its validity and produce incorrect information. In the following, algorithms will therefore be presented that allow tracking changes in the true battery characteristic and adapting the characteristic maps of the monitoring system accordingly.

Some special features of battery characteristics have to be taken into account for the design of adaptation algorithms:

- The occurrence of measurements is often unequally distributed over the parameter space.
- Most parameters that describe the battery behaviour show a monotonous and smooth change along the input variables.
- The battery behaviour is affected by more influencing variables than can be considered in the characteristic map. A certain scattering of the measurement values at the same operating point is therefore inevitable.
- Changes in the battery characteristic due to ageing are generally relatively slow.

An example for the unequally distributed measurement points are temperature and battery state of charge of an automotive battery. Temperatures above 0 °C and states of charge around 70 % are much more frequent than e.g. -15 °C and 20 % SOC, yet the latter combination is a critical situation for battery performance and has therefore to be covered by the characteristic map. This discrepancy can – at least partially – be solved by taking the smooth shape of the characteristics into account. If, for example, the power capability of a battery differs significantly from the characteristic map at 20 °C, one can assume that it will differ similarly at 10 °C and 30 °C. Yet, an assumption for operating points more distant in the parameter space is much more uncertain. An adaptation algorithm should therefore adapt the characteristic map in the vicinity of the current operating point more then distant areas of the input state space.

The scattering of measurement values should not disturb the characteristic map, certain low-pass behaviour of the self-adaptation is therefore necessary. Low-pass filtering limits the adaptation speed, which is however uncritical due to the fact that the battery characteristic changes rather slowly [20, 22].

6.3.1 Basic algorithm

For the mathematical description of the self-adaptation algorithms, the generalised input values – which could be temperature or state of charge as in the examples above – are $x_1, x_2, \ldots x_N$, where N is the number of input dimensions. The function value that characterises the battery behaviour – which could be a battery performance parameter such as power capability or a model parameters such as the series resistance of a battery – will generically be named y.

The characteristic of the battery can then be described by

$$y = y(x_1, x_2, \ldots x_N) = y(\vec{x}). \tag{6.106}$$

If the real characteristic value y_0 of the battery is measured at a certain operating point $\vec{x}_0 = (x_{1,0}, x_{2,0} \ldots x_{N,0})$, the local error of the stored characteristic map compared to the real battery behaviour can be calculated:

$$\Delta y(\vec{x}_0) = y_0 - y(\vec{x}_0). \tag{6.107}$$

The characteristic is updated by adding this error multiplied by a smoothing function $h(\vec{x})$ to the original characteristic:

$$y_{\text{new}}(\vec{x}) = y(\vec{x}) + \Delta y(\vec{x}_0) \cdot h(\vec{x}, \vec{x}_0). \tag{6.108}$$

Based on the requirements discussed above, the smoothing function $h(\vec{x})$ should affect the vicinity of the operating point more than distant regions in the input space. A mathematical function that meets this requirement is the bell-shaped curve (Gauss error distribution curve):

$$h(\vec{x}, \vec{x}_0) = \alpha \cdot \left(\mathrm{e}^{-\left(\frac{x_1 - x_{1,0}}{\sigma_1}\right)^2} \cdot \mathrm{e}^{-\left(\frac{x_2 - x_{2,0}}{\sigma_2}\right)^2} \ldots \cdot \mathrm{e}^{-\left(\frac{x_N - x_{N,0}}{\sigma_N}\right)^2} \right). \tag{6.109}$$

The factor α is the height of the curve at the current operating point $\vec{x}_0 = (x_{1,0} \ldots x_{N,0})$, it defines the strength of the low-pass filtering. For $\alpha = 1$ the characteristic would be locally set to the measured value without any damping of measurement scattering, for $\alpha = 0$ no adaptation would occur. The value of α depends on the application, it has to be chosen as a compromise between fast adaptation of the map (large α) and good damping of measurement scattering (small α). α may also be varied during operation; after a replacement of the battery a large value is beneficial to adapt fast to the new situation, while during normal operation a small value is beneficial.

The values of σ_1 to σ_N in equation 6.109 define the width of the bell-shaped curve in each of the input dimensions. For a symmetric curve, these values can be normalised to the input range

$$\begin{aligned} \sigma &= \frac{\sigma_1}{\max(x_1) - \min(x_1)} = \frac{\sigma_2}{\max(x_2) - \min(x_2)} = \ldots \\ &= \frac{\sigma_N}{\max(x_N) - \min(x_N)} \end{aligned} \tag{6.110}$$

and only σ has to be defined as a parameter. If the characteristic was measured at one "corner" of the input space, the adaptation of function values at the opposite corner would be smaller by a factor of $\mathrm{e}^{-\left(N/\sigma^2\right)}$. Figure 6.21 shows an example of the smoothing function h for two input dimensions ($N = 2$).

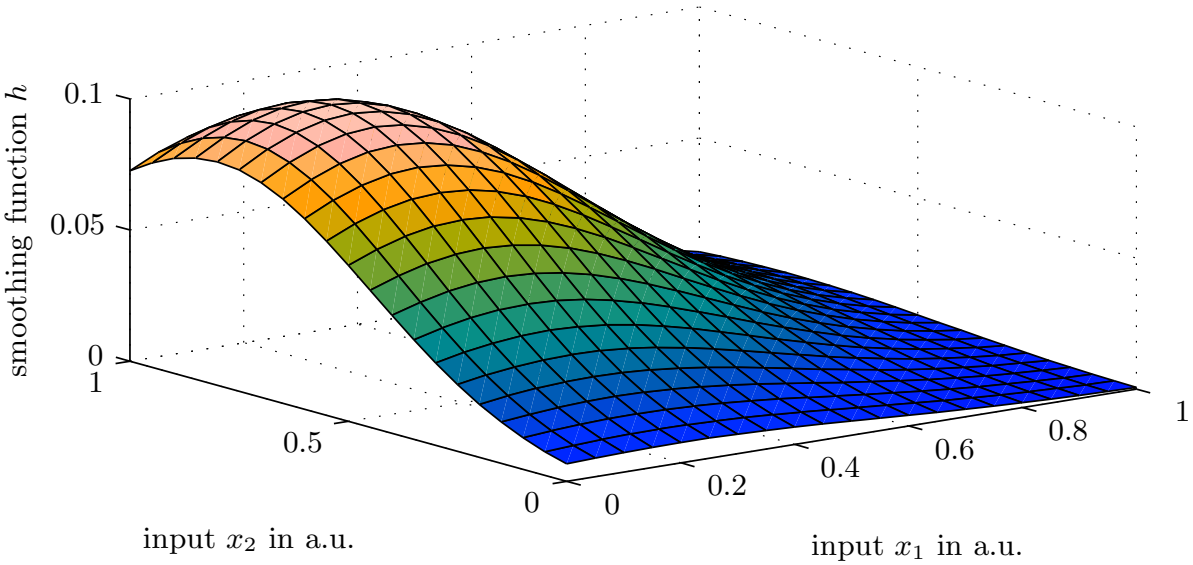

Figure 6.21: Example of the bell-shaped smoothing function for two input dimensions with maximum height $\alpha = 0.1$ and normalised width $\sigma = 0.5$. The curve is centred at the operating point $x_1 = 0.2$ and $x_2 = 0.8$.

6.3.2 Characteristic map as a look-up table

A characteristic map can be implemented as a look-up-table, in this case the vectors

$$\begin{aligned} \vec{x}_1 &= [x_{1,1}, x_{1,2}, \ldots x_{1,M_1}] \\ \vec{x}_2 &= [x_{2,1}, x_{2,2}, \ldots x_{2,M_2}] \\ \vec{x}_3 &= [x_{3,1}, x_{3,2}, \ldots x_{3,M_3}] \\ &\vdots \\ \vec{x}_N &= [x_{N,1}, x_{N,2}, \ldots x_{N,M_N}] \end{aligned} \tag{6.111}$$

form the basis of the table. Each input dimension has a number M of supporting points x, M can be different for each dimension. The function values are stored in an N-dimensional table $\mathbf{Y}$ that contains $M_1 \cdot M_2 \ldots \cdot M_N$ elements. Function values for operating points that fall between the supporting values can be determined by interpolation.

The steps for one iteration of the adaptation are:

1. Measurement of the input variables $x_{1,0}, x_{2,0} \dots x_{N,0}$ that define the current operating point $\vec{x}_0$ and of the associated function value y_0.
2. Reading or interpolation of the predicted function value y for $\vec{x}_0$ from the look-up table $\mathbf{Y}$.
3. Calculation of the local prediction error $\Delta y = y_0 - y(\vec{x}_0)$.
4. Calculation of the smoothing function for the same base vectors as the look-up table, the result is a table $\mathbf{H}$ the same size as $\mathbf{Y}$.
5. Update the look-up table: $\mathbf{Y}_{\text{new}} = \mathbf{Y} + \Delta y \cdot \mathbf{H}$.

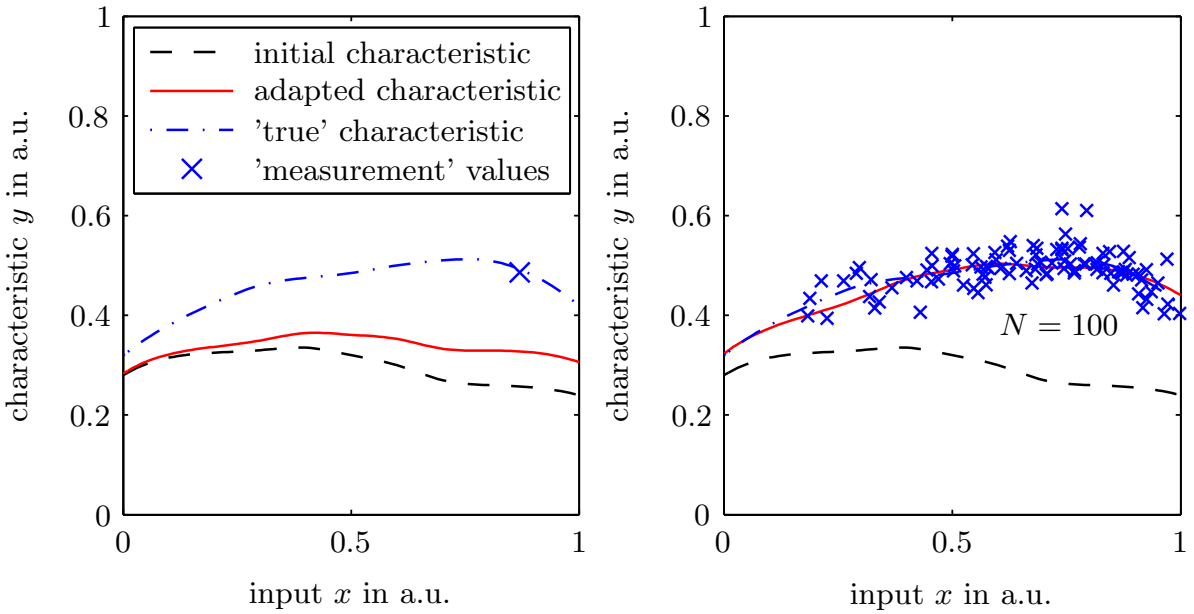

Figure 6.22: One-dimensional example for the adaptation of a characteristic with the proposed method after one measurement update (left) and after 100 updates (right). Parameters for this example: $\alpha = 0.3$, $\sigma = 0.5$.

For a more efficient implementation with respect to memory requirement the update of $\mathbf{Y}$ can be executed element by element instead of calculating the complete table $\mathbf{H}$. Still the memory requirements may be large, especially if many input dimensions are required. For example, a look-up table that takes temperature, state of charge, power and pulse duration as input variables (cf. [22]) and has ten supporting points in each dimension would require a memory for 10000 values (not including the base vectors) or approximately 20 kByte of memory for 16bit variables.

Figure 6.22 shows a one-dimensional example of a self-adapting characteristic with simulated measurement values. The left figure shows the characteristic after the first adaptation iteration, the characteristic "bows" toward the measurement value[24]. The

[24]The value of $\alpha = 0.3$ is larger than usual to show the effect more clearly.

right figure shows the characteristic after 100 iterations with unequally distributed, scattered synthetic measurement values[25].

This general form of self-adaptation can track virtually any characteristic if σ is small enough and if sufficient measurement points are available in the complete parameter space. However, in practice some regions of the input parameter space are rarely or never updated, it is therefore necessary to extrapolate to these regions. This can be done by fitting a smooth analytic function to the "raw" look-up-table as a last step in the procedure described above. If this function is able to represent the real characteristic well, it will provide a good extrapolation and additionally remove unphysical waviness from the characteristic map.

6.3.3 Characteristic map as a polynomial approximation

Many smooth characteristics can be approximated by a polynomial function of second order. This type of function can be fitted to a self-adapting look-up table, as described above, yet the combination of a look-up table with a least squares regression requires both extensive memory and computational effort, which is undesirable for an implementation on low-cost controllers.

In the following, a procedure will be described that directly adapts the polynomial coefficients and thus allows a very efficient implementation of self-adapting characteristics maps.

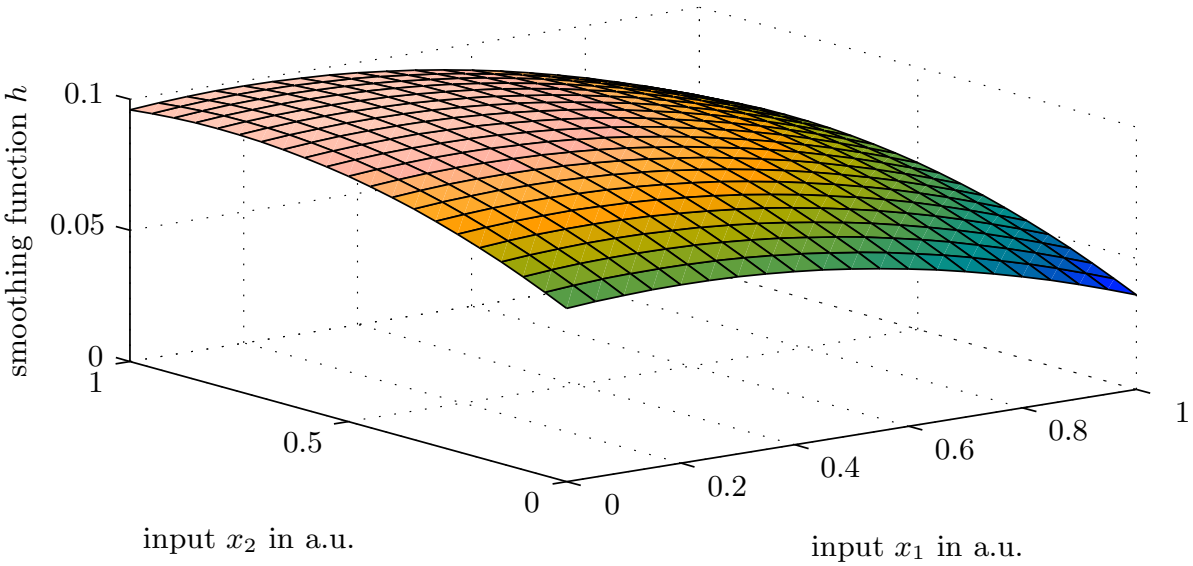

Figure 6.23: Example of the polynomial smoothing function for two input dimensions with maximum height $\alpha = 0.1$ and normalised coefficient $c'_{h,0} = -\alpha/2$. The curve is centred at the operating point $x_1 = 0.2$ and $x_2 = 0.8$.

We assume a characteristic with N input dimensions that is described by a second-

[25]The x-values have been generated as pseudo-random numbers centred at $x = 0.75$ with a standard deviation of 0.3. The y-values have been calculated by adding pseudo-random scattering with a standard deviation of 0.03 to a smooth curve ('true' characteristic).

order polynomial without cross-terms[26]:

$$y = a + \sum_{k=1}^{N} b_k \cdot x_k + \sum_{k=1}^{N} c_k \cdot x_k^2. \tag{6.112}$$

If the smoothing function h is also described by a second-order polynomial without cross-terms (cf. figure 6.23)

$$h = a_h + \sum_{k=1}^{N} b_{h,k} \cdot x_k + \sum_{k=1}^{N} c_{h,k} \cdot x_k^2, \tag{6.113}$$

equation 6.108 can be reduced to an adaptation of the polynomial parameters instead of the function values:

$$\begin{aligned} y_{\text{new}} &= y + \Delta y \cdot h \\ &= a_{\text{new}} + \sum_{k=1}^{N} b_{k,\text{new}} \cdot x_k + \sum_{k=1}^{N} c_{k,\text{new}} \cdot x_k^2. \end{aligned} \tag{6.114}$$

with

$$\begin{aligned} a_{\text{new}} &= a + \Delta y \cdot a_h \\ b_{k,\text{new}} &= b_k + \Delta y \cdot b_{h,k} \\ c_{k,\text{new}} &= c_k + \Delta y \cdot c_{h,k}. \end{aligned} \tag{6.115}$$

The smoothing function h has to be centred on the current operating point $\vec{x}_0 = (x_{1,0}, x_{2,0} \ldots x_{N,0})$, equation 6.113 can be therefore be rewritten:

$$h = a'_h + \sum_{k=1}^{N} b'_{h,k} \cdot (x_k - x_{k,0}) + \sum_{k=1}^{N} c'_{h,k} \cdot (x_k - x_{k,0})^2 \tag{6.116}$$

with

$$\begin{aligned} a_h &= a'_h - \sum_{k=1}^{N} \left(b'_{h,k} \cdot x_{k,0} - c'_{h,k} \cdot x_{k,0}^2 \right) \\ b_{h,k} &= b'_h - 2c'_{h,k} \cdot x_{k,0} \\ c_{h,k} &= c'_h. \end{aligned} \tag{6.117}$$

The coefficients a'_h, b'_h and c'_h define the shape of the smoothing function, they are constants and independent of the current operating point. a'_h defines the height of the smoothing function at $\vec{x}_0$:

$$a'_h = \alpha. \tag{6.118}$$

[26] A general second-order polynomial includes cross-terms of the type $d_{k,l} \cdot x_k \cdot x_l$ with $k \neq l$. Polynomials with cross-terms are briefly discussed at the end of this section.

For a smoothing function that is symmetric to the operating point, the linear coefficients have to be equal to zero:

$$b'_{h,k} = 0 \quad \text{for all } k. \tag{6.119}$$

The coefficient of the square term determines the width of the curve. Unlike the bell-shaped curve, a second order polynomial does not converge to zero far away from the origin, yet a zero crossing of the curve has to be avoided. Negative values of the smoothing curve would cause the characteristic to move away from the measured values instead of approaching it. Boundary values can be calculated by demanding that the value of the polynomial at the longest possible distance from the origin may not be smaller than zero:

$$h(\max(\vec{x}) - \min(\vec{x})) = a'_h + \sum_{k=1}^{N} c'_{h,k} \cdot (\max(x_k) - \min(x_k))^2 \stackrel{!}{\geq} 0. \tag{6.120}$$

For a unique solution of this equation an additional symmetry has to be defined by normalising to the input range:

$$\begin{aligned} c'_{h,0} &= c'_{h,1} \cdot (\max(x_1) - \min(x_1))^2 \\ &= c'_{h,2} \cdot (\max(x_2) - \min(x_2))^2 \dots \\ &= c'_{h,N} \cdot (\max(x_N) - \min(x_N))^2. \end{aligned} \tag{6.121}$$

The inequation for $c'_{h,0}$ then is

$$c'_{h,0} \geq -\frac{a'_h}{N} = -\frac{\alpha}{N}. \tag{6.122}$$

The steps for one iteration of the direct adaptation of polynomial coefficients are:

1. Measurement of the input variables $x_{1,0}, x_{2,0} \dots x_{N,0}$ that define the current operating point $\vec{x}_0$ and of the associated function value y_0.
2. Calculation of the predicted function value y for $\vec{x}_0$ from the polynomial function.
3. Calculation of the local prediction error $\Delta y = y_0 - y(\vec{x}_0)$.
4. Calculation of the polynomial coefficients $a_{h,k}$, $b_{h,k}$ and $c_{h,k}$ from α, $c'_{h,1} \dots c'_{h,N}$ and the current operating point $\vec{x}_0$ according to equations 6.118, 6.118 and 6.122.
5. Update of the polynomial parameters according to equation 6.116.

The first three steps are basically the same as for the look-up table, except that the function value $y(\vec{x}_0)$ is obtained from an analytical function instead from a table.

Figure 6.23 shows a 2-dimensional example of a polynomial smoothing function with $c'_{h,0} = -\frac{a'_h}{N}$. Comparison with the bell-shaped curve of figure 6.21 shows that the polynomial smoothing function is much less localised.

In figure 6.24 the adaptation of a look-up-table by a bell-shaped smoothing function is compared to the direct adaptation of polynomial coefficients described above. The

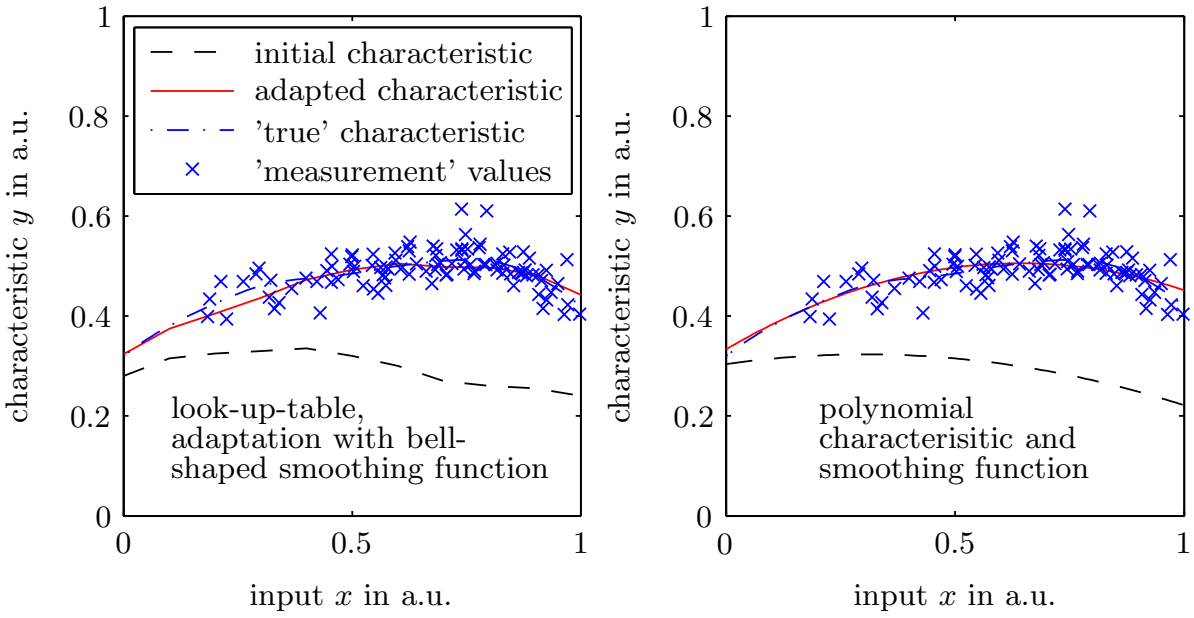

Figure 6.24: Comparison of the self adaptation of a one-dimensional look-up-table with a bell-shaped smoothing function (left, $\alpha = 0.3$, $\sigma = 0.5$, identical to figure 6.22) and direct adaptation of polynomial coefficients with a polynomial smoothing function (right, $\alpha = 0.1$ and $c'_{h,0} = -\alpha$) after 100 updates.

test data and the initial characteristic are identical to the example of figure 6.22. Both procedures produce similar results, yet the direct adaptation of polynomials produces slightly worse results at the regions with few measurement points due to the "broader" smoothing function. This disadvantage, however, becomes crucial if the true, measured characteristic differs significantly from the characteristic initially defined in the monitoring system.

The savings with respect to memory and computation time are, however, immense compared to the adaptation of look-up tables, especially for characteristics with many input variables. For the example given at the end of section 6.3.2 with four input dimensions, only nine polynomial coefficients have to be stored and updated instead of 10000 supporting values that would be necessary for ten supporting points in each dimension.

A disadvantage of the method is that in a general polynomial of the form

$$y = a + \sum_{k=1}^{N} b_k \cdot x_k + \sum_{k=1}^{N} c_k \cdot x_k^2 + \sum_{k=1}^{N} \sum_{l \neq k} d_{k,l} \cdot x_k \cdot x_l. \tag{6.123}$$

the cross-terms $d_{k,l} \cdot x_k \cdot x_l$ cannot be adapted. The reason for this is that cross-terms always lead to an asymmetric surface and are thus not suitable for a smoothing function. Still, a general polynomial of the form shown above can be used for the characteristic and adapted with the smoothing function of equation 6.113, but only the coefficients a, b_k and c_k are affected by the adaptation, all $d_{k,l}$ stay unchanged.

Chapter 7

Impedance-based battery monitoring in automotives

In this chapter two application examples of impedance-based battery monitoring are presented. In both the passive impedance measurement technique explained in section 6.2 is employed. Following the structure of chapter 5, a system for monitoring the ageing of EDLCs and a cranking capability prognosis for lead-acid batteries are explained.

7.1 Monitoring of EDLCs in vehicles

EDLCs are currently discussed as an energy storage system in conventional and hybdrid electric vehicles. In conventional vehicles a module of EDLCs could supply the peak power for the cranking of the combustion engine [105]. Due to the low energy density of EDLCs a battery will still be necessary to supply other electrical loads, yet it could be optimised for high energy density at the cost of peak load performance. In an hybrid electric vehicle EDLCs can deliver additional boost power and accept charge during regenerative braking [160].

In these applications series connections of a few to more than hundred EDLCs will be used, depending on the application. To avoid premature deterioration of the cells the individual cells have to be protected by voltage balancing circuitry. In addition to that, a monitoring of the individual cells would be preferable to detect unfavourable voltage or temperature conditions and to identify weak cells.

7.1.1 Monitoring system

A prototype platform that combines cell balancing and monitoring of individual cells on the basis of a six cell module has been developed and built up by the author. The prototype consists of a printed circuit board that is mounted directly on the capacitors with all necessary circuitry for the cell balancing. As a control platform an ADuC8xx SAR evaluation board [3] equipped with a ADuC8012 microcontroller [5] has been used. The ADuC8012 is a low-cost controller with a 8051 instruction set that has an integrated 12 bit analogue to digital converter with an 8-channel multiplexer. The six cell voltages are buffered by differential amplifiers (OP491 [4]) with an amplification of 0.84 and di-

rectly measured by the on-chip ADC of the microcontroller. Current is measured with a 0.5 mΩ measurement resistor, the voltage across the resistor is amplified by a differential amplifier with an amplification of 17.7 and a reference voltage of 1.25 V from a precision reference voltage IC is added to allow for bidirectional measurements. The resulting positive measurement voltage is measured with the on-chip ADC of the microcontroller. All analogue inputs are equipped with a first order low pass with a corner frequency of 340 Hz to reduce aliasing errors. The sample rate for the voltage and current measurement was limited by the program execution of the controller to $f_s = 640\,\text{Hz}$[1]. The measurement, analysis and control algorithms are programmed in C and flashed by serial download to the 8 kByte on-chip program memory.

The digital outputs of the controller are used to control the balancing circuitry. Circuitry and algorithms for the cell balancing will not be discussed here, since they are out of the scope of this thesis[2].

7.1.2 Measurement algorithm

In addition to monitoring of the cell voltage, the impedance of the individual EDLC cells have been measured with the passive impedance measurement procedure described in section 6.2.

The implementation of the measurement algorithms was strongly influenced by the capabilities of the low-cost controller. The sample rate was limited by the execution time of the digital filters and the computation of the impedance values. As a compromise a sample rate of 640 Hz could be achieved with a second order band pass. The band pass has been optimised with respect to computation speed by replacing as many multiplications as possible by bit-shift operations and by introducing additional scaling factors necessary for integer computations.

The corner frequencies of the digital bandpass filter are 17 Hz and 53 Hz, the maximum gain is 0.78 at 30 Hz.

Figure 7.1 shows the filter structure used for both the low and the high-pass filter, the filter coefficients are given in table 7.1, the filter characteristic is shown in figure 7.2.

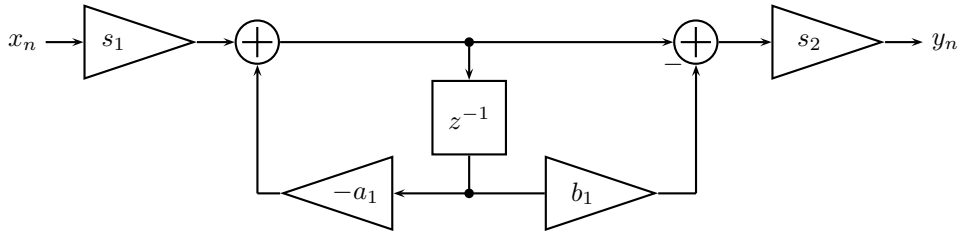

Figure 7.1: Block diagram of a first order IIR filter.

In addition to the impedance measurement method described in section 6.2.1, a variant of the algorithm has been implemented and tested.

[1] To eliminate anti-aliasing entirely the analogue filter should provide a significant damping at $f_s/2 = 320\,\text{Hz}$. The corner frequency of the analogue filter of 340 Hz is a compromise between a high usable frequency range and low remaining aliasing error.

[2] Results of the work regarding cell balancing for EDLCs have been published in [26].

coefficient	low pass	high pass
s_1	4	7/8
s_2	1/4	1/4
a_1	1/2	7/8
b_1	−1	1

Table 7.1: Coefficients of the 2nd order Butterworth bandpass filter optimised for fast bit-shift operations.

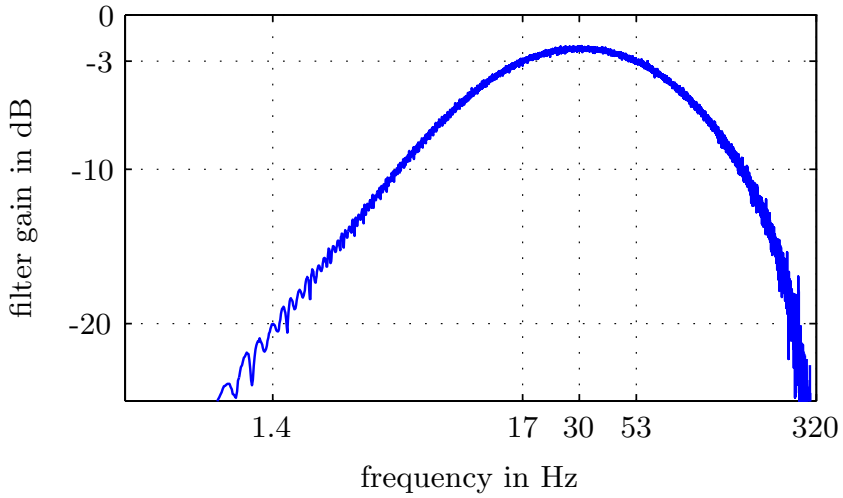

Figure 7.2: Filter characteristic of the the second order IIR filter of figure 7.1 and table 7.1.

Since the EDLCs in the module are connected in series – as in most applications – the same current flows through each of the capacitors. To identify deteriorated capacitors within a string, it is therefore sufficient to compare the mean square values of the voltages with each other.

For a series connection of M EDLCs, the expression

$$\tilde{z}_i^2 = \frac{\tilde{Z}_i^2}{\frac{1}{M}\sum_{k=1}^{M}\tilde{Z}_k^2} = \frac{\tilde{U}_{\mathrm{rms},i}^2}{\frac{1}{M}\sum_{k=1}^{M}\tilde{U}_{\mathrm{rms},k}^2} \tag{7.1}$$

is the relative impedance squared of cell number i with respect to the average cell impedance squared.

The main advantage of this relative impedance measurement is that the relatively costly current measurement can be abandoned.

To obtain the impedance modulus the calculation of the root of expression 7.1 is necessary. A monitoring system could, however, also display a warning message if $\tilde{z}^2$ exceeds a certain limit. A limit of $\tilde{z}^2 = 1.7$ would, for example, mean that the resistance of the specific cell is higher than that of the others by a factor of $\sqrt{1.7} \approx 1.3$.

7.1.3 Measurement results

Measurements for the determination of the accuracy have been carried out at a test bench with square wave current profiles with different fundamental frequencies in the range of 9 to 36 Hz and an amplitude of 50 A.

Figure 7.3 summarises the results of the measurements, the aged device (cell # 2) can be clearly distinguished from the others, the variation of the impedance for one device at different fundamental frequencies is low. The impedance decreases slightly with increasing frequency, which reflects the impedance characteristic of an EDLC in the given frequency range. This effect can also be seen in figure 7.4, which shows the results of impedance measurements on the six EDLC cells (type B of table 5.1). The measurements were carried out with a precision impedance spectrometer (ISEA EISmeter [16]) in a frequency range of 10 mHz to 1 kHz with zero bias current.

The accuracy of the measurement has been determined by comparing the results obtained with the microcontroller system with reference impedance measurements. The average modulus of the relative error is 3.6 % for the lowest and 2 % the highest excitation frequency. Thus, best results are obtained for an excitation frequency near the centre frequency of the bandpass filter. For lower frequencies, the signal power and thus the signal-to-noise ratio is lower due to the damping of the filter, which causes larger errors. Larger frequencies could not be measured due to restrictions of the test bench. Figure 7.4 (right) also shows that the difference of the modulus and the real part of the impedance in the frequency range of the bandpass filter is negligible.

As discussed in section 5.1.3, the modulus of the impedance at high frequencies is an estimate of the series resistance of the EDLC. The relative error of this estimation is a function of the model parameters and the measurement frequency and can be calculated with equation 5.10. With the model parameters, which have been determined from

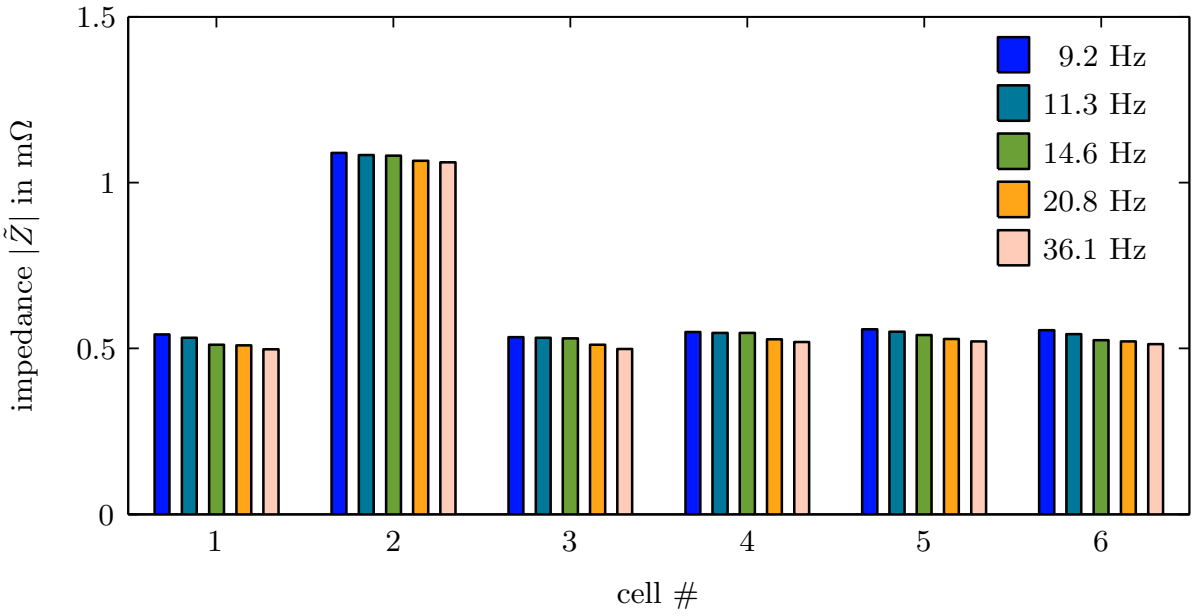

Figure 7.3: Results of the passive impedance measurement for square wave excitations with different fundamental frequencies.

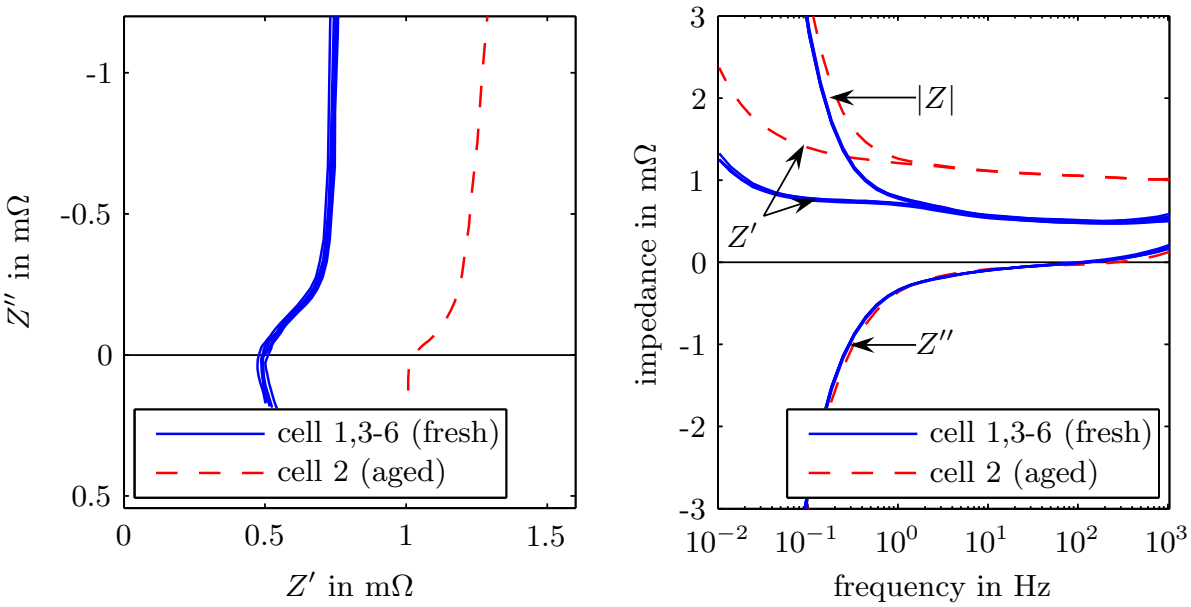

Figure 7.4: Results of the reference impedance measurements on the six EDLC cells (type B of table 5.1). The aged cell exhibits an strongly increased series resistance, as can be seen from both the Nyquist diagram (left) and the semi-logarithmic plot (right).

the impedance spectra by non-linear least-squares fitting (cf. section 2.9), the relative error can be calculated. For the new cells, the relative error according to equation 5.10 is between 22 % at 9.2 Hz and 11 % at 36.1 Hz. This is in good accordance with the measured impedance values shown in figure 7.3, which are approximately 10 to 20 % higher than R_s from table 7.2. For aged cells the relative error becomes smaller, since R_s increases.

Table 7.2: Parameters of the impedance model (eq. 3.13) for a fresh and an aged cell (type B of table 5.1) of the test module.

	R_s in mΩ	R_{el} in mΩ	L_s in nH	A_{dl} in $F/s^{(1-\gamma)}$	γ
cell 1 (fresh)	0.47	0.76	30	585	0.988
cell 2 (aged)	1.00	0.75	16	571	0.972

For a precise determination of the series resistance R_s, passive impedance measurements at higher frequencies would be beneficial. Yet, for a monitoring system that has to detect changes in the performance of the cells it is of little importance that the measured value does not represent the model parameter perfectly. If only the symmetry of the cells has to be monitored, the relative measurement can be used. The results for the relative impedance measurement according to equation 7.1 are shown in figure 7.5. Again, the aged cell can be clearly distinguished from the other cells. The relative errors are in a range of ±3.6 % with an average modulus below ±2 %. Regarding the maximum relative errors, EDLCs with an impedance difference of ±7 % can be distinguished.

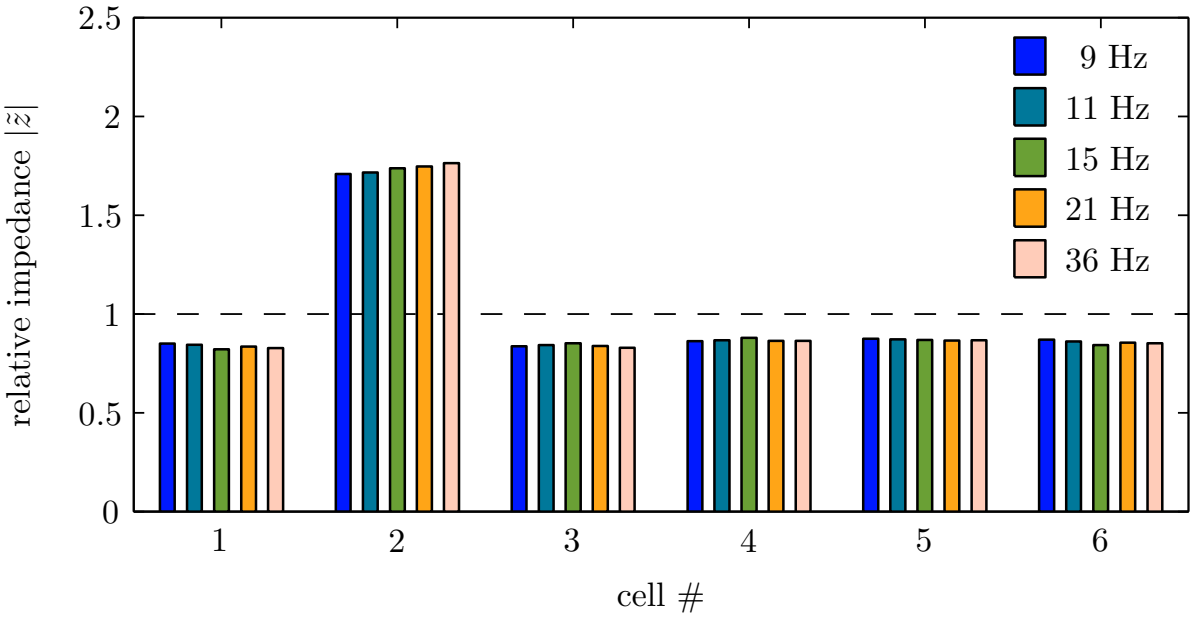

Figure 7.5: Relative impedance calculated from voltage measurements for square wave excitations with different fundamental frequencies.

7.2 Cranking capability prognosis for lead-acid batteries

The main task of a battery in a conventional vehicle is to start the combustion engine. If the battery is weak, it is virtually always the cranking that fails. Due to the increasing number of electric loads in modern vehicles, the battery is even more likely to be in a condition were cranking is no longer possible. The result is an increase of breakdowns due to battery failure for new cars of nearly 200 % within the last 10 years [2]. For upcoming vehicles with stop-start operation, the demand of a reliable prognosis whether the engine can be started again after a stop at the traffic light will therefore be essential.

The battery behaviour during high current discharge pulses was discussed in section 5.2. In the following, an algorithm for the prediction of the cranking capability is developed that can be parameterised by the passive impedance measurement technique introduced in section 6.2.

7.2.1 Cranking current profile

As has been mentioned before, cranking of a car is the process of accelerating the combustion engine by means of an electric starter motor until the engine is able to run on its own. The necessary power for the acceleration is supplied by the starter battery, the special characteristic of this process with respect to the battery load profile is its high current demand of several hundred amperes and the short duration of only a few hundred milliseconds.

Even two consecutive engine starts do not produce exactly identical current characteristics. For a consistent and simplified discussion, the cranking current can therefore

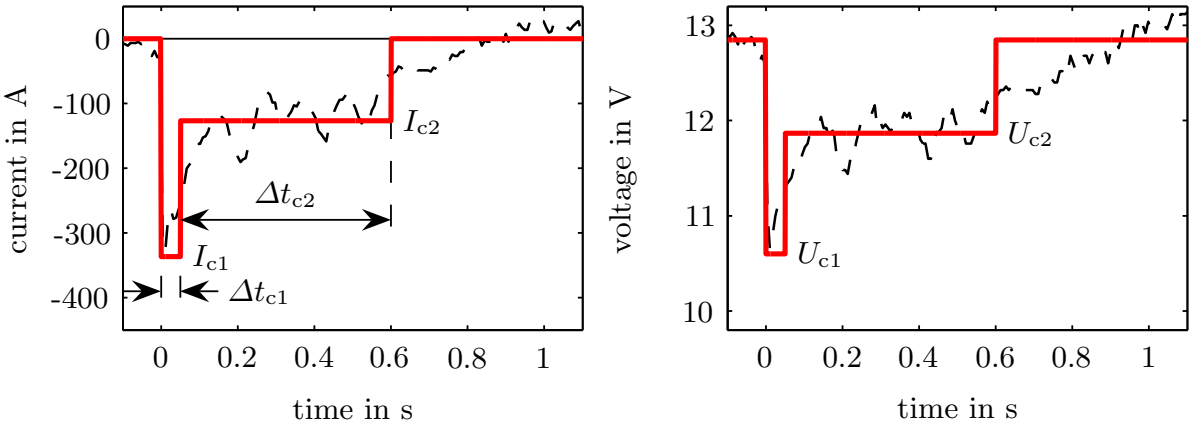

Figure 7.6: Current and voltage profile of a simplified cranking pulse and its characteristic parameters. The dashed line shows the measured cranking pulse of figure 1 (left) for comparison.

be approximated by a two-step profile, as shown in figure 7.6. The first step represents the inrush current I_{c1}, which for a successful start is the maximum cranking current. The battery voltage drops nearly simultaneously to U_{c1}. The current I_{c2} represents the acceleration phase, the corresponding voltage is U_{c2}. Both are average values, the ripple caused by the compression cycles is neglected.

7.2.2 Measurement algorithm

The main aim of the cranking capability prognosis is to determine the lowest voltage that will occur during the next cranking event. During most starts, the lowest voltage will occur within the first milliseconds of cranking, when the starter is still at halt and the hold-off torque has to be overcome.[3]

At this instance, the electrical equivalent circuit equals that shown in figure 7.7.

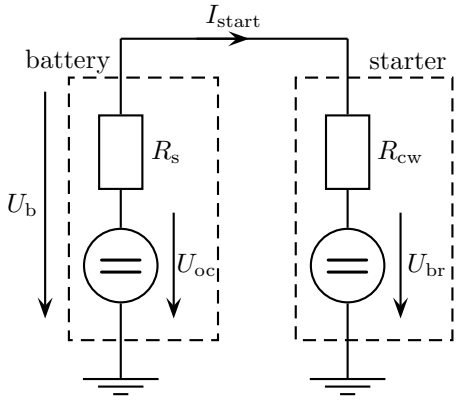

Figure 7.7: Equivalent circuit of battery and starter at beginning of cranking, when the engine and the starter are still at halt.

[3] A detailed description of the cranking procedure and an analysis of the electrical system consisting of the battery and the starter are described in the appendix A.2.

In the battery only the series resistance R_s is effective, since all other resistive components are shunted by the double layer capacitance. For the starter, only the cable and winding resistance R_{cw} and the voltage across the brushes U_{br} cause a voltage drop. The inductance of the battery, the cables and the windings of the starter can be neglected for this analysis. The inductance of the windings is significantly larger than that of the battery, therefore the current slope is determined by the starter and the voltage drop across the battery inductance is negligible. The lowest battery voltage therefore occurs when the current (and not the current slope) is at its maximum, at this moment the current slope and consequently the voltage across both the battery inductance and the starter inductance are zero.

Following this reasoning, the inrush current I_{c1} could be calculated (cf. appendix A.2). This step can be omitted and the minimum battery voltage[4] U_{c1} can be calculated directly according to the voltage divider R_s and R_{cw}, the voltage across the brushes U_{br} and the open circuit voltage of the battery U_{oc}:

$$U_{c1} = \min(U_b) = U_{oc} - (U_{oc} - U_{br}) \cdot \frac{R_s}{R_s + R_{cw}}. \tag{7.2}$$

If the voltage across the brushes U_{br} is known, all other parameters of equation 7.2 can be – and have to be – determined or estimated from battery voltage and current.

The open circuit voltage U_{oc} can be measured at times when the vehicle parks. During a typical ride, the state of charge and thus the open circuit voltage does not change significantly and can be assumed constant. For long driving periods or if the engine is off and electrical consumers are active for a considerable time, SOC may, however, change markedly. Since an SOC-estimator is part of virtual any modern battery monitoring system, the OCV-change can be compensated for calculating the OCV from the OCV-SOC-characteristic (cf. section 4.2.2).

The cable and winding resistance R_{cw} can be learned from past engine starts and stored in a look-up-table as a function of temperature, if necessary. By measuring the maximum current and the minimum voltage – which occur simultaneously – during cranking, R_{cw} can be calculated, again taking the electrical equivalent circuit of figure 7.7 into account:

$$R_{cw} = \frac{\min(U_b) - U_{br}}{\max(|I_{start}|)}. \tag{7.3}$$

The series resistance of the battery can be determined by a passive impedance measurement as described in section 6.2. Theoretically, the real part of the impedance at high frequencies should equal the series resistance. Yet, the maximum current is reached a few milliseconds after the beginning of the start and the charge transfer resistance begins to be effective, thus the optimum frequency is generally in the range of 10 to 100 Hz.

In order to predict the further development of the voltage during cranking, in principle the impedance model presented in 5.2 could be parameterised from passive impedance measurements. Yet, this approach did not yield satisfying results under real-world conditions.

[4] In figure 1 (right) the voltage later during cranking drops below the initial voltage drop. Yet, the initial drop to a minimum and an – at least temporary – recovery of the voltage is typical for all starts and the following reasoning holds even if U_{c1} is only a local minimum.

The main reason is that the current ripple available in the power net of a conventional vehicle has a significant signal content in the frequency region above approximately 10 Hz, but low frequency signals are either very weak or occur only sporadic. Measuring the low frequency part of the battery impedance with a purely passive technique is therefore difficult, the measurement data scatters significantly and cannot be acquired continuously. As a consequence, the data that could be used to determine model parameters, for example by a least squares fit, is too closely together with respect to the parameter frequency, often not measured at the same time and has a significant measurement inaccuracy.

As an alternative, the simplified prognosis described in section 5.2.3 has been applied. For the current I_{c2} of the second cranking phase the value of the preceding cranking event has been used for the results presented in the following section.

A refined procedure for the prediction of I_{c2} is the usage of a characteristic that describes the dependence of I_{c2} on the oil temperature – a value that is measured in every vehicle – in combination with a self-adaptation algorithm that enables the characteristic to follow changes due to deterioration of the motor oil. Such a self-adaptation algorithm is described in section 6.3[5].

7.2.3 Monitoring system

For the development and testing of the cranking capability prognosis, a commercial battery sensor has been used as a data-logger for recording battery current, voltage and temperature. The algorithms have been tested off-line with the measured data. By using a commercial battery sensor for the acquisition of the data, it could be assured that the data has the same properties regarding sample rate, measurement range, resolution and accuracy as an algorithm implemented on this device would "see" it.

Table 7.3: Performance data of the battery sensor IBS [62, 150].

quantity	range	resolution	linearity	offset	noise
voltage	6...18 V	1.0 mV[a]	±0.2 %	±5.0 mV	2.0 mVpp
	±10 A	1.0 mA	±1.0 %	±5.0 mA	5.0 mApp
current	±300 A	10 mA	±1.0 %	±50 mA	75 mApp
	-1500...0 A	50 mA	±1.0 %	±0.5 A	0.15 App

[a] Measurement resolution is 0.5 mV, but currently reduced by software to 1 mV.

The sensor has been supplied by Hella KGaA Hueck & Co., a supplier of the automotive industry. The sensor consists basically of a 116 µΩ measurement resistor and an ADuC7030 microcontroller from Analog Devices [7]. The controller has two independent 16bit Σ-Δ-ADCs that simultaneously sample current and voltage. The current channel is additionally equipped with a programmable gain amplifier (PGA) that can be set to amplification values between 1 and 512 to adapt on the input range. Table 7.3 summarises the technical data of the sensor.

[5] A necessary extension will be the detection of rapid changes due to an oil change.

The sensor is connected to the minus-pole of the starter battery and to the ground connection of the car body. The data is measured with a sample rate of $f_s = 1\,\text{kHz}$ and sent with the same rate via LIN-bus to a notebook where it is recorded.

7.2.4 Measurement results

Measurements have been carried out in a conventional compact car (Ford Fiesta, diesel, 50 kW) with a flooded lead-acid starter battery in early summer 2007. The drive cycle contains mainly city traffic, the engine has been switched off manually whenever the car stopped at a traffic light in order to emulate stop-start operation that will probably be standard in future vehicles. The complete drive cycle is composed of two drive periods of approximately 30 and 20 minutes and parking periods before, between and after the drives, as shown in figure 7.8.

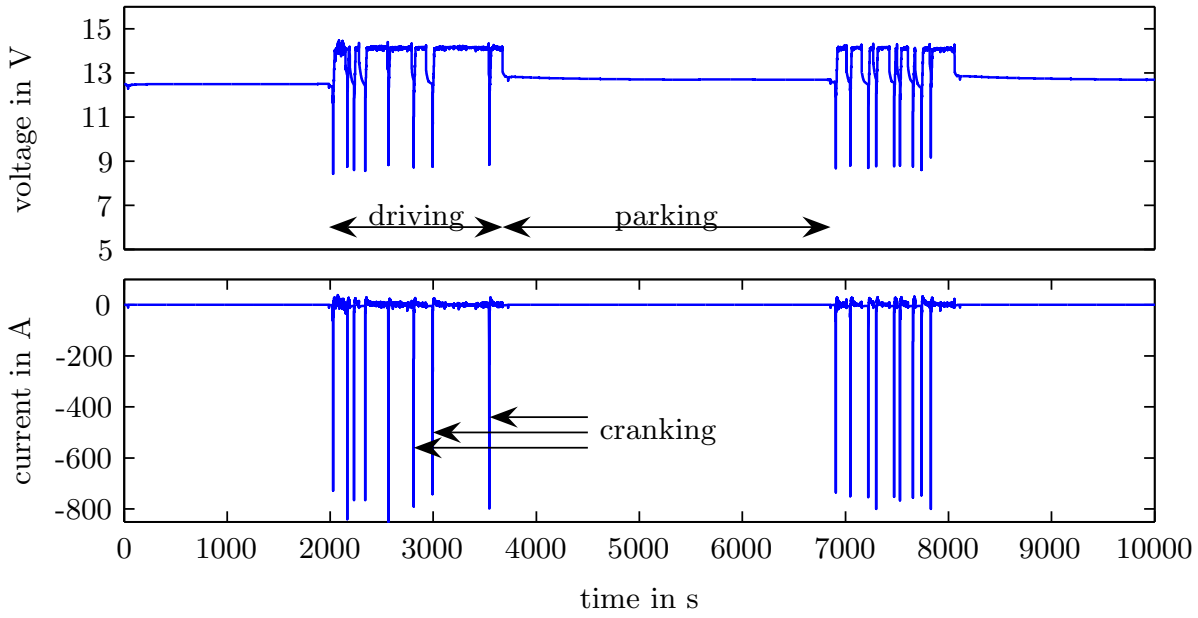

Figure 7.8: Battery current and voltage profile recorded during a test drive with a compact car in urban traffic. The engine was switched off manually at any stop to emulate stop-start functionality.

Impedance values and the cranking prognosis have been calculated off-line in a Matlab-Simulink simulation model that takes the measured data as an input. All calculations are based only on current and past measurements, i.e. the same information that would be available if the algorithms were implemented on the controller.

The open circuit voltage U_{oc} was measured during rest periods, i.e. when the battery current was below 200 mA. The value at the end of the parking period was held and used for the cranking prognosis during driving.[6] Figure 7.9 (top) shows the developing of U_{oc}.

[6]The open circuit voltage determined with this procedure is not equal to the equilibrium potential of the battery; the quiescent current and concentration gradients in the battery cause additional overpotentials. The influence of these overpotentials on the cranking voltage is however small.

The resistance of the starter windings and cable is determined directly after each cranking event according to equation 7.3. As can be seen in figure 7.9 (bottom), the measured resistance is nearly constant, the variations are in the range of ±5 %.

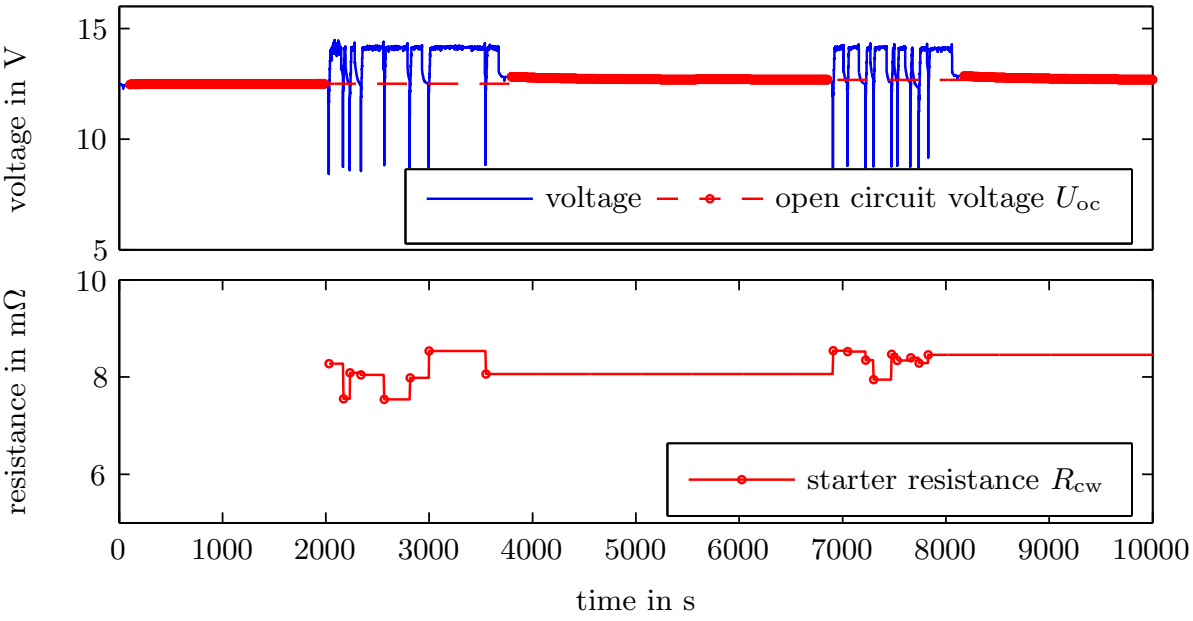

Figure 7.9: Open circuit voltage U_{oc} (top) and starter resistance R_{cw} (bottom) for the drive profile of figure 7.8. Dots denote the values determined by the estimation algorithm, the values are held until the next estimation is possible.

The real part and modulus of the impedance and the effective frequencies are measured in two frequency ranges with the passive measurement technique described in section 6.2. The digital bandpass filters used for the selection of the frequency bands are 4th order Butterworth filters with a filter structure as shown in figure 6.14. The coefficients and characteristic of the filter with the lower frequency range of 5 to 20 Hz are shown in table 6.1 and figure 6.15, respectively. The coefficients of the bandpass filter for the higher frequency range of 100 to 400 Hz have been calculated using a the same filter design tool (*Matlab Filter Realization Wizard* [97]). The measurements are updated every five seconds. Only impedance values that pass the criteria described in section 6.2.7 are used for the cranking prognosis; each value is held until the next valid measurement provides a new value. The development of the real part of the impedance and the effective frequencies is shown in figure 7.10. During the parking periods the current noise is too weak for passive measurements, thus prior to the first driving period no data is available. The real part of the impedance in the frequency range of 100 to 400 Hz is a good estimation of the series resistance of the battery

$$R_s \approx \widetilde{Z}'(100 \ldots 400\,\mathrm{Hz}). \tag{7.4}$$

The scattering of these measurement values is small, which is in good accordance to the fact that the series resistance of a battery varies only little within this frequency range and is insensitive to direct current.

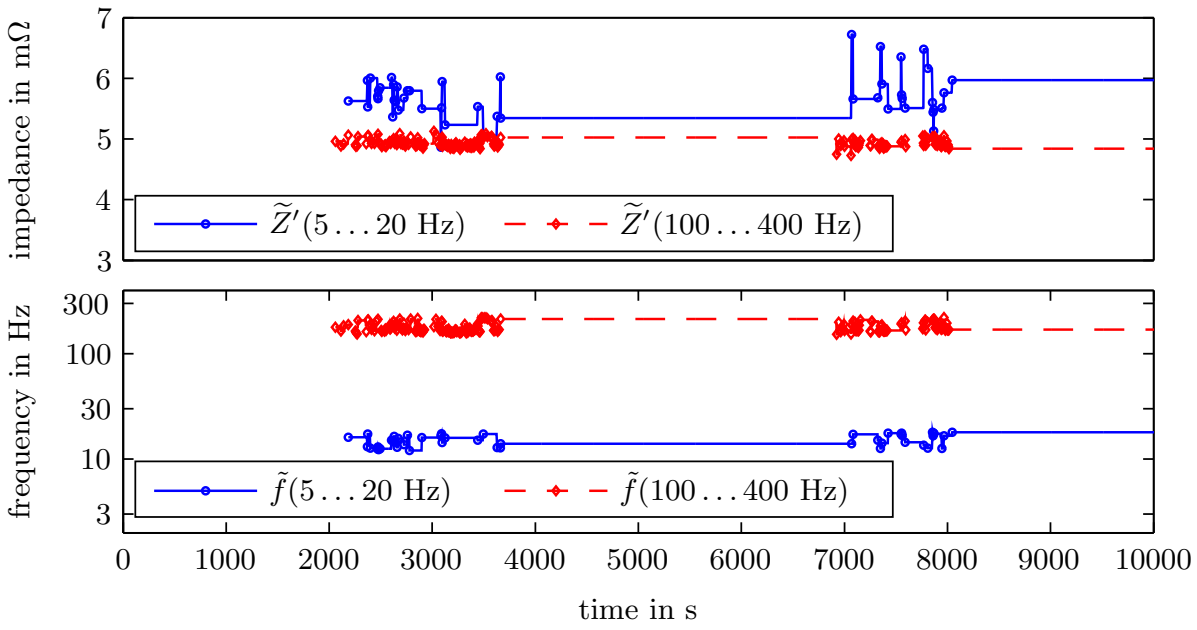

Figure 7.10: Real part of the impedance $\widetilde{Z}'$ (top) and corresponding effective frequency $\tilde{f}$ (bottom) determined by passive impedance measurements in three different frequency ranges. Frequencies shown in the legend are the corner frequencies of 4th order band-pass filters.

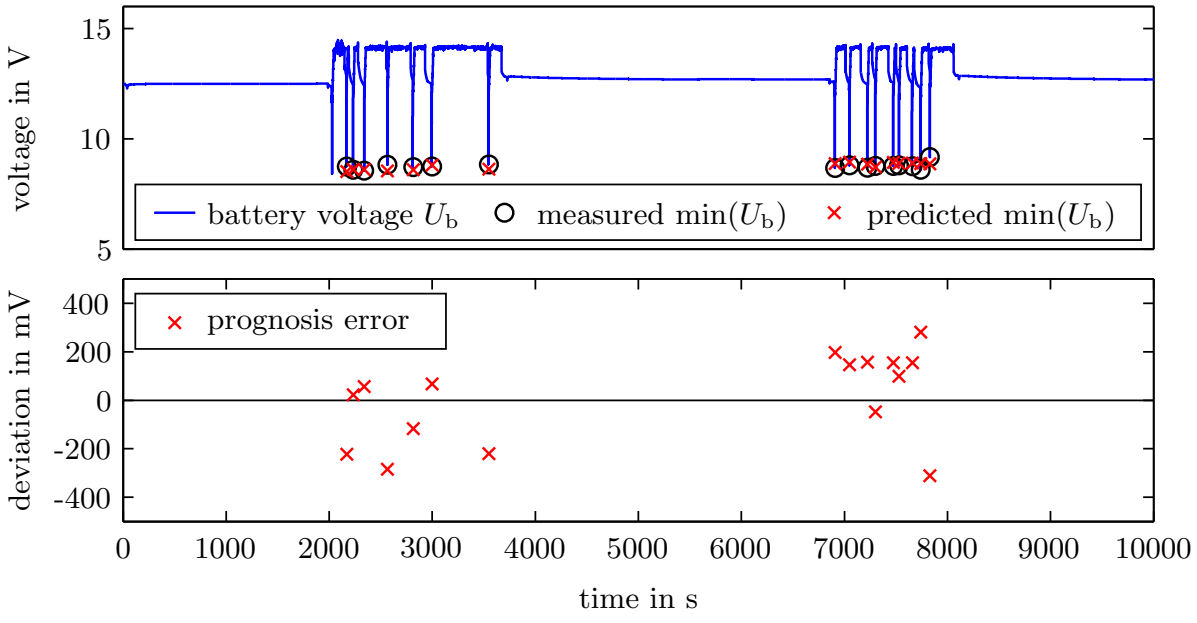

Figure 7.11: Prognosis of the minimum voltage during cranking (top) according to equation 7.2 based on the measured impedance $\widetilde{Z}'(100\ldots400\,\text{Hz}) \approx R_\text{s}$, the measured starter resistance R_cw and the estimated open circuit voltage U_oc. The prognosis error (bottom) is positive if the predicted voltage is higher than the measured voltage.

The frequency limits for the low frequency impedance had to be chosen more tightly, since the impedance for low frequencies changes significantly more with frequency. Yet, the smaller frequency interval causes smaller signal intensity and thus larger measurement errors. The frequency range of 5 to 20 Hz has been chosen as a compromise and centred at a frequency with sufficient ripple current. Still, the scattering is significantly larger than for the high frequency impedance.

The minimum cranking voltage U_{c1} is predicted according to equation 7.2 with $R_s = \widetilde{Z}'(100 \ldots 400\,\mathrm{Hz})$. The result is shown in figure 7.11 and compared to the measured voltage. The deviation of the predicted and the measured values varies in a range of approximately $\pm 300\,\mathrm{mV}$ around zero, which corresponds to less than 5 % of the operating voltage range. The remaining error is the result of an accumulation of the inaccuracies of the estimated open circuit voltage U_{oc}, the starter resistance R_{cw} and the impedance $\widetilde{Z}'(100 \ldots 400\,\mathrm{Hz})$.

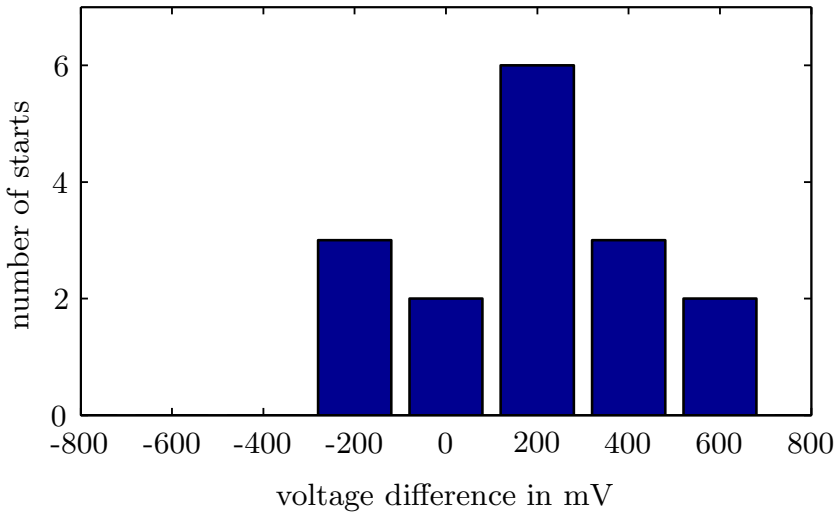

Figure 7.12: Prognosis error of the average voltage during the second cranking phase (cf. figure 7.6 for the drive profile of figure 7.8. The prognosis is based on the current I_2 of the preceding start and equation 7.5.

Due to the large scattering of the low frequency impedance values, a parameterisation of an impedance model is not possible. The voltage during the second cranking phase was therefore predicted according to the simplified prognosis, i.e. the voltage U_{c2} is calculated as

$$U_{c2} = U_{oc} - I_{c2} \cdot \widetilde{Z}'(5 \ldots 20\,\mathrm{Hz}). \tag{7.5}$$

The number of cranking events and the narrow operating range in the drive profile are not sufficient for the parameterisation and adaptation of a characteristic map of I_{c2}. Therefore, for each prognosis the measured current I_{c2} of the preceding start was used.

The deviations of the predicted and measured voltage U_{c2} are shown in figure 7.12. The error distribution is wider than for U_{c1} and shows a systematic error of approximately 200 mV.

Two reasons can be identified for the larger deviations in the second cranking phase. Firstly, the effective measurement frequency was higher than optimal, which explains

the systematic error. At higher frequencies a lower impedance is measured (cf. section 3.2.4) and thus the voltage drop was underestimated. Measurements in a lower frequency band however showed significantly higher measurement errors, since the signal strength was too low. Secondly, the complete parameterisation of an impedance model was not possible, also because impedance values at lower frequencies were not accessible with sufficient accuracy. The direct prognosis based on one impedance value significantly simplifies the processes in a battery during a high rate discharge and consequently exhibits a lower precision. Still, the value of U_{c2} can provide additional information about the cranking performance of the battery, though the prediction is less accurate.

The measurement accuracy at low frequencies could be significantly enhanced if the passive measurement approach is supplemented by actively controlled excitation signals. Such a signal could in principle easily be created by switching electric loads such as the seat heater or the window defroster with a well defined frequency. These signals could be active once in a while and only for a few seconds and thus be unnoticed by the driver. Since the fundamental frequency of such a signal is known very precisely, a narrow bandpass could be used in the algorithm and thus both the signal to noise ratio as well as the accuracy of the measurement frequency could be increased significantly. However, this procedure would require changes in the vehicles main control and could thus not be tested yet.

For a successful cranking, however, the initial voltage drop to U_{c1} is the essential criterion. This value can be predicted based on the real-time measurement of the series resistance of the battery with a precision that is more than sufficient for a reliable prognosis.

With the continuous monitoring of the series resistance of the battery by the passive impedance measurement a very reliable cranking prognosis is possible. The algorithm does not depend on secondary information about the state of charge or state of health, which may be inaccurate. Instead, an increased battery resistance and the corresponding risk of a cranking failure can be detected directly. This is especially useful for vehicles with stop-start automatic, which stop the combustion engine each time the vehicle stops, e.g. at a traffic light. In city traffic with many stop phases, the average load on the battery may be higher than the power supply from the alternator and the battery could reach a critical state. With a cranking prognosis, this state can be detected and, if necessary, the stopping of the engine can be inhibited. In addition, if a permanently increased battery resistance is detected, a maintenance warning can be displayed for the driver.

Chapter 8

Summary and future perspectives

Impedance spectroscopy is a valuable tool for the analysis of electrochemical storage devices. The transformation of the measured time series of voltage and current into the frequency domain provides an alternative view on the available information about the device under test. Describing storage devices by means of electric models based on impedance measurements provides a convenient and effective way of modelling their electric behaviour. The applicability of this approach, however, depends strongly on the system.

The two types of storage devices analysed in this thesis – the electrochemical double-layer capacitor and the lead-acid battery – represent two extremes. The electric behaviour of the double layer capacitor is dominated by one electrostatic process and with a nearly linear characteristic and can thus be described well by an impedance model. Side reactions have virtually no influence on the dynamic behaviour of an EDLC, yet on a large time scale ageing causes changes in the electric behaviour. The ageing model developed in section 5.1 therefore extends the validity range of the impedance model to the lifetime of the device and provides valuable information for the monitoring of these devices.

The lead-acid battery, by contrast, is a complex electrochemical system in which numerous non-linear processes are active in parallel. The characteristic time constants of these processes vary over several orders of magnitude and overlap considerably. A closed description of the electric behaviour of a lead-acid battery for its complete operating range by one impedance model is therefore virtually impossible. One attempt to solve this problem is the combination of impedance models with physical models operating on a time basis [166]. These models are, however, generally too complex for an implementation on battery monitoring systems. The approach followed in section 5.2 therefore was to focus on a special operating mode – high power discharge pulses – and to develop a significantly less complex model with a limited validity range. These models can easily be implemented on a microcontroller and could be parameterised by impedance measurements or characteristic maps.

Monitoring of ageing processes and the prediction of the pulse power performance are only two aspects of battery monitoring. Further important aspects are, amongst others, the determination of the state of charge and the actual capacity of a battery. In chapter 4 the conventional methods as well as the numerous attempts to employ impedance measurements for the different aspects of battery monitoring are discussed

in a literature survey. In all publications and for a wide variety of battery technologies some correlation of impedance with battery state is reported. Yet, these correlations are often ambiguous or so weak compared to other disturbing influences that it is questionable whether they could be distinguished except under laboratory conditions. Still, for special applications such as stand-by batteries where the operating mode is well defined, impedance measurements for battery monitoring have already found their way into applications [49–52, 65].

The requirements for impedance measurements for monitoring systems differ significantly from those for laboratory measurement instrumentation. Monitoring systems have to cope with significant noise and far from ideal measurement conditions and at the same time have to be much more cost efficient. Passive impedance measurements that use the system noise as excitation signal allow reducing the measurement instrumentation to a voltage and current measurement and a digital controller unit. Former approaches for passive impedance measurements however employed either spectral analysis, which requires expensive equipment [127], or simply calculate a resistance value that lacks any information about frequency and phase angle of the impedance [77]. The novel measurement algorithm presented in section 6.2 fills this gap and provides a method that requires few resources on a microcontroller and still provides accurate and extensive information about the battery impedance. The measurement algorithm is based on the calculation of effective values of voltage and current and the average real power, a concept that was first presented for simple resistance measurements on lead-acid batteries by Walter et al. [179]. This concept has been significantly extended by the calculation of modulus and imaginary part of the impedance, the employment of digital band-pass filters that allow flexible definition of frequency ranges and a measurement procedure for the effective frequency. Compared to spectral analysis techniques, the proposed method has a lower frequency resolution, which is however no disadvantage for passive measurements. In contrary, the shifting of the frequency selection into digital filters adds an additional degree of freedom to the algorithm, which allows optimizing the measurement for signals with a blurred and fluctuating frequency spectrum. The calculation of the effective frequency reverts the classical measurement procedure; instead of defining a distinct measurement frequency beforehand, the measurement is extended to a frequency interval and the corresponding 'centre of gravity' of the frequency is determined afterwards. For passive impedance measurements, the measurement conditions cannot be controlled, the quality of the measurement results therefore varies significantly. A good understanding of the factors that influence the accuracy is therefore essential for the design of the system and the selection of the valid measurement values, sections 6.2.6 and 6.2.7 address this issue.

Real-time impedance measurements determine the current state of the storage device; anticipatory energy management, however, requires some information about the battery behaviour in other than the momentary situation. Characteristic maps can provide this information, but since the characteristics of electrochemical storage devices change due to ageing, the maps have to be adapted accordingly. In section 6.3 algorithms for the self-adaptation of characteristic maps are presented, these learning-algorithms can be applied to multi-dimensional look-up-tables or characteristic functions and are not restricted to impedance data.

Two application examples for the application of passive impedance measurements for battery monitoring are given in chapter 7. In section 7.1 the passive impedance measurement technique is applied to the monitoring of EDLCs. The measurement algorithms were implemented on a low-cost controller and tested experimentally on a module of six EDLCs. Measurement errors less than 4 % could be achieved, which is sufficient for the tracking of ageing effects. Moreover, with a variation of the measurement algorithm the distribution of the cell impedances in a stack can be determined even without a current measurement.

For the cranking-capability prognosis presented in section 7.2, the system comprised of battery and starter motor has been analysed. The prediction method that resulted from this analysis combines passive impedance measurements with the estimation of the open circuit voltage and the starter resistance. The algorithm was validated in simulations and with measurement data that was recorded with a modified commercial battery monitoring system, the results can therefore directly be transferred to the application. Deviations in the range of ±300 mV for the lowest voltage during cranking were obtained with the proposed method, which is sufficiently accurate for a system with a nominal voltage of 12 V. The prediction of the further voltage development during cranking showed somewhat larger deviations; it is however also of less importance for the determination of the cranking capability.

The impedance based cranking capability prognosis based on the algorithms presented here is currently brought to series-production readiness by automotive manufacturers and suppliers and will be part of many battery monitoring systems in future vehicles.

The measurement accuracy for EDLC monitoring system could be increased by more accurate measurement instrumentation and a floating point controller, yet at higher system costs. In the current implementation, only one impedance value per cell is evaluated, an extension to more parameters of the impedance model is possible and mainly limited by the measurement accuracy and the available excitation signals.

For the cranking prognosis some improvement could probably also be achieved by higher measurement precision. Especially a higher accuracy for the low-frequency measurements would be necessary to derive more model parameters from the raw impedance values, which is currently not possible. However, in contrary to the 'good-natured' EDLC the complex behaviour of the lead-acid battery significantly contributes to the prediction errors. Even ideal impedance measurements would not eliminate errors that originate from simplified models and the estimation of other parameters such as the cranking current, the starter resistance and the open circuit voltage.

In this thesis impedance based battery monitoring has been dealt with for two types of storage devices and mainly for automotive applications. The concept can be transferred to other applications and technologies. Currently the lithium-ion battery gains importance as a storage device for electric and hybrid electric vehicles. With respect to complexity and non-linearity of its electric behaviour, it is in between the EDLC and the lead-acid battery. The modelling of its electric performance with relatively simple impedance models and the parameterisation of these models by passive impedance measurements therefore seems possible. The passive impedance measurement could be applied to any system with significant current ripple as excitation noise. In principle,

the method is not even restricted to storage devices but could be applied to the monitoring of the impedance of other systems such as cables or electric machines as well. The strength of the method is its ability to use signals that are distributed over a frequency range, whenever distinct excitation frequencies are present – as in the example of a UPS shown in figure 6.5 – a discrete Fourier transformation can be applied.

For battery monitoring system passive impedance measurement is a valuable extension and can provide additional information about the storage device and improve reliability and accuracy. Nonetheless it is not suitable for a stand-alone solution, but should always be combined with other methods for the determination of the battery state that have different strengths and weaknesses.

Bibliography

[1] D. Adams. *Life, the Universe and Everything.* Del Rey, 1995. ISBN 0 345 39182 9.

[2] Allgemeiner Deutscher Automobil-Club. ADAC Statistik Batteriepannen 1996 und 2006 – Was ist mit den Batterien los? [Online]. Available http://www.adac.de, Aug. 2007.

[3] Analog Devices. *ADuC8xx SAR evaluation board reference guide.*

[4] Analog Devices. *Micropower single-supply rail-to-rail input/output op amps OP191/OP292/OP491 (Technical Datasheet)*, 2002.

[5] Analog Devices. *MicroConverter multichannel 12-Bit ADC with embedded flash MCU ADuC7030 (Technical Datasheet)*, 2003.

[6] Analog Devices. *MicroConverter integrated, precision battery sensor ADuC7030 (Preliminary Technical Datasheet)*, 2005.

[7] Analog Devices. *MicroConverter integrated, precision battery sensor ADuC7032 (Preliminary Technical Datasheet)*, 2006.

[8] E. Barsoukov and J. R. Macdonald, editors. *Impedance spectroscopy - theory, experiment, and applications.* John Wiley & Sons, Inc., 2nd edition, 2005.

[9] R. T. Barton and P. J. Mitchell. Estimation of the residual capacity of maintenance-free lead-acid batteries Part 1. Identification of a parameter for the prediction of state-of-charge. *J. Power Sources*, 27(4):287–295, Oct. 1989.

[10] H.-J. Bartsch. *Taschenbuch mathematischer Formeln.* Fachbuchverlag Leipzig im Carl-Hanser-Verlag, München, Wien, 18th edition, 1999. ISBN 3 446 21048 2.

[11] H. Baum. *Autoelektrik, Autoelektronik.* Vieweg Verlag, Braunschweig, 2002. ISBN 3 528 13872 6.

[12] D. Berndt. *Maintenance-free batteries.* Research Studies Press Ltd., 2nd edition, 1977. ISBN 0 86380 198 6.

[13] D. Berndt. *Blei-Akkumulatoren.* VDI-Verlag GmbH, Düsseldorf, 1986. ISBN 3 18 400534 8.

[14] P. Blanchard. Electrochemical impedance spectroscopy of small Ni-Cd sealed batteries: Application to state of charge determinations. *J. Appl. Electrochem.*, V22(12):1121–1128, Dec. 1992.

[15] H. Blanke, O. Bohlen, S. Buller, R. W. De Doncker, B. Fricke, A. Hammouche, D. Linzen, M. Thele, and D. U. Sauer. Impedance measurements on lead-acid batteries for state-of-charge, state-of-health and cranking capability prognosis in electric and hybrid electric vehicles. *J. Power Sources*, 144(2):418–425, June 2005.

[16] H. Blanke, T. Sanders, M. Kiel, T. Baumhöfer, B. Fricke, and D. U. Sauer. EIS-meter - The art of impedance spectroscopy on batteries and fuel cells. In U. Brill and D. U. Sauer, editors, *Impedanzspektroskopie*, volume 99 of *Technische Mitteilungen*, pages 184–188. Haus der Technik, 2006. ISSN 0040 1439.

[17] H. Bode. *Lead-acid batteries*. John Wiley & Sons, 1977. ISBN 0 471 08455 7.

[18] O. Bohlen. Algorithmus zur Bestimmung der Batteriekapazität bei dynamischen Lastprofilen. Diploma thesis, Fachhochschule Oldenburg - Ostfriesland - Wilhelmshafen in Emden, Fraunhofer Institut für Solare Energiesysteme ISE, 2001.

[19] O. Bohlen. Konzepte und Verfahren zur Batteriediagnostik im Fahrzeug. In *Seminar Energiespeicher für Bordnetze und Antriebssysteme*. Haus der Technik, Essen, Feb. 2007.

[20] O. Bohlen, H. Blanke, S. Buller, B. Fricke, A. Hammouche, D. Linzen, M. Thele, R. W. De Doncker, and D. U. Sauer. Battery monitoring for automotive batteries is not a miracle – Some practicable algorithms to identify state-of-function parameters. In *EVS, Internat. Electric Vehicle Symp., 21*, Monaco, 2005.

[21] O. Bohlen, S. Buller, R. De Doncker, M. Gelbke, and R. Naumann. Impedance based battery diagnosis for automotive applications. In *Power Electronics Specialists Conference, 2004. PESC 04. 2004 IEEE 35th Annual*, volume 4, pages 2792–2797, 2004.

[22] O. Bohlen, J. B. Gerschler, D. U. Sauer, P. Birke, and M. Keller. Robust algorithms for a reliable battery diagnosis - managing batteries in hybrid electric vehicles. In *EVS, Internat. Electric Vehicle Symp., 22*, pages 2010–2021, Yokohama, Japan, 2006.

[23] O. Bohlen, A. Hammouche, and D. U. Sauer. Impedanzbasierte Zustandsdiagnose für Energiespeicher in Automobilen. In U. Brill and D. U. Sauer, editors, *Impedanzspektroskopie (1. Symposium Impedanzspektroskopie)*, volume 99 of *Technische Mitteilungen*, pages 88–95. Haus derTechnik, 2006. ISSN 0040-1439.

[24] O. Bohlen, J. Kowal, and D. U. Sauer. Ageing behaviour of electrochemical double layer capacitors: Part I. Experimental study and ageing model. *J. Power Sources*, 172(1):468–475, Oct. 2007.

[25] O. Bohlen, J. Kowal, and D. U. Sauer. Ageing behaviour of electrochemical double layer capacitors: Part II. Lifetime simulation model for dynamic applications. *J. Power Sources*, In Press, Corrected Proof:–, 2007.

[26] O. Bohlen and D. U. Sauer. How to achieve the maximum lifetime for supercapacitors - A quantitative analysis of cell balancing systems and a proposal for improved cell protection concepts. In *22nd Internat. Electric Vehicle Symp., EVS22*, pages 2022 – 2033, Yokohama, Japan, 2006.

[27] G. Bopp, H. Gabler, D. U. Sauer, A. Jossen, W. Höhe, J. Mittermeier, M. Bächler, P. Sprau, B. Willer, and M. Wollny. A systematic effort to define evaluation and performance parameters and criteria for lead-acid batteries in PV systems. In *Proceedings of the 13th European Photovoltaic Solar Energy Conference and Exhibition*, 1995.

[28] B. A. Boukamp. Impedance spectroscopy, strength and limitations (Impedanzspektroskopie, Stärken und Grenzen). *Technisches Messen*, 71(9):454–459, Sept. 2004.

[29] S. Buller. *Impedance-based simulation models for energy storage devices in advanced automotive power systems*. Phd thesis, RWTH Aachen University, Institute for Power Electronics and Electrical Drives ISEA, 2002.

[30] S. Buller, E. Karden, D. Kok, and R. De Doncker. Modeling the dynamic behavior of supercapacitors using impedance spectroscopy. *Industry Applications, IEEE Transactions on*, 38(6):1622–1626, 2002.

[31] S. Buller, M. Thele, R. W. De Doncker, and E. Karden. Impedance-based simulation models of supercapacitors and Li-ion batteries for power electronic applications. *Industry Applications, IEEE Transactions on*, 41(3):742–747, 2005.

[32] K. Bundy, M. Karlsson, G. Lindbergh, and A. Lundqvist. An electrochemical impedance spectroscopy method for prediction of the state of charge of a nickel-metal hydride battery at open circuit and during discharge. *J. Power Sources*, 72(2):118–125, Apr. 1998.

[33] A. Burke. Ultracapacitors: why, how, and where is the technology. *J. Power Sources*, 91:37–50, 2000.

[34] A. Burke, M. Miller, and Z. McCaffrey. The world-wide status and application of ultracapacitors in vehicles: Cell and module performance and cost and system considerations. In *EVS, Internat. Electric Vehicle Symp., 22*, pages 1385–1400, Yokohama, Japan, 2006.

[35] K. Champlin and K. Bertness. Results of discrete frequency immittance spectroscopy (DFIS) measurements of lead acid batteries. In *Telecommunications Energy Conference, 2001. INTELEC 2001. Twenty-Third International*, pages 433–440, 2001.

[36] K. S. Champlin. Method and apparatus for determining battery properties from complex impedance/admittance. US patent US6037777, Mar. 14, 2000.

[37] B. E. Conway. *Electrochemical supercapacitors: scientific fundamentals and technological applications*. Kluwer Academic / Plenum Publishers, New York, 1999. ISBN 0 306 45736 9.

[38] M. Cox and K. Bertness. Vehicle-integrated battery and power system management based on conductance technology to enable intelligent generating systems (inGEN). *Society of Automotive Engineers, Inc.*, (01TB-128), 2002.

[39] M. Cox, K. Bertness, and J. Klang. Field results of battery management technology integration into a vehicle application. *Society of Automotive Engineers, Inc.*, (2002-01-3259), 2002.

[40] M. Cox, P. Bomya, and J. Klang. Aspects of a robust in-vehicle lead-acid battery monitoring system (inGEN). *Society of Automotive Engineers, Inc.*, (03AE-17), 2003.

[41] R. W. De Doncker, A. Hammouche, E. Karden, and B. Fricke. Method and device for determining the charge of a battery. World patent WO2005/031380A1, Apr. 7, 2005.

[42] R. de Levie. On porous electrodes in electrolyte solutions : I. Capacitance effects. *Electrochim. Acta*, 8(10):751–780, Oct. 1963.

[43] R. de Levie. On porous electrodes in electrolyte solutions - IV. *Electrochim. Acta*, 9(9):1231–1245, September 1964.

[44] R. de Levie. The influence of surface roughness of solid electrodes on electrochemical measurements. *Electrochim. Acta*, 10(2):113–130, February 1965.

[45] J.-L. Dellis. easyfit - Fit experimental data is easy. [Online]. Available http://www.mathworks.com/matlabcentral/fileexchange, Feb. 2007.

[46] Deutsches Kupfer-Institut e.V. *Kupfer in der Elektrotechnik - Kabel und Leitungen*, Mar. 2000.

[47] H. Douglas and P. Pillay. Sizing ultracapacitors for hybrid electric vehicles. In *Industrial Electronics Society, 2005. IECON 2005. 32nd Annual Conference of IEEE*, 2005.

[48] EPCOS AG. *UltraCap 600 F / 2.5 V (B49410-A2605-Q000) datasheet*, 2004.

[49] D. Feder, T. Croda, K. Champlin, and M. Hlavac. Field and laboratory studies to assess the state of health of valve-regulated lead acid batteries. I Conductance/capacity correlation studies. In *Telecommunications Energy Conference, 1992. INTELEC '92., 14th International*, pages 218–233, 4-8 Oct. 1992.

[50] D. O. Feder, T. G. Croda, K. S. Champlin, S. J. McShane, and M. J. Hlavac. Conductance testing compared to traditional methods of evaluating the capacity of valve-regulated lead/acid batteries and predicting state-of-health. *J. Power Sources*, 40(1-2):235–250, Dec. 1992.

[51] D. O. Feder, M. J. Hlavac, and W. Koster. Evaluating the state-of-health of flooded and valve-regulated lead/acid batteries. A comparison of conductance testing with traditional methods. *J. Power Sources*, 46(2-3):391–415, 1993.

[52] D. O. Feder, M. J. Hlavac, and S. J. McShane. Updated status of conductance/capacity correlation studies to determine the state-of-health of automotive and stand-by lead/acid batteries. *J. Power Sources*, 48(1-2):135–161, Feb. 1994.

[53] H. Funato, A. Forrai, Y. Yanagita, and Y. Kato. New estimation method of state of batteries based on system identification. In *Diagnostics for Electric Machines, Power Electronics and Drives, 2003. SDEMPED 2003. 4th IEEE International Symposium on*, pages 345–348, 2003.

[54] F. Gallego, J. Bigorra, M. Seguer, J. Sánchez, J. Samitier, M. Puig, and X. Moneo. In-vehicle and lab test of state-of-power monitoring systems for automotive batteries. *SAE Technical Paper Series*, (2001-01-332), 2001. ISSN 0148-7191.

[55] G. Goertzel. An algorithm for the evaluation of of finite trigonometric series. *American Math. Monthly*, 65:34–35, 1958.

[56] M. L. Gopikanth and S. Sathyanarayana. Impedance parameters and the state-of-charge. II. Lead-acid battery. *J. Appl. Electrochem.*, V9(3):369–379, May 1979.

[57] A. Hammouche, E. Karden, and R. W. De Doncker. Monitoring state-of-charge of Ni-MH and Ni-Cd batteries using impedance spectroscopy. *J. Power Sources*, 127(1-2):105–111, Mar. 2004.

[58] B. Hariprakash, S. K. Martha, A. Jaikumar, and A. K. Shukla. On-line monitoring of lead-acid batteries by galvanostatic non-destructive technique. *J. Power Sources*, 137(1):128–133, Oct. 2004.

[59] A. W. Hassel. Impedanzspektroskopie in der Korrosions und Werkstoffforschung. In U. Brill and D. U. Sauer, editors, *Impedanzspektroskopie (1. Symposium Impedanzspektroskopie)*, volume 99 of *Technische Mitteilungen*, pages 43–45. Haus der Technik, 2006. ISSN 0040 1439.

[60] A. Heim. Intelligenter Batteriesensor: Schlüsselkomponente für das Energiemanagement der Zukunft (Intelligent Battery Sensor: Key component of active energy flow control in motor vehicles over the whole product line). In *Elektronik im Kraftfahrzeug (Electronic Systems for Vehicles), 11. Internationale Tagung der VDI - Gesellschaft Fahrzeug- und Verkehrstechnik, Baden-Baden*, volume 1789 of *VDI-Berichte*. VDI-Verlag Düsseldorf, Sept. 2003. ISSN: 0083-5560.

[61] A. Heim. Intelligenter Batteriesensor – Schlüsselkomponente aktiver Energieflussregelung. In *Tagung Energiemanagement und Bordnetze Haus der Technik*, 2004.

[62] Hella KGaA Hueck & Co. *Powermanagement – Der Intelligente Batteriesensor (IBS)*, 2005.

[63] R. Herlt. Verfahren und Vorrichtung zur Überwachung der Leistungsgrenze einer Starterbatterie. German patent DE3808559C2, Apr. 21, 1994.

[64] J. Häffner, B. Frey, M. Merkle, and K. Schiller. Batteriezustandserkennung BZE und Elektronischer Batterie-Sensor EBS. In *Tagung Energiemanagement und Bordnetze im Haus der Technik*, 2004.

[65] M. Hlavac, D. Feder, T. Croda, and K. Champlin. Field and laboratory studies to assess the state of health of valve-regulated lead acid and other battery technologies using conductance testing. In *Telecommunications Energy Conference, 1993. INTELEC '93. 15th International*, volume 2, pages 375–383, 1993.

[66] F. Huet. A review of impedance measurements for determination of the state-of-charge or state-of-health of secondary batteries. *J. Power Sources*, 70(1):59–69, Jan. 1998.

[67] F. Huet, R. Nogueira, P. Lailler, and L. Torcheux. Investigation of the high-frequency resistance of a lead-acid battery. *J. Power Sources*, 158(2):1012–1018, Aug. 2006.

[68] F. Huet, R. P. Nogueira, L. Torcheux, and P. Lailler. Simultaneous real-time measurements of potential and high-frequency resistance of a lab cell. *J. Power Sources*, 113(2):414–421, Jan. 2003.

[69] M. Hughes, R. T. Barton, S. A. G. R. Karunathilaka, and N. A. Hampson. The estimation of the residual capacity of sealed lead-acid cells using the impedance technique. *J. Appl. Electrochem.*, V16(4):555–564, July 1986.

[70] S. A. Ilangovan. Determination of impedance parameters of individual electrodes and internal resistance of batteries by a new non-destructive technique : 2. Theoretical approach. *J. Power Sources*, 50(1-2):33–45, 1994.

[71] Isabellenhütte Heusler GmbH & Co. KG. *Front end data acquisition for battery management system in automotive applications*, 2002.

[72] Isabellenhütte Heusler GmbH & Co. KG. *Preliminary specification for battery management ASIC*, 2002.

[73] Isabellenhütte Heusler GmbH & Co. KG. *Sensor module with IHM-A-1500*, 2002. preliminary data sheet, version 2.0.

[74] R. Isermann. *Identifikation dynamischer Systeme: Besondere Methoden, Anwendungen*, volume 2. Springer Verlag, 2nd edition, 1992. ISBN 3 540 55468 8.

[75] R. Isermann. *Identifikation dynamischer Systeme: Grundlegende Methoden*, volume 1. Springer Verlag, 2nd edition, 1992. ISBN 3 540 54924 2.

[76] R. Isermann. *Digital control systems: fundamentals, deterministic control.* Springer-Verlag, 1998. ISBN 3 540 50266 1.

[77] R. J. Kaiser. *Optimierung eines Batteriemanagementsystems zum Einsatz in photovoltaischen Stromversorgungssystemen.* Phd thesis, Universität Ulm, Fraunhofer Institut für Solare Energiesysteme ISE, 2005.

[78] E. Karden. *Using low-frequency impedance spectroscopy for characterization, monitoring, and modeling of industrial batteries.* Phd thesis, RWTH Aachen University, Institute for Power Electronics and Electrical Drives ISEA, 2001.

[79] E. Karden, S. Buller, and R. W. De Doncker. A frequency-domain approach to dynamical modeling of electrochemical power sources. *Electrochim. Acta*, 47(13-14):2347–2356, May 2002.

[80] Z. Kerner and T. Pajkossy. On the origin of capacitance dispersion of rough electrodes. *Electrochim. Acta*, 46(2-3):207–211, Nov. 2000.

[81] R. Kötz and M. Carlen. Principles and applications of electrochemical capacitors. *Electrochim. Acta*, 45(15-16):2483–2498, May 2000.

[82] R. Kötz, M. Hahn, and R. Gallay. Temperature behavior and impedance fundamentals of supercapacitors. *J. Power Sources*, 154(2):550–555, Mar. 2006.

[83] J. Lagarias, J. A. Reeds, M. H. Wright, and P. E. Wright. Convergence properties of the Nelder-Mead simplex method in low dimensions. *SIAM Journal of Optimization*, 9(1):112–147, 1998.

[84] D. Lahav and J. Appelbaum. Internal impedance of nickel-cadmium batteries with applications to space. *J. Power Sources*, 38(3):295–301, May 1992.

[85] M. Laidig and J. Wurst. Technology implementation of stationary battery failure prediction. In *Battery Conference on Applications and Advances, 1994, Proceedings of the Ninth Annual*, pages 168–172, 1994.

[86] H. Laig-Hörstebrock and E. Meißner. Verfahren zur Bestimmung der Startfähigkeit einer Starterbatterie eines Kraftfahrzeugs. German Patent DE19950424A1, Apr. 26, 2001.

[87] W. Lajnef, J.-M. Vinassa, O. Briat, S. Azzopardi, and C. Zardini. Study of ultracapacitors dynamic behaviour using impedance frequency analysis on a specific test bench. In *Industrial Electronics, 2004 IEEE International Symposium on*, volume 2, pages 839–844, 2004.

[88] D. Linden and T. B. Reddy, editors. *Handbook of batteries.* Mcgraw-Hill Professional, 3rd edition, 2001. ISBN 0 0713 5978 8.

[89] D. Linzen. *Impedance-based loss calculation and thermal modeling of electrochemical energy storage devices for design considerations of automotive power systems.* Phd thesis, RWTH-Aachen University, Institute for Power Electronics and Electrical Drives ISEA, 2006.

[90] D. Linzen, S. Buller, E. Karden, and R. De Doncker. Analysis and evaluation of charge balancing circuits on performance, reliability and lifetime of supercapacitor systems. In *Industry Applications Conference, 2003. 38th IAS Annual Meeting. Conference Record of the*, volume 3, pages 1589–1595, 2003.

[91] P. Liu, M. Verbrugge, and S. Soukiazian. Influence of temperature and electrolyte on the performance of activated-carbon supercapacitors. *J. Power Sources*, 156(2):712–718, June 2006.

[92] A. Lohner. *Batteriemanagement für verschlossene Bleibatterien am Beispiel von Unterbrechungsfreien Stromversorgungen.* Phd thesis, RWTH Aachen, Institute for Power Electronics and Electrical Drives ISEA, 1998. ISBN 3 86073 681 7.

[93] J. R. Macdonald, editor. *Impedance spectroscopy - emphasizing solid materials and systems.* John Wiley & Sons, Inc., 1987. ISBN 0 471 83122 0.

[94] J. R. Macdonald and J. A. Garber. Analysis of impedance and admittance data for solids and liquids. *J. Electrochem. Soc.*, 124(7):1022–1030, 1977.

[95] J.-N. Marie-Francoise, H. Gualous, and A. Berthon. Supercapacitor thermal- and electrical-behaviour modelling using ANN. *Electric Power Applications, IEE Proceedings-*, 153(2):255–262, 2006.

[96] M. F. Mathias and O. Haas. Effect of counterion type on charge transport at redox polymer-modified electrodes. *Journal of Physical Chemistry*, 97(36):9217–9225, 1993.

[97] The Mathworks, Inc. *Documentation for MathWorks products*, Oct. 2006. [Online]. Available http://www.mathworks.com.

[98] Maxwell Technologies. Diehl selects Maxwell Technologies' BOOSTCAP(R) Ultracapacitors to power emergency actuation systems for aircraft doors and slides. press release, Apr. 14, 2005.

[99] Maxwell Technologies SA. *BOOSTCAP 350 F / 2.5 V (BCAP0350-A01) datasheet*, 2004.

[100] R. Mäckel. Trends in der Batterieüberwachung. In *Tagung Energiemanagement und Bordnetze im Haus der Technik*, 2004.

[101] T. Meier, T. Leibecke, C. Eckmann, U. W. Gosch, M. Grossherr, H. P. Bruch, H. Gehring, and S. Leonhardt. Electrical impedance tomography: changes in distribution of pulmonary ventilation during laparoscopic surgery in a porcine model. *Langenbeck's Archives of Surgery*, V391(4):383–389, Aug. 2006.

[102] E. Meißner. Verfahren zur Bestimmung der Leistungsfähigkeit einer Speicherbatterie. German patent DE10107583A1, Aug. 29, 2002.

[103] E. Meissner and G. Richter. Vehicle electric power systems are under change!: Implications for design, monitoring and management of automotive batteries. *J. Power Sources*, 95(1-2):13–23, Mar. 2001.

[104] E. Meissner and G. Richter. Battery monitoring and electrical energy management: precondition for future vehicle electric power systems. *J. Power Sources*, 116(1-2):79–98, July 2003.

[105] H. Michel. Ultracap-Module, leistungsfähige Energiespeicher für Hybridfahrzeuge. In G. für Verkehr Braunschweig e.V., editor, *Hybridfahrzeuge und Energiemanagement*, 2004. ISBN 3 937655 00 X.

[106] S. Nagashima, K. Takahashi, T. Yabumoto, S. Shiga, and Y. Watakabe. Development and field experience of monitoring system for valve-regulated lead-acid batteries in stationary applications. *J. Power Sources*, In Press, Corrected Proof:–, 2006.

[107] R. Naumann. Spannungs-, strom- und impedanzbasierte Methoden der Batteriediagnose: Möglichkeiten und Grenzen. In M. Schöllmann, editor, *Energiemanagement und Bordnetze, Moderne Bordnetzarchitekturen und innovative Lösungen für Energiemanagementsysteme in Kraftfahrzeugen*, volume 41 of *Haus der Technik Fachbuch*, pages 11–32, Essen, Oct. 2004. Expert Verlag.

[108] S. R. Nelatury and P. Singh. Extracting equivalent circuit parameters of lead-acid cells from sparse impedance measurements. *J. Power Sources*, 112(2):621–625, Nov. 2002.

[109] S. R. Nelatury and P. Singh. Equivalent circuit parameters of nickel/metal hydride batteries from sparse impedance measurements. *J. Power Sources*, 132(1-2):309–314, May 2004.

[110] R. Nelms, D. Cahela, and B. Tatarchuk. Modeling double-layer capacitor behavior using ladder circuits. *Aerospace and Electronic Systems, IEEE Transactions on*, 39(2):430–438, 2003.

[111] Nesscap, Ltd. *NESSCAP 600 F / 2.7 V (ESHSP-0600C0-002R7) datasheet*, 2004.

[112] J. Niu, B. E. Conway, and W. G. Pell. Comparative studies of self-discharge by potential decay and float-current measurements at C double-layer capacitor and battery electrodes. *J. Power Sources*, 135(1-2):332–343, Sept. 2004.

[113] J.-R. Ohm and H. D. Lüke. *Signalübertragung*. Springer-Verlag Berlin Heidelberg New York, 9th edition, 2005. ISBN 3 540 22207 3.

[114] J. Olk and M. Rosenmayr. Systematische Entwicklung des Energiemanagements (Systematical Development of Power Management). In *Elektronik im Kraftfahrzeug (Electronic Systems for Vehicles), 11. Internationale Tagung der VDI - Gesellschaft Fahrzeug- und Verkehrstechnik, Baden-Baden*, volume 1789 of *VDI-Berichte*. VDI-Verlag Düsseldorf, Sept. 2003. ISSN: 0083-5560.

[115] A. V. Oppenheim and R. W. Schafer. *Discrete-time signal processing*. Prentice Hall signal processing series. Prentice-Hall, Inc., 1989.

[116] A. V. Oppenheim and R. W. Schafer. *Zeitdiskrete Signalverarbeitung*. Grundlagen der Schaltungstechnik. R. Oldenbourg Verlag München Wien, 2nd edition, 1995. ISBN 3 486 22948 6.

[117] A. K. Padhi, K. S. Nanjundaswamy, and J. B. Goodenough. Phospho-olivines as positive-electrode materials for rechargeable lithium batteries. *J. Electrochem. Soc.*, 144(4):1188–1194, 1997.

[118] T. Pajkossy. Impedance spectroscopy at interfaces of metals and aqueous solutions – Surface roughness, CPE and related issues. *Solid State Ionics*, 176(25-28):1997–2003, Aug. 2005.

[119] Y. H. Pan, V. Srinivasan, and C. Y. Wang. An experimental and modeling study of isothermal charge/discharge behavior of commercial Ni-MH cells. *J. Power Sources*, 112(1):298–306, Oct. 2002.

[120] T. Parks and C. Burrus. *Digital filter design*. Wiley & Sons Inc., 1987. ISBN 0 471 82896 3.

[121] S. Piller, M. Perrin, and A. Jossen. Methods for state-of-charge determination and their applications. *J. Power Sources*, 96(1):113–120, June 2001.

[122] V. Pop, H. J. Bergveld, P. H. L. Notten, and P. P. L. Regtien. State-of-the-art of battery state-of-charge determination. *Meas. Sci. Technol.*, 16:R93–R110, Oct. 2005.

[123] J. E. B. Randles. Kinetics of rapid electrode reactions. *Discuss. Faraday Soc.*, 1:11–19, 1947.

[124] T. Repo, G. Zhang, A. Ryyppo, and R. Rikala. The electrical impedance spectroscopy of Scots pine (Pinus sylvestris L.) shoots in relation to cold acclimation. *J. Exp. Bot.*, 51(353):2095–2107, 2000.

[125] B. W. Ricketts and C. Ton-That. Self-discharge of carbon-based supercapacitors with organic electrolytes. *J. Power Sources*, 89(1):64–69, July 2000.

[126] D. Riu, N. Retiere, and D. Linzen. Half-order modelling of supercapacitors. In *Industry Applications Conference, 2004. 39th IAS Annual Meeting. Conference Record of the 2004 IEEE*, volume 4, pages 2550–2554, 2004.

[127] R. S. Robinson. System noise as a signal source for impedance measurements on batteries connected to operating equipment. *J. Power Sources*, 42(3):381–388, Feb. 1993.

[128] S. Rodrigues, N. Munichandraiah, and A. K. Shukla. AC impedance and state-of-charge analysis of a sealed lithium-ion rechargeable battery. *J. Solid State Electrochem.*, V3(7):397–405, Sept. 1999.

[129] S. Rodrigues, N. Munichandraiah, and A. K. Shukla. A review of state-of-charge indication of batteries by means of a.c. impedance measurements. *J. Power Sources*, 87(1-2):12–20, Apr. 2000.

[130] M. Rothert, B. Willer, C. Schmitz, G. Bopp, D. U. Sauer, and A. Jossen. Verschiedene Ansätze zur Ladezustandsbestimmung. In J. Garche, editor, *Elektrochemische Speichersysteme für regenerative Energieversorgungsanlagen*, pages 211–232. Forschungsverbund Sonnenenergie, 1999. ISSN 0949 1082.

[131] A. J. Salkind, C. Fennie, P. Singh, T. Atwater, and D. E. Reisner. Determination of state-of-charge and state-of-health of batteries by fuzzy logic methodology. *J. Power Sources*, 80(1-2):293–300, July 1999.

[132] J. Samittier Marti, M. Puig Vidal, O. Ruiz Sanchez, D. Guasch Murillo, J. Bigorra Vives, and J. Giro Roca. Method for dynamically measuring the state of health and charge of a car battery and device for implementing said method. US patent US6876174B1, Apr. 5, 2005.

[133] T. Sanders. ISEA EISmeter. internal communication, RWTH Aachen University, Institute for Power Electronics and Electrical Drives ISEA, Jan. 2007.

[134] C. Sarfert. Verfahren zur Zustandserkennung eines Energiespeichers. German patent DE19959019A1, June 13 2001.

[135] C. Sarfert. Verfahren und Vorrichtung zur Zustandserfassung von technischen Systemen wie Energiespeicher. European patent EP1231475A2, Aug. 14, 2002.

[136] S. Sathyanarayana, S. Venugopalan, and M. L. Gopikanth. Impedance parameters and the state-of charge. I. Nickel-cadmium battery. *J. Appl. Electrochem.*, V9(1):125–139, Jan. 1979.

[137] D. U. Sauer. Modelling of local conditions in flooded lead/acid batteries in photovoltaic systems. *J. Power Sources*, 64(1-2):181–187, 1997.

[138] D. U. Sauer. *Optimierung des Einsatzes von Blei-Säure-Akkumulatoren in Photovoltaik-Hybrid-Systemen unter spezieller Berücksichtigung der Batteriealterung*. Phd thesis, Universität Ulm, 2003.

[139] D. U. Sauer and O. Bohlen. Batteriediagnostik und Batteriemonitoring. In P. D.-I. U. Brill, editor, *Neue elektrische Antriebskonzepte für Hybridfahrzeuge*, number 80 in Haus der Technik Fachbuch, chapter 21, pages 339–361. Expert Verlag, 2007. ISBN 978-3-8169-2677-1.

[140] D. U. Sauer, O. Bohlen, T. Sanders, W. Waag, R. Schmidt, and J. Gerschler. Batteriezustanderkennung: Mögliche Verfahrens- und Algorithmenansätze, Grenzen der Batteriezustandserkennung. In M. Schöllmann, editor, *Energiemanagement und Bordnetze II*, pages 1–30. Expert-Verlag, Renningen, 2007. ISBN 13 978-3-8169-2649-8.

[141] D. U. Sauer, G. Bopp, A. Jossen, J. Garche, M. Rothert, and M. Wollny. State of charge - What do we really speak about ? In *Proceedings of the 21st International Telecommunications Energy Conference - INTELEC´99*, 1999.

[142] D. U. Sauer, E. Karden, B. Fricke, H. Blanke, M. Thele, O. Bohlen, J. Schiffer, J. B. Gerschler, and R. Kaiser. Charging performance of automotive batteries–An underestimated factor influencing lifetime and reliable battery operation. *J. Power Sources*, 168:22–30, 2007.

[143] D. U. Sauer, J. Schiffer, M. Thele, and O. Bohlen. Review of monitoring technologies for lead-acid batteries. In *Advanced Automotive Battery Converence, Hawaii*, June 2005.

[144] J. Schiffer. Experiments regarding the self discharge of electrochemical double layer capacitors. internal communication, RWTH Aachen University, Institute for Power Electronics and Electrical Drives ISEA, 2007.

[145] C. A. Schiller, F. Richter, E. Gülzow, and N. Wagner. Relaxation impedance as a model for the deactivation mechanism of fuel cells due to carbon monoxide poisoning. *Phys. Chem. Chem. Phys.*, 3:2113–2116, 2001.

[146] C. A. Schiller, F. Richter, E. Gülzow, and N. Wagner. Validation and evaluation of electrochemical impedance spectra of systems with states that change with time. *Phys. Chem. Chem. Phys.*, 3:374–378, 2001.

[147] C. A. Schiller and W. Strunz. Impedanzmessungen - Sein oder Schein. In U. Brill and D. U. Sauer, editors, *Impedanzspektroskopie*, volume 99 of *Technische Mitteilungen*, pages 12–18. Haus der Technik, 2006. ISSN 0040 1439.

[148] D. Schlichthärle. *Digital filters: basics and design*. Springer Verlag Berlin Heidelberg New York, 2000. ISBN 3 540 66841 1.

[149] W. Schmickler. *Grundlagen der Elektrochemie*. Vieweg, 1996. ISBN 3 528 06755 1.

[150] R. Schmidt. personal communictation, May 2007. Hella KGaA Hueck & Co.

[151] A. Schneuwly, M. Bärtschi, V. Hermann, G. Sartorelli, R. Gallay, and R. Koetz. BOOSTCAP double-layer capacitors for peak power automotive applications. In *AABC (Advanced Automotive Battery Conference)*, pages 1/15–15/15, 2002.

[152] E. Schoch. Verfahren und Anordnung zur Ermittlung der Startfähigkeit einer Starterbatterie eines Verbrennungsmotors. German patent DE10056970A1, May 23, 2002.

[153] E. Schoch. Erfahrungen und Entwicklungslinien von Batteriemanagement und -diagnostiksystemen. In *Seminar Energiespeicher für Bordnetze und Antriebssysteme, Essen*, Mar. 2007.

[154] F. Schöpe. *Batteriemanagement für Nickel-Cadmium Akkumulatoren*. Phd thesis, RWTH Aachen, Institute for Power Electronics and Electrical Drives ISEA, 1994. ISBN 3 86073 232 3.

[155] S. Seki, Y. Kobayashi, H. Miyashiro, A. Yamanaka, Y. Mita, and T. Iwahori. Degradation mechanism analysis of all-solid-state lithium polymer secondary batteries by using the impedance measurement. *J. Power Sources*, 146(1-2):741–744, Aug. 2005.

[156] P. Singh, C. Fennie, and D. Reisner. Fuzzy logic modelling of state-of-charge and available capacity of nickel/metal hydride batteries. *J. Power Sources*, 136(2):322–333, Oct. 2004.

[157] P. Singh and D. Reisner. Fuzzy logic-based state-of-health determination of lead acid batteries. In *Telecommunications Energy Conference, 2002. INTELEC. 24th Annual International*, pages 583–590, 29 Sept.-3 Oct. 2002.

[158] P. Singh, R. Vinjamuri, X. Wang, and D. Reisner. Fuzzy logic modeling of EIS measurements on lithium-ion batteries. *Electrochim. Acta*, 51(8-9):1673–1679, Jan. 2006.

[159] V. Srinivasan, J. W. Weidner, and J. Newman. Hysteresis during cycling of nickel hydroxide active material. *J. Electrochem. Soc.*, 148(9):A969–A980, Sept. 2001.

[160] B. Staib. Innovation UltraCap from EPCOS. In *Seminar Energiespeicher für Bordnetze und Antriebssysteme, Essen*, 2005.

[161] W. Steffens. *Verfahren zur Schätzung der inneren Größen von Starterbatterien.* Phd thesis, RWTH Aachen University, Institute for Power Electronics and Electrical Drives ISEA, 1987.

[162] K. P. Ta and J. Newman. Proton intercalation hysteresis in charging and discharging nickel hydroxide electrodes. *J. Electrochem. Soc.*, 146(8):2769–2779, Aug. 1999.

[163] P.-L. Taberna, G. Chevallier, P. Simon, D. Plee, and T. Aubert. Activated carbon-carbon nanotube composite porous film for supercapacitor applications. *Mater. Res. Bull.*, 41(3):478–484, Mar. 2006.

[164] P. L. Taberna, C. Portet, and P. Simon. Electrode surface treatment and electrochemical impedance spectroscopy study on carbon/carbon supercapacitors. *Applied Physics A: Materials Science & Processing*, 82(4):639–646, Mar. 2006.

[165] K. Takeno, M. Ichimura, K. Takano, J. Yamaki, and S. Okada. Quick testing of batteries in lithium-ion battery packs with impedance-measuring technology. *J. Power Sources*, 128(1):67–75, Mar. 2004.

[166] M. Thele. *A contribution to the modelling of the charge acceptance of lead-acid batteries – using frequency and time domain based concepts.* Phd thesis, RWTH Aachen University, Institute for Power Electronics and Electrical Drives ISEA. personal communication.

[167] M. Thele, O. Bohlen, D. U. Sauer, and E. Karden. Development of a voltage-behavior model for NiMH batteries using an impedance-based modeling concept. *J. Power Sources*, 175(1):635–643, Jan. 2008.

[168] M. Thele, S. Buller, D. Sauer, R. De Doncker, and E. Karden. Hybrid modeling of lead-acid batteries in frequency and time domain. *J. Power Sources*, 144(2):461–466, June 2005.

[169] M. Thele, E. Karden, E. Surewaard, and D. Sauer. Impedance-based overcharging and gassing model for VRLA/AGM batteries. *J. Power Sources*, 158(2):953–963, Aug. 2006.

[170] M. Thele, J. Schiffer, E. Karden, E. Surewaard, and D. Sauer. Modeling of the charge acceptance of lead-acid batteries. *J. Power Sources*, 168(1):31–39, May 2007.

[171] U. Tietze and C. Schenk. *Halbleiter-Schaltungstechnik*. Springer Verlag Berlin Heidelberg New York, 11th edition, 1999. ISBN 3 540 42849 6.

[172] U. Tietze and C. Schenk. *Electronic circuits - handbook for design and application*. Springer Berlin, Heidelberg, New York, 2nd edition, 2006. ISBN 3 540 00429 7.

[173] J. Tinnemeyer. Fuzzy logic method and apparatus for battery state of health determination. US patent US7072871B1, July 4, 2006.

[174] J. A. Tinnemeyer. Multiple model impedance spectroscopy techniques for testing electrochemical systems. *J. Power Sources*, 136(2):246–249, Oct. 2004.

[175] U. Tröltzsch. *Modellbasierte Zustandsdiagnose von Gerätebatterien*. Phd thesis, Universität der Bundeswehr München, Fakultät für Elektrotechnik und Informationstechnik, 2005.

[176] M. Verbrugge and E. Tate. Adaptive state of charge algorithm for nickel metal hydride batteries including hysteresis phenomena. *J. Power Sources*, 126(1-2):236–249, Feb. 2004.

[177] V. V. Viswanathan, A. J. Salkind, J. J. Kelley, and J. B. Ockerman. Effect of state of charge on impedance spectrum of sealed cells Part I: Ni-Cd cells. *J. Appl. Electrochem.*, V25(8):716–728, Aug. 1995.

[178] V. V. Viswanathan, A. J. Salkind, J. J. Kelley, and J. B. Ockerman. Effect of state of charge on impedance spectrum of sealed cells Part II: Lead acid batteries. *J. Appl. Electrochem.*, V25(8):729–739, Aug. 1995.

[179] J. Walter, S. Buller, E. Karden, F. Gronwald, S. Schröder, and R. W. D. Doncker. Nützliche Störungen: Batteriediagnose mit Hilfe von Bordnetzstörungen und Impedanzspektroskopie Useful Noise: Battery-diagnostics using existing noise and impedance spectroscopy. In *VDI-Tagung Elektronik im Kraftfahrzeug Baden-Baden*, 2001.

[180] B. Wu, M. Mohammed, D. Brigham, R. Elder, and R. E. White. A non-isothermal model of a nickel-metal hydride cell. *J. Power Sources*, 101(2):149–157, Oct. 2001.

[181] T. Yamazaki, K. Sakurai, and K. Muramoto. Estimation of the residual capacity of sealed lead-acid batteries by neural network. In *Telecommunications Energy Conference, 1998. INTELEC. Twentieth International*, pages 210–214, 1998.

[182] S. Yoon, J. H. Jang, B. H. Ka, and S. M. Oh. Complex capacitance analysis on rate capability of electric-double layer capacitor (EDLC) electrodes of different thickness. *Electrochim. Acta*, 50(11):2255–2262, Apr. 2005.

[183] Y. F. Zhong and P. Singh. Fuzzy logic modeling of on-line impedance measurements on VRLA batteries at different temperatures. In *EVS, Internat. Electric Vehicle Symp., 20*, pages 1–10, 2003.

Appendix

A.1 Literature survey

Table 1: Direct impedance parameters for battery state

characteristic impedance values	state var.	reference	comment
transition frequency $f_{\pm}$	SOC	[15] [41] [57]	The transition frequency is the frequency at which $Z''(f_{\pm}) = 0$; it is correlated to the double layer capacitance and thus to active electrode surface.
resistance $R_{\pm} = \lvert\underline{Z}(f_{\pm})\rvert$	SOC	[67]	Flooded lead-acid battery (2 V, 45 Ah, tubular plates, CEAC-Exide). Discussion of a possible correlation of resistance fluctuations with SOC.
$\lvert\underline{Z}(0.237\,\mathrm{Hz})\rvert$ and $\arg(\underline{Z}(1.0\,\mathrm{Hz}))$ at $I_{\mathrm{DC}} = 0$	SOC	[158]	Li-ion battery packs (Sanyo 18650) for defibrillators. Impedance data analysis by fuzzy logic. SOC is defined as a remaining number of current pulses.
$\lvert\underline{Z}(0.237\,\mathrm{Hz})\rvert$, $\arg(\underline{Z}(0.56\,\mathrm{Hz}))$ and $\arg(\underline{Z}(36.6\,\mathrm{Hz}))$ at $I_{\mathrm{DC}} = 0$	SOH	[158]	Li-ion battery packs (Sanyo 18650) for defibrillators. Impedance data analysis by fuzzy logic. SOC is defined as a remaining number of charge/discharge cycles.
$\lvert\underline{Z}(158.5\,\mathrm{Hz})\rvert$ and $\arg(\underline{Z}(15.85\,\mathrm{Hz}))$ at $I_{\mathrm{DC}} = 0$	SOC	[157]	Lead-acid battery packs (2.5 Ah) for defibrillators. Impedance data analysis by fuzzy logic. SOC is defined as a remaining number of defined current pulses.
$\lvert\underline{Z}(103\,\mathrm{Hz})\rvert$ and $\arg(\underline{Z}(10.2\,\mathrm{Hz}))$ at $I_{\mathrm{DC}} = 0$	SOC	[157]	Sealed lead-acid battery packs (Hawker 2.5 Ah) for UPS. Impedance data analysis by fuzzy logic. SOC is defined as a remaining number of defined current pulses.

Continued on next page...

Table 1 – continued

characteristic impedance values	state var.	reference	comment
$Z'(10\,\mathrm{Hz})$, $Z'(3981.1\,\mathrm{Hz})$, $Z'(251.1\,\mathrm{Hz})$, $Z''(10\,\mathrm{Hz})$ and $Z''(251\,\mathrm{Hz})$ at $I_{\mathrm{DC}} = 0$	SOC/C	[156]	NiMH batteries (Sanyo 2.7 Ah). Impedance data analysis by fuzzy logic. Determination of SOC and full charge capacity C from the same set of input parameters.
$\lvert\underline{Z}(37.1\,\mathrm{Hz})\rvert$ and $\arg(\underline{Z}(5.042\,\mathrm{kHz}))$ at $I_{\mathrm{DC}} < 0$ (discharge)	SOC	[183]	Sealed lead-acid battery packs (Hawker 2.5 Ah). Impedance data analysis by fuzzy logic.
$\Re\{\underline{Z}^{-1}\}(10\,\mathrm{Hz})$ and $\Re\{\underline{Z}^{-1}\}(25\,\mathrm{Hz})$ at $I_{\mathrm{DC}} = 0$	C/SOH	[49] [65]	Flooded and sealed lead-acid batteries with high capacities. UPS application. The conductance is defined as the real part of the complex admittance $\underline{Z}^{-1}$.
$\arg(\underline{Z})$, equivalent series and parallel resistance at $f = 0.006 \ldots 0.9\,\mathrm{Hz}$	SOC	[129] [177] [178]	NiCd-batteries and lead-acid batteries.
$\lvert\underline{Z}(90\,\mathrm{Hz})\rvert$, $\lvert\underline{Z}(190\,\mathrm{Hz})\rvert$ and $\lvert\underline{Z}(570\,\mathrm{Hz})\rvert$ at $I_{\mathrm{DC}} \geq 0$ (open circuit and charging)	SOC	[84]	NiCd-batteries (7 Ah Saft VO7S4). Linear correlation, but less than 10 % impedance change for the complete SOC range. Measurements at different temperatures, charging currents and ageing states.
$\arg(\underline{Z})$, equivalent series and parallel resistance at $f = 10 \ldots 100\,\mathrm{Hz}$ and $I_{\mathrm{DC}} = 0$	SOC	[56]	Lead-acid batteries (gelled electrolyte, 7.5 Ah). Change of the charge transfer resistance identified as main influence on the impedance.
$\arg(\underline{Z})$, equivalent series and parallel resistance at $f = 10 \ldots 30\,\mathrm{Hz}$ and $I_{\mathrm{DC}} = 0$	SOC	[136]	NiCd-batteries (4 Ah). Change of the double-layer capacitance identified as main influence on the impedance.

Continued on next page...

Table 1 – continued

characteristic impedance values	state var.	reference	comment
$\lvert\underline{Z}(1\,\mathrm{Hz})\rvert$ at $I_{\mathrm{DC}} \neq 0$	SOC	[129] [14]	Small NiCd-batteries (0.85 Ah). Correlation found for constant charge and discharge conditions. Correlation is ambiguous if the cell is overcharged.
equivalent series capacitance at $f = 0.025 \ldots 0.5\,\mathrm{Hz}$ at $I_{\mathrm{DC}} = 0$	SOC	[128, 129]	Li-Ion battery blocks (7.2 V, 1.25 Ah).
impedance spectrum for $f = 0.6 \ldots 239\,\mathrm{Hz}$ at $I_{\mathrm{DC}} \leq 0$ (open circuit and discharge)	SOC	[32]	Small NiCd cells (Varta VH2100, 2.4 Ah). Correlation of impedance spectra to SOC by means of partial least squares (PLS) method.
$\lvert\underline{Z}(1\,\mathrm{kHz})\rvert$ at $I_{\mathrm{DC}} = 0$	SOH/C	[165]	Lithium-ion battery packs for cell phones. Extensive study on 800 devices of 10 types in fresh and deteriorated condition.

Table 2: Impedance model parameters for battery state

model	model parameter	state var.	reference	comment
series connection of two RC parallel-circuits plus series resistance and inductance	capacitance of first RC-circuit, conductance (R^{-1}) of second RC-circuit	SOC	[35]	Lead-acid batteries. Interpretation of capacitance as ionic double layer capacitance, conductance associated with the exchange current, both at the negative electrode.
series connection of two RC parallel-circuits plus series resistance	series resistance	SOC	[53]	NiCd batteries. Pseudo-random binary signal and square-wave current as excitation.
series connection of two RC parallel-circuits plus series resistance	series resistance	SOC	[58]	Lead-acid batteries (6 V/4 Ah VRLA). Useful correlation restricted to SOC below 20 % and above 90 %.
Modified Randle's circuit with CPE elements	ohmic resistance, charge transfer resistance, double-layer capacitance	SOC	[129] [177] [178]	NiCd-batteries and lead-acid batteries. Good correlations for NiCd-batteries only over limited SOC ranges.
Series resistance plus RC-circuit	ohmic resistance, charge transfer resistance, double-layer capacitance	SOC	[14] [66] [129]	Small NiCd-batteries (0.85 Ah). Correlation found for constant charge and discharge conditions. Correlation is ambiguous if the cell is overcharged.
Randle's circuit	time constant $\tau = R_{\mathrm{ct}} \cdot C_{\mathrm{dl}}$	SOC	[66] [69]	Sealed lead-acid batteries (2.5 Ah). Analysis of fresh and aged cells, characteristic of τ over SOC similar for both types but shifted.

Continued on next page...

Table 2 – continued

model	model parameter	state var.	reference	comment
Set of different impedance models	different model parameters	SOC, CCA	[174]	Lead-acid batteries (SLI). CCA is *cold cranking amps* according to SAE J537 standard. The algorithm implemented in a commercial device (*Cadex Spectro*) and fits spectra to all models and selects valid models depending on the quality of the fit. The model parameters for SOC or SAE are evaluated according to an internal library.

A.2 Cranking of a combustion engine

The process of cranking can be subdivided into several steps. With the turning of the key an electric contact is closed that connects the battery to the solenoid switch. The solenoid switch connects the starter motor mechanically to the engine and closes the electric contact for the starter motor. At this moment the engine and the starter are still at halt. In most passenger cars the starter motor is a permanent magnet machine, thus at halt no induction voltage is present and the load to the battery is only the resistance and the inductance of the cables and the windings of the machine. The current increases within a few milliseconds until it reaches its peak value, as can be seen in figure 1 (left) at $t = 0$.

The torque of a permanent magnet machine is proportional to current, when current reaches its peak value the torque is also at its maximum and can overcome the initial breakaway torque. Thereupon the engine accelerates until the first compression occurs. This is followed by several compression cycles that cause a pronounced torque and current ripple (cf. figure 1 (left) for $0.1\,\mathrm{s} < t < 0.6\,\mathrm{s}$). The average torque and consequently also the average current during this phase of cranking is relatively constant. When the engine is self-propelling it eventually overtakes the starter, thus the starter torque and current drop to near zero. Finally the reset spring of the solenoid switch mechanically disconnects the starter from the engine and opens the electric contact. Engine speed increases further and the generator starts charging the battery ($t > 0.9\,\mathrm{s}$ in figure 1 (left)) [11].

From a mechanical point of view cranking is successful if the necessary engine speed is reached and maintained long enough. This requires a certain torque of the starter motor that compensates the hold-back torque of the engine. Both torque and speed cannot be maintained simultaneously if the battery voltage drops too low. Figure 1 (right) shows the battery voltage and current for a cranking attempt with a deep discharged battery. The initial breakaway torque could be overcome, yet the necessary engine speed is not reached because the battery voltage under load is too low. The cranking attempt ends

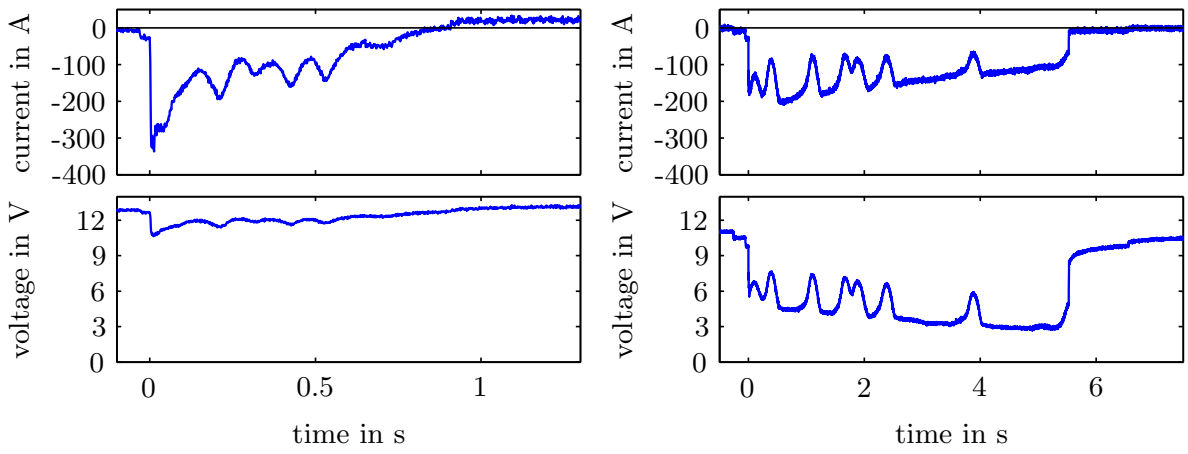

Figure 1: Battery current and voltage during cranking in a compact car (VW Polo, petrol engine). The battery (MOLL Kamina 70 Ah) was fully charged for the successful start (left) and deep discharged for the failed cranking (right), both at room temperature.

unsuccessful after more than five seconds.

In modern vehicles the problem has shifted more to the electrical side. If the battery voltage drops below a certain threshold, electronic systems in the vehicle may stop operating or malfunction. This threshold voltage is defined by the car manufacturer, a typical value is 7.5 V. This fact simplifies the cranking prognosis to a certain degree; the main criterion for a successful cranking is that the voltage during the first high current peak does not drop below the threshold voltage.

For a better understanding of the currents and voltages during cranking a system with a permanent magnet machine as starter motor shall be analysed briefly. The momentum of a permanent magnet motor can be expressed as

$$M = c_1 \cdot B \cdot l_{\mathrm{Fe}} \cdot d \cdot I = c_{\mathrm{M}} \cdot I, \tag{1}$$

with the starter torque M, the magnetic induction B caused by the permanent magnets, the length of the magnetic path l_{Fe} in the iron, the diameter d of the rotor, a constant c_1 determined by the number of poles and the geometry of the rotor and the current I. For a permanent magnet motor B is a machine constant as well, so the factor $c_1 \cdot B \cdot l_{\mathrm{Fe}} \cdot d$ can be summarised by the constant c_{M}.

The induced voltage in the rotor is

$$U_{\mathrm{ind}} = 2\pi \cdot c_2 \cdot B \cdot l_{\mathrm{Fe}} \cdot d \cdot n = c_{\mathrm{U}} \cdot n \tag{2}$$

with a second geometry factor c_2 and the rotary speed n; the term $2\pi \cdot c_2 \cdot B \cdot l_{\mathrm{Fe}} \cdot d$ can be subsumed to a constant c_{U}. The battery voltage U_{b} during cranking equals the induction voltage plus the voltage drop across the cable and winding resistance R_{cw} and the voltage drop U_{br} across the carbon brushes[1]:

$$U_{\mathrm{b}} = R_{\mathrm{cw}} \cdot I + U_{\mathrm{br}} + U_{\mathrm{ind}}. \tag{3}$$

Inserting equations 1 and 2 into equation 3 allows expressing the battery voltage as a function of rotor speed and torque:

$$U_{\mathrm{b}} = \frac{R_{\mathrm{cw}}}{c_{\mathrm{M}}} \cdot M + U_{\mathrm{br}} + c_{\mathrm{U}} \cdot n \tag{4}$$

The battery voltage required for a certain torque and a certain rotary speed is thus a linear combination of characteristic machine constants with torque and rotary speed and a constant voltage drop across the carbon brushes.

The necessary rotary speed can be assumed relatively constant for a certain engine, the torque however depends strongly on the viscosity of the machine oil and hence on temperature. Oil viscosity decreases with sinking temperature; at low temperatures the required torque is therefore significantly higher than at moderate temperatures. Additionally, at low temperatures the battery performance is low due to the increased electrolyte resistance, which explains why most cranking failures occur at cold weather.

The induction voltage at an initial rotary speed $n = 0$ is $U_{\mathrm{ind}} = 0$, the current can therefore be calculated from equation 3:

$$I_{\mathrm{c1}} = \frac{U_{\mathrm{b}} - U_{\mathrm{br}}}{R_{\mathrm{cw}}}. \tag{5}$$

[1]The voltage drop across the carbon brushes is approximately 1.2 V each, i.e. 2.4 V for plus and minus pole together, and relatively independent of current [11].

The cable and winding resistance is relatively fixed for a given vehicle. The change of the resistance with temperature can be compensated for using the temperature coefficient of the electrical conductivity of copper ($\alpha_{\mathrm{Cu}} = 0.0039\,\mathrm{K}^{-1}$ [46]). The duration Δt_{c1} of the first phase is in the range of a few 10 milliseconds.

The second phase of the cranking pulse can be approximated by a constant current discharge, where the current I_{c2} depends only on the necessary cranking torque M_{crank} according to equation 1:

$$I_{\mathrm{c2}} = \frac{M_{\mathrm{crank}}}{c_{\mathrm{M}}}. \tag{6}$$

The estimation of I_{c2} is more difficult than the determination of the inrush current, since the motor torque does not only depend strongly on temperature, but also on the type, quality and age of the motor oil. Moreover, I_{c2} is not constant but exhibits a significant ripple. In a simplified cranking pulse, as shown in section 7.2.1, figure 7.6, I_{c2} represents an average over the duration of the second cranking phase. The duration Δt_{c2} of the second phase varies, yet in a modern vehicle successful cranking last less than one second.

A.3 List of symbols

Conventions:

$\underline{x}$	complex number
x'	real part of $\underline{x}$
x''	imaginary part of $\underline{x}$
$\vec{x}$	vector
$\mathbf{X}$	matrix

Symbols:

a	place holder for an arbitrary model parameter
a_{init}	initial value of an arbitrary model parameter
$a_{1\ldots l}$	feedback coefficients of a digital filter
a_h	polynomial coefficient of a smoothing function h
a'_h	polynomial coefficient of a smoothing function h centred at the current operating point
a_i	activity of a reactant
$a_{i_{\text{end}}}$	activity of an end product of a chemical reaction
$a_{i_{\text{start}}}$	activity of a starting material of a chemical reaction
$a_{i_{\text{end}}}$	activity of an end product of an electrochemical reaction
$a_{i_{\text{start}}}$	activity of a starting product of an electrochemical reaction
a_{lin}	constant element of a linear approximation of the modulus of the impedance
a'_{lin}	constant element of a linear approximation of the real part of the impedance
a_{new}	polynomial coefficient after adaptation
b	auxiliary variable of the Goertzel-algorithm
$b_{0\ldots k}$	feed-forward coefficients of a digital filter
b_h	polynomial coefficient of a smoothing function h
b'_h	polynomial coefficient of a smoothing function h centred at the current operating point
$b_{k,\text{new}}$	polynomial coefficient after adaptation
b'_{lin}	constant factor of a linear approximation of the real part of the impedance
b_{lin}	constant factor of a linear approximation of the modulus of the impedance
c	concentration of ions in the electrolyte
c_0	constant concentration of ions in the electrolyte
c_1	geometry factor constant of an electric machine
c_2	geometry factor constant of an electric machine
c_a	relative ageing rate of a double layer capacitor at nominal conditions
c_h	polynomial coefficient of a smoothing function h
c'_h	polynomial coefficient of a smoothing function h centred at the current operating point

$c_{k,\mathrm{new}}$	polynomial coefficient after adaptation
c_{M}	electric machine constant that links torque and current
c_{neg}	ion concentration at the negative electrode
$c_{\mathrm{neg},0}$	ion concentration at the negative electrode at equilibrium
c_{pos}	ion concentration at the positive electrode
$c_{\mathrm{pos},0}$	ion concentration at the positive electrode at equilibrium
c_T	ageing parameter of a double layer capacitor related to temperature
c_{U}	electric machine constant that links voltage and rotary speed
c_{U}	ageing parameter of a double layer capacitor related to voltage
d	rotor diameter of an electric machine
d	polynomial coefficient
f	frequency
$\tilde{f}$	effective frequency, where the approximated values $\widetilde{Z}'$ and $\widetilde{Z}^2$ are identical with real impedance values
f_{c}	corner frequency of a filter
f_{h}	high frequency (several 100 Hz)
f_{p}	frequency that corresponds to a pulse duration Δt_{p}
f_{s}	sample frequency
$f_{\pm}$	transition frequency
i	instantaneous current
$\tilde{i}$	bandlimited current signal
$\widehat{i}$	amplitude of a sinusoidal current signal
$\underline{i}_0$	current at the pore mouth ($x = 0$)
i_{dc}	direct current
$i_{\mathrm{dc,max}}$	lower threshold direct current
$i_{\mathrm{dc,min}}$	upper threshold direct current
i_{err}	current signal with measurement error
i_{leak}	leakage current
δi	time derivative of the current $\delta i \equiv \frac{\mathrm{d}i}{\mathrm{d}t}$
Δi	current difference from one time step to the next
j	complex variable $j = \sqrt{-1}$
j	current density
j_0	exchange current density
j_i	number of equivalents of one reactant involved in a reaction
$j_{i_{\mathrm{end}}}$	number of equivalents of an end product of an electrochemical reaction
$j_{i_{\mathrm{start}}}$	number of equivalents of a starting product of an electrochemical reaction
k	integer number
k_I	quotient of the maximum and the average current squared, $k_I = \max(i^2(t))/I_{\mathrm{rms}}^2$
$k_{I,\mathrm{max}}$	upper threshold of k_I
k_γ	optimization factor for the approximation of CPE behaviour by RC-circuits
l	integer number
l	pore length
l_{Fe}	length of the magnetic path in an electric machine
n	integer number

n	number of electrons involved in a reaction
p	instantaneous power
$\tilde{p}$	bandlimited instantaneous power signal
r_i	relative measurement error (tolerance) of current
r_u	relative measurement error (tolerance) of voltage
$r_{C\mathrm{dl}}$	relative error of the model parameter C_{dl}
r_{DZ}	relative error of Z'',Z'' or $\lvert Z\rvert$ caused by a finite discrete sampling
$r_{R\mathrm{el}}$	relative error of the model parameter R_{el}
$r_{R\mathrm{s}}$	relative error of the model parameter R_{s}
$r_{R,\lvert Z\rvert}$	relative error for the approximation of the model parameters R_{s} and R_{el} by a measurement of $\lvert Z\rvert$
r_{TI^2}	relative error of I^2_{rms} caused by a finite integration time
r_{TP}	relative error of P caused by a finite integration time
r_{TU^2}	relative error of U^2_{rms} caused by a finite integration time
r_{TZ}	relative error of Z'',Z'' or $\lvert Z\rvert$ caused by a finite integration time
r_{TZ^2}	relative error of Z^2 caused by a finite integration time
$r_{TZ'}$	relative error of Z' caused by a finite integration time
$r_{TZ''}$	relative error of Z'' caused by a finite integration time
$r_{T\widetilde{\omega}^2_{\mathrm{sqr}}}$	relative error of $\widetilde{\omega}^2_{\mathrm{sqr}}$ caused by a finite integration time
r_Z	relative error of Z'',Z'' or $\lvert Z\rvert$
$r_{\Delta t}$	relative measurement error due to a synchrony error
s	scaling coefficient of a digital filter
s	random noise signal
s_i	random current noise signal
s_u	random voltage noise signal
t	time
t_{eq}	equivalent ageing time
Δt	synchrony error, time lag between current and voltage measurement
Δt_{c1}	duration of the first phase of a simplified cranking pulse
Δt_{c2}	duration of the second phase of a simplified cranking pulse
Δt_{p}	pulse duration
u	instantaneous voltage
$\tilde{u}$	bandlimited voltage signal
$\widehat{u}$	amplitude of a sinusoidal voltage signal
$\underline{u}_0$	voltage at the pore mouth ($x = 0$)
u_{dc}	direct voltage
$u_{\mathrm{dc,max}}$	lower threshold direct voltage
$u_{\mathrm{dc,min}}$	upper threshold direct voltage
u_{err}	voltage signal with measurement error
Δu	voltage difference from one time step to the next
w'	weighting factor for least squares fitting
w''	weighting factor for least squares fitting
x	arbitrary (input) signal
$\vec{x}_{1\ldots N}$	base vector of a look-up table

$\vec{x}_0$	current operating point
y	arbitrary (output) signal
y	complex (output) signal
y	arbitrary characteristic
$\vec{y}_0$	true characteristic value at $\vec{x}_0$
Δy	local prediction error
z	basic element of the z-transform
z_x	impedance values per unit length of a pore along the pore axis
z_y	impedance values per unit length of a pore perpendicular to the pore axis
$\tilde{z}$	relative impedance (with respect to the average of several cells) determined in a limited frequency range
A_{dl}	magnitude of a constant-phase element (CPE)
$A_{\max}$	maximum input range of a quantiser (analogue-to-digital converter)
A_{eff}	effective internal surface of the electrode
B	number of bits of a quantiser (analogue-to-digital converter)
B	magnetic induction
C	capacitance
C	battery capacity
C_{20}	battery capacity for a 20 hour discharge ($C_{20} = I_{20} \cdot 20\,\mathrm{h}$)
C_{av}	available battery capacity at nominal current and temperature
C_{dl}	double-layer capacitance
$C_{\mathrm{dl},0}$	double-layer capacitance of a new device
C_{p}	parallel capacitance
C_{s}	series capacitance
C_{N}	nominal battery capacity current and temperature
C_{OP}	operational battery capacity
$C_{\mathrm{OP,av}}$	operational capacity available at nominal current and temperature
D	diffusion constant
DI^2_{rms}	mean square value of the time derivative of the current
$\widetilde{DI}^2_{\mathrm{rms}}$	DI^2_{rms} in a limited frequency band
E_{a}	activation energy
$\mathcal{F}\{\ldots\}$	Fourier transform
ΔG	Gibbs free energy
ΔG_{S}	Gibbs free energy at standard conditions (all activities equal to zero)
ΔG_{end}	Gibbs free energy of an end product of a chemical reaction
$\Delta G_{\mathrm{start}}$	Gibbs free energy of a starting material of a chemical reaction
$\underline{H}$	complex transfer function
$\mathbf{H}$	look-up table of the smoothing function
$\underline{H}_I$	complex transfer function of a filter for a current signal
$\underline{H}_U$	complex transfer function of a filter for a voltage signal
ΔH	enthalpy
I	current
$\underline{I}$	complex current spectrum
$\overline{I}$	mean value of the current, current offset
I_0	exchange current of the Butler-Volmer equation

I_{20}	20 hour discharge current of a battery ($I_{20} = C_{20}/20\,\mathrm{h}$)
I_{c1}	current during the first phase of cranking
I_{c2}	current during the second phase of cranking
I_{rms}	root mean square value of a current signal
$I_{rms,dist}$	root mean square value of a current signal disturbed by random noise
$I_{rms,err}$	root mean square value of a current signal with measurement error
$I_{rms,min}$	threshold for the root mean square value of a current signal
$\widetilde{I}_{rms}$	root mean square value of a bandlimited current signal
I_{start}	current during the cranking
I_{CHA}	charging current
I_{DC}	direct current
I_{DCH}	discharging current
I_N	nominal (discharge) current
L_s	series inductance
M	torque
M	integer constant
M_{crank}	cranking torque necessary for starting the combustion engine
N	integer constant
$\mathbf{P}$	set of parameters
$\overline{P}$	average effective power
$\widetilde{I}_{rms}$	effective power of bandlimited current and voltage signals
$\overline{P}_{dist}$	average power calculated from signals disturbed by random noise
$\overline{P}_{err}$	average power calculated from signals with measurement error
$\overline{P}_{\Delta t}$	average power calculated from signals with synchrony error Δt
Q_{dch}	amount of charge discharged from a full battery
$Q_{dch,av}$	Q_{dch} discharged at nominal temperature and with nominal current
$\Re\{\cdot\}$	real part of $\cdot$
R	resistance
R_{am}	resistance of the active mass
R_{ct}	charge transfer resistance
$R_{ct,0}$	charge transfer resistance for very small currents
$R_{ct,DCH}$	charge transfer resistance for discharge currents
R_{cw}	cable and winding resistance of a starter motor
R_{el}	resistance of electrolyte in pores
$R_{el,0}$	resistance of electrolyte in pores of a new device
R_k	non-linear series resistance (pulse power impedance model)
R_p	parallel resistance
R_s	series resistance
$R_{s,0}$	series resistance of a new device
R_{LS}	large-signal resistance
$R_{\pm}$	series resistance at the transition frequency $f_{\pm}$
$R_{\Delta u/\Delta i}$	internal resistance calculated from $\Delta u(t)/\Delta i(t)$
$R_{du/di}$	limit of $R_{\Delta u/\Delta i}$ for $\Delta t \to 0$
S	noise power
S_i	current noise power
S_u	voltage noise power

SNR	signal to noise ratio
SNR_i	signal to noise ratio of the current measurement
SNR_u	signal to noise ratio of the voltage measurement
SOC	state of charge
SOC_{av}	available state of charge at nominal current and temperature
SOC_{OP}	operational state of charge
$SOC_{\mathrm{OP,av}}$	operational state of charge available at nominal current and temperature
SOC_{N}	state of charge referred to the nominal capacity C_{N}
S_{Q}	quantisation noise power
ΔS	entropy
T	time interval, integration interval, time between sampled values
T	absolute temperature
ΔT	temperature difference, parameter of the ageing function
U	voltage
$\underline{U}$	complex voltage spectrum
$\overline{U}$	mean value of the voltage, voltage offset
U_0	voltage parameter of the ageing function
U_0	equilibrium potential
$U_{0,\mathrm{S}}$	equilibrium potential at standard conditions
U_{b}	battery voltage
U_{br}	voltage drop across the brushes of a permanent magnet motor
U_{c1}	voltage during the first phase of cranking
U_{c2}	voltage during the second phase of cranking
U_{fresh}	lowest voltage during a discharge profile of a fresh battery
U_{ind}	induced voltage in an electric machine
U_{low}	lower voltage limit
U_{min}	lowest voltage during a discharge profile
U_{oc}	open circuit voltage
U_{r}	rated voltage of a device
U_{rms}	root mean square value of a voltage signal
$U_{\mathrm{rms,dist}}$	root mean square value of a current signal disturbed by random noise
$U_{\mathrm{rms,err}}$	root mean square value of a current signal with measurement error
$U_{\mathrm{rms,min}}$	threshold for the root mean square value of a current signal
$\widetilde{U}_{\mathrm{rms}}$	root mean square value of a bandlimited current signal
$\underline{U}_{\Delta t}$	voltage spectrum measured with synchrony error Δt with respect to current
U_{N}	nominal battery voltage
ΔU_{ct}	charge transfer overpotential
$\Delta U_{\mathrm{ct,DCH}}$	charge transfer overpotential for discharge currents
ΔU_{con}	concentration overpotential
ΔU_{dif}	diffusion overpotential
ΔU_{s}	resistive overpotential
ΔU	voltage difference, parameter of the ageing function
$\underline{X}$	complex spectrum of an arbitrary (input) signal

$\underline{X}$	denominator of a transfer function
$\underline{Y}$	complex spectrum of an arbitrary (output) signal
$\underline{Y}$	numerator of a transfer function
$\mathbf{Y}$	look-up table of a characteristic map
$\mathbf{Y}_{\mathrm{new}}$	updated value of $\mathbf{Y}$
$\underline{Z}$	complex impedance $\underline{Z} = Z' + jZ''$
Z'	real part of the complex impedance $\underline{Z}$
Z''	imaginary part of the complex impedance $\underline{Z}$
$\widetilde{Z}$	complex impedance averaged over a limited frequency range
$\underline{Z}_{\mathrm{dist}}$	impedance calculated from signals disturbed by random noise
$\underline{Z}_{\mathrm{err}}$	impedance calculated from signals with measurement error
$\underline{Z}_{\mathrm{e}}$	measured impedance value
$\underline{Z}_{\mathrm{m}}$	impedance value from a model
$\underline{Z}_{\mathrm{p}}$	pore impedance of an EDLC
$\underline{Z}_{\mathrm{pg}}$	generalized pore impedance
$\underline{Z}_{\mathrm{EDLC}}$	impedance of an electrochemical double layer capacitor
$\underline{Z}_{\mathrm{EDLC,std}}$	impedance of an EDLC according to the standard model
$\underline{Z}_{\mathrm{RCp}}$	impedance of a parallel RC-circuit
$\underline{Z}_{\mathrm{RCs}}$	impedance of a series RC-circuit
$\underline{Z}_{\mathrm{W}}$	Warburg impedance
$\underline{Z}_{\mathrm{W}}$	Warburg impedance
$\underline{Z}_{\mathrm{W}\infty}$	Warburg impedance for semi-infinite diffusion
$\underline{Z}_{\mathrm{ZARC}}$	impedance of a ZARC-element
$\lvert Z_{\mathrm{ZHIT}}\rvert$	modulus of the impedance calculated by the Z-HIT transform
$\underline{Z}_{\Delta t}$	impedance calculated from signals with synchrony error Δt
$\widetilde{\underline{Z}}_{\Delta t}$	$\underline{Z}_{\Delta t}$ averaged over a limited frequency range
α	symmetry factor of the Butler-Volmer equation
γ_k	correction factor of the Z-HIT
γ	exponent of a constant-phase element (CPE)
δi	time derivative of a current signal $\delta i = \mathrm{d}i/\mathrm{d}t$
$\widetilde{\delta i}$	time derivative of a band limited current signal
ν	integration variable of the angular frequency ω
ν	number of moles of ions
ω	angular frequency $\omega = 2\pi \cdot f$
$\widetilde{\omega}$	effective angular frequency, $\widetilde{\omega} = 2\pi\widetilde{f}$
$\widetilde{\omega}_{\mathrm{sqr}}$	effective angular frequency for a quadratic approximation of the impedance
ω_l	lower boundary angular frequency of a bandlimited signal
ω_s	start angular frequency for the calculation of the Z-HIT
ω_s	end angular frequency for the calculation of the Z-HIT
ω_u	upper boundary angular frequency of a bandlimited signal
ϕ	phase angle $\phi = \arg(\underline{Z})$
ϕ	electric potential

σ	parameter that defines the width of of a Gauss curve
σ_{err}	standard deviation of errors
$\sigma_{Z'}$	standard deviation of the real part of measured impedance values
$\sigma_{Z''}$	standard deviation of the imaginary part of measured impedance values
φ	constant phase shift, phase angle of a signal at $t = 0$
τ	integration variable of time t
ζ	Riemann Zeta function
Δ	step size of a quantiser (analogue-to-digital converter)
Ω	standardized frequency $\Omega = \omega(R_{\mathrm{el}}A_{\mathrm{dl}})^{1/\gamma}$

A.4 List of constants

e	=	1.6021773	$\cdot 10^{-19}$	As	elementary charge
F	=	9.6485341	$\cdot 10^{4}$	As/mol	Faraday constant ($F = N_{\mathrm{A}} \cdot e$)
N_{A}	=	6.0221367	$\cdot 10^{23}$	mol^{-1}	Avogadro number
R_{m}	=	8.314510		$\mathrm{J\ mol^{-1}\ K^{-1}}$	universal gas constant

A.5 List of abbreviations

ADC	Analogue to Digital Converter
ASIC	Application-Specific Integrated Circuit
AGM	Absorbed Glass Mat
ANN	Artificial Neural Network
CAN	Controller Area Network
CCA	Cold Cranking Amps
CNLS	Complex Non-linear Least Squares (fit)
CPE	Constant Phase Element
dBFS	deciBel Full Scale (unit)
DFT	Discrete Fourier Transform
DOD	Depth Of Discharge
EDLC	Electrochemical Double-Layer Capacitor
EV	Electric Vehicle
FFT	Fast Fourier Transform
FIR	Finite Impulse Response (filter)
HEV	Hybrid Electric Vehicle
HIT	Hilbert Transform
IIR	Infinite Impulse Response (filter)
KK	Kramers-Kronig (transform)
LIN	Local Interconnect Network
LTI	Linear Time-Invariant (system)
MCU	Micro Controller Unit
NiCd	Nickel-Cadmium (battery)
NiMH	Nickel-Metal-Hydride (battery)
OCV	Open-Circuit Voltage
PCB	Printed Circuit Board
PGA	Programmable Gain Amplifier
PLS	Partial Least Squares (analysis)
PTFE	PolyTetraFluoroEthylene
RMS	Root Mean Square
RC	Resistor-Capacitor (parallel circuit)
SLI	Starting-Lighting-Ignition (battery)
SNR	Signal-to-Noise Ratio
SOC	State Of Charge
SOF	State Of Function
SOH	State Of Health
SRAM	Static Random Access Memory
UPS	Uninterruptible Power Supply
VRLA	Valve-Regulated Lead-Acid (battery)
ZARC	Resistor in parallel with a CPE-element

A.6 Deutsche Zusammenfassung

Kapitel 1: Einleitung

Elektrische Energiespeicher gewinnen immer mehr an Bedeutung in der Automobiltechnik. Zum einen hat die Belastung der konventionellen Starterbatterie durch die zunehmende Elektrifizierung moderner Fahrzeuge stark zugenommen, zum anderen wird der Energiespeicher in Elektro- und Hybridfahrzeugen ein essentieller Bestandteil des Antriebsstrangs. Ein sicherer Betrieb der Batterie ist nur möglich, wenn ihr innerer Zustand zu jedem Zeitpunkt während des Betriebs bekannt ist. Hierzu sind Batterieüberwachungssysteme notwendig.

Die vorliegende Dissertation befasst sich mit dem Einsatz der Impedanzmessung - eines Verfahrens, das unter Laborbedingungen seit langem zur Diagnose von elektrischen und elektrochemischen Systemen verwendet wird - in Batterieüberwachungssystemen.

Kapitel 2: Impedanzspektroskopie

Impedanzspektroskopie ist ein Messverfahren, mit dem sich die elektrische Übertragungsfunktion, die Impedanz, eines Systems bestimmen lässt. Hierzu wird ein sinusförmiger Strom der Frequenz f in das zu untersuchende System eingeprägt und die Spannungsantwort gemessen. Aus dem Verhältnis der Amplituden und der Phasenverschiebung des Ein- und Ausgangssignals lässt sich die komplexe Impedanz $\underline{Z}(f)$ ermitteln.

Elektrochemische Systeme wie Batterien weisen in der Regel nichtlineares Verhalten auf. Um die Impedanzspektroskopie dennoch anwenden zu können, wird während der Messung ein Gleichstrom überlagert, durch den der Arbeitspunkt eingestellt wird. Hierbei muss jedoch darauf geachtet werden, dass ein quasi-stationärer Zustand eingehalten wird. Bei nichtlinearen Systemen ist die Unterscheidung von Groß- und Kleinsignalverhalten wichtig, dies wird anhand der Butler-Volmer-Charakteristik einer elektrochemischen Reaktion erläutert.

Für nicht-sinusförmige Anregungssignale und für den Fall, dass durch Nichtlinearitäten Oberwellen entstehen, müssen Ein- und Ausgangssignal durch geeignete Verfahren in den Frequenzbereich transformiert werden. Soll dies nur für wenige Frequenzen geschehen, sind digitale Verfahren wie die Diskrete Fourier-Transformation oder der Goertzel-Algorithmus geeignet, deren Grundlagen erläutert werden.

Um die Grundlagen für die Interpretation der experimentellen Ergebnisse zu schaffen, werden die Messtechnik, das Messverfahren sowie typische Darstellungsweisen der gemessenen Impedanzspektren erläutert. Darüber hinaus wird mit der Z-HIT ein Verfahren beschrieben, mit dem sich die Gültigkeit der Messung überprüfen lässt.

Kapitel 3: Elektrochemische Energiespeicher

Zwei Technologien werden in der vorliegenden Arbeit detailliert behandelt: der Elektrochemische Doppelschichtkondensator und die Blei-Säure-Batterie.

Im Doppelschichtkondensator geschieht die Energiespeicherung im Wesentlichen im elektrischen Feld, das sich an der Grenzschicht zwischen Elektrode und Elektrolyt –

der elektrochemischen Doppelschicht - aufbaut. Doppelschichtkondensatoren mit hoher Leistungsdichte werden heute aus hochporösen Kohlenstoff-Elektroden aufgebaut, die auf Ableitern aus Aluminium-Folie aufgebracht und gewickelt sind. Als Elektrolyt dienen Salze in organischen Lösungsmitteln wie Acetonitril.

Das elektrische Verhalten von Doppelschichtkondensatoren lässt sich sehr gut mit Impedanzmodellen beschreiben. Ein wesentlicher Bestandteil des Standard-Modells ist die Porenimpedanz, die sich im Frequenzbereich durch einen analytischen Ausdruck darstellen und als elektrisches Ersatzschaltbild durch einen Kettenleiter modellieren lässt. Im Gegensatz zum Standardmodell erkennt man in Messungen bei niedrigen Frequenzen keinen Übergang zum Verhalten eines idealen Kondensators, sondern einen konstanten Phasenwinkel der Impedanz kleiner als 90°. Um dieses charakteristische Verhalten gut abbilden zu können, wurde das Standard-Modell so modifiziert, dass eine sehr gute Übereinstimmung zwischen Modell und Messung im gesamten untersuchten Frequenzbereich besteht.

Die Bleibatterie stellt ein deutlich komplexeres elektrochemisches System dar. Im Gegensatz zum Doppelschichtkondensator wird nur ein sehr kleiner Teil der Energie im elektrischen Feld der Doppelschicht gespeichert. Der größte Teil der Energiewandlung geschieht elektrochemisch durch die Umwandlung sowohl der Elektrodenmaterialien als auch des Elektrolyten. Das elektrische Verhalten der Bleibatterie wird bestimmt durch die Gleichgewichtsspannung, die wesentlich durch die Konzentration des Elektrolyten und damit den Ladezustand bestimmt wird, und einer Überlagerung verschiedener Überspannungen. Neben der Überspannung durch den Widerstand der Elektroden und des Elektrolyten verursachen die Reaktionen an den Grenzflächen sowie Transportprozesse im Elektrolyten und in den porösen Elektroden Potentialdifferenzen, die im Gegensatz zur Widerstandsüberspannung nichtlinear mit dem Strom verknüpft sind. Diese Effekte lassen sich in weiten Teilen ebenfalls durch elektrische Ersatzschaltbilder modellieren. Hierbei müssen jedoch langsame Ausgleichsprozesse und Effekte der räumlichen Verteilung der Reaktionen teilweise vernachlässigt werden. Das grundlegende Ersatzschaltbild einer Elektrode wird dargestellt und die Zusammenhänge der Modellparameter mit physikalischen Größen erläutert.

Erst mit der Kenntnis der zugrunde liegenden physikalischen und elektrochemischen Prozesse lassen sich die Ergebnisse von Impedanzmessungen an Batterien und Doppelschichtkondensatoren richtig interpretieren und auch die Grenzen der impedanzbasierten Analyse erkennen.

Kapitel 4: Batteriediagnose und Batterieüberwachung

Der Zustand einer Batterie ist durch eine Vielzahl innerer Größen bestimmt. Für technische Anwendungen interessieren jedoch vor allem die makroskopischen Kenngrößen Kapazität, Ladezustand, Leistungsfähigkeit und Alterungszustand. Für diese Größen werden Definitionen angegeben und deren Bedeutung für die Batteriediagnose und das Batteriemanagement erläutert. Ebenso werden die klassischen Verfahren für deren Bestimmung vorgestellt.

Eine umfassende Literaturrecherche befasst sich zudem mit der Impedanzmessung zur Bestimmung von Zustandsgrößen verschiedener Batterietechnologien. Für alle gängigen Batterietypen, die in Fahrzeugen zum Einsatz kommen, werden in der Literatur

charakteristische Zusammenhänge zwischen einzelnen Impedanzwerten oder Modellparametern und den Zustandsgrößen, wie dem Ladezustand und der Kapazität der Batterie, beschrieben. Häufig werden diese Zusammenhänge jedoch von anderen Effekten so stark überlagert, dass sie für praktische Anwendungen nur bedingt nutzbar sind. Die vorliegende Arbeit konzentriert sich daher auf Untersuchungen zur Leistungsfähigkeit und zum Alterungszustand, zweier Größen die eng mit der Impedanz der verknüpft sind.

Es existieren bisher nur sehr wenige kommerzielle Systeme, die Impedanzmessungen zur Zustandsbestimmung nutzen. Diese arbeiten mit aktiver Anregung und erfordern daher eine spezielle Messtechnik. Daher wird in Kapitel 6 ein passives Messverfahren vorgeschlagen, das nur geringe Anforderungen an die Messtechnik stellt.

Kapitel 5: Impedanzanalyse unter Laborbedingungen

Für den Doppelschichtkondensator und die Blei-Säure-Batterie wurde je ein Aspekt der impedanzbasierten Diagnose und Modellierung detailliert ausgearbeitet. Die Änderung des elektrischen Verhaltens von Doppelschichtkondensatoren aufgrund von Alterungsprozessen wurde systematisch in beschleunigten Alterungstests untersucht.

Abbildung 5.1 zeigt die Impedanzspektren eines Doppelschichtkondensators, der bei erhöhter Temperatur und Spannungslage über mehrere Wochen gelagert wurde. Die Veränderung der Impedanzspektren und damit die Verschlechterung der elektrischen Eigenschaften lassen sich durch Veränderung der Parameter des in Kapitel 3 erläuterten Impedanzmodells gut beschreiben. Auf Basis der Ergebnisse von Untersuchungen an drei verschiedenen Typen kommerziell verfügbarer Doppelschichtkondensatoren wurde ein Alterungsmodell entwickelt, mit dessen Hilfe sich die charakteristischen Veränderungen der Modellparameter aus den Spannungs- und Temperaturverläufen während des Betriebs bestimmen lassen. Die Kenntnis der charakteristischen Veränderungen der Modellparameter kann darüber hinaus zur gezielten Beobachtung dieser Kennwerte durch ein Zellüberwachungssystem genutzt werden.

Hierzu wird ein vereinfachtes Messverfahren vorgestellt und die Genauigkeit dieses Verfahrens in Abhängigkeit der Messfrequenz analytisch bestimmt.

Für die Blei-Säure-Batterie wurden Modelle zur Bestimmung der Hochstromfähigkeit, basierend auf elektrischen Ersatzschaltbildern, entwickelt. Hierzu wurde bei verschiedenen Ladezuständen und Temperaturen systematisch sowohl das elektrische Verhalten bei Pulsbelastung untersucht als auch Impedanzmessungen durchgeführt. Mithilfe der Impedanzmodelle lässt sich der zeitliche Verlauf der Batteriespannung bei Pulsbelastung sehr gut nachbilden. Diese Modelle können mithilfe von Impedanzmessungen parametriert werden, jedoch müssen dabei wesentliche Unterschiede im Klein- und Großsignalverhalten der Batterien berücksichtigt werden. Abbildung 5.12 zeigt den gemessenen Spannungsverlauf während eines Startvorgangs in einem Kleinwagen sowie die entsprechenden Simulationsergebnisse. Zum Vergleich sind ebenfalls diejenigen Ergebnisse dargestellt, die sich bei der Simulation mit einem einfachen ohmschen Innenwiderstand (R) und mit einem Ersatzschaltbild bestehend aus nur einem Serienwiderstand und einem RC-Glied (R-RC) ergeben.

Für die Prognose des Spannungseinbruchs bei Pulsbelastung wird zudem ein vereinfachtes Verfahren vorgeschlagen, dass Impedanzmesswerte direkt mit dem Spannungseinbruch nach einer bestimmten Pulsdauer korreliert. Hierzu wurden umfangreiche Mess-

reihen an unterschiedlichen Starterbatterien bei verschiedenen Ladezuständen und Temperaturen durchgeführt und ausgewertet.

Kapitel 6: Algorithmen für die Batterieüberwachung

Um die Rahmenbedingungen für eine Impedanzmessung im Fahrzeug aufzuzeigen, werden typische Stromprofile in verschiedenen Anwendungen miteinander verglichen und der prinzipielle Aufbau eines Mikrocontroller-basierten Batteriesensors, wie er Stand der Technik ist, dargestellt. Der Einsatz von Impedanzmessungen zur Batterieüberwachung im Kraftfahrzeug beschränkt sich bisher auf sehr wenige Beispiele. Serienmäßig wird die klassische Impedanzspektroskopie bisher nicht im Kraftfahrzeug eingesetzt, da die notwendige Messtechnik zu aufwändig und störanfällig wäre. Daher wurde im Rahmen dieser Arbeit ein Messverfahren ausgearbeitet, das rein passiv arbeitet und vorhandene Bordnetzstörungen als Signalquelle nutzt. Dadurch ist das Verfahren sehr robust und stellt nur geringe Anforderungen an die Messtechnik und die Rechenleistung des Batterieüberwachungs-Systems.

Das Verfahren basiert auf der Berechnung der Effektivwerte von Batteriestrom und -spannung sowie der mittleren Wirkleistung in einem bestimmten Frequenzbereich. Der Frequenzbereich wird hierbei durch digitale Filter eingestellt, in Abbildung 6.7 als Bandpass bezeichnet. Aus den Effektivwerten und der Wirkleistung lassen sich direkt das Betragsquadrat und der Realteil der Impedanz bestimmen, aus diesen Größen wiederum auch der Betrag des Imaginärteils.

Da sich die Breite der digitalen Bandpassfilter frei einstellen lässt, können mit diesem Verfahren auch Signale ausgewertet werden, die über einen Frequenzbereich "verwischt" sind oder deren Frequenz sich zeitlich ändert. Solche Signale finden sich häufig in Automobil-Bordnetzen. Da diese Frequenzunschärfe des Verfahrens für die Auswertung der Messwerte problematisch wäre, wurde zudem ein Verfahren entwickelt, mit dem sich eine effektive Frequenz bestimmen lässt, die dem quadratisch gewichteten Schwerpunkt des Spektrums entspricht. Somit wird im Gegensatz zur klassischen Impedanzmessung zunächst die Impedanz in einem relativ breiten Frequenzbereich gemessen und im Nachhinein die zugehörige Messfrequenz bestimmt.

Das hier beschriebene Verfahren wird mathematisch hergeleitet. Aus dieser theoretischen Beschreibung wurden die Genauigkeiten für verschiedene Rahmenbedingungen wie Messdauer, Abtastrate und Synchronität der Spannungs- und Strommessung bestimmt. Zudem wird der Einfluss verschiedener Störgrößen und Messfehler analytisch diskutiert. Geeignete digitale Filter werden in einem eigenen Abschnitt beschrieben. Da sich bei passiven Messverfahren die Messbedingungen nicht beeinflussen lassen, werden häufig ungenaue oder fehlerhafte Messwerte ermittelt. Der Bewertung der Messsignale und der Auswahl gültiger Messwerte ist daher ebenfalls ein eigener Abschnitt gewidmet.

Ein Vergleich mit gängigen Messverfahren der Spektralanalyse zeigt, dass das vorgestellte Verfahren dann vorteilhaft ist, wenn zum einen unscharfe oder zeitlich veränderliche Anregungssignale vorliegen und zum anderen die Ressourcen der Messtechnik und Datenverarbeitung beschränkt sind. Beides ist in Anwendungen im Automobilbereich der Fall.

Durch die passive Impedanzmessung kann der momentane Zustand des Speichers bestimmt werden; um die Charakteristik des Systems im gesamten Arbeitsbereich dar-

stellen zu können, sind zusätzlich Kennfelder notwendig. Weil sich die Eigenschaften elektrochemischer Systeme durch Alterungsprozesse stetig ändern, führen starre Kennfelder zwangsläufig mit der Zeit zu falschen Ergebnissen. Da diese Änderungen jedoch verhältnismäßig langsam vonstatten gehen, können Kennfelder nachgeführt werden. Zu diesem Zweck wurden effiziente und robuste Verfahren entwickelt, die aus dem Vergleich des realen Systems und des Kennfelds vorhandene Kennfelder adaptieren. Hierzu werden Ausgleichsfunktionen verwendet, durch die die Kennfelder nicht nur im aktuellen Arbeitspunkt nachgeführt werden, sondern auch in Arbeitsbereichen, in denen nur selten Messpunkte zur Verfügung stehen. Das Verfahren unterdrückt zudem den Einfluss einzelner Ausreißer und ist daher robust gegen Messfehler. Abbildung 6.22 zeigt schematisch den Ablauf des Nachlernens am Beispiel einer einfachen Kennlinie. Als Ausgleichsfunktion wird hier eine Gauß-Kurve verwendet, die die alte Kennlinie am momentanen Arbeitspunkt am stärksten nachführt. Mit zunehmendem Abstand zum momentanen Messwert nimmt auch der Einfluss der Ausgleichsfunktion ab.

Neben einem Verfahren für Kennfelder, die als Wertetabelle abgelegt sind, wurde ein Verfahren zum Nachlernen polynomischer Kennfelder entwickelt. Hierbei werden die Polynomkoeffizienten direkt nachgeführt – dieses Verfahren lässt sich daher besonders effizient auf Controllern mit wenig Speicherplatz implementieren.

Kapitel 7: Impedanzbasierte Batterieüberwachung in Kraftfahrzeugen

Die konkrete Umsetzung der passiven Impedanzmessung zur Batterieüberwachung wird abschließend anhand zweier Beispiele erläutert und experimentell belegt. Hierzu werden die beiden Schwerpunktthemen aus Kapitel 5, die Alterung von Doppelschichtkondensatoren und die Pulsleistungsfähigkeit von Blei-Säure-Batterien wieder aufgegriffen.

Auf einem Energiespeicher-Modul, bestehend aus Doppelschichtkondensatoren und einer Überwachungselektronik, wurde das passive Impedanz-Messverfahren implementiert. Kern des Messsystems ist ein 8-bit Mikrocontroller, mit dessen AD-Wandlern die Spannungs- und Stromwerte erfasst und auf dem die notwendigen Berechnungen durchgeführt werden. Als digitales Filter zur Frequenzauswahl wurde ein Bandpass erster Ordnung mit Eckfrequenzen bei 17 und 53 Hz verwendet

Abbildung 7.3 zeigt die mit diesem System gemessenen Innenwiderstände der sechs Zellen. Als Testsignale wurden rechteckförmige Stromverläufe mit verschiedenen Frequenzen verwendet. Der Innenwiderstand der einzelnen Zellen kann mit diesem sehr günstigen Messsystem mit Abweichungen von 2 bis 4 % – je nach Anregungssignal – bestimmt werden. Im normalen Betrieb ist somit die Überwachung der Zellen möglich und schadhafte Zellen können sicher erkannt werden. Eine Variante des Messverfahrens erlaubt zudem den Verzicht auf die Strommessung, wenn lediglich die relative Verteilung der Innenwiderstände innerhalb eines Moduls bestimmt werden soll.

Für Starter-Batterien in konventionellen Fahrzeugen wurde ein Verfahren zur Vorhersage der Startfähigkeit ausgearbeitet. Auf Basis eines Ersatzschaltbildes des Systems, bestehend aus Anlasser und Batterie, lässt sich der Verlauf des Startstroms und der Batteriespannung während eines typischen Startvorgangs erklären und daraus Annahmen für die Prognose des Startvorgangs ableiten. So kann der Widerstand des Starters

und der Zuleitungen aus vergangenen Starts bestimmt werden und hieraus, zusammen mit dem Innenwiderstand der Batterie, der tiefste zu erwartende Spannungseinbruch während des folgenden Starts prognostiziert werden.

Für die Bestimmung des Innenwiderstandes wird ebenfalls das Verfahren zur passiven Impedanzmessung eingesetzt. Durch Wahl geeigneter digitaler Filter können so Impedanzwerte in verschiedenen Frequenzbereichen bestimmt werden. Die Eignung dieser Impedanzwerte für die Startfähigkeitsprognose hängt zum einen von den Eigenschaften der Batterie, zum anderen aber auch von den Charakteristika der Eingangssignale ab.

Für die Prognose des tiefsten Spannungseinbruchs erwies sich ein Frequenzbereich zwischen 100 und 400 Hz als optimal, da hier sowohl eine ausreichende Signalintensität im Bordnetz als auch eine gute Korrelation des Impedanzwertes in diesem Frequenzbereich mit dem im Zeitbereich erkennbaren Großsignal-Innenwiderstand der Batterie gegeben sind.

Das Mess- und Prognoseverfahren wurde in der Simulationsumgebung Matlab - Simulink entwickelt und erprobt. Als Datenbasis der Simulationen dienten Messreihen, die mit einem Batteriesensor aufgenommen wurden, der bereits in Serienfahrzeugen eingesetzt wird. Dadurch ist sichergestellt, dass die verwendeten Daten in allen Aspekten wie Auflösung, Abtastrate, Genauigkeit und Störungen denen im realen System gleichen.

Abbildung 7.11 zeigt die gemessene und prognostizierte Minimalspannung während einer Testfahrt mit einem konventionellen Fahrzeug der Kompaktklasse. Jeder deutliche Spannungseinbruch entspricht einem Startvorgang, der nach jedem Ampelstopp manuell durchgeführt wurde, um einen Stopp-Start-Betrieb in modernen Fahrzeugen zu emulieren. Zwischen Prognose und Messung der Startfähigkeit ergeben sich Abweichungen, die weniger als 3 % der Nennspannung der Batterie entsprechen.

Kapitel 8: Zusammenfassung und Ausblick

Die im Rahmen dieser Arbeit entwickelten Verfahren stellen einen Beitrag zur Batterieüberwachung in modernen Kraftfahrzeugen dar. Hierbei wurde die Impedanzspektroskopie als Diagnosewerkzeug zur Bestimmung des inneren Zustands des Energiespeichers verwendet. Für die Zustandsbestimmung von Energiespeichern ist die Impedanzmessung ein wertvolles Hilfsmittel, kann andere Verfahren jedoch nicht ersetzen, sondern nur ergänzen.

Die Anforderungen an die Impedanzmessung in einem Batterieüberwachungssystem unterscheiden sich grundlegend von Messungen im Laborumfeld. Daher wurde ein Verfahren für die passive Impedanzmessung im Fahrzeug entwickelt, das auf kostengünstiger Messtechnik implementiert werden kann und robust gegenüber Störungen ist. Dieses Verfahren wird bereits von Automobilherstellern und -zulieferern in aktuellen Serienentwicklungen zur Startfähigkeitsprognose eingesetzt. Die ebenfalls entwickelten Verfahren zur Nachführung von Kennfeldern ergänzen die Impedanzmessung, die jeweils nur eine Momentaufnahme des Batteriezustands erlaubt.

Zwei Speichersysteme wurden detailliert untersucht: der Doppelschichtkondensator bezüglich seines Alterungsverhaltens und die Blei-Säure-Batterie hinsichtlich ihrer Pulsbelastbarkeit. Für beide Systeme wurden grundlegende Untersuchungen durchgeführt sowie konkrete Anwendungsbeispiele ausgearbeitet und validiert.

Die entwickelten Verfahren sind auch auf andere Speichertechnologien übertragbar. So ist die Kenntnis sowohl der Alterung als auch der Pulsbelastbarkeit von Lithium-Ionen-Batterien ein wichtiger Aspekt bei der Betriebsführung in zukünftigen Hybridfahrzeugen. Bezüglich ihres elektrischen Verhaltens ähneln Lithium-Ionen-Batterien in einigen Aspekten der Bleibatterie, in einigen den Doppelschichtkondensatoren.

Eine Übertragung der beschriebenen Verfahren auf Energiespeicher in anderen Anwendungsgebieten ist ebenfalls möglich, Impedanzmessung und Kennfeldnachführung sind grundsätzlich auch nicht an Energiespeicher gebunden.

A.7 Lebenslauf

Persönliche Angaben

Name:	Oliver Sven Bohlen
Geburtsdatum:	1.4.1975
Geburtsort:	Zweibrücken
Adresse:	Schedelstraße 1, 80687 München
Eltern:	Peter Bohlen und Monika Bohlen (geb. Knerr)
Familienstand:	verheiratet mit Anja Wibranski

Schulausbildung

1981 - 1983	Städt. Gemeinschaftsgrundschule Knittkuhl, Düsseldorf
1983 - 1985	Breitenau-Grundschule Plön
1985 - 1987	Internatsgymnasium Schloss Plön
1987 - 1991	Gymnasium Walldorf
1991 - 1994	Gymnasium am Römerkastell Alzey, Abschluss Allgemeine Hochschulreife

Zivildienst

11/1994 - 01/1996	Naturschutzzentrum Hessen e.V. in Wetzlar, Bereich Umwelterziehung

Praktikum

04/1996 - 08/1996	Praktikum bei Wagner&Co. Solartechnik in Cölbe

Hochschulstudium

09/1996 - 02/2001	Studium der Physiktechnik an der Fachhochschule Ostfriesland in Emden
08/1998 - 12/1998	Praxissemester am Institut für Solare Energieversorgungstechnik ISET in Kassel
05/2000 - 01/2001	Diplomarbeit am Fraunhofer-Institut für Solare Energiesysteme ISE in Freiburg
02/2001	Abschluss des Studiums zum Diplom-Ingenieur (FH)

Berufliche Tätigkeit

02/2001 - 03/2001	Wissenschaftliche Hilfskraft am Fraunhofer-Institut für Solare Energiesysteme ISE in Freiburg
04/2001 - 06/2007	Wissenschaftlicher Mitarbeiter am Institut für Stromrichtertechnik und Elektrische Antriebe (ISEA) an der RWTH Aachen, Arbeitsgruppe Elektrochemische Energiewandlung und Speichersystemtechnik
seit 08/2007	Mitarbeiter der BMW AG in München